1000
15mm
10kV
20µm
X2000
#3548
512 X 480

Mechanism

Mechanism

Mechanism

SAMSUNG EX. 1002 - 1017/4148

Mechanism

SAMSUNG EX. 1002 - 1018/4148

Mechanism

SAMSUNG EX. 1002 - 1019/4148

Mechanism

SAMSUNG EX. 1002 - 1020/4148

Mechanism

SAMSUNG EX. 1002 - 1021/4148

SIONYX1403000045.0064

Light absorption

Total reflectance

SAMSUNG EX. 1002 - 1023/4148

Light absorption

Total transmittance

SAMSUNG EX. 1002 - 1024/4148

Summary

- Novel technique for producing spikes
- Unity light absorption
- Luminescence?
- Field emission?

SAMSUNG EX. 1002 - 1025/4148

Potential applications

- Photovoltaics
- Display technology
- Medicine

SAMSUNG EX. 1002 - 1026/4148

SAMSUNG EX. 1002 - 1027/4148

Other materials

SAMSUNG EX. 1002 - 1028/4148

XP-002539196

Sensors and Actuators A, 36 (1993) 209–217

Infrared detection using thermally isolated silicon diode

Yong-Ping Xu, Ruey-Shing Huang and Graham A Rigby
School of Electrical Engineering, University of New South Wales, P O Box 1, Kensington, NSW 2033 (Australia)

(Received June 2, 1992, in revised form December 8, 1992, accepted December 22, 1992)

Abstract

A new silicon-diode-based infrared thermal detector has been developed The silicon diode, as a temperature-sensing device, is built on a thin cantilever structure that is formed by micromachining The thickness of the cantilever is about 5 μm A thin layer of bismuth is evaporated on the cantilever as an infrared radiation absorber With cantilever dimensions of 264 μm × 112 μm × 5 μm and an active area measuring 102 μm × 102 μm, the fabricated detector array yields a responsivity of 5 3 V/W and a detectivity of $2\ 7 \times 10^7$ cm $Hz^{1/2}/W$ An improved silicon-diode-based infrared thermal detector is also proposed, its superior performance has been realized in a discrete form and will be implemented in an integrated form in the future

Introduction

Infrared (IR) detectors are generally divided into two categories IR photon detectors and IR thermal detectors The former are based on the interaction between the incident photons, quantized energy particles, and the electrons in the materials, while the latter are based on the effect of temperature change caused by the heat absorbed from incident radiation upon the detector Although the photon detector has high sensitivity and fast response, IR thermal detectors are still popular in some industrial and commercial applications, since they have a number of advantages including wide spectral response, room-temperature operation, and low cost There are several types of IR thermal detectors available, such as thermopiles [1, 2], bolometers [3], and pyroelectric devices [4] among others Thermopiles are based on the self-generating Seebeck effect, in which an external power-supply circuit is not needed and there is no offset in the output signal However, for thermopiles consisting of metal elements, generally speaking, a large number of metal strips is required to realize a relatively high sensitivity, since the Seebeck coefficients in metal materials are very low (typically, 50 μV/K) This will result in a detector with a large size, in order to accommodate the large number of strips Although the Seebeck coefficient in silicon thermopiles is rather high (typically, 0 5–1 mV/K), it is proportional to the logarithm of the resistivity of silicon strips [5] So the high sensitivity normally comes with a high ohmic resistance, which inherently has a large Johnson noise in the detector

This paper describes a new silicon-diode-based infrared thermal detector (SDITD) array, which is fabricated by standard IC processes and micromachining The detector structure and its fabrication processes are first described, then a theoretical analysis of the SDITD is given, in which the performance of the detector is calculated The experimental results of the detector are presented with some discussion Finally, a modified silicon-diode-based infrared thermal detector (MSDITD) is proposed, which has been constructed and tested in a discrete form This new detector can be readily integrated into a monolithic detector array

Detector structure and fabrication

The basic structure of the SDITD array is shown in Fig 1 The cantilever beam is formed to create a large thermal resistance between its suspended end and the silicon supporting rim Bismuth, a heat-absorption material, is evaporated on the cantilever to absorb the incident infrared radiation and generate a temperature difference between the cantilever beam and the silicon rim A silicon diode is fabricated in the cantilever, adjacent to the absorption area, acting as a temperature-sensing device When the silicon diode is forward biased at

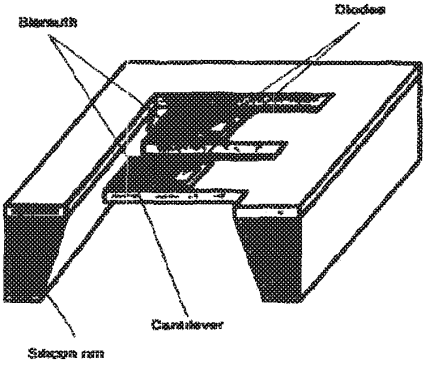
0924-4247/93/$6 00

© 1993 — Elsevier Sequoia All rights reserved

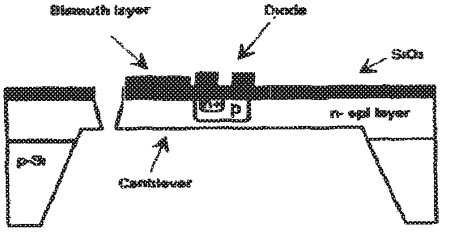
BNSDOCID: <XP_____2539196A_1_>

SIONYX1403000045.0071

SAMSUNG EX. 1002 - 1029/4148



(a)



(b)

Fig 1 Structure of the SDITD array (a) schematic diagram (b) cross section

a constant current, the voltage developed across the diode changes as a function of temperature Thus, the incident infrared radiation can be sensed by measuring the voltage change across the silicon diode

The SDITD array is implemented by standard IC processes and micromachining A p-type 8–15 Ω cm (100) silicon wafer is used as the starting material An n-type epilayer is grown on the substrate, with a resistivity of 4 Ω cm and a thickness of 15 μm Silicon membranes are first formed on the wafer by KOH anisotropic etching and the p–n junction stop technique [6] Since the etching starts from the p-type substrate and stops at the n-type epilayer, these membranes, where the detector arrays will reside, have the same thickness as the epilayer When the membranes are formed, a typical IC process is employed to fabricate the diodes After the metallization, the heat-absorbing layer of bismuth is evaporated on the membranes and defined by lift-off photolithography The final step of the process is to etch the membranes into

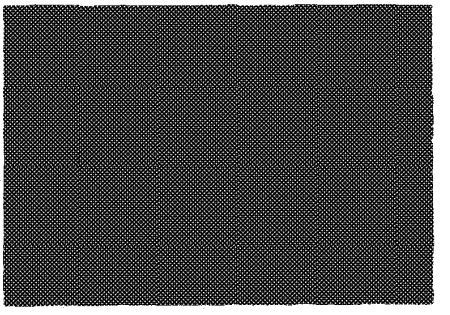


Fig 2 Photograph of a fabricated SDITD array

cantilevers, using plasma etching with photoresist as etching mask The wafer is first plasma etched from the frontside of the wafer to etch grooves to a depth that determines the thickness of the cantilever, this is followed by a backside blank etching to thin down the wafer The etching proceeds until the front grooves are reached and the cantilevers are formed The final thickness of the cantilever is about 5 μm After the cantilevers are fabricated, the photoresist is removed, and the detectors are ready for test A photograph of a fabricated detector is shown in Fig 2

Theoretical analysis

A thermal detector is typically characterized by the following parameters responsivity, noise equivalent power, specific detectivity, noise equivalent temperature difference and time constant The responsivity, R_v, is defined by

$$R_v = \frac{V_s}{\Phi_{in}} \tag{1}$$

where V_s is the output voltage of the detector and Φ_{in} is the incident radiation power

In the case of the silicon diode detector, the output voltage is proportional to the temperature difference, hence eqn (1) can be rewritten as

$$R_v = \frac{\alpha \Delta T}{\phi_{in} A_d} \tag{2}$$

where α is the temperature coefficient of the silicon diode voltage, ΔT is the temperature difference between cantilever and silicon rim, ϕ_{in} is the inci-

BNSDOCID: <XP_____2539196A_1_>

SIONYX1403000045.0072

SAMSUNG EX. 1002 - 1030/4148

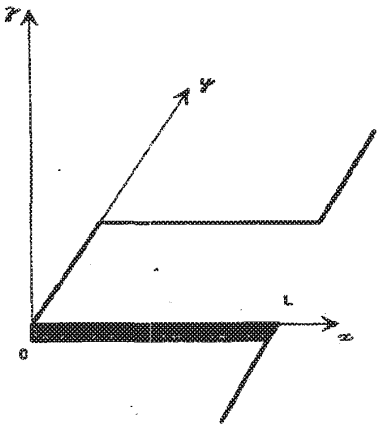


Fig 3 Coordinates arrangement for the temperature-difference simulation

dent radiation power density, and A_d is the active detector area

The temperature difference on the cantilever can be calculated using a two-dimensional model The coordinates are arranged as shown in Fig 3 According to the Fourier Law, the basic equation of heat transfer in a solid is

$$\rho c \frac{\partial u}{\partial t} = \kappa \nabla^2 u + \Phi' \tag{3}$$

where u is the temperature, ρ is the density of the material, c is the specific heat, κ is the thermal conductivity, and Φ' is the incident radiation power per unit volume

For the cantilever structure, if we assume that (a) there is no heat flow through conduction into or out of the edges of the cantilever and along the z direction ($\partial^2 u/\partial z^2 = 0$), and (b) the radiative loss through the air around the cantilever is negligible, then eqn (3) can be rewritten as

$$\frac{\partial u}{\partial t} = \frac{\kappa}{\rho c}\left[\frac{\partial^2 u}{\partial x^2} + \frac{\partial^2 u}{\partial y^2}\right] + \frac{\eta \phi_m}{\rho c d} \tag{4}$$

where ϕ_m is the incident radiation power density per unit area, η is the absorptance of the absorber, which is defined as the ratio of the absorbed radiation flux over the incident radiation flux [7], and d is the thickness of the cantilever In steady state, $\partial u/\partial t = 0$ and eqn (4) becomes

$$\frac{\partial^2 u}{\partial x^2} + \frac{\partial^2 u}{\partial y^2} = -\frac{\eta \phi_m}{\kappa d} \tag{5}$$

For the cantilever with n layers of different materials, the denominator, κd, can be simply replaced by $\Sigma_{i=1}^{n} \kappa_i d_i$, where the κ_i and d_i are the thermal conductivity and the thickness of the ith layer, respectively, if we assume that there is no temperature gradient along the z direction By applying the first central-difference approximation to second partial derivatives of temperature with respect to the distance, we have

$$\frac{\partial^2 u}{\partial x^2} = \frac{u_{i,j+1} - 2u_{i,j} + u_{i,j-1}}{\Delta x^2} \tag{6}$$

and

$$\frac{\partial^2 u}{\partial y^2} = \frac{u_{i+1,j} - 2u_{i,j} + u_{i-1,j}}{\Delta y^2} \tag{7}$$

With the coordinates arranged as shown in Fig 3 and the boundary condition $u = u_0$ when $x = L$, where u_0 is the temperature of the silicon rim and L is the length of the cantilever, the equation can be solved numerically for our detector, which has a cantilever consisting of two layers, silicon dioxide and silicon The thicknesses of the SiO_2 and silicon layers are 0 5 and 5 μm, respectively, and the thermal conductivities of SiO_2 and silicon are 0 14 [8] and 0 85 W/cm K [2], respectively. The size of the cantilever is 264 μm × 112 μm and the active area is 112 μm × 112 μm The incident radiation power density is 1 W/cm^2 The absorptance of the absorber η, is assumed to be equal to one in this simulation The result of the simulation is shown in Fig 4 Obviously, the temperature difference generated by the incident radiation along the

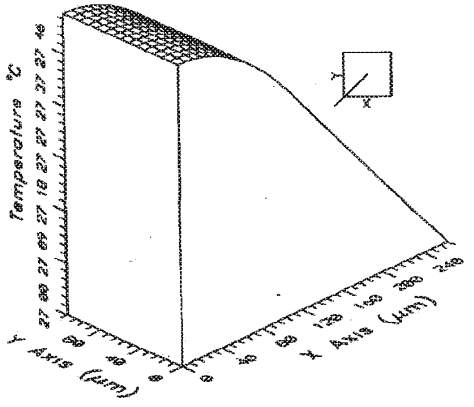


Fig 4 Simulated temperature distribution on the cantilever

BNSDOCID: <XP 2539196A_1_>

SIONYX1403000045.0073

SAMSUNG EX. 1002 - 1031/4148

cantilever is related to the distance from the silicon supporting rim the longer the distance, the higher the temperature difference

Silicon diodes are commonly used as temperature-sensitive devices, where, for a given current passing the diode, the forward p–n junction voltage drop is a measure of temperature The temperature coefficient of the p–n junction voltage can be estimated with some measured parameters, though it depends on the fabrication process The $I-V$ characteristic of the diode is

$$I_D(T) = I_s(T)\exp\left(\frac{qV_D}{kT}\right) \tag{8}$$

where I_D is the current through the diode, V_D is the voltage across the diode, q is the electron charge, k is the Boltzmann constant, T is the absolute temperature, and $I_s(T)$ is given by

$$I_s(T) = CT^3\exp\left(-\frac{qV_{G0}}{kT}\right) \tag{9}$$

where C is a constant, and V_{G0} is the band-gap voltage extrapolated to 0 K By substituting eqn (9) into eqn (8) and solving the diode junction voltage, we have

$$V_D(T) = V_{G0} + \frac{kT}{q}[\ln I_D(T) - \ln C - 3\ln T] \tag{10}$$

The term $\ln C$ in eqn (10) can be determined by letting $T = T_0$, the reference temperature, then

$$\ln C = \ln I_D(T_0) - 3\ln T_0 + \frac{q}{kT}[V_D(T_0) - V_{G0}] \tag{11}$$

If we substitute eqn (11) into eqn (10), and assume that the diode is biased at a constant I_D which is independent of the temperature, then V_D can be expressed by

$$V_D(T) = V_{G0} - \left[\frac{V_{G0} - V_D(T_0)}{T_0}\right]T - \frac{3k}{q}T\ln\left(\frac{T}{T_0}\right) \tag{12}$$

This equation shows that the diode voltage $V_D(T)$ is not linearly dependent on the temperature, but has higher-order components as well

In the temperature sensor, the higher-order terms introduce errors in measuring the temperature But, in the case of a thermal infrared sensor this is less significant, as the temperature range to be measured is rather small, being limited by the thermal resistance of the structure To estimate the error introduced by the higher-order components, we differentiate $V_D(T)$ with respect to T, and obtain

$$\frac{dV_D(T)}{dT} = -\left[\frac{V_{G0} + 3\dfrac{kT_0}{q} - V_D(T_0)}{T_0} + 3\frac{k}{q}\ln\left(\frac{T}{T_0}\right)\right] \tag{13}$$

If we approximate eqn (13) by the first three terms of its Taylor expansion at T_0, and let

$$\alpha = -\frac{V_{G0} + 3\dfrac{kT_0}{q} - V_D(T_0)}{T_0} \tag{14}$$

then eqn (13) becomes

$$\frac{dV_D(T)}{dT} \approx \alpha - \frac{3k}{q}\left[\frac{\Delta T}{T_0} - \frac{1}{2}\left(\frac{\Delta T}{T_0}\right)^2\right] \tag{15}$$

where $\Delta T = T - T_0$ and α is the linear term of the temperature coefficient, which is typically about -2 mV/K If the detector is operating at room temperature (300 K) and $\Delta T \ll T_0$, the error introduced by the higher-order term is

$$\varepsilon < 0\,87\Delta T \quad (\mu V/K) \tag{16}$$

ΔT is normally only a few degrees For example, if $\Delta T = 10$ K, the introduced error is only about 8 67 μV, which is less than 0 5% of the linear term In our case, with a measured $V_D(T_0)$ of 645 mV, the linear term α of the temperature coefficient is calculated to be $-1\,97$ mV/K For an incident radiation power of 1 W/cm^2, ΔT is 0 9 K, and the error calculated is only 0 78 μV, or 0 04% of the linear term Therefore, the temperature coefficient of diode voltage V_D can be approximated by the linear term α

With the calculated α and ΔT, the responsivity of the detector can be found from eqn (2) The result is shown in Fig 5, where the size of the cantilever is 264 μm × 112 μm, the active area is 112 μm × 112 μm, the thickness of SiO_2 is 0 5 μm, and the thickness of silicon is 5 μm The diode is located about 112 μm away from the cantilever tip, so the actual responsivity of the detector is about 6 5 V/W

The noise equivalent power (*NEP*) of a detector is defined as the required incident radiation power

BNSDOCID: <XP_____2539196A_I_>

SIONYX1403000045.0074

SAMSUNG EX. 1002 - 1032/4148

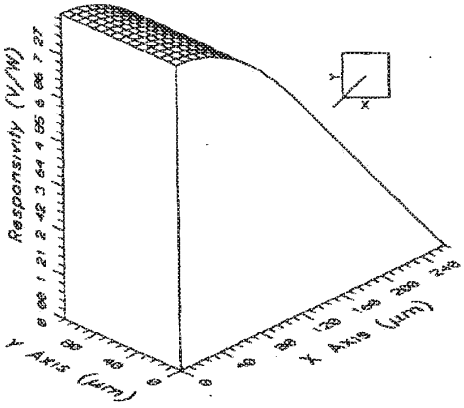


Fig 5 Simulated responsivity profile of the SDITD

when the signal-to-noise ratio of the detector equals one Thus

$$NEP = V_n/R_v \tag{17}$$

where V_n is the rms value of the noise voltage of the detector The detector noise is basically the noise of the diode, which consists of two noise sources, Johnson noise and shot noise If we assume that shot noise dominates the noise response, since the ohmic resistance, from which the Johnson noise originates, is usually very small in a diode, then the noise of the detector can be expressed as

$$v_n^2 = 2qI_D\,\Delta f \quad \text{or} \quad V_n^2 = 2qI_D r_D^2\,\Delta f \tag{18}$$

where $r_D = kT/qI_D$ With I_D operated at 100 μA, the calculated noise voltage is 1 5 nV/Hz$^{1/2}$, and the NEP of the detector is 2 3 × 10^{-10} W/Hz$^{1/2}$

The specific detectivity of the detector is defined by normalizing the NEP to detector active area and noise bandwidth

$$D^* = (A_d/\Delta f)^{1/2}/NEP \tag{19}$$

With A_d equal to 1 04 × 10^{-4} cm^2, D^* is 4 4 × 10^7 cm Hz$^{1/2}$/W

The detector time constant can be calculated by using a one-dimensional model If we assume that the thermal time constant is dominant, the time constant can be expressed as $\tau = H/K$, where H is the heat capacity of the cantilever and K is the thermal conductance from the diode to the silicon rim In our detector structure

$$\tau = pcLL'/\kappa \tag{20}$$

TABLE I SDITD performance

Parameter	Unit	Simulation	Measured value
Cantilever dimension	μm^2		264 × 112
Cantilever thickness	μm		5
Active area	μm^2		102 × 102
Responsivity, R_v (500 °C, 26 Hz)	V/W	6 5	5 3
Noise equivalent power NEP (500 °C)	W/Hz$^{1/2}$	2 3 × 10^{-10}	3 8 × 10^{-10}
Specific detectivity, D^* (500 °C, 1 Hz)	cm Hz$^{1/2}$/W	4 4 × 10^7	2 7 × 10^7
Time constant, τ	ms	0 78	1 8

where L is the length of the cantilever, measured as 264 μm, and L' is the distance between the diode and the silicon rim, which was measured as 144 μm For silicon, the density ρ is 2 33 g/cm^3, the specific heat c is 0 75 W s/g K, and κ is 0 85 W/cm K, so the time constant, τ, is calculated to be 0 78 ms Note that the time constant is directly proportional to the length of the cantilever Thus, in detector design a compromise must be made between responsivity and response time constant In the case of a thermopile detector, the minimum size of the detector is limited by the number of thermopiles, as a large number of thermocouples in series is normally involved It could be difficult to design if a faster detector is required For the diode-based detector, the design can be flexible, since the diode only occupies a small area, therefore, a faster detector can be achieved compared with the thermopile detector The calculated performance parameters of the detector are summarized in Table I

Experimental results and discussion

Fabricated detector chips are mounted in a DIP package with an opening window to pass infrared radiation The detectors are tested using a blackbody (500 °C) radiation source The detector is positioned 13 6 cm away from the blackbody without using any optical lens A chopper is placed between the detector and the blackbody The incident radiation power density is 10 mW/cm^2, which is calibrated by an infrared radiometer The actual incident radiation power upon the detector is 1 04 × 10^{-6} W The typical responsivity measured for these detectors is 5 3 V/W, which is slightly lower than the calculated value This is attributed

BNSDOCID: <XP_____2539196A_1_>

SIONYX1403000045.0075

SAMSUNG EX. 1002 - 1033/4148

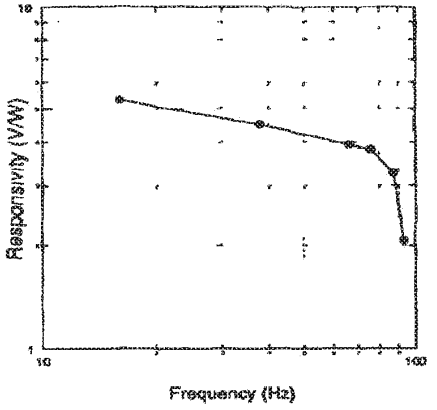


Fig 6 Frequency response of the responsivity of the SDITD

to the heat loss through the air, and the less than unity absorptance of bismuth The time constant is characterized by the measurement of the frequency response of the responsivity, and the result is shown in Fig 6 The corner frequency is estimated to be 90 Hz, which gives a time constant of 1 8 ms This is relatively fast for a thermal detector

The measured noise of the detector is very small, and its accuracy is limited by our measuring instrumentation set-up The estimated noise voltage of the detector is about 2 nV/Hz$^{1/2}$ The noise equivalent power, *NEP*, is measured to be $3\,8 \times 10^{-10}$ W/Hz$^{1/2}$, which corresponds to the minimum incident power density of $3\,6 \times 10^{-6}$ W/cm^2 Hz$^{1/2}$, and the measured specific detectivity is about $2\,7 \times 10^7$ cm Hz$^{1/2}$/W These measured results are summarized in Table 1

Noise is always a problem in thermal detector applications, since the output signal of the detector is normally very small The noise is not only from the detector itself, but also from external noise sources Therefore, the noise pick-up in the signal-conditioning circuit will reduce the signal-to-noise ratio of the whole system, especially when the output signal of the detector is very small compared to the noise pick-up One way to solve this problem is to increase the output signal level of the detector without losing much of its signal-to-noise ratio A modified silicon-diode-based infrared thermal detector (MSDITD) is proposed, as shown in Fig 7, designed for promoting its output signal level The detector incorporates a current mirror circuit by

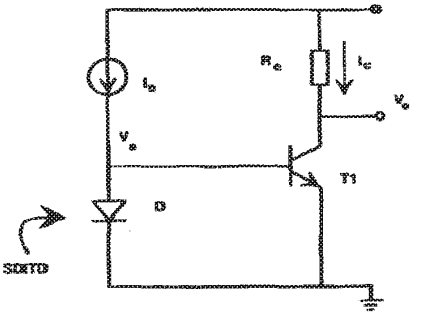


Fig 7 Schematic diagram of the MSDITD

adding a transistor to the SDITD, where the detector diode, D, is built on the cantilever and the transistor, T1, is on the bulk silicon The transistor here acts as a preamplifier, which amplifies the signal from the SDITD The advantage of this structure is that no extra biasing circuit is needed for the transistor Thus, the preamplifier is rather simple and can be readily integrated in the SDITD The output voltage at the collector of the transistor, i e , the output of the MSDITD, can be expressed simply by

$$V_0 = -g_m R_c V_s$$

where V_s is the output signal of the SDITD Obviously, in the MSDITD, the output signal of the SDITD is amplified by a factor of $-g_m R_c$ The same amplification factor applies to the responsivity of the MSDITD, R_{vm}, which can be represented as

$$R_{vm} = \frac{V_0}{\Phi_m} = -g_m R_c R_{vd}$$

where R_{vd}, equal to V_s/Φ_m, is the responsivity of the SDITD Thus, the responsivity of the MSDITD is also increased by the same factor

Apart from the responsivity, the additional noise originating from the transistor T1 also needs to be considered Applying a hybrid-π model to the transistor, the noise equivalent circuit of the MSDITD is drawn in Fig 8, where the circuit on the left-hand side of the dotted line represents the SDITD where V_s is the output signal voltage, $r_D = kT/qI_D$ is the output resistance, $E_{ns} = (2qI_D r_D^2)^{1/2}$ is the output noise voltage for unit bandwidth, and the noise on the ohmic resistance of the SDITD is neglected At the output, the signal-to-noise ratio of the MSDITD can be expressed by

BNSDOCID: <XP ___2539196A__I_>

SIONYX1403000045.0076

SAMSUNG EX. 1002 - 1034/4148

$$\frac{S_0^2}{N_0^2}=\frac{V_0^2}{V_{n0}^2}=\frac{g_m^2R_c^2V_s^2\dfrac{r_x^2}{(r_D+r'_{bb}+r_x)^2}}{E_{nc}^2+I_{nc}^2R_c^2+g_m^2R_c^2\dfrac{r_x^2}{(r_D+r'_{bb}+r_x)^2}[E_{ns}^2+E_{nb}^2+I_{nb}^2(r_D+r'_{bb})^2]} \tag{21}$$

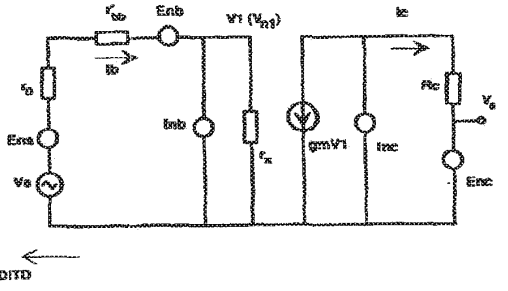


Fig 8 Noise equivalent circuit of the MSDITD

where $E_{nb}^2=4kTr'_{bb}$, $E_{nc}^2=4kTR_c$, $E_{ns}^2=2qI_Dr_D^2$, $I_{nb}^2=2qI_b$, $I_{nc}^2=2qI_c$ for unit bandwidth The $1/f$ noise is not considered at this stage, and will be discussed later in this Section If we choose $I_c=I_D$, hence $r_D=r_e=r_x/\beta$, and assume $(r_D+r'_{bb})\ll r_x$, eqn (21) can be rewritten as

$$\frac{S_0^2}{N_0^2}=\frac{V_s^2}{2qI_Dr_D^2}\frac{1}{2\left(1+\dfrac{1}{g_mR_c}+\dfrac{r'_{bb}}{r_D}\right)+\dfrac{1}{\beta}\left(1+\dfrac{r'_{bb}}{r_D}\right)^2} \tag{22}$$

or

$$\frac{S_0^2}{N_0^2}=\frac{S_i^2}{N_i^2}\frac{1}{2\left(1+\dfrac{r'_{bb}}{r_D}\right)}\leqslant\frac{1}{2}\frac{S_i^2}{N_i^2} \tag{23}$$

where $1/g_mR_c\ll 1$ and $(1+r'_{bb}/r_D)^2/\beta\ll 1$ are assumed, S_i, N_i represent the signal and noise at the input of the transistor, respectively Note that the factor $V_s^2/2qI_Dr_D^2$ in eqn (22) is the square of the signal-to-noise ratio of the SDITD, S_i^2/N_i^2 Therefore, for the MSDITD the maximum signal-to-noise ratio can be

$$\frac{S_0}{N_0}(\max)=\frac{\sqrt{2}}{2}\frac{S_i}{N_i} \tag{24}$$

which is lower than that of the SDITD, since there is extra noise contributed by the transistor T1 This will reduce the specific detectivity of the MSDITD According to the above analysis, we can conclude that compared with the SDITD, the responsivity of the MSDITD is increased by a factor of $-g_mR_c$, whereas its specific detectivity is decreased by at least about 30%

TABLE 2 Experimental results of MSDITD

Parameter	Unit	SDITD	MSDITD
Responsivity, R_v (500 °C, 26 Hz)	V/W	3 8	408
Noise voltage, V_n (at 26 Hz)	nV/Hz$^{1/2}$	1 5	690
Noise equivalent power, *NEP* (500°C)	W/Hz$^{1/2}$	$3\,9\times10^{-10}$	$1\,7\times10^{-10}$
Specific detectivity, D^* (500 °C, 1 Hz)	cm Hz$^{1/2}$/W	$2\,6\times10^{7}$	$6\,0\times10^{6}$
Time constant, τ	ms	1 8	1 8

While the experimental work on integrated monolithic MSDITD is yet to be pursued, a discrete MSDITD was constructed and tested A stand-alone SDITD was first measured, then an external transistor and a resistor were configured to the SDITD as in Fig 7 to form the MSDITD, where I_D was set to 100 μA and $I_c=136$ μA with $R_c=22$ kΩ Table 2 summarizes the measured results for the individual SDITD and MSDITD As expected, the responsivity of the MSDITD is increased by a factor of 107 compared to that of the SDITD, which is very close to the theoretical value of g_mR_c ($g_mR_c=115$) However, the detectivity is reduced by 70%, well below the estimated maximum reduction value (30%) This is believed to be due mainly to two factors First, the contribution from the $1/f$ noise in the transistor is not taken into account in the above theoretical analysis The noise measurement shows that the noise at low frequency (below 80 Hz) is about twice as much as that at a frequency above 80 Hz, as shown in Fig 9 Since the transistor used here is not specially designed for this purpose, the noise feature of the transistor can be improved by a proper device layout and processing designed for noise reduction to minimize the degradation in detectivity The second factor is the noise pick-up from the externally connected transistor T1, since any noise pick-up will degrade the noise equivalent

BNSDOCID: <XP_____2539196A__1_>

SIONYX1403000045.0077

SAMSUNG EX. 1002 - 1035/4148

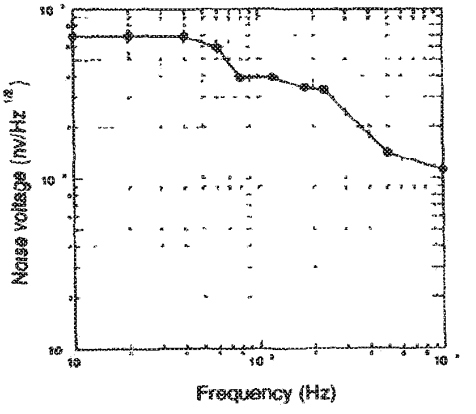


Fig 9 Measured noise spectrum of the MSDITD

power (*NEP*), and hence the specific detectivity This can be improved in the integrated MSDITD The time constant of the MSDITD remains the same as that of the SDITD, as it is essentially determined by the thermal capacity of the cantilever

Conclusion

A new silicon-diode-based infrared thermal detector has been developed The theoretical analysis, design, fabrication, and test results of the detector have been presented The detector uses a silicon diode, built on a cantilever structure, to sense the temperature difference generated by absorption of the incident IR radiation To ensure good IR absorption, an evaporated bismuth thin film was used as an IR absorption coating The detector was fabricated by standard IC processes and micromachining With a diode detector fabricated in a cantilever measuring 264 μm × 112 μm × 5 μm, a responsivity of 5 3 V/W and a specific detectivity of $2\,7 \times 10^7$ cm $Hz^{1/2}$/W were achieved The detector has a time constant of 1 8 ms, which is faster than that of other types of thermal detectors In order to promote the output signal level of the detector, a modified silicon-diode-based infrared thermal detector was also constructed and tested in a discrete form Compared with the simple SDITD, measured results of the modified detector demonstrate that while maintaining the fast time response, the responsivity was increased by a factor of 107, however, the specific detectivity was reduced by more than 70% The degradation in detectivity is attributed to the 1/*f* noise associated with the transistor and the noise pick-up from the externally connected transistor

Acknowledgements

The authors would like to thank Dr M Gross at the School of Electrical Engineering for performing plasma etching, Dr M Unewisse at the School of Physics for his assistance in detector testing, and the staff of the IC Laboratory at the School of Electrical Engineering for their general support, all from the University of New South Wales, Australia

References

1 P M Sarro, H Yashiro, A W van Herwaarden and S Middelhoek, An integrated thermal infrared sensing array, *Sensors and Actuators*, *14* (1988) 191–201
2 I H Choi and K D Wise, A silicon-thermopile-based infra-red sensing array for use in automated manufacturing, *IEEE Trans Electron Devices*, *ED-33* (1986) 72–79
3 T P Vogl, G A Shifrin and B J Leon, Generalized theory of metal-film bolometers, *J Opt Soc Am*, *52* (1962) 957–964
4 D L Polla, R S Muller and R M White Fully-integrated ZnO on silicon pyroelectric infra-red detector array, *Tech Digest, IEDM, San Francisco CA, USA, Dec 9–12 1984*, pp 382–384
5 G D Neveld, Thermopiles fabricated using silicon planar technology, *Sensors and Actuators*, *3* (1983) 179–183
6 T N Jackson M A Tischler and K D Wise, An electrochemical P–N junction etch-stop for the formation of silicon microstructures, *IEEE Electron Device Lett*, *EDL-2* (1981) 44–45
7 A Vasko, *Infra-red Radiation*, Iliffe Books, London, 1963, p 42
8 H F Wolf, *Semiconductors*, Wiley-Interscience, New York, 1971, p 87

Biographies

Yong-Ping Xu graduated from the Department of Physics, Nanjing University, Nanjing, China, in 1977 He joined the Qingdao Semiconductor Research Institute, Qingdao, China, in 1977, where he initially worked on integrated circuit processing technology, and later on the design of analog integrated circuits Since 1987, he has been with the School of Electrical Engineering, the University of New South Wales, Sydney, Australia From 1987–

BNSDOCID: <XP_____2539196A_1_>

SIONYX1403000045.0078

SAMSUNG EX. 1002 - 1036/4148

1988, he was a visiting research fellow at the Joint Microelectronics Research Center (JMRC), where he was involved in the development of solid-state sensors and analog integrated circuits Since 1989, he has been working towards the Ph D degree His current research interests are integrated circuit design, solid-state sensors, and micromachining technology

Ruey-Shing Huang received the B Eng degree from National Cheng Kung University, Taiwan, the M S degree from National Chiao Tung University, Hsinchu, Taiwan in 1969 and 1971, respectively, and the Ph D degree from the University of New South Wales, Sydney, Australia in 1978

He joined the Department of Electrical Engineering, Cornell University, Ithaca, USA, in 1978 as a post-doctoral research associate, where he was involved in the development of MESFET/SOS for high-frequency applications

From 1979–1986, he was a professor with the Department of Electrical Engineering, National Tsing Hua University, Hsinchu, Taiwan His research work was in the area of MOS integrated circuit technology and solid-state sensors In 1983–1984, he spent his study leave at the University of New Mexico, Alburquerque, USA, engaged in CVD nitride studies for MNOS radiation hard devices

In 1986 he joined the School of Electrical Engineering and Computer Science, University of New South Wales, Sydney, Australia His current interests are MOS integrated circuit design, SOI technology, and solid-state microsensors

Graham A Rigby received his B Sc and M Sc degrees from the University of Melbourne, Australia In 1966 he received a Ph D in electrical engineering from the University of California, Berkeley He was an assistant professor at the University of California, Berkeley, for the following two years In 1968 he joined AWA Microelectronics (Australia), initially as senior design engineer and later as group general manager In 1982 he was appointed professor of electrical engineering at the University of New South Wales and director of the Joint Microelectronics Research Centre He is currently head of the School of Electrical Engineering

Professor Rigby has served on many Government bodies, including the Australian Science and Technology Council and the Australian Research Council His research interests are in IC technology and analog IC design He is a fellow of the Australian Academy of Technical Sciences and Engineering, the Institution of Engineering (Australia) and the Institution of Radio and Electronic Engineers

BNSDOCID: <XP_____2539196A_I_>

SIONYX1403000045.0079

SAMSUNG EX. 1002 - 1037/4148

Intensity Enhancement in Textured Optical Sheets for Solar Cells

ELI YABLONOVITCH AND GEORGE D. CODY

Abstract—We adopt a statistical mechanical approach toward the optics of textured and inhomogeneous optical sheets. As a general rule, the local light intensity in such a medium will tend to be $2n^2(x)$ times greater than the externally incident light intensity, where $n(x)$ is the local index of refraction in the sheet. This enhancement can contribute toward a $4n^2(x)$ increase in the effective absorption of indirect-gap semiconductors like crystalline silicon.

I. Introduction

IN THE PAST DECADE, there have been a number of suggestions for the use of light trapping by total internal reflection to increase the effective absorption in the indirect-gap semiconductor, crystalline silicon. The original suggestions [1], [2] were motivated by the prospect of increasing the response speed of silicon photodiodes while maintaining high quantum efficiency in the near-infrared.

Subsequently, it was suggested [3] that light trapping would have important benefits for solar cells as well. High efficiency could be maintained while reducing the thickness of semiconductor material required. Additionally, the constraints on the quality of the silicon could be relaxed since the diffusion length of minority carriers could be reduced proportionate to the degree of intensity enhancement. With such important advantages, interest in this approach has continued, but progress in this field has been hindered because there was no method available to calculate the degree of enhancement to be expected.

For example, St. John [1] mentions that total internal reflection will result in two or more passes of the light rays with a proportionate intensity enhancement. On the other hand, Redfield [3] regards the number of light passes, or degree of enhancement, as an adjustable parameter which could vary anywhere between 1 and 100 and he plots the collection efficiency as a function of this parameter. In calculating the ideal efficiency of silicon solar cells, Loferski *et al.* [4] seemed to imply that perfect light trapping might be possible, which corresponds to an infinite degree of enhancement.

It is the purpose of this paper to show that the degree of intensity enhancement to be expected due to total internal reflection is $2n^2$ which for silicon is ≈ 25. In other words, a light ray in silicon may be expected to make 25 passes on average before escaping. With a proper angular average of the longer path length of oblique rays, the "effective" absorption enhancement factor is $4n^2$ over the case of single pass normally incident rays. Also, we will show that the geometrical details of the silicon shape are relatively unimportant. Whether the silicon is simply roughened on one side [1], [2] or whether precisely angled grooves are etched into the surface [3], [4], the overriding tendency will be for an enhancement factor of $4n^2$ provided only that the surface is sufficiently strongly textured. Finally, we will show that in an inhomogeneous sheet, for example a composite, the enhancement will be given by the same formula employing the local index of refraction $n(x)$.

Manuscript received May 25, 1981; revised September 28, 1981.

The authors are with the Corporate Research-Science Laboratories, Exxon Research and Engineering Co., Linden, NJ 07036.

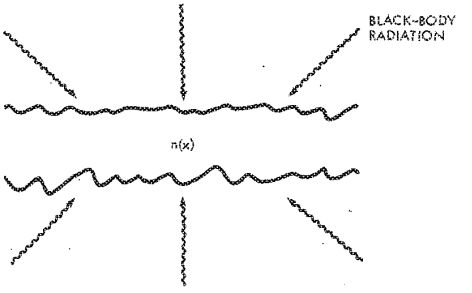


Fig. 1. An inhomogeneous and textured optical sheet with position-dependent index of refraction $n(x)$ immersed in black-body radiation.

Two distinct derivations will be presented in the following two sections. In Section II, we will give a derivation based on statistical mechanics. Such an approach is very powerful and it can be generalized to situations where geometrical optics is inapplicable (though we will not attempt such a generalization in this paper). In Section III, a geometrical optics derivation will be presented. Its simplicity will permit us to better recognize some of the prerequisites and limitations of this type of intensity enhancement. Finally, in Section IV, we will show how these considerations are modified in the presence of absorption. Two specific solar cell structures will be mathematically analyzed.

II. Statistical Mechanical Derivation

Consider an inhomogeneous optical slab with position-dependent index of refraction $n(x)$ as illustrated in Fig. 1. Let the index of refraction vary sufficiently slowly in space, so that a density of electromagnetic modes may be defined, at least locally inside the sheet.

Now place the optical medium into a region of space which is filled with black-body radiation in a frequency band $d\omega$ at a temperature T. When the electromagnetic radiation inside the medium approaches equilibrium with the external black-body radiation, the electromagnetic energy density [5] is

0018-9383/82/0200-0300$00.75 © 1982 IEEE

SIONYX1403000045.0080

SAMSUNG EX. 1002 - 1038/4148

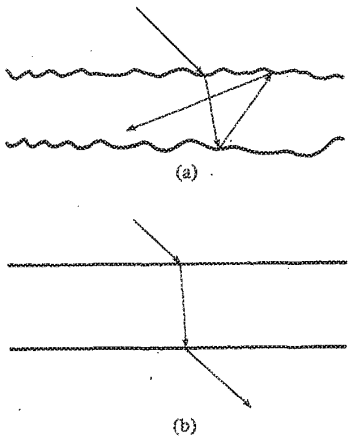


Fig. 2. Two optical sheets with qualitatively different surface textures. (a) Angular randomization and intensity enhancement do occur. (b) In a plane-parallel slab, there is no angular randomization and no intensity enhancement.

$$U = \frac{\hbar\omega}{\exp\{\hbar\omega/kT\} - 1} \frac{d\Omega k^2\, dk}{(2\pi)^3}. \tag{1}$$

This is the standard Planck formula for black-body radiation in a vacuum, but as Landau and Lifshitz show [5], it can be adapted to any optical medium by making $k = n\omega/c$. In addition, the energy density may be changed to an intensity I (power per unit area), by multiplying (1) by the group velocity $v_g = d\omega/dk$. Making both changes in (1) we obtain

$$I \equiv Uv_g = \frac{\hbar\omega}{\exp\{\hbar\omega/kT\} - 1} \frac{d\Omega n^2\, \omega^2}{(2\pi)^3\, c^2}\, d\omega. \tag{2}$$

This differs from the vacuum black-body intensity simply by the factor n^2. Therefore, the intensity of light in a medium which is in equilibrium with external black-body (bb) radiation is n^2 times greater

$$I_{\text{int}}(\omega, x) = n^2(\omega, x)\, I^{\text{bb}}_{\text{ext}}(\omega). \tag{3}$$

This factor comes about simply due to the fact that the density of states in such a medium is proportional to n^2 and the equipartition theorem guarantees equal occupation of the states, internal as well as external.

Now let us decide whether or to what degree the situation changes when an arbitrary external radiation field replaces the black-body radiation. Since we are considering a transparent medium, inelastic events such as absorption and reemission at another frequency are not permitted. Therefore, each spectral component may be considered individually. In this circumstance, departure of the external field from an exact black-body frequency distribution will not affect (3), which will remain valid separately at each frequency ω.

A much more serious question, which will be the main focus of this paper, is: What happens when the external radiation field departs from the isotropic distribution of black-body radiation? This situation is illustrated in Fig. 2(a), where the external light is shown to be collimated. If the surface of the optical sheet is quite irregular in shape, then the light rays, upon entering the medium, will lose all memory of the external incident angle after the first, or at most the second, scattering from a surface. In other words, all correlation with the external angle will be lost almost immediately upon refraction or total internal reflection, especially when averaged over the illuminated surface of the sheet. If this condition is satisfied, then a collimated incident beam of intensity I_{ext} will produce, inside the optical sheet, a random angular distribution of light, no matter which direction the beam happens to be coming from. Therefore, a collimated beam, when subdivided so that it illuminates the optical medium equally from all directions produces identical internal light distributions under those respective conditions. The condition of isotropic illumination is, however, equivalent to that of black-body illumination. Therefore, (3) remains valid whether the external field is isotropic as in the black-body case or whether it is collimated.

$$I_{\text{int}}(\omega, x) = n^2(\omega, x)\, I_{\text{ext}}(\omega). \tag{4}$$

Equation (4) will be corrected for certain surface transmission factors in Section III, but it is a key formula in this paper. It rests on the assumption that all correlation of the internal rays with the external angle of incidence is lost almost immediately upon entering the medium and/or upon averaging over the illuminated surface. Even optical sheets with ordered surface textures will show the type of randomization we are discussing here. The reasons are as follows:

a) If light randomization does not occur upon the entering refraction, it can occur on the first internal reflection.

b) If not on the first reflection, then on the second.

c) If not then, it can still be the result of a spatial average over the illuminated surface area.

d) If not even then, it can still result from angular averaging due to motion of the source, like the sun moving through the sky.

In other words, there is a rather overwhelming tendency toward randomization in the angular distribution of light and toward the validity of (4), but it is not always satisfied.

Consider the simple plane-parallel slab shown in Fig. 2(b). Clearly, there is no intensity enhancement in that case.[1] To distinguish between the class of geometries for which (4) is valid and the class of geometries in which it is invalid is a problem in ergodic theory and in measure theory. We will not attempt in this paper to distinguish between these two classes mathematically in the measure theory sense. Instead, we will assume that the statistical approach is valid except in those few geometries where a cursory inspection shows that randomization cannot occur under any of the circumstances listed earlier, a) to d). Equation (4) will be valid provided any of those prerequisites, a) to d), is satisfied.

Now consider the situation shown in Fig. 3. In that geometry, the light is confined to a half space by the presence of a white reflective plane. In effect, the light intensity external to the optical sheet has been doubled by virtue of reflection from the white surface. The total intensity enhancement will then be given by

[1] Another situation in which (4) is not valid is an optically thick turbid sheet illuminated from only one side. In this case, angular averaging is no problem, but spatial averaging will be incomplete. The side of the sheet away from the source of illumination will be dark.

SIONYX1403000045.0081

SAMSUNG EX. 1002 - 1039/4148

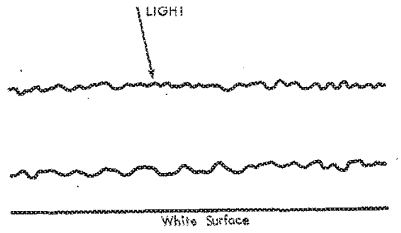


Fig. 3. A white reflective surface effectively doubles the external intensity and increases the enhancement factor to $2n^2$.

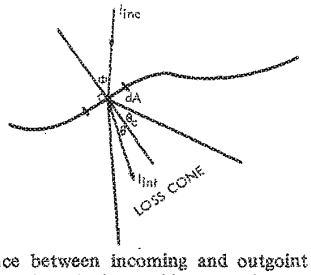


Fig. 4. The balance between incoming and outgoint radiation determines the internal intensity I_{int}.

$$I_{int}(\omega, x) = 2n^2(\omega, x)\, I_{inc}(\omega) \tag{5}$$

where $I_{inc}(\omega)$ is the incident light intensity.

One of the key implicit assumptions that we have not emphasized earlier is that there be no absorption, either within the volume or on the surface of the medium. Optical absorption effects will be treated in Section IV.

The main conclusion of this section is that a statistical mechanical approach results in the intensity enhancement given in (5). The factor $2n^2$ can be quite substantial; i.e., approximately 25 for silicon and approximately 15 for TiO_2. Even conventional glass with an index of 1.5 has an enhancement factor equal to 4.5. In view of the importance of this result, we give an alternative derivation based on geometrical optics in the next section.

III. Geometrical Optics Derivation

Our approach is based on "Detailed Balancing" of the light which is incident on a small area element dA, and the light in the loss cone which escapes from it. Consider the geometry shown in Fig. 4. Let I_{inc} be the incident radiation power per area element dA. A fraction $T_{inc}(\phi)$ of this light will be transmitted through the incoming interface, where ϕ is the angle of incidence. This must be balanced by the internal radiation which escapes. Let us assume that the internal radiation is isotropic due to the randomizing influence of refraction and reflection from the textured interfaces as discussed in the previous section. Let B_{int} be the internal intensity per unit internal solid angle. The internal intensity I_{int} on both sides of an area element dA is given by

$$I_{int} = \int B_{int} \cos\theta \, d\Omega$$

where $\cos\theta$ is the reduction of intensity on the area element due to oblique incidence. In this paper we will follow the convection that internal intensity I_{int} is bidirectional while the incident intensity I_{inc} is unidirectional. Therefore

$$I_{int} = 2 \times 2\pi \int_0^{\pi/2} B_{int} \cos\theta \sin\theta \, d\theta$$

$$I_{int} = 2\pi B_{int}.$$

Only a small fraction of this power per unit area will escape, since the loss cone solid angle is much less than 4π steradians. The intensity which escapes is

$$I_{esc} = 2\pi \int_0^{\theta_c} \frac{I_{int}}{2\pi} T_{esc}(\theta) \cos\theta \sin\theta \, d\theta \tag{6}$$

where $n \sin\theta_c = 1$ and θ is the internal angle of incidence. If we substitute a weighted average transmission factor $\overline{T_{esc}}$ for the angle-dependent surface transmission factor $T_{esc}(\theta)$, then the integral in (6) may be easily computed

$$I_{esc} = I_{int} \frac{\overline{T_{esc}}}{2n^2}.$$

If we now apply the principle of "Detailed Balancing," the entering intensity is made equal to the escaping intensity

$$T_{inc}(\phi)\, I_{inc} = I_{int} \times \frac{\overline{T_{esc}}}{2n^2}.$$

Therefore

$$I_{int} = 2n^2 \times \frac{T_{inc}(\phi)}{\overline{T_{esc}}} \times I_{inc}. \tag{7}$$

As (7) shows, the enhancement may be increased beyond $2n^2$ if $T_{inc}(\phi)$, the transmission factor into the medium, is greater than $\overline{T_{esc}}$, the average transmission factor out of the medium. Of course, time-reversal invariance guarantees that $T_{inc}(\phi) = T_{esc}(\theta)$. If the incident radiation is isotropic then the ratio $\overline{T_{inc}}/\overline{T_{esc}} = 1$ would appear in (7), ensuring that the enhancement factor is $2n^2$ as it must be for black-body radiation. For collimated radiation, an additional small enhancement $T_{inc}(\phi)/\overline{T_{esc}}$ is possible, but this comes at the expense of angular selectivity. This is fully consistent with the ordinary "Brightness Theorem" of geometrical optics [6], which states that intensity increases must come at the expense of angular selectivity. Because of the tendencies toward angular averaging described in Section II, the factor $T_{inc}(\phi)/\overline{T_{esc}}$ will be approximated as unity and, for most purposes, (7) can be rewritten

$$I_{int} = 2n^2 \times I_{inc}. \tag{8}$$

It is interesting that (8) itself could also have been derived directly from the "Brightness Theorem" [6] by taking note of the fact that the brightness defined in a medium differs from that in a vacuum simply by the factor n^2.

The intensity increases discussed thus far in this paper do not necessarily translate directly into absorption enhancements. This will be the subject of the following section.

IV. Absorption Enhancement

Two types of absorption can modify the results we have presented thus far; volume absorption in the textured optical sheet and surface absorption. In general, both types may be

SIONYX1403000045.0082

SAMSUNG EX. 1002 - 1040/4148

expected to be present. For example, in a semiconductor solar cell material, there would be absorption in the semiconductor itself and also at the surfaces due to absorption in the "transparent" electrodes, and due to imperfect reflectors at the rear surface. In this section, we will model the intensity-enhancement effects allowing for absorption. First we will set up a general method. Then we will model two specific geometries that might be of interest for solar cells.

The approach we will follow is to balance the input of light from external sources with the loss of light from the optical medium by absorption and refraction through the escape cone. The light input is $A_{\text{inc}} I_{\text{inc}} T_{\text{inc}}$, where A_{inc} is the surface area on which light is incident and the other symbols have the same meaning as before. To estimate the loss of light, we will proceed along the same lines as in Section III. We will assume that the light internal to the medium is isotropic due to the randomizing influence of refraction and reflection. There will be three contributions to light which is lost:

1) Light will escape through the escape cone at the rate

$$\frac{A_{\text{esc}} I_{\text{int}} \overline{T_{\text{esc}}}}{2n^2}$$

where A_{esc} is the surface area from which light can escape, which is not necessarily equal to A_{inc}, and the other symbols have the same meaning as before.

2) Light may be absorbed due to imperfect reflection from the boundaries

$$\int_0^{\pi/2} \eta A_{\text{refl}} I_{\text{int}} \cos\theta \sin\theta \, d\theta = \frac{\eta A_{\text{refl}} I_{\text{int}}}{2}$$

where η is the fractional absorption due to imperfect reflection at the boundaries and A_{refl} is the surface area of imperfect reflection.

3) Finally, there may be absorption within the bulk

$$\int \frac{\alpha I_{\text{int}}}{2\pi} \, dV \, d\Omega \approx \alpha l I_{\text{int}} A_{\text{inc}} \int_0^{\pi} \sin\theta \, d\theta = 2\alpha l I_{\text{int}} A_{\text{inc}} \quad (9)$$

where dV is a volume element in the bulk, α is the absorption coefficient, and (9) may be regarded as a definition of the effective thickness l. This will be approximately the mean thickness of the sheet. Equation (9) implicitly assumes that the bulk absorption is sufficiently weak that I_{int} is uniform throughout the volume.

Equating the light gained to the light lost

$$A_{\text{inc}} T_{\text{inc}} I_{\text{inc}} = \left\{ \frac{A_{\text{esc}} \overline{T_{\text{esc}}}}{2n^2} + \frac{\eta A_{\text{refl}}}{2} + 2\alpha l A_{\text{inc}} \right\} I_{\text{int}}. \quad (10)$$

Regarding I_{int} as the unknown, the expression may be rewritten

$$I_{\text{int}} = \frac{T_{\text{inc}} I_{\text{inc}}}{\{(A_{\text{esc}}/A_{\text{inc}})(\overline{T_{\text{esc}}}/2n^2) + (\eta/2)(A_{\text{refl}}/A_{\text{inc}}) + 2\alpha l\}}. \quad (11)$$

Although (11) is much more complex than (7) and (8), there are many realistic situations where the simpler expressions are adequate approximations.

One of the main questions we have in this paper is the extent to which the effects we have been discussing will act to enhance volume absorption. Using (11) the volume absorption may be written

$$2\alpha l A_{\text{inc}} I_{\text{int}} = \frac{2\alpha l A_{\text{inc}} T_{\text{inc}} I_{\text{inc}}}{\{(A_{\text{esc}}/A_{\text{inc}})(\overline{T_{\text{esc}}}/2n^2) + (\eta/2)(A_{\text{refl}}/A_{\text{inc}}) + 2\alpha l\}}.$$

The fraction of the incoming light which is absorbed in the volume is

$$f_{\text{vol}} \equiv \frac{2\alpha l A_{\text{inc}} I_{\text{int}}}{A_{\text{inc}} I_{\text{inc}}} = \frac{2\alpha l T_{\text{inc}}}{\{(A_{\text{esc}}/A_{\text{inc}})(\overline{T_{\text{esc}}}/2n^2) + (\eta/2)(A_{\text{refl}}/A_{\text{inc}}) + 2\alpha l\}}. \quad (12)$$

This reduces simply to the transmission factor T_{inc} of the incoming light in the limit of very high absorption coefficient α.

A corresponding expression may be written for the total fraction absorbed, including absorption due to imperfect reflection at the surfaces

$$f_{\text{tot}} = \frac{2\alpha l + (\eta/2)(A_{\text{refl}}/A_{\text{inc}})}{(A_{\text{esc}}/A_{\text{inc}})(\overline{T_{\text{esc}}}/2n^2) + (\eta/2)(A_{\text{refl}}/A_{\text{inc}}) + 2\alpha l} T_{\text{inc}}. \quad (13)$$

The absorption enhancement in (12) and (13) is of direct interest for weakly absorbing indirect-gap semiconductors like crystalline silicon. As (12) shows, volume absorption can be very substantial even when αl is only $1/4n^2$ which is 1/50 for silicon. The absorption enhancement factor is twice the intensity enhancement factor due to angle averaging effects. The use of these formulas is best illustrated by some specific examples.

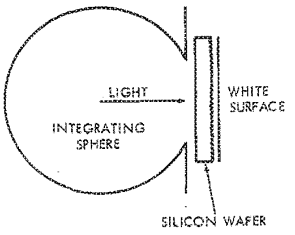


Fig. 5. The integrating sphere was used to determine the light absorbed in the silicon wafer. A comparison is made between the reflectivity of a wafer with a rough ground rear surface (as shown) and with a polished rear surface. In the former case, there was some light lost out the edges of the silicon wafer as well as by absorption.

Consider the reflectivity of a silicon wafer as measured on an integrating sphere, which is shown in Fig. 5. For these measurements, a white reflective medium was placed behind the wafer. The front surface of the wafer was polished. The main idea is to compare the overall reflectivity when the rear surface is either ground rough or polished smooth. The comparison is made in Fig. 6. With both surfaces polished, we have a plane parallel plate, the situation described in Fig. 2(b) where angular randomization within the silicon does *not* occur. The light simply makes a round trip in the wafer.

On the other hand, if the rear surface of the silicon is ground rough, internal angular randomization does occur. We may apply (12) and (13) to this situation. The Fresnel transmission of the silicon front surface T_{inc} is about 0.68. The areas A_{esc}

SIONYX1403000045.0083

SAMSUNG EX. 1002 - 1041/4148

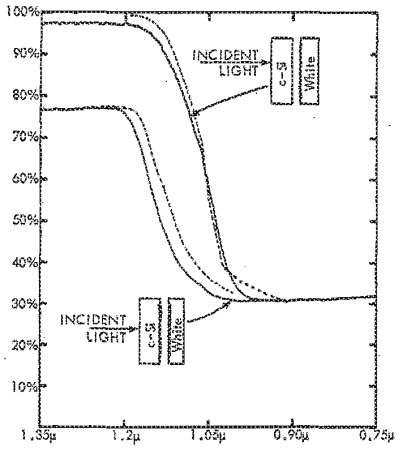


Fig. 6. The reflectivity of a silicon wafer whose rear surface is either ground rough or smoothly polished. Smooth lines are experiment. The dashed lines are theory. The theory for the rough ground surface is (13) in the text. The theory for the smooth polished surface assumes simple round-trip absorption.

and A_{inc} are the same and equal to the front surface area. The rear surface was covered with $MgCO_3$ an almost perfect white reflector, which is frequently used as a reference of whiteness. In the geometry of Fig. 5, the edges of the silicon wafer are actually external to the integrating sphere. Some of the internally trapped light, therefore, escapes across the cylindrical surface defined by the periphery of the round opening in the integrating sphere. This cylindrical surface in the silicon can be regarded as an imperfect reflector of area $A_{refl} = 2\pi rl$ where r is the radius of the opening in the integrating sphere. Therefore

$$A_{refl}/A_{inc} = 2\pi rl/\pi r^2 = 2l/r.$$

The parameters in this experiment were $r = 1$ cm and $l = 0.025$ cm. The quantity η which represents the departure from unit reflectivity at this edge is difficult to estimate *a priori*, since it depends on the details of the roughness. The value $\eta = 0.82$ describes well the wavelength-independent backscattered light in Fig. 6 in the transparent region between 1.2 and 1.35 μm. With these values for parameters and the known wavelength-dependent [7] absorption coefficient, a fairly good fit is obtained between $(1 - f_{tot})$ from (13) and experiment through the band-edge transition wavelengths (dashed and smooth lines, respectively, in Fig. 6).

The geometry described in Figs. 5 and 6 is a very favorable one for solar cells and was first described [1], [2] some time ago. Fig. 6 shows clearly the shift of the effective absorption edge toward the infrared for the light-trapping case.

Another geometry which has received some interest [8], consists of grains of silicon embedded in a glass sheet as shown in Fig. 7. It has already been recognized that the light which falls in the glass between the grains is not wasted. It tends to be trapped and eventually find its way into the silicon grains. We may analyze that situation in a similar way as previously. Let us denote the quantities pertaining to the incident light by the subscript 1, those pertaining to the silicon by the subscript

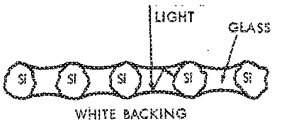


Fig. 7. A composite sheet consisting of silicon grains in a glass matrix. The theory in the text shows that even the light which falls between the grains will tend to be absorbed ultimately by the silicon.

2, and those pertaining to the glass by subscript 3. Let us also assume that the white backing layer is perfectly reflective. The energy balance for the glass may be written

$$\frac{A_{23}\bar{T}_{23}I_2}{2(n_2/n_3)^2} + A_{13}T_{13}I_1 = \left(\frac{A_{13}\bar{T}_{13}}{2n_3^2} + \frac{A_{23}\bar{T}_{23}}{2}\right)I_3 \quad (14)$$

where the first expression on the left-hand side is the light escaping from the silicon into the glass and the second expression is the incident light. On the right-hand side are the two terms describing the escape of light into the air and into the silicon, respectively. A similar energy balance may be written for the silicon

$$\frac{A_{23}\bar{T}_{23}I_3}{2} + A_{12}T_{12}I_1 = \left(\frac{A_{12}\bar{T}_{12}}{2n_2^2} + \frac{A_{23}\bar{T}_{23}}{2(n_2/n_3)^2} + 2\alpha l A_{12}\right)I_2. \quad (15)$$

Here there is an additional term due to absorption and l represents a typical absorption thickness of the silicon grain. Equations (14) and (15) should be regarded as two simultaneous equations in the two unknowns I_2 and I_3. A specific numerical solution would be helpful in estimating the extent to which light falling between the grains tends to be wasted. For this purpose, let us assume that the area of the sheet occupied by the silicon grains A_{12} equals the area A_{13} filled in by the glass. For numerical simplicity, let us assume also that A_{23} is also the same area. For the indices of refraction take $n_2 = 3.53$ in the silicon and $n_3 = 1.5$ in the glass. For the transmission factor $\bar{T}_{23}$ of the glass-silicon interface, take the normal incidence Fresnel reflectivity, $1 - (n_2 - n_3)^2/(n_2 + n_3)^2 = 0.84$. Let us assume there is an antireflection coating for the incident rays into the silicon so that $T_{12} \approx 0.96$ which is the same as the transmission coefficient into the glass. With these values of parameters, the simultaneous equations (14) and (15) can be solved

$$I_2 = \left(\frac{0.8316}{\alpha l + 0.0319}\right)0.96I_1 \quad (16)$$

where $0.96I_1$ is the transmitted incident intensity, and the quantity in parentheses is a type of enhancement factor. The important implications of (16) become apparent only upon examination of its various limits. Consider, for example, the situation in the region of wavelengths within the bandgap of silicon where $\alpha = 0$. Then

$$I_2 = \frac{0.8316 \times 0.96}{0.0319}I_1$$

which just happens to be $25I_1 = 2n_2^2 I_1$. This, of course, must be according to the considerations of Section II.

SIONYX1403000045.0084

SAMSUNG EX. 1002 - 1042/4148

The most important parameter we are interested in is the absorption in the silicon. This may be expressed as

$$2\alpha l I_2 = \frac{1.6632\,\alpha l}{0.0319 + \alpha l} \times 0.96 I_1 \tag{17}$$

when normalized to the area of the silicon grains.

In the limit of very small αl the enhancement factor is $2n_2^2$ as before. In the limit of large αl, i.e., in the visible wavelength range for silicon

$$\lim_{\alpha \to \infty} 2\alpha l I_2 = 1.6632 \times 0.96 I_1 . \tag{18}$$

According to (18), the power absorbed by the silicon exceeds the power actually falling on the silicon by a factor 1.6632 This is because the silicon collects not only those rays which it intercepts directly, but also a major fraction of those intercepted by the glass. Since only a fraction of the incident light will tend to escape the glass, the balance (≈ 0.66) will tend to be collected by the adjacent silicon grains. In other words, 83 percent of the light which enters the sheet will end up being used, in spite of the fact that the area coverage of the silicon grains is only 50 percent. If the surface area ratios were more favorable than the conservative assumptions in this calculation, then an even greater fraction of the light would end up in the silicon. The extraordinary utility of the structure described in Fig. 7 is doubly confirmed when it is also realized that because of the enhancement in the low-absorption regime, the thickness of the layer of grains can be reduced by 50. Therefore, all the advantages of a thin solar cell, mentioned in the Introduction of this paper would accrue to the structure in Fig. 7. Not the least of which is the likelihood of that structure being cheaper to fabricate than conventional silicon solar cells.

The methods described in this section are meant to suggest the approach which can be used for intensity enhancement in the presence of absorption. Refinements are still needed for the high-absorption case. The formulas given here tend to underestimate the absorption in that instance, since they assume randomization; but the absorption may be complete before randomization sets in.

In this paper, we have shown the utility of a statistical mechanical approach toward the optics of textured and inhomogeneous sheets. This work was mainly motivated by its applicability toward solar cells and other types of solar collectors. The basic enhancement factor for intensity of $2n^2$ becomes $4n^2$ for bulk absorption and n^2 for surface absorption, due to angle averaging effects. It is because many semiconductors tend to have large indices of refraction n, that these effects are particularly important in those materials.

Acknowledgment

The authors would like to thank Prof. R. M. Swanson for pointing out an error in the original manuscript.

References

[1] A. E. St. John, "Multiple internal reflection structure in a silicon detector which is obtained by sandblasting," U.S. Patent 3 487 223, 1969.

[2] O. Krumpholz and S. Maslowski, "Schnelle photodioden Mit Wellenlangen unabhangigen Demodulationseigenschaften," *Z. Angew. Phys.*, vol. 25, p. 156, 1968.

[3] D. Redfield, "Multiple-pass thin-film silicon solar cell," *Appl. Phys. Lett.*, vol. 25, p. 647, 1974.

[4] M. Spitzer, J. Shewchun, E. S. Vera, and J. J. Loferski, "Ultra-high efficiency thin silicon p-n junction solar cells using reflective surfaces," in *Proc. 14th IEEE Photovoltaic Specialists Conf.* (San Diego, CA, 1980), p. 375.

[5] L. D. Landau and E. M. Lifshitz, *Electrodynamics of Continuous Media.* New York: Pergamon, 1969.

[6] M. Born and E. Wolf, *Principles of Optics.* New York: Macmillan, 1964.

[7] M. Neuberger and S. J. Welles, *Silicon.* Springfield, VA: Clearinghouse for Federal Scientific and Technical Information, 1969, p. 113.

[8] J. S. Kilby, J. W. Lathrop, and W. A. Porter, "Light energy conversion," U.S. Patent 4 136 436, 1979. T.S.T. Velde, "Electrical monograin layers and method for making same," U.S. Patent 3 625 688, 1971.

SIONYX1403000045.0085

SAMSUNG EX. 1002 - 1043/4148

Nuclear Instruments and Methods in Physics Research A 624 (2010) 520–523

Contents lists available at ScienceDirect

Nuclear Instruments and Methods in Physics Research A

journal homepage: www.elsevier.com/locate/nima

NIR sensitivity enhancement by laser treatment for Si detectors

K. Yamamoto [a], A. Sakamoto [a,*], T. Nagano [a], K. Fukumitsu [b]

[a] Solid State Division, Hamamatsu Photonics K.K., 1126-1, Ichino-cho, Higashi-ku, Hamamatsu City, Japan
[b] Electron Tube Division, Hamamatsu Photonics K.K., 314-5, Shimokanzo, Iwata City, Japan

ARTICLE INFO

Available online 31 March 2010

Keyword:
NIR sensitivity enhancement

ABSTRACT

The light absorption coefficient of silicon is high in the short wavelengths, but much lower in the long wavelengths (longer than 900 nm). Thus it is necessary to use thicker silicon wafers to manufacture high-sensitivity light sensors for long wavelength applications. However, this imposes constraints on applied voltage, dark current, response speed, and cost. This then leads to limitations on device characteristics and possible applications.

As an alternative to using thicker silicon wafers to enhance the NIR sensitivity of silicon photodiodes, we used an ultra-short pulse laser to form "black silicon" structures on the surface of silicon photodiodes. At 1064 nm, QE was improved from 25% to 72%. Future research will determine how this technology can also be applied to enhancing the NIR sensitivity of image sensors such as CCDs.

© 2010 Elsevier B.V. All rights reserved.

1. Introduction

The light absorption coefficient of silicon is high at short wavelengths, so ultraviolet and visible light are fully absorbed. On the other hand, most near-infrared light is not absorbed because of the extremely low absorption coefficient, so the NIR sensitivity of a silicon detector is relatively lower. Fig. 1 shows absorption length and coefficient for silicon. Absorption length is the length at which incident light attenuates to $1/e$ (37%) by absorption. It is more than 250 μm for 1064 nm wavelength light, though only 10 μm for approx. 830 nm wavelength light. Therefore, thicker silicon wafers must be used to enhance NIR sensitivity [1].

Currently, most photodetectors for NIR applications – such as photodiodes (PD), avalanche photodiodes (APD), charge-coupled devices (CCD), complementary metal oxide semiconductor (CMOS) devices – are manufactured from thicker wafers. Although this improves NIR sensitivity, it leads to some other difficulties. For instance, response speed becomes slower due to long carrier drift time and large resistance for detectors that have a long active layer. Also, it becomes necessary to apply a higher voltage for full depletion (Fig. 2). This is especially a concern with APDs, which use high voltage to produce high gain. Devices must be designed in such a way that the higher voltage requirement does not significantly increase dark current. The relation between response speed and sensitivity is a trade-off, making NIR silicon detectors inconvenient.

In our search to improve NIR sensitivity and response speed at the same time, we examined the "black silicon" structure. Microstructures of wavelength order were created on the surface of silicon by using an ultra-short pulse laser (Fig. 3). Such microstructures were intended to capture the long wavelength light that escapes normal silicon. In theory, this would increase the possibility of absorption, and thus produce enhanced sensitivity [2,3].

2. Surface treatment by ultra-short pulse laser

When materials are irradiated by a short-pulse laser (msec to nsec), they evaporate and the heated part melts and is removed. The size of the processed part is more than a micron. However, when an ultra-short pulse laser (psec to fsec) is used, the irradiation ends before generating heat and it enables formation of nanometer-sized microstructures.

Fig. 4 shows microscopic images of irradiated titanium samples by (a) nsec and (b) psec lasers. The laser wavelength was 1064 nm (ND:YAG laser) with a spot size diameter of 100 μm. Fig. 4(a) shows that the surface melted and only the processing of the spot size was obtained. By comparison, Fig. 4(b) shows microstructures smaller than the laser wavelength. It is surmised that these microstructures are formed by the interference between the incident light and scattering waves/plasma waves on the surface of the material, and the minimal thermal effects thereof. This principle was applied to the formation of black silicon structures in our research [4,5].

* Corresponding author.
E-mail address: akira-s@ssd.hpk.co.jp (A. Sakamoto).

0168-9002/$ - see front matter © 2010 Elsevier B.V. All rights reserved.
doi:10.1016/j.nima.2010.03.128

SIONYX1403000046.0001

SAMSUNG EX. 1002 - 1044/4148

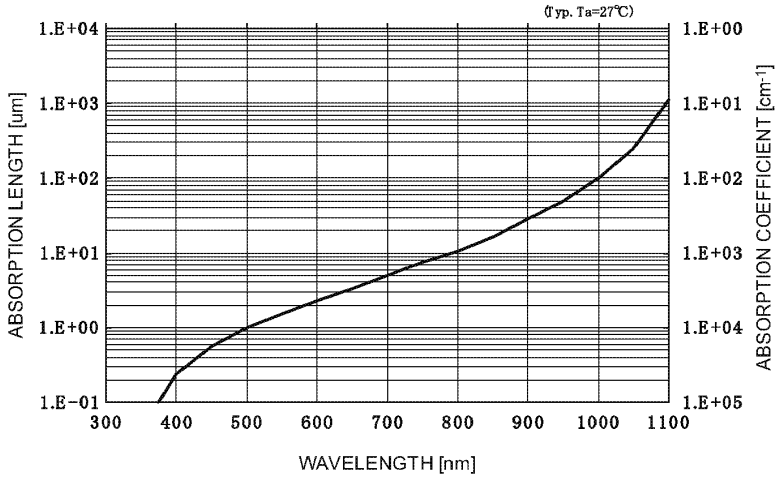


Fig. 1. Light absorption length of silicon [1].

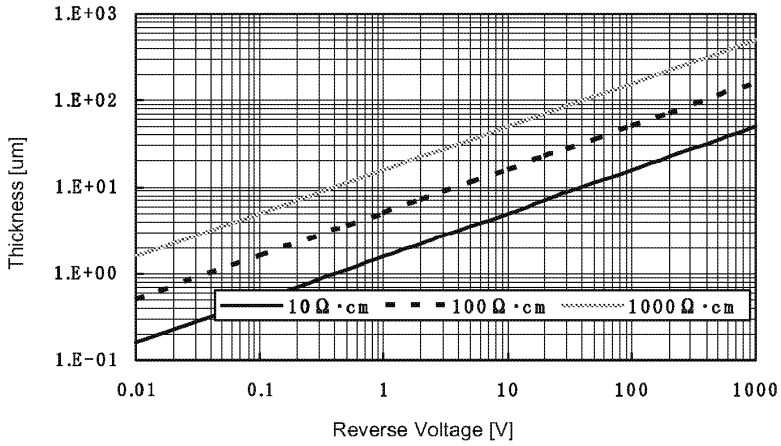


Fig. 2. Relation of full-depletion voltage of Si PD to wafer thickness.

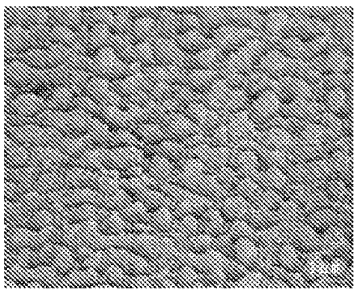


Fig. 3. SEM image of black silicon structure.

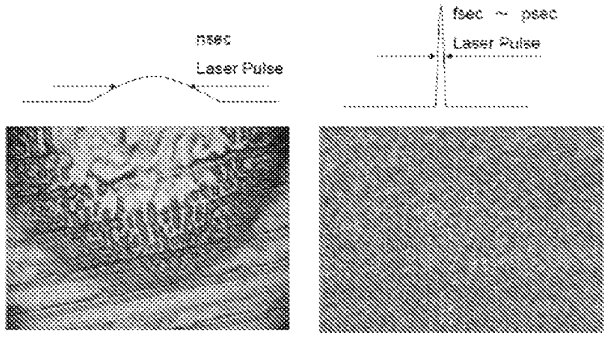


Fig. 4. Laser irradiation on Ti.

3. Optimization of laser conditions

A Ti:Sapphire laser (800 nm, 1 kHz) was used to process the silicon surface. First, we investigated the relation between the microstructure and transmittance. Absorption and transmittance are related by the following equation:

$$A = 1 - T - R$$

where A, T, and R are the absorption, transmittance, and reflection, respectively. Black silicon structure was formed on the backside

SIONYX1403000046.0002

SAMSUNG EX. 1002 - 1045/4148

Table 1
Typical laser conditions.

	Sample 1	Sample 2	Sample 3
Laser	–	Ti:Sapphire	
Wavelength	–	800 nm	
Frequency	–	1 kHz	
Energy	–	300 μj	400 μj
Microstructure size	–	<1 μm	$\fallingdotseq 1$ μm

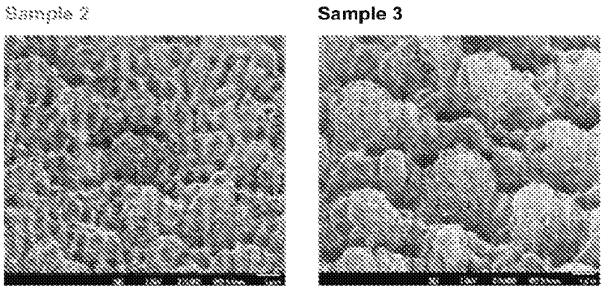


Fig. 5. SEM images of microstructures.

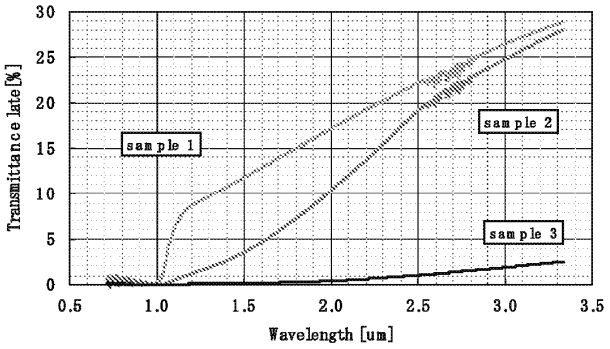


Fig. 6. Relation between structure and light transmittance.

silicon surface so that reflection is the same. We tried several laser conditions and measured the transmittance of samples. Table 1 shows typical conditions. Corresponding to Table 1, Fig. 5 shows SEM images of two samples and Fig. 6 shows transmittance. There is a remarkable difference of transmittance according to the structure. At the wavelength of 1064 nm, transmittance late of sample 3 has been improved to 1/100, compared with sample 1. We adopted the laser conditions that showed the lowest transmittance (condition for sample 3) for the processing of silicon photodetectors.

4. Development for NIR-enhanced Si photodiodes

We used standard type Si photodiodes by Hamamatsu Photonics (Figs. 7 and 8). They are 5 mm diameter in size and 0.27 mm thick. The backside surface was processed by the ultra-short pulse laser, and black silicon structure was formed. We measured the photosensitivity on the condition of 0 biases of the processed PDs and compared them to a reference PD which was not processed by an ultra-short pulse laser. Fig. 9 shows the photosensitivity of the processed PDs. Sensitivity was improved in the range from 950 to 1150 nm. At the wavelength of 1064 nm, quantum efficiency improved from 25% to 72%.

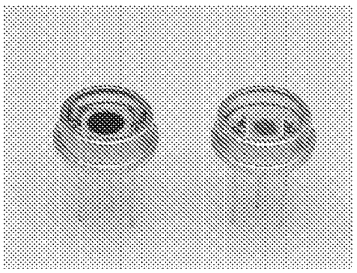


Fig. 7. Si photodiode and APD.

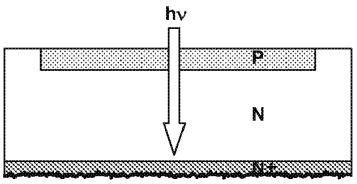


Fig. 8. Si photodiode cross-section.

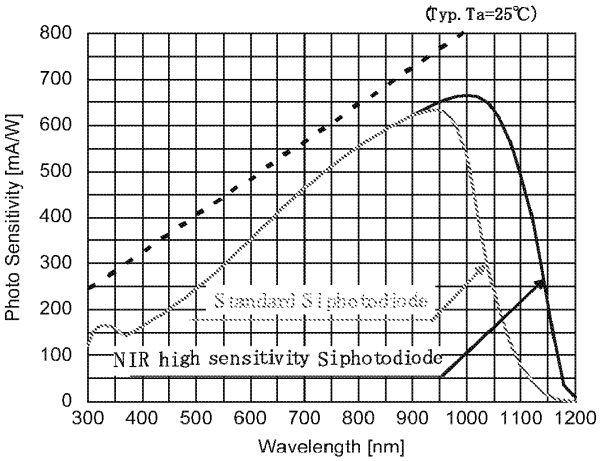


Fig. 9. Spectral response characteristics.

According to the transmittance data, absorption in the silicon increased even at wavelengths longer than 1200 nm, but sensitivity of the PD did not increase. The effect of laser processing was simply a large part of the light reflected back into the silicon bulk and to increase the length of the light path of long-wavelength light, with no effect on the bandgap of the silicon. For this reason, light above the cut-off wavelength of silicon (1200 nm), even if it was absorbed, did not generate an electron–hole pair and affect the sensitivity of the PD as such.

In addition to sensitivity, temperature dependence is an important characteristic of Si PDs. Sensitivity generally improves with an increase of the absorption coefficient and a decrease of the bandgap energy when temperature rises. This can be seen particularly at long wavelengths. We measured the temperature coefficient using the same laser-processed PDs as above. Results are shown in Fig. 10. At 1064 nm, temperature coefficient improved from 0.6%/°C to 0.2%/°C. Because the laser-processed PD has higher sensitivity at NIR wavelengths than the reference PD, the effect of temperature on sensitivity was extremely small.

SIONYX1403000046.0003

SAMSUNG EX. 1002 - 1046/4148

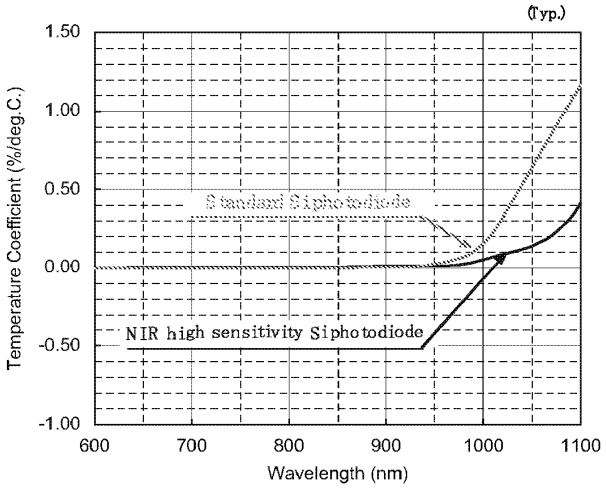


Fig. 10. Temperature-dependence characteristics.

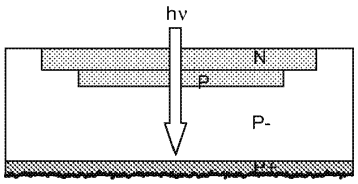


Fig. 11. APD cross-section.

5. Applied development to APD

Similarly, we performed laser material processing of Si APDs and performed the spectral sensitivity measurement. This was done on an Si APD with a light-sensitive area of 3 mm diameter and wafer thickness of 0.15 mm. An Si APD with the same structure but which was not laser processed was used for comparison Fig. 11.

The photosensitivity of both surface incidence and backside incidence was measured on the condition of full depletion bias, as shown in Figs. 12 and 13, respectively. Since the effective area of APD is small, backside incidence was also evaluated because of its decreased capacity and its ability to handle high-speed response. Unlike conventional photodiodes, an avalanche gain effect can be produced in APDs when high voltage is applied, thus increasing sensitivity.

Measurements of surface incidence and backside incidence confirmed a shift in the peak sensitivity wavelength to the long wavelength side. As mentioned above, the application of high voltage to an APD does increase the device's sensitivity in the NIR region, although this does not shift the wavelength of peak sensitivity. However, as a result of laser processing by ultra-short pulse laser, even at low bias the APD demonstrated high sensitivity at long wavelengths.

6. Summary

As an alternative method to using thicker silicon wafers to improving the NIR sensitivity of photodetectors, the application of laser processing to form "black silicon" microstructures on an Si photodiode was investigated. The following characteristics were obtained from a processed Si photodiode: QE increase from 25% to 72% (λ=1064 nm), and temperature coefficient improvement from 0.6%/°C to 0.2%/°C (λ=1064 nm). Future investigation will determine how this method can be applied to improve the NIR characteristics of image sensors.

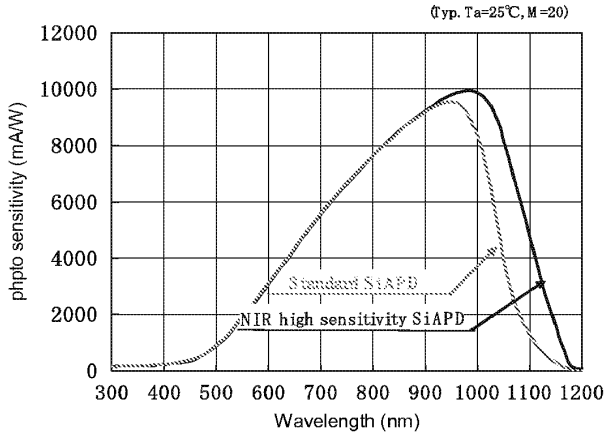


Fig. 12. Spectral response characteristics.

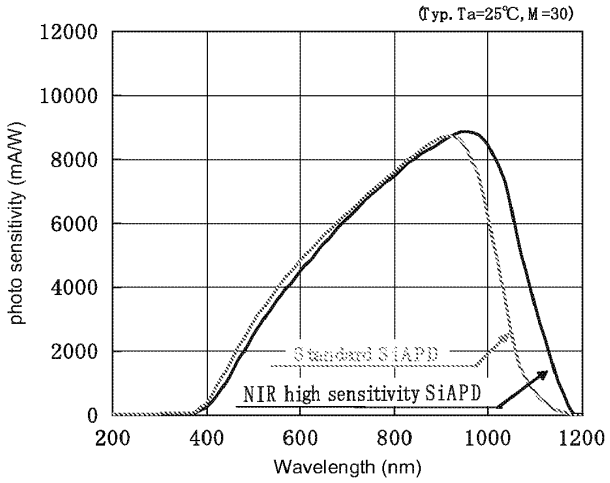


Fig. 13. Spectral response characteristics.

References

[1] W.C. Dash, R. Newman, Phys. Rev. 99 (1955) 1151.
[2] James E. Carey, Catherine H. Crouch, Mengyan Shen, Eric Mazur, Opt. Lett. 30 (14) (2005) 1773 July.
[3] Zhihong Huang, James W. Carey, Mingguo Liu, Xiangyi Guo, Eric Mazur, Joe C. Campbell, Appl. Phys. Lett. 89 (2006) 033506.
[4] B.N. Chichkov, C. Momma, S. Nolte, F. Alvensleben, A. Tunnermann, Appl. Phys. A 63 (1996) 109.
[5] E.E.B. Campbell, D. Ashkenasi, A. Rosenfeld, Mater. Sci. Forum 301 (1999) 123.

SIONYX1403000046.0004

SAMSUNG EX. 1002 - 1047/4148

Two-Stage Charge Transfer Pixel Using Pinned Diodes for Low-Noise Global Shutter Imaging

Keita Yasutomi [1], Shinya Itoh [1], Shoji Kawahito [1] and Toshihiro Tamura [2]

[1]Shizuoka University, 3–5–1, Johoku, Hamamatsu, Shizuoka, 432–8011 Japan
[2]Photron Ltd., Imaging Division Product Development Group, Japan

Abstract— **This paper describes a new type of global electronic shutter pixel for CMOS image sensors. A global electronic shutter is necessary for imaging fast-moving objects without motion blur or distortion. The proposed pixel has two potential wells with pinned diode structure for two-stage charge transfer that enables a global electronic shuttering and reset noise canceling.**

A prototype high-speed image sensor fabricated in 0.18μm standard CMOS image sensor process consists of the proposed pixel array, 12-bit column-parallel cyclic ADC arrays and 192-channel digital outputs. The sensor achieves a good linearity at low-light intensity, demonstrating the perfect charge transfer between two pinned diodes. The input referred noise at the pixel level is measured to be 6.3 e^-, which is three to four times smaller than that of conventional CMOS image sensors with global electronic shutter pixels.

Index Terms— **CMOS image sensor, Global electronic shutter, High-speed, two-stage charge transfer, reset noise canceling.**

I. Introduction

A global electronic shutter, with which all pixels start and end integration at the same time, is necessary for imaging fast-moving objects without motion blur. CMOS image sensors with the global shuttering function are required for many applications such as high-speed cameras, automotive and industrial applications. To realize a global electronic shutter in CMOS image sensors, two kinds of techniques are reported. One uses a five-transistor (5T) pixel [1], [2]. This 5T pixel with one additional transistor for shuttering to a 4T pixel of CMOS image sensors has very simple structure, but it is difficult to attain low noise performance, because of the large reset noise caused by the use of floating diffusion as an analog memory for global shuttering. The other uses a charge amplifier and sample-and-hold circuits in each pixel [3]. This pixel can reduce reset noise and enhance the sensitivity by the charge amplifier. However, this pixel has large pixel size due to the complicated circuits.

This paper presents a new type of global electronic shutter pixel. The proposed pixel features two-stage charge transfer using different-depth potential wells in two pinned diodes. Using this structure, the reset noise at the floating diffusion can be canceled by the true correlated double sampling(CDS) operation, while attaining a global shuttering function. The pinned diode structure prevents signal electrons to be captured at Si-SiO_2 interface traps and reduces the resulting image lag and charge transfer noise[4]. As a result, very low noise level when compared with the conventional global shutter pixels is expected. Furthermore, dark current is also reduced with the pinned diode structure.

II. Proposed Pixel

A. Structure and Operation

Fig.1 shows the proposed pixel structure and potential profile. The pixel has two pinned diodes: photodiode (PD) and storage diode (SD). For perfect charge transfer between the two pinned diodes, voltage difference V_D is necessary. The V_D is built by slit-shaped PD structure shown in Fig.3 [5]. It can be implemented with a standard CMOS image sensor technology, without any special processing steps. The SD and a floating diffusion (FD) which has a role of charge detection are connected with a transfer gate TX. The voltage change of the FD due to transferred photo-charge is read out through a source follower amplifier. To reduce the number of transistors in a pixel, a floating diffusion driving technique [6] is used. Fig.2 shows the timing diagram of the proposed pixel. The operation at the beginning of a frame is as follows. First, an accumulated charge in the PD is transferred to the SD as a first transfer. The first transfer realizes a global electronic shutter function. If the first transfer is not perfect, some amount of charge is left in the PD. The residual charge causes image lag and noise. Therefore, the PD is reset through GR gate and consequently the residual charge is drained. After that, all the pixel signals are read out. To readout the signal, each horizontal pixel line is selected by sequentially setting V_R to high level, and then the FD of the selected pixel is reset. The reset level is read out through a buffer amplifier. Then, the signal charge is transferred from the SD to FD as a second transfer and the resulting signal voltage in the FD is read out. By taking the difference between the reset and signal levels, the reset noise and the fixed pattern noise are cancelled.

B. Simulation Results

Simulation results of potential distribution(x-x' direction) by changing GS gate voltage are shown in Fig.4. Larger V_D leads to a higher charge transfer efficiency. The maximum V_D, however, is limited by the minimum width of n-type region which is determined by the design rule of fabrication technology. In the layout shown in Fig.3, V_D of 0.2V is obtained using the smallest width of n-type region. The slit-shaped PD structure may not be efficient if large amount of electrons must be stored for attaining wide dynamic range.

SIONYX1403000046.0005

SAMSUNG EX. 1002 - 1048/4148

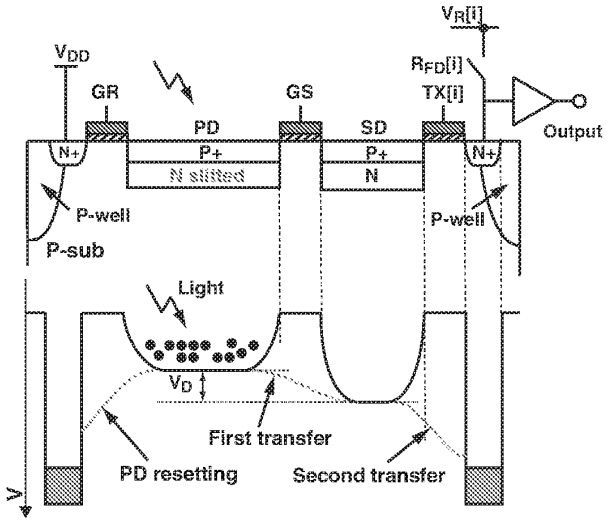


Fig. 1. Proposed pixel structure and potential profile

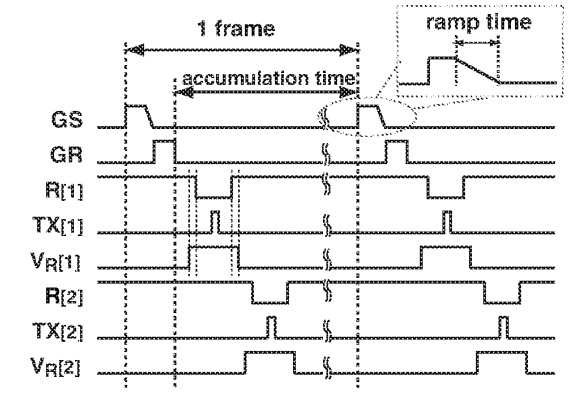


Fig. 2. Timing diagram

In the designed slit-shaped structure, the saturation number of electrons is 18000e^- according to a simulation result. This value is sufficiently large when compared with those of recent CMOS image sensors.

Fig.5 shows the simulation results of the residual charge as a function of the accumulated charge in the PD. The horizontal and vertical axes represent the number of accumulated electrons in the PD before the first charge transfer and the number of residual electrons in the PD, respectively. In this simulation, the falling edge of the input pulse of the GS gate is ramped to increase the charge transfer efficiency(Fig.2). This result indicates that the residual charge depends on the accumulated charge and a perfect charge transfer is possible when the accumulated charge is small. Therefore the sensitivity degradation does not occur at low-light intensity. Since the residual charge due to the incomplete charge transfer is drained through the GR gate, image lag can be avoided.

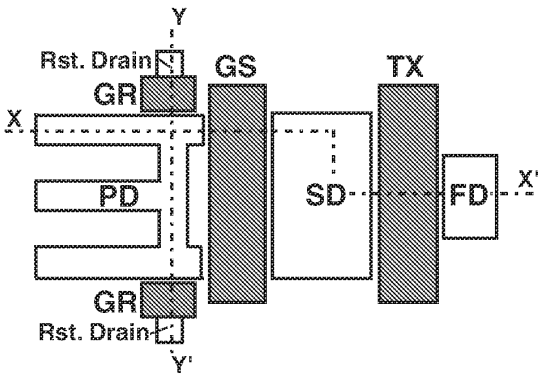


Fig. 3. Pixel layout

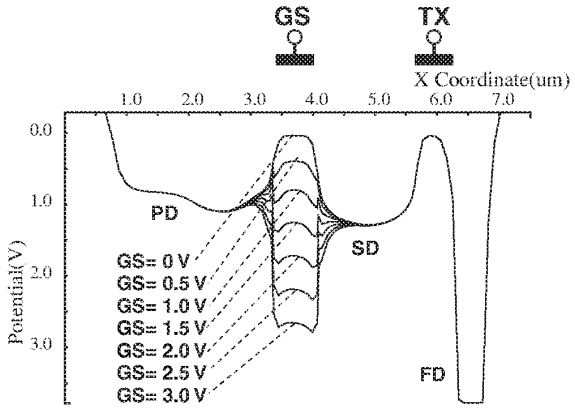


Fig. 4. Potential distribution at the first charge transfer (x-x')

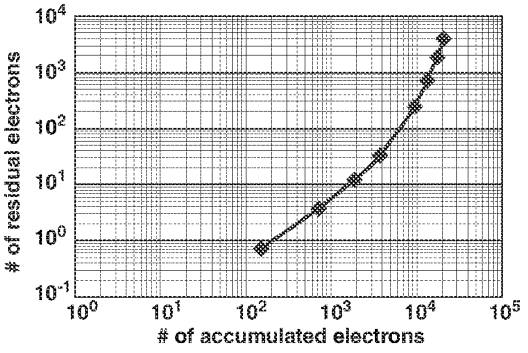


Fig. 5. the dependency of the residual charge on the accumulated charge in PD

III. Experimental Results

A prototype high-speed CMOS image sensor with the proposed pixel is designed and implemented. A chip photograph of the developed high-speed image sensor with 0.18-μm one poly four-metal standard CMOS image sensor technology is shown in Fig.6. The image array has 1024 $\times$ 1024 pixels with the pixel pitch of 7.5μm. The chip size is 10mm $\times$ 13mm.

SAMSUNG EX. 1002 - 1049/4148

Two 512 cyclic ADC arrays [3] are integrated at the upper and lower sides of the image array. The sensor has the digital parallel output of 192 channels.

Fig.7 shows output characteristics of the image sensor. The image sensor output range of 0 to 1V is assigned to the half of 12 bit digital code range, i.e., 0 to 2047. The sensor output has obviously large nonlinearity at high light intensity when compared with a linear line whose gradient is fitted to the measured result at the origin. As Fig.5 predicts the incomplete charge transfer in high light intensity region causes a large residual charge, and the resulting nonlinearity. On the other hand, the output has a good linearity at low light intensity, showing that perfect charge transfer can be achieved for the relatively small number of accumulated electrons in the PD. The nonlinearity at high light intensity can be an issue for some application, but Larger V_D can improve the charge transfer characteristic and thereby results in a good linearity. The Larger V_D can be created by controling doping profiles of PD and SD independently, which requires additional processing steps to a standard CMOS image sensor technology.

Table I summarizes the performance of the sensor. The input referred noise of the sensor, including the pixel and column cyclic ADC is measured to be 81 e^-. The random noise of the cyclic ADC only is 78 e^-. Therefore random noise of the sensor is dominated by the column cyclic ADC. This large noise is due to the digital switching noise for the high-speed digital readout. This noise has to be reduced in the future design. To measure the essential pixel noise, the analog output to directly read out the pixel output, is measured by an off-chip 14-bit ADC. The input referred noise of the pixel only is measured to be 6.3 e^-. The equivalent number of noise electrons due to reset noise $\overline{N_{n,reset}}$ is given by

$$\overline{N_{n,reset}} = \sqrt{\frac{V_{th}}{G_C}} \quad (1)$$

where V_{th} is the thermal voltage, which is 25.9mV at 27 °C . The conversion gain G_C is measured to be 33 μV/e^-. Therefore $\overline{N_{n,reset}}$ is calculated to be 28 e^- and it increases to 40 e^- after the readout in case of the uncorrelated double sampling in a conventional 5T global shutter pixel. The achieved noise level of 6.3 e^- in the proposed structure where the reset noise can be canceled is smaller than 1/6 of the conventional global shutter pixel. The input referred noise of the pixel is three to four times smaller than the conventional CMOS image sensor with the a global electronic shutter function [2].

As shown in Table I, the dark current of the proposed pixel is measured to be 284e^-/sec at ambient temperature of 18 °C . This dark current level of the proposed pixel is much smaller than that of 5T pixels using surface PD [1]. The dark current of the proposed pixel can be further reduced by optimizing the size and structure of the PD and SD.

A sample image captured at 1000fps is shown in Fig.8. This sample image is synthesized with eight regions of an image captured separately by a logic analyzer with a large-size memory. This is because data of 24 channels only are obtained at a time due to the limitation of the experimental environment. The image indicates that the sensitivity degradation does not occur at low-light intensity. The image quality is not good enough because of the vertical fixed pattern noise and row random noise. These noises come from column cyclic ADCs and digital read circuits. These noises are not essential and can be reduced by re-examining the design details because a high-speed CMOS image sensor(512 × 512pixels, 3500fps) using almost the same ADC architecture as of the present paper has been implemented and shows a good image quality[3]. Fig.9 shows 30 consecutive frames from a video sequence captured at 1000fps. To show the motion of fast moving object("chopper blade", rotating at 15Hz), 128×144 pixels only is shown. The edge of the chopper blade has neither motion blur nor distortion, showing the effectiveness of the global electronic shutter.

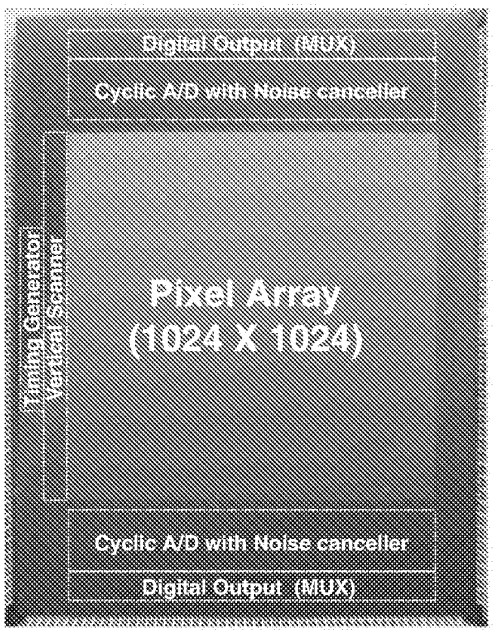


Fig. 6. chip photo(10mm×13mm)

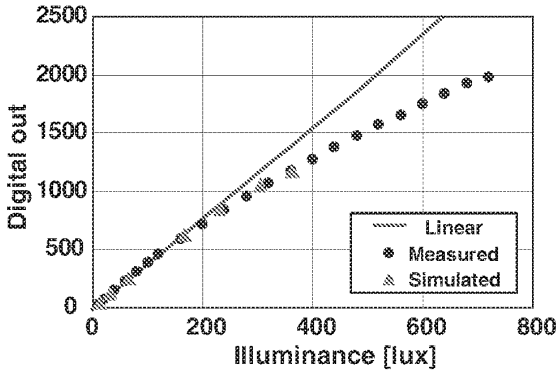


Fig. 7. output characteristic

SAMSUNG EX. 1002 - 1050/4148

TABLE I

PERFORMANCE SUMMARY

Technology	0.18-μm standard CIS 1P4M
Chip size	13mm(H) $\times$ 10mm(V)
Effective pixels	1024(H) $\times$ 1024(V)
Pixel size	7.5 μm $\times$ 7.5μm
Frame rate	>1000fps
Sensitivity	0.95 V/lux·sec
Conversion gain	33 μV/e$^-$
Random noise(sensor)	81 e$^-$
Random noise(pixel only)	6.3 e$^-$
Random noise(ADC only)	78 e$^-$
Fixed pattern noise	229 e$^-$
Dark current	284 e$^-$/sec at 18 °C
ADC resolution	12bit(Full scale 2V$_{\text{peak to peak}}$)
Power supply	1.8V(Digital)/3.3V(Analog)
Power consumption	1.2W(@500fps)

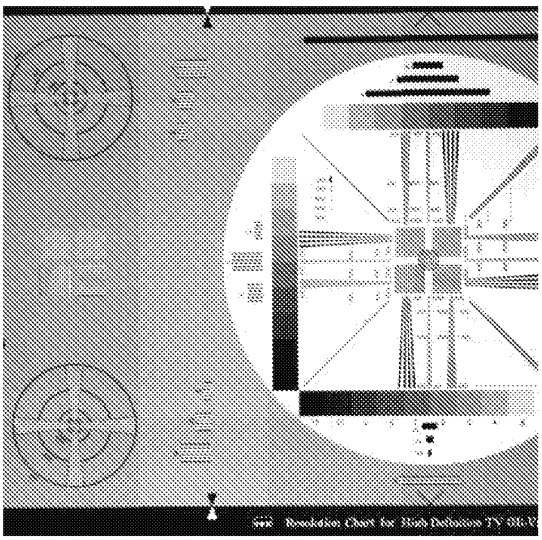


Fig. 8. Sample image at 1000fps

IV. CONCLUSIONS

In this paper, a global electronic shutter pixel which enables reset noise canceling and reduced dark current has been described. The proposed pixel has two pinned diodes that have different-depth potential wells. The voltage difference between the potential wells is generated by slitted photodiode structure. A prototype high-speed image sensor with 1M pixels is fabricated using 0.18um standard CMOS image sensor technology. The sensor achieves a good linearity at low light intensity, demonstrating the perfect charge transfer between two pinned diodes. The output characteristic of the sensor shows a good agreement with the simulation results using a device simulator. The noise measurement results indicate that the proposed pixel successfully cancels the reset noise, and the resulting input referred noise is as small as 6.3 e$^-$.

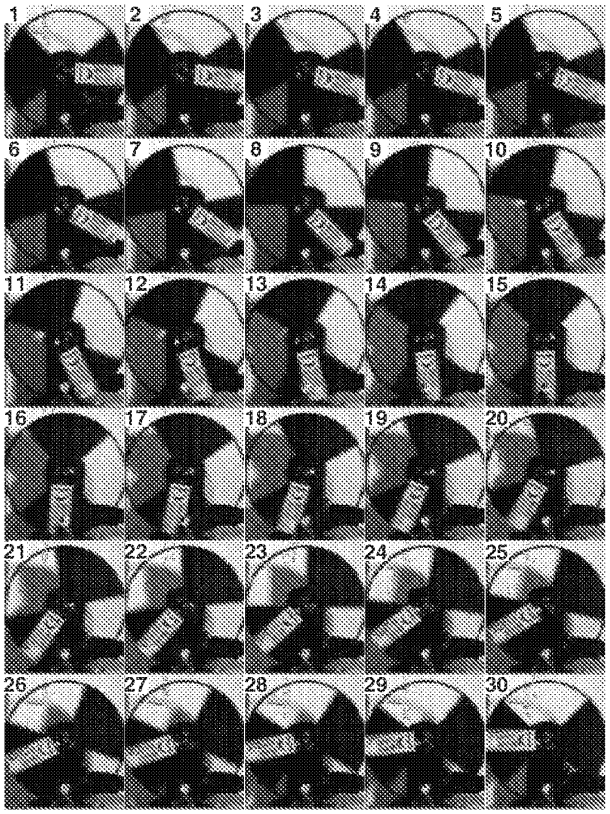


Fig. 9. Image sequence at 1000fps

ACKNOWLEDGMENT

This work was partly supported by the Knowledge Cluster Initiative of the Ministry of Education, Culture, Sports, Science and Technology, and the 21st Century COE Program on "Nanovision Science". The authors wish to thank Dr. M. Furuta of Toshiba Corp.(formerly Shizuoka Univ.) for his helps on the designing the prototype sensor.

REFERENCES

[1] A.Krymski and N.Tu, "A 9-V/Lux-s 5000-Frames/s 512×512 CMOS Sensor", IEEE Trans. ED, Vol.50, No.1, pp.136-143, (2003)

[2] N.Bock, A.Krymski, A.Sarwari, M.Sutanu, N.Tu, K.Hunt, M.Cleary, N.Khaliullin, and M.Brading, "A Wide-VGA CMOS Image Sensor with Global Shutter and Extended Dynamic Range" IEEE Workshop on CCDs and Advanced Image Sensors, pp.222-225, (Jun. 2005)

[3] M.Furuta, Y.Nishikawa, T.Inoue and S.Kawahito, "A High-Speed, High-Sensitivity Digital CMOS Image Sensor With a Global Shutter and 12-bit Column-Parallel Cyclic A/D Converters", IEEE J.Solid-State Circuits, Vol.42, No.4, pp.766-773, (2007).

[4] N. Teranishi, A. Kohno, Y. Ishihara, K. Arai, "No image lag photodiode structure in the interline CCD image sensor", Tech. Dig., Int. Electron Device Meeting, pp. 324-327, Dec. 1982.

[5] H.J.Yoon, S.Itoh, and S.Kawahito, "A CMOS Image Sensor With In-Pixel Two-Stage Charge Transfer for Fluorescence Lifetime Imaging", IEEE Trans. ED, Vol.56, No.2, pp.214-221, (Feb. 2009)

[6] K.Mabuchi, N.Nakamura, E.Funatsu, T.Abe, T.Umeda, T.Hoshino, R.Suzuki and H.Sumi, "CMOS Image Sensor Using a Floationg Diffusion Driving Buried Photodiode",ISSCC Dig. Tech. Papers, pp.82-83 (Feb.2004)

SIONYX1403000046.0008

SAMSUNG EX. 1002 - 1051/4148

Light trapping effect from randomized textures of Ag/ZnO back reflector on hydrogenated amorphous and nanocrystalline silicon based solar cells

Baojie Yan, Guozhen Yue, Laura Sivec, Jessica M. Owens, Ken Lord, Jeffrey Yang, and Subhendu Guha
United Solar Ovonic LLC, 1100 West Maple Road, Troy, Michigan 48084

Chun-Sheng Jiang
National Renewable Energy Laboratory, 1617 Cole Blvd, Golden, CO 80401

ABSTRACT

We report our progress in the optimization of Ag/ZnO back reflectors (BR) for a-Si:H and nc-Si:H solar cells. Theoretically, a BR with a smooth metal surface and a textured dielectric surface would be more desirable. A smooth metal/dielectric interface reduces the plasmonic resonance loss and parasitic losses due to light trapped in sharp angles; a textured dielectric/semiconductor interface provides scattering for light trapping. In order to obtain sufficient light scattering at the ZnO/silicon interface, a highly textured ZnO layer is normally used. However, a highly textured ZnO surface causes deterioration of nc-Si:H material quality. In addition, to make a highly textured ZnO surface, a thick ZnO layer is needed, which could introduce additional absorption in the bulk ZnO layer and reduce the photocurrent density. Therefore, Ag/ZnO BR structures for nc-Si:H solar cells needs to be optimized experimentally. In this study, we found that an optimized Ag/ZnO BR for nc-Si:H solar cells is constructed with textured Ag and thin ZnO layers. Although a textured Ag layer might cause certain losses resulting from plasmonic absorption, the enhanced light scattering by a moderately textured Ag layer makes it possible to use a thin ZnO layer, where the absorption in the ZnO layer is low. With such a BR, we achieved a short-circuit current density of over 29 mA/cm^2 from a nc-Si:H single-junction solar cell. Using the high performance nc-Si:H cell in an a-Si:H/nc-Si:H/nc-Si:H triple-junction structure, we achieved an initial active-area efficiency of 14.5% with a total current density exceeding 30 mA/cm^2.

Key words: a-Si:H, nc-Si:H, solar cell, light trapping, back reflector.

1. INTRODUCTION

Hydrogenated amorphous silicon (a-Si:H) and nanocrystalline silicon (nc-Si:H) as low cost materials have been used as absorber layers in thin film silicon solar cells. Their absorption coefficients are better than that of crystal silicon (c-Si), allowing a-Si:H and nc-Si:H solar cells to be much thinner than c-Si solar cells. However, the intrinsic layers of a-Si:H and nc-Si:H cannot be made thick enough to generate a high photocurrent density without severely sacrificing fill factor (FF) even when *p-i-n* or *n-i-p* structures are used to enhance photo-carrier collection because a-Si:H and nc-Si:H have poorer transport characteristics than c-Si. In order to make the solar cells have a reasonable FF the *i* layer thicknesses are normally 200-300 nm and 1-3 μm for a-Si:H and nc-Si:H, respectively. To resolve the generation and collection issue, one normally uses a light trapping method to enhance the photocurrent density. The commonly used light trapping techniques are light scattering by textured transparent conductive oxides (TCO) in *p-i-n* solar cell structures on superstrates or by textured back reflectors (BR) in *n-i-p* solar cells on substrates. A conventional textured BR is with a metal/dielectric bi-layer structure deposited on non-transparent substrates such as stainless steel (SS) or polymer. Silver and aluminum are two of the metals used as reflectors and ZnO is used as the dielectric layer to avoid the mixture of metals with silicon and provide a buffer of refractive index matching [1,2]. The textures of the metal and dielectric layers result in light scattering. The scattered light with an angle greater than the total reflection angle is trapped in the solar cell and enhances the photocurrent density.

Thin Film Solar Technology II, edited by Alan E. Delahoy, Louay A. Eldada, Proc. of SPIE
Vol. 7771, 777102 · © 2010 SPIE · CCC code: 0277-786X/10/$18 · doi: 10.1117/12.859867

SIONYX1403000046.0009

SAMSUNG EX. 1002 - 1052/4148

SAMSUNG EX. 1002 - 1053/4148

Light trapping was proposed and has been studied since the early 80s. Yabonovitch and his colleagues [3,4] theoretically studied the light trapping by perfect randomized textured BRs. Based on statistical ray optics, they derived that the light intensity in a dielectric material slab with an absolutely randomized textured surface and a perfect reflector of hundred percent reflectance. They demonstrated that when a light beam illuminates normally to the top surface, the intensity of the light in a non-absorptive dielectric slab is $2n^2$ times of the light intensity outside the slab. The intensity outside of the slab is twice the incident light intensity because the reflected light is the same as the incident light. They also discussed the situation of absorptive materials. Using the same configuration, they derived that the enhancement in a weak absorption regime could be $4n^2$. The $4n^2$ factor has been widely used in the literature, especially nowadays when the light trapping in thin film silicon solar cells has become a very hot topic. Several new light trapping approaches have been proposed [5-9]. A theoretical study showed that under certain conditions, the $4n^2$ classical limit could be exceeded [9].

United Solar has actively studied light trapping with randomized textured BRs. In the early stage, Ag/ZnO and Al/ZnO BRs were developed for a-Si:H/a-SiGe:H/a-SiGe:H triple-junction solar cells [1,2], which had resulted in the 13% stable record cell efficiency [10]. Recently, we have focused on the optimization of Ag/ZnO BRs for nc-Si:H solar cells. Significant progress has been made [11-13]. Using the optimized Ag/ZnO BRs, we have made a new record efficiency with an a-Si:H/nc-Si:H/nc-Si:H triple-junction structure [13]. In this paper, we present the progress in the optimization of Ag/ZnO BRs for effective light trapping in nc-Si:H solar cells and the improvement in cell efficiency with a-Si:H/nc-Si:H/nc-Si:H triple-junction structures on Ag/ZnO BRs.

2. EXPERIMENTAL

Ag/ZnO BRs were deposited on SS substrates in both batch and roll-to-roll systems. Batch machines are used in the laboratory and roll-to-roll machine are used in both the R&D laboratory and production lines. Both the metal and ZnO layers can be textured by adjusting the deposition parameters and/or the thicknesses of the layers. The textures of the ZnO layers were also increased by chemical etching using 5% HCl. The surface and interface texture on the BR are measured with atomic-force-microcopy (AFM) and scanning electron microscopy (SEM). The layered structures of the BR as well as nc-Si:H solar cells were examined using cross-sectional transmission electron microscopy (X-TEM). The crystalline structures are characterized by X-ray scattering spectroscopy. The optical properties of BRs are characterized using light scattering with a He-Ne laser and reflection spectrum measurements. In the light scattering measurements, the scattered light intensities are measured as a function of angles with respect to the sample surface, where the incident light is normal to the sample surface. In the reflection measurements, the total and diffuse reflection spectra are measured in the wavelength range from 200 nm to 2500 nm.

Thin film *n-i-p* structured nc-Si:H single-junction and a-Si:H/nc-Si:H/nc-Si:H triple-junction solar cells were deposited using multi-chamber PECVD systems on various substrates such as SS and Ag/ZnO coated SS. The intrinsic layers were deposited with very high frequency (VHF) glow discharge techniques at different deposition rates and hydrogen profiles [14]. Details of the solar cell optimization were published elsewhere [14-16]. Current-density versus voltage (J-V) curves of solar cells were measured under an AM1.5 solar simulator at 25°C. External quantum efficiency (QE) spectra were measured in the wavelength range between 300 nm and 1200 nm. Short-circuit current density (J_{sc}) values were obtained by integrals of the AM1.5 solar spectrum with the measured QE spectra.

3. RESULTS AND DISCUSSION

3.1. Optimization of Ag/ZnO back reflector for nc-Si:H solar cells

Figure 1 (left) shows a X-TEM image of Ag/ZnO BR on a c-Si substrate and (right) a schematic of light scattering at the ZnO and Ag surfaces. One can see that both the Ag and ZnO layers are textured, which are normally believed by the nature of polycrystalline growth. The textures on the ZnO are pronounced due to the thick

SIONYX1403000046.0010

layer. Because the overall device performance depends on both light absorption in the intrinsic layer and carrier extraction from the intrinsic layer, several factors need to be considered for optimizing Ag/ZnO BR to improve nc-Si:H solar cell performance. First, the light scattering needs to be strong enough for effective light trapping; second, the loss in the BR and doped layers should be minimized; and third, the nc-Si:H material quality should be minimally impacted by the BR structure. From the light scattering point of view, highly textured Ag/ZnO and ZnO/Si interfaces are desirable. In particular, the textures at the Ag/ZnO interface are more effective at scattering than from the ZnO/Si interface because most of the light is reflected at the Ag/ZnO interface. However, a highly textured Ag/ZnO interface could cause a significant plasmonic loss and some other parasitic loss in narrow angle valleys. Therefore, one needs to take these two factors into consideration when optimizing Ag textures. The scattering at the ZnO/Si interface also contributes to the light trapping. An extra texture comes from the nature of the polycrystalline growth of the ZnO layer. It has been observed that texture increases with ZnO film thickness. Normally, a thick ZnO is needed for enough texture at the ZnO/Si interface to scatter light effectively. A side effect of increasing ZnO thickness is that it causes an extra absorption in the thick ZnO layer. Therefore, one might need to avoid using a very thick ZnO layer unless the bulk absorption coefficient is significantly low. Another side effect is that nc-Si:H deposited on a highly textured surface has a poorer material quality. The nc-Si:H materials contain nanometer sized crystallites embedded in amorphous tissues. The crystallites have the tendency to form clusters (called large grains), which normally grow perpendicular to the local surface. When the substrate has high texture, nearby clusters of crystallites meet each other, resulting in high defect density and poor cell performance. Therefore, we must compromise between the substrate texture and nc-Si:H material quality. Because the scattering at the Ag/ZnO interface is more effective than at the ZnO/Si interface, one might have a good chance to improve the nc-Si:H solar cell performance using textured Ag and thin ZnO if the plasmonic absorption and parasitic loss are not significant. It is clear that the all the arguments seem to have advantages. Thus, suitable BR structures for nc-Si:H need to be optimized experimentally.

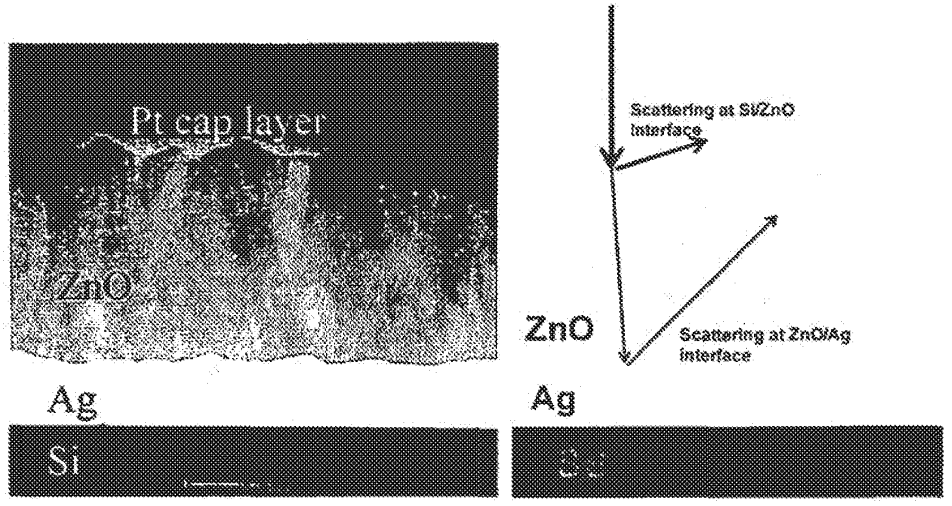


Figure 1. (left) X-TEM of Ag/ZnO BR on a c-Si substrate and (right) schematic of light scattering at the Si/ZnO and ZnO/Ag interfaces.

Figure 2 plots measured total and diffuse reflection spectra of four Ag/ZnO BR coated SS substrates. From the total reflection, we make the following observations. First, the flat Ag and thin ZnO (130 nm) combination gives the highest total reflection. Texturing the Ag layer causes a plasmonic resonance frequency shift to longer wavelengths, but it is still too far away to affect the long wavelength region. Therefore, the plasmonic absorption loss is not an obvious issue. Second, the texture of the Ag also reduces the reflectance over the whole wavelength region. Two reasons could explain this observation: light trapping in the ZnO layer and parasitic loss in sharp angles. Because ZnO has a refractive index of 2, the scattered light with an angle larger than the critical angle (30

SIONYX1403000046.0011

SAMSUNG EX. 1002 - 1054/4148

degrees) of total reflection will be trapped in the ZnO layer. However, this portion of absorptance will be recovered when a Si layer is deposited on the ZnO layer. Unfortunately, the parasitic loss in sharp angles will never be recovered. At this moment, we do not know how much of the loss is due to the light trapping and how much is lost in sharp angles. Third, the two samples with thick ZnO (2 μm) showed similar total reflection spectra with very low reflectance in the short wavelength region. Because the increase in ZnO thickness should not affect the Ag/ZnO interface, we believe that the interface plasmonic absorption should not be increased. The reduced reflectance is mainly from the increased ZnO bulk absorption and/or enhanced light trapping due to the increased texture by the thick ZnO layer.

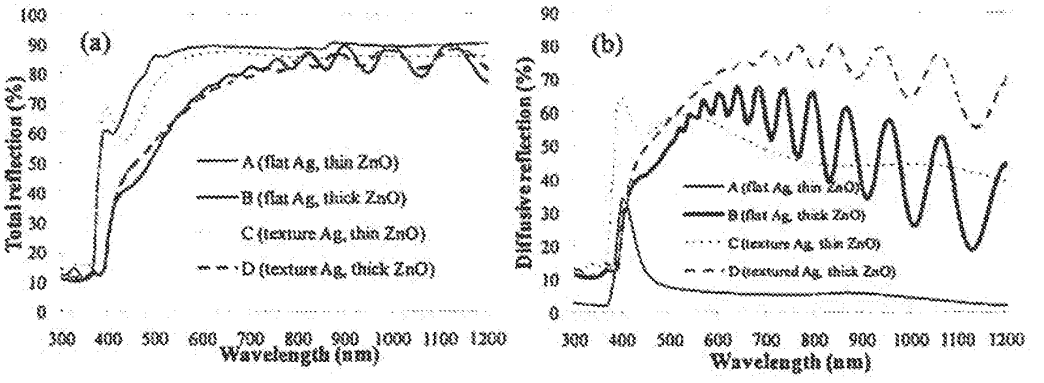


Figure 2. Total and diffuse reflection spectra of four different Ag/ZnO BR structures.

The diffuse reflection spectra also show several interesting phenomena. The BR with textured Ag and thick ZnO has the highest diffuse reflectance, followed by the sample with flat Ag and thick ZnO, which means the extra texture from the thick ZnO indeed results in effective light scattering. The diffuse reflectance of the BR with textured Ag and thin ZnO is not as high as the one with textured Ag and thick ZnO, but the average values are not lower than the one with flat Ag and thick ZnO. The BR with flat Ag and thin ZnO has very low diffuse reflectance, indicating poor light trapping when solar cells are deposited on it.

Optical properties give some indication of light trapping in solar cells. But, the real test has to be in solar cells themselves. Table I lists the performances of nc-Si:H solar cells deposited on the four types of BRs, where the open circuit voltage (V_{oc}) and FF were obtained from J-V measurements and the J_{sc} from integrals of QE data measured under the short circuit condition and AM1.5 solar spectrum. The photocurrent density from the QE measured under -2V is used to evaluate the recombination loss. The RMS represents the root mean square of the surface textures in the AFM images. It is clear that the solar cell on the BR with textured Ag and thin ZnO has the best performance, where even the J_{sc} is the highest. Figure 3 shows the comparison of AFM images taken from the BRs with textured Ag but with thin and thick ZnO layers. It clearly shows that the lateral feature sizes are very similar on the two samples, but the feature sizes in the vertical direction are different, where the samples with the thick ZnO have larger vertical feature sizes (large RMS) than the one with the thin ZnO layer. The large vertical feature sizes produce smaller angles in the valleys on BRs, where a high density of defects and micro-cracks could occur [13,17]. Consequently, a poor nc-Si:H solar cell performance is obtained on the BRs with the textured Ag and the thick ZnO layers.

In order to confirm that the poor cell performance on the BR with high surface texture is caused by nc-Si:H material quality, we measured the QE curves under the short circuit condition and under -2.0 V reverse bias. The difference between the two QE curves reflects the recombination loss due to a poor nc-Si:H material quality. The results listed in Table I show that high substrate texture indeed causes a large recombination loss, which is normally through defects in the bandgap. In addition, the FF and V_{oc} are also poor in the cells on highly textured BRs. The FF reflects the capability to extract photo-generated carriers, which could be collected by the electrodes through the

SIONYX1403000046.0012

SAMSUNG EX. 1002 - 1055/4148

build-in electric field or recombined through the defect states. A high defect density corresponds to a poor FF. The V_{oc} follows the same trend as FF because the recombination through defects also reduces the charge accumulation in the doped layers under the open circuit condition. From the solar cell performance data, we are convinced that nc-Si:H solar cells should not be deposited on highly textured substrates. In order to have enough scattering with moderate textures, the BR structure with textured Ag and thin ZnO layers is logically a good choice.

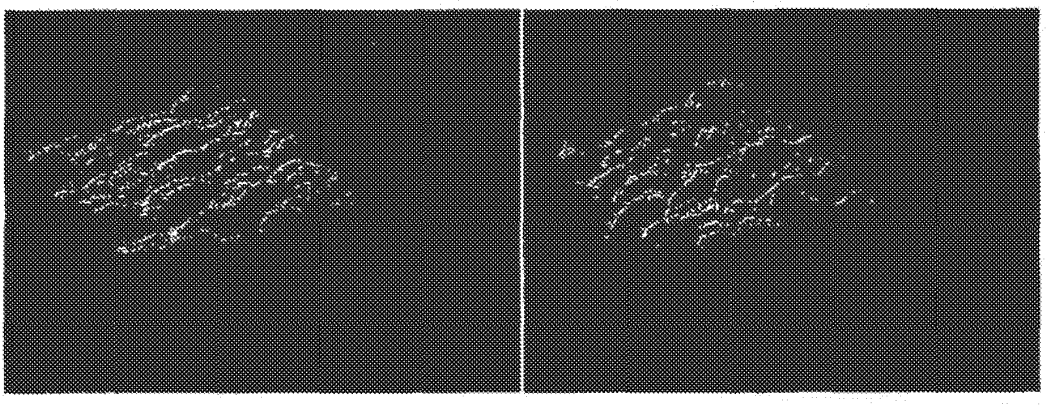


Figure 3. AFM images of two BRs, where the left image is from the BR with the textured Ag layer and thin ZnO layer and the right one is from the BR with the thick Ag layer and thick ZnO layer.

Table I: J-V characteristics and BR descriptions of four nc-Si:H solar cells deposited with the same recipe but on different BRs.

Run No.	V_{oc} (V)	FF	QE current density (mA/cm^2)			Eff (%)	BR structure	RMS (nm)
			0 V	-2 V	Diff.			
18004	0.482	0.608	26.25	26.50	0.95%	7.69	Textured Ag/thin ZnO	33
18005	0.431	0.563	24.59	25.51	3.70%	5.97	Textured Ag/thick ZnO	52
18014	0.502	0.645	22.59	22.72	0.58%	7.31	Flat Ag/thin ZnO	14
18018	0.476	0.528	25.72	26.21	1.91%	6.46	Flat Ag/thick ZnO	42

3.2. High efficiency solar cells

We deposited nc-Si:H single-junction solar cells on the optimized Ag/ZnO BRs. The device structure and material quality were systematically optimized. We have employed an improved seed layer and hydrogen dilution profiling technique [14] to ensure an optimum structure along the growth direction. Using these techniques, the solar cell performance was significantly improved. A J_{sc} of 29.11 mA/cm^2 has been achieved, with V_{oc}=0.516 V, FF=0.647, and efficiency=9.72%. Using the same BR, we further optimized the growth recipe to obtain the highest efficiency. An initial active-area efficiency of 10.21% (V_{oc}=0.540 V, FF=0.680, and J_{sc}=27.80 mA/cm^2) was achieved as shown in Fig. 4.

Having developed high J_{sc} and high efficiency recipes, we fabricated a-Si:H/nc-Si:H/nc-Si:H triple-junction cells on the optimized BRs with textured Ag and thin ZnO, where the nc-Si:H bottom cell was made using the high J_{sc} recipe, and the nc-Si:H middle cell was made using the high efficiency recipe. The initial and the stabilized results after 1000 hours of light soaking are shown in Table II. Sample 18321 shows the best initial active-area efficiency of 14.5%, and sample 18323 shows the highest total-current density of >30 mA/cm^2. For stability results, the light-induced degradations are <1.0% in V_{oc} and 4-7% in FF, which we believe are mainly from a-Si:H top cells. The top cell current was degraded by ~4%. While the bottom cell current did not show any degradation. This is consistent with our previous results where we demonstrated that red light with a photon energy smaller than the a-Si:H bandgap did not cause degradation in nc-Si:H cells [18]. We also noticed that the middle cell current was

SIONYX1403000046.0013

SAMSUNG EX. 1002 - 1056/4148

degraded by 1-2%. This is probably because the middle cell also sees some blue light. Overall, depending on the current mismatch, the efficiency degrades by 4-11%. The best stabilized active-area efficiency is 13.5%, which is from sample 18328 having a strong bottom cell limited current. This efficiency is higher than our previously reported efficiency of 13.2% from the same triple-junction structure [19]. The stable J-V characteristics of the best device and the QE curves are plotted in Figure 5.

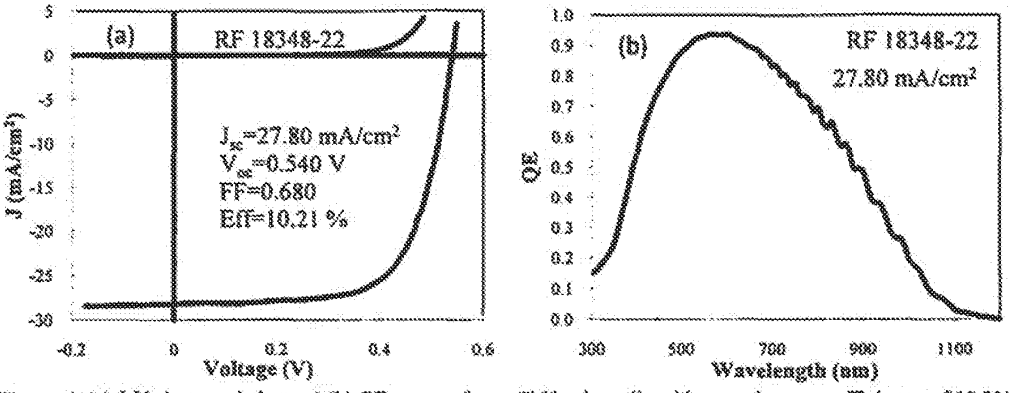


Figure 4. (a) J-V characteristics and (b) QE curve of a nc-Si:H solar cells with an active-area efficiency of 10.2%.

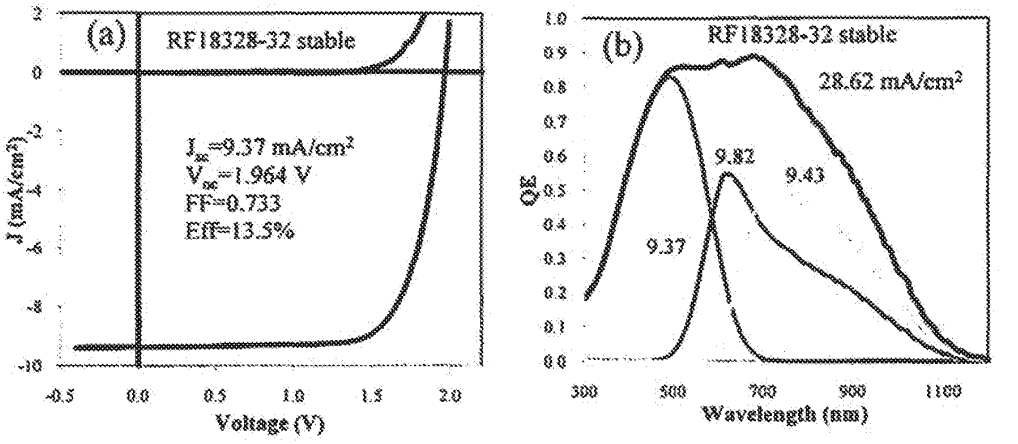


Figure 5. (a) Stable J-V characteristics; and (b) QE curves of an a-Si:H/nc-Si:H/nc-Si:H triple-junction solar cell with the stabilized active-area efficiency of 13.5%.

Table II. Initial and stable J-V characteristics of a-Si:H/nc-Si:H/nc-Si:H triple-junction solar cells. The bold numbers are used to calculate the active-area efficiencies.

Sample No.	State	V_{oc} (V)	FF	QE(mA/cm²)				Eff (%) (active area)
				Total	Top	Mid	Bott	
18321-32	Initial	2.024	0.741	29.23	9.70	9.65	9.88	14.5
	Stable	2.012	0.692	28.78	9.32	9.51	9.95	13.0
18323-32	Initial	1.943	0.738	30.04	9.87	10.23	9.94	14.2
	Stable	1.924	0.693	29.49	9.45	10.02	10.02	12.6
18328-32	Initial	1.971	0.768	28.95	9.76	9.94	9.25	14.0
	Stable	1.964	0.733	28.62	9.37	9.82	9.43	13.5

SIONYX1403000046.0014

SAMSUNG EX. 1002 - 1057/4148

4. SUMMARY

We have systematically studied the structural and optical properties of Ag/ZnO BRs for high efficiency nc-Si:H single-junction and a-Si:H/nc-Si:H/nc-Si:H triple-junction solar cells. We studied light scattering, optical loses and texture effect on nc-Si:H quality in four types of BR structures: flat Ag/thin ZnO, flat Ag/thick ZnO, textured Ag/thin ZnO, and textured Ag/thick ZnO. We found that when the BR texture comes from the Ag layer, light can be scattered efficiently. When the ZnO layer is very thick, and hence textured, it can also be effective at scattering. However, it causes poorer nc-Si:H quality which reduces cell performance. After compromising between optical properties and nc-Si:H quality, we found that a substrate with textured Ag and thin ZnO is the best BR for nc-Si:H solar cells. Using the best Ag/ZnO BRs and improved nc-Si:H material quality and device design, we achieved an initial active-area efficiency of over 10% with J_{sc} larger than 29 mA/cm^2. We also achieved 14.5% initial and 13.5% stable active-area efficiency with a-Si:H/nc-Si:H/nc-Si:H triple-junction solar cells.

ACKNOWLEDGMENTS

We thank the Research and Development team at United Solar Ovonic for their collaboration and assistance. This work has been supported by US DOE under SAI Program contract No. DE-FC36-07 GO 17053.

REFERENCES

[1] A. Banerjee and S. Guha, J. Appl. Phys. 69, 1030 (1991).
[2] A. Banerjee, J. Yang, K. Hoffman, and S. Guha, Appl. Phys. Lett. 65, 472 (1994).
[3] E. Yablonovitch, J. Opt. Soc. Am. 72, 899 (1982).
[4] T. Teidje, E. Yablonovitch, G. D. Cody, and B. G. Brooks, IEEE Trans. On Electron Devices 31, 711 (1984).
[5] Stuzman C. Eisele, C. E. Nebel, and M. Stusmann, J. Appl. Phys. 89, 7722 (2001)
[6] B. Curtin, R. Biswas, and V. Dalal, Appl. Phys. Lett. 95, 231102 (2009).
[7] S. Pillai, K. R. Catchpole, T. Trupke, and M. A. Green, J. Appl. Phys. 101, 093105 (2007).
[8] V. E. Ferry, M. A. Verschuuren, H. B. T. Li, R. E. I. Schropp, H. A. Atwater, and A. Polman, Appl. Phys. Lett. 95, 183503 (2009).
[9] Z. Yu, A. Raman, and S. Fan, "*Fundamental limit of light trapping in grating structures*", to be published.
[10] J. Yang, A. Banerjee, and S. Guha, Appl. Phys. Lett. 70, 2975 (1997).
[11] B. Yan, J. M. Owens, C.-S. Jiang, J. Yang, and S. Guha, Mater. Res. Soc. Symp. Proc. 862, 603 (2005).
[12] J. Yang, B. Yan, G. Yue, and S. Guha, Mater. Res. Soc. Symp. Proc. 1153, A13-2 (2009).
[13] G. Yue, L. Sivec, J. M. Owens, B. Yan, J. Yang, and S. Guha, Appl. Phys. Lett. 95, 263501 (2009).
[14] B. Yan, G. Yue, J. Yang, S. Guha, D.L. Williamson, D. Han, and C. Jiang, Appl. Phys. Lett. 85, 1955 (2004).
[15] B. Yan, G. Yue, X. Xu, J. Yang, and S. Guha, Phys. Status Solidi A, 207, 671 (2010).
[16] B. Yan, G. Yue, and S. Guha, Mater. Res. Soc. Symp. Proc. 989, 335 (2007).
[17] Y. Nasuno, M. Kondo, and A. Matsuda, Proc. of the 28th IEEE Photovoltaic Specialists Conference, Anchorage Alaska, USA (IEEE, New York, 2000), p.142.
[18] B. Yan, G. Yue, J.M. Owens, J. Yang, and S. Guha, Appl. Phys. Lett. 85, 1925 (2004).
[19] G. Yue, B. Yan, G. Ganguly, J. Yang, and S. Guha, Appl. Phys. Lett. 88, 263507 (2006).

SIONYX1403000046.0015

SAMSUNG EX. 1002 - 1058/4148

C25

Surface studies and microstructure fabrication using femtosecond laser pulses

A thesis presented

by

Rebecca Jane Younkin

to

The Division of Engineering & Applied Sciences

in partial fulfillment of the requirements

for the degree of

Doctor of Philosophy

in the subject of

Physics

Harvard University

Cambridge, Massachusetts

August 2001

SIONYX1403000046.0016

SAMSUNG EX. 1002 - 1059/4148

©2001 by Rebecca Jane Younkin
All rights reserved.

SIONYX1403000046.0017

SAMSUNG EX. 1002 - 1060/4148

Abstract

Surface studies and microstructure fabrication using femtosecond laser pulses

Advisor: Eric Mazur

Author: Rebecca Jane Younkin

In the first of the two experiments described in this thesis, we constructed and characterized an apparatus for performing ultrafast surface spectroscopy on Pt (111). A combination of an optical parametric amplifier and a difference frequency generation stage allow us to create optical pulses with wavelengths in the range 550 nm−7.3 μm and pulsewidths of approximately 100 fs. We also developed methods for using the infrared output of this apparatus in infrared-visible sum-frequency generation at a Pt-vacuum interface. Our attempts to time-resolve a chemical reaction taking place at this interface were unsuccessful because of power limitations, but the techniques that we developed should be applicable in related experiments.

In the second series of experiments, we created arrays of conical microstructures on the surface of silicon by irradiating a silicon wafer with trains of ultrashort pulses in the presence of an ambient gas. The microstructures are typically tens of micrometers high and separated by several micrometers. We showed that the morphology of the structures is highly dependent on the species of ambient gas, the gas pressure, the laser fluence, and the number of laser pulses used. The sharpest structures are made in halogen-containing gases, such as SF_6 or Cl_2. The use of N_2 or air results in blunt, rounded structures.

In this thesis, I discuss the application of these silicon microstructures in optoelectronics and vacuum microelectronics. I note that surfaces covered with these microstructures have striking optical properties: structures made in SF_6 absorb approximately 90% of incident light with wavelengths between 250 nm and 2.5 μm. The

SIONYX1403000046.0018

SAMSUNG EX. 1002 - 1061/4148

sharp conical structures also show high field-emission current. The remarkable and potentially useful optical and field-emitting properties of the structures are the result of the conical morphology of the laser-induced microstructures and the impurities introduced into the silicon during irradiation.

SIONYX1403000046.0019

SAMSUNG EX. 1002 - 1062/4148

Table of Contents

Abstract *iii*

Table of Contents *v*

List of Figures *viii*

List of Tables *x*

Acknowledgements *xi*

1 Introduction and Overview **1**

2 Tunable sources of infrared pulses for ultrafast surface science **4**
2.1 Introduction 4
2.2 Optical parametric amplifier 5
2.2.1 Background 5
2.2.2 Experimental 8
2.2.3 OPA performance 11
2.3 Difference frequency generation 13
2.3.1 Background 14
2.3.2 Experimental 16
2.3.3 DFG characterization 19
2.4 Application to surface science 20
2.4.1 Background 22
2.4.2 Apparatus 24
2.4.3 Alignment procedures for experiments in vacuum 27
2.4.4 Overlapping the infrared and visible pulses in time 28
2.4.5 Preparation of the CO/Pt(111) surface 29
2.4.6 Results of experimental trials 30
2.4.7 Future work 31

SIONYX1403000046.0020

SAMSUNG EX. 1002 - 1063/4148

3 Formation of silicon microstructures **32**
3.1 Introduction . . . 32
3.2 Background . . . 33
3.2.1 Structures formed with ion-bombardment . . . 34
3.2.2 Vapor-liquid-solid growth of silicon whiskers . . . 37
3.2.3 Laser interactions with solids . . . 38
3.2.4 Laser-induced periodic structures . . . 42
3.3 Apparatus . . . 44
3.4 Procedure for making microstructured silicon . . . 46
3.5 Evolution of microstructures during laser irradiation . . . 47
3.6 Properties of microstructures . . . 50
3.7 Dependence of morphology on ambient gas species . . . 52
3.7.1 Shapes of microstructures . . . 53
3.7.2 Microstructure number density . . . 53
3.8 Microstructures formed with low fluence . . . 56
3.9 Discussion . . . 57
3.9.1 Formation mechanisms . . . 58
3.9.2 Effects of ambient gas . . . 60
3.10 Future work . . . 62

4 Optical Properties of Microstructured Surfaces **64**
4.1 Introduction . . . 64
4.2 Background . . . 65
4.3 Experimental . . . 66
4.4 Results . . . 68
4.4.1 Unmodified Si(111) . . . 68
4.4.2 Surfaces patterned in SF_6 . . . 70
4.4.3 Surfaces patterned in other gases . . . 72
4.5 Discussion . . . 75
4.5.1 Multiple reflections . . . 75
4.5.2 Introduction of states into the band gap . . . 78
4.6 Applications . . . 80
4.6.1 Silicon solar cells . . . 81
4.6.2 Silicon photodetectors . . . 83
4.7 Future Work . . . 84

5 Field emission by laser-induced conical microstructures **86**
5.1 Introduction . . . 86
5.2 Background . . . 87
5.2.1 Field-emission from a metal . . . 87
5.2.2 Field-emission from a semiconductor . . . 91
5.3 Apparatus and procedure . . . 92

SIONYX1403000046.0021

SAMSUNG EX. 1002 - 1064/4148

5.4 Field emission results 94
5.5 Discussion 96
5.5.1 Two field-emission regimes 97
5.5.2 Ohmic response for high biases 97
5.6 Applications of field emitters 98
5.6.1 Flat panel displays 99
5.6.2 Microwave sources and electron beams 99
5.6.3 Other applications 101
5.7 Future work 101
5.7.1 Apparatus modifications 101
5.7.2 Structures made with different gases 102
5.7.3 Chemical modification of microstructured surfaces 103
5.7.4 Controlled placement of microstructures 104

6 Summary and Conclusions **105**

References **108**

SIONYX1403000046.0022

SAMSUNG EX. 1002 - 1065/4148

List of Figures

2.1 Range of OPA and DFG tuning. 5
2.2 Tuning curve for the OPA 7
2.3 Schematic of OPA layout. 8
2.4 Signal and idler spectra. 12
2.5 Idler wavelength *vs.* signal. 13
2.6 Energy of the OPA *vs.* wavlength. 14
2.7 Autocorrelations of the pump and signal beams 15
2.8 DFG and idler wavelengths *vs.* signal. 17
2.9 Schematic of DFG layout. 18
2.10 Output of DFG stage using LIO crystal. 20
2.11 Output of DFG stage using AGS crystal. 21
2.12 Cross-correlation of the DFG output with the 800-nm pump 22
2.13 Schematic of sum-frequency generation process 23
2.14 Apparatus for surface sum-frequency generation. 25

3.1 Silicon microstructures made with femtosecond laser irradiation. . . . 33
3.2 Schematic of apparatus for silicon microstructuring. 45
3.3 SEM images of microstructures formed with varying numbers of pulses 48
3.4 SEM image of microstructures, showing ripple pattern around border 49
3.5 SEM images of microstructures formed with four different ambient gases 52
3.6 Number density of microstructures as a function of background partial pressure 55
3.7 SEM image of spots irradiated with low fluences 57
3.8 SEM image of debris collected during microstructure formation 61

4.1 Schematic of measurements using Hitachi U-4001 spectrophotometer . 67
4.2 Optical properties of unmodified crystalline silicon and CaF_2. 69
4.3 Microstructures with three different characteristic sizes. 70
4.4 Reflectance of samples of microstructures, all made in SF_6. 71
4.5 Transmittance of samples of microstructures made in SF_6. 72
4.6 Absorptance of samples of microstructures, all made in SF_6. 73
4.7 Reflectance of samples made in 4 different gases. 74

SIONYX1403000046.0023

SAMSUNG EX. 1002 - 1066/4148

4.8 Transmittance of samples made in 4 different gases. 75
4.9 Absorptance of samples made in 4 different gases. 76
4.10 Multiple reflections on sides of microstructures 77
4.11 Impurity states due to sulfur 79
4.12 Distribution of solar radiation 83

5.1 Potential energy of an electron at the surface of a metal. 88
5.2 Potential energy of an electron at the surface of a semiconductor. . . 91
5.3 Schematic of apparatus for measuring field emission from silicon microstructures. 93
5.4 Measurements of field emission current *versus* applied bias voltage for sample of microstructures made in SF_6 95
5.5 Fowler-Nordheim plot of data shown in Fig. 5.4 96
5.6 Schematic of a display based on field emission 100
5.7 Square arrays of microstructures made using masks 104

SIONYX1403000046.0024

SAMSUNG EX. 1002 - 1067/4148

List of Tables

3.1 Boiling points of compounds produced in etching of Si 60

SIONYX1403000046.0025

SAMSUNG EX. 1002 - 1068/4148

Acknowledgements

I am indebted to many people for their direct contributions to the work described in this thesis, and to many people for their indirect contributions, in the form of suggestions, advice, moral support, and friendship, during my time at Harvard.

I would first like to thank my advisor, Prof. Eric Mazur, for welcoming me into his remarkable research group and for providing all of his students with a collegial and engaging environment within Harvard. I am grateful to Eric for his guidance through the several projects I worked on in his lab and especially for his support of my development as a scientist and teacher. Eric provided a fine example for me of a professor who combines both excellent research and the best teaching. I know that in my future work I will draw heavily on what I learned through working with him.

I am also grateful to the other members of my thesis committee, Prof. Michael Tinkham and Prof. Cynthia Friend for their suggestions as I completed this work and for their comments on the thesis. Prof. Friend and her group taught me everything I know about surface chemistry, as well as a great deal about experimental methods. I also appreciate very much her advice and help during my job search.

Being a student at Harvard allowed me access to many resources and opportunities. The finest resource Harvard offered was the many talented people, especially graduate students and post-docs, with whom I worked. During my first few years at Harvard, I learned an enormous amount from Karl Berggren, Eunice Cheung, Arthur Chu, Nynke Dekker, Kent Johnson, J.D. Paul, Alison Stoddart, and Joseph Thywis-

SIONYX1403000046.0026

SAMSUNG EX. 1002 - 1069/4148

sen. I would like to "warmly" thank them for our time in the lab together as well as for their continued friendship as we have all taken our separate paths.

I am grateful to the students in the Mazur group for welcoming me so graciously into their midst when I was a fifth-year student with no understanding of the "ultra-fast" world. They patiently taught me the ropes and within a very short time I felt completely at home with them.

The work described in Chapter 2 of this thesis was done in collaboration with Jon Ashcom. Our experiments benefited greatly from Jon's hard work and his careful and thorough experimental style. The long hours hunting for tiny signals were made much more enjoyable by our animated discussions and by Jon's wonderfully cynical humor. Jon and I both learned from Andre Brodeur's example in his construction of the optical parametric amplifier used in those experiments.

The work described in the final three chapters of this thesis was the product of a close collaboration with Jim Carey, Catherine Crouch, Josh Levinson, Michael Sheehy, and Li Zhao. I would like the thank Jim Carey for his continued excellent work on this project and for his wonderful enthusiasm for all the various paths the work has taken. I am also grateful for his patience while I was engaged in job-hunting and thesis-writing and yet was trying to remain involved in the project. It has been a pleasure to work with our two excellent post-docs, Catherine Crouch and Josh Levinson. Catherine's solid state physics background, in particular, has helped me to fill in gaps in my own understanding. Josh provided the chemistry expertise for our project during his time in our group. His vast knowledge and experimental skill were a great help to all of us, and his corny jokes always gave us a laugh. Michael Sheehy recently filled the role of chemist in our subgroup and was entrusted with the care of our temperamental UHV chamber. I wish him the best of luck with it. Li Zhao led much of the early work on field emission from laser-induced silicon microstructures. Although our time in the lab did not overlap much, I am grateful

SIONYX1403000046.0027

SAMSUNG EX. 1002 - 1070/4148

to Li for his important contributions to those experiments.

There are many other members of the Mazur group with whom I did not directly work but from whom I learned a great deal. I would like to thank Nan Shen and Chris Schaffer for teaching me their tricks for operating the laser system. I also thank Paul Callan, Albert Kim, and Chris Roeser for providing an outside perspective to some of our problems and for valuable suggestions. Adam Fagen's education research gave me new insights into teaching techniques and I appreciate the talks we have had about pedagogy. All of these folks became great friends of mine and I will miss the time we spent together in the lab or over lunch, talking about our projects and joking around.

This thesis improved dramatically as a result of the comments of a number of helpful readers. Jon Ashcom and Jim Carey provided valuable suggestions on several of the chapters. Catherine Crouch and Karl Berggren generously read the entire document, painstakingly noting my awkward or passive sentences and forcing structure onto my paragraphs. I am grateful for their efforts and hope I have become a better writer because of their help.

I would like to thank my first physics teacher, the late Ronald Geballe, Professor Emeritus at the University of Washington. Dr. Geballe managed to get a group of 13-year-olds interested in everthing from the structural stability of King Kong's skeleton to the emission spectra of atomic gases. I was fortunate to have a teacher with an intense interest in teaching science to young people at all stages and I benefited greatly from Dr. Geballe's advice and support, even during graduate school.

I am grateful to my parents and sisters for supporting me in my education. They did not always understand what I was working on or why on earth I was doing it, but they always asked "How's the laser?" and wanted reprints of my publications, just the same. I found inspiration in my grandmother, Mary Kelly, as she has continued her own education. I thank her for providing an example to me: if she could finish her thesis at age 77, then I should be able to finish mine, too.

SIONYX1403000046.0028

SAMSUNG EX. 1002 - 1071/4148

Finally, I would like to dedicate this thesis to my husband, Karl Berggren, who was my strongest ally and greatest friend throughout graduate school. Even when my experiments did not go as well or as quickly as I hoped, Karl always had confidence in me and that meant a great deal to me. Furthermore, he helped me to remember that there is life outside the lab, and he has made that life far richer.

SIONYX1403000046.0029

SAMSUNG EX. 1002 - 1072/4148

Chapter 1

Introduction and Overview

Researchers in science and technology now have available to them a unique tool for observing processes that take place with femtosecond timescales and for creating novel nonlinear interactions with matter: ultrashort laser pulses. This thesis presents two sets of experiments that use this tool. The first set of experiments employs ultrashort pulses in an attempt to time-resolve a chemical reaction taking place on a surface (chapter 2). The second set of experiments uses the high peak intensity of the pulses to permanently modify a silicon surface, creating surface features with a number of remarkable and potentially useful properties (chapters 3, 4, and 5).

Chapter 2 addresses the construction and characterization of an apparatus for ultrafast spectroscopy of adsorbates on Pt (111). I describe the use of an optical parametric amplifier and difference-frequency-generation stage to create coherent tunable radiation across the wavelength range of 550 nm–7.3 μm. I discuss the process of infrared-visible sum-frequency generation and outline our implementation of this technique to try to observe a chemical reaction on the femtosecond timescale.

Chapter 3 discusses the formation of conical silicon microstructures in the presence of reactive background gases using 100-femtosecond laser pulses. I describe how the structures develop during irradiation and how their morphology depends

SIONYX1403000046.0030

SAMSUNG EX. 1002 - 1073/4148

on experimental parameters, such as the ambient gas species and the laser fluence. I present possible mechanisms for the formation of these structures and proposes future experiments that could resolve the actual mechanism at work.

The laser-induced microstructures show great promise for use in a number of applications. Both the shapes of the conical structures and the impurities introduced in them during fabrication contribute to the utility of these microstructures in applications in optoelectronics and vacuum microelectronics. Chapters 4 and 5 deal with the microstructures' physical properties that are important in these applications.

In chapter 4, I discuss the optical properties of laser-induced conical structures. The structures show remarkably enhanced absorption of infrared radiation, relative to unpatterned silicon. I review some of the other techniques currently used to increase the absorptance of crystalline silicon. I then present our experiments that measure the reflectance, transmittance, and absorptance of samples of microstructured silicon. I discuss how the morphology and chemical composition of the structures leads to enhanced absorptance, and give reasons for the observed variation in absorptance with structure size and ambient gas. Finally, I discuss the future work that is necessary to make laser-structured surfaces practical in optoelectronic devices such as solar cells and infrared optical detectors.

Chapter 5 focuses on the field-emission properties of the conical microstructures. I first give a short review of the theory behind field emission from metals and semiconductors, and then present the experiments that demonstrate that the emission observed from the laser-induced microstructures is indeed field-emission and not, for example, thermionic emission. I discuss some of the interesting features in the response of the emission current to the applied bias voltage. I then identify several applications of field-emitters in vacuum microelectronic devices and outline some future experiments to further quantify and improve the overall performance of our field-emitting structures.

SIONYX1403000046.0031

SAMSUNG EX. 1002 - 1074/4148

The variety of experiments presented in this thesis demonstrates the broad utility of the femtosecond pulsed laser. While the work described here opens the door to several new applications for ultrashort laser pulses, it also suggests that we have only scratched the surface in exploiting this exceptional tool.

SIONYX1403000046.0032

SAMSUNG EX. 1002 - 1075/4148

Chapter 2

Tunable sources of infrared pulses for ultrafast surface science

2.1 Introduction

The high peak powers and peak intensities accessible with subpicosecond-duration pulsed lasers allow nonlinear frequency conversion techniques that greatly expand the frequency range within which experiments can be performed. This chapter describes the construction of a source of tunable IR pulses between wavelengths of 550 nm and 7.3 μm. This source combines two processes, optical parametric amplification (OPA) and difference frequency generation (DFG). By using these two nonlinear techniques, along with frequency doubling, as shown in Fig. 2.1, we can reach most of the electromagnetic spectrum with wavelengths between 550 nm and 7.3 μm. We constructed our apparatus specifically to produce laser pulses with a wavelength of 4.9 μm, which allowed us to access the vibrational states of adsorbates on Pt (111) (see section 2.4).

This chapter also describes the experiments conducted using the OPA/DFG setup,

SIONYX1403000046.0033

SAMSUNG EX. 1002 - 1076/4148

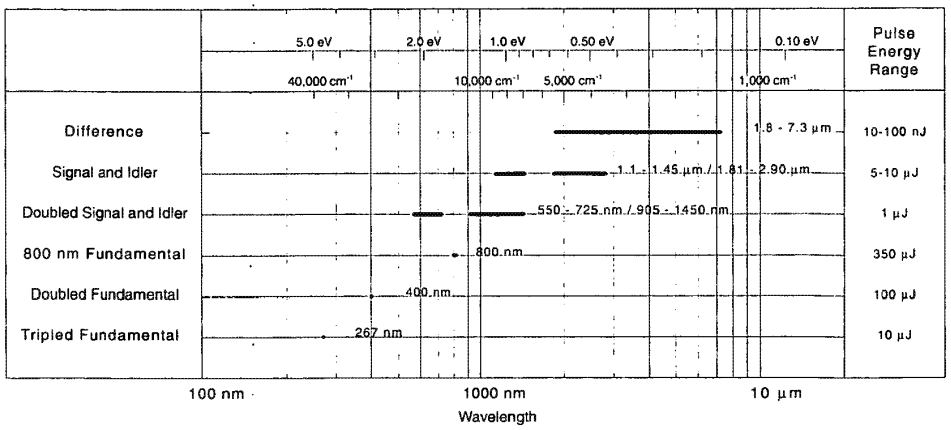


Figure 2.1: Range of wavelengths that can be obtained using each of the listed optical processes. Laser wavenumbers and photon energies are noted on the top axis, laser wavelength is on the bottom axis, and energy per pulse is noted along the right axis.

including the goals of those investigations and notes on some of the procedures followed.

2.2 Optical parametric amplifier

The first frequency-modification process our laser beam undergoes is optical parametric amplification, in which the 800-nm fundamental beam is converted into two beams with tuning ranges of approximately 1.1–1.45 μm and 1.8–2.9 μm.

2.2.1 Background

In optical parametric generation, a nonlinear optical crystal converts one input photon into two output photons whose energies' sum equals the energy of the input photon. ("Parametric," in this context, refers to the fact that the material returns to its original energy state after the process; there is no net gain or loss of energy by the crystal.) The two output photons are commonly known as the "signal" (shorter

SIONYX1403000046.0034

SAMSUNG EX. 1002 - 1077/4148

wavelength) and "idler" (longer wavelength) photons, and the input photon is referred to as the "pump" photon. Thus, the condition for conservation of energy is:

$$\frac{1}{\lambda_{signal}} + \frac{1}{\lambda_{idler}} = \frac{1}{\lambda_{pump}} . \tag{2.1}$$

This condition is satisfied, of course, by many possible pairs of signal and idler wavelengths, so additional constraints are required to specify the particular output pair desired. In our implementation, the constraints are provided by the wavelength of a seed input pulse, which stimulates the creation of the signal beam, and, more importantly, by the phase-matching conditions of the crystal. Optical parametric amplification was first observed in KH_2PO_4 in 1965 [1].[1] Shortly thereafter, the first tunable infrared optical source based on optical parametric oscillation in $LiNbO_3$ was demonstrated [2]. Since then, optical parametric oscillators (OPO's) and optical parametric amplifiers (OPA's) have become widely used as sources of tunable radiation. The theory describing OPA/OPG is discussed in Byer and Herbst [3] and Yariv [4], among others; experimental work in this area is the subject of a feature issue in J. Opt. Soc. B [5]. The use of β-barium borate (BBO) crystals in optical parametric generators represents a substantial advancement [6], since their high second-order susceptibility and high damage thresholds allowed the first OPA's with sub-picosecond pulses. Many experiments have since taken advantage of the femtosecond-pulse output of BBO OPA's [7, 8, 9, 10, 11, 12], including instruments that generate pulses shorter than 10 fs [13].

Our BBO-based OPA uses type-II phase matching [14], in which the polarizations of the two output beams are orthogonal. Type-II phase matching allows higher conversion efficiencies than type-I phase matching, in which the signal and idler have the

[1] Optical parametric generation (OPG) refers to the general process described by eqn. 2.1. Optical parametric amplification refers to an OPG process that is seeded by an external source, which stimulates emission of "signal" photons with a particular wavelength. An optical parametric oscillator refers to an optical cavity containing an OPG crystal; the output of the OPG process is constrained by the modes of the cavity.

SIONYX1403000046.0035

SAMSUNG EX. 1002 - 1078/4148

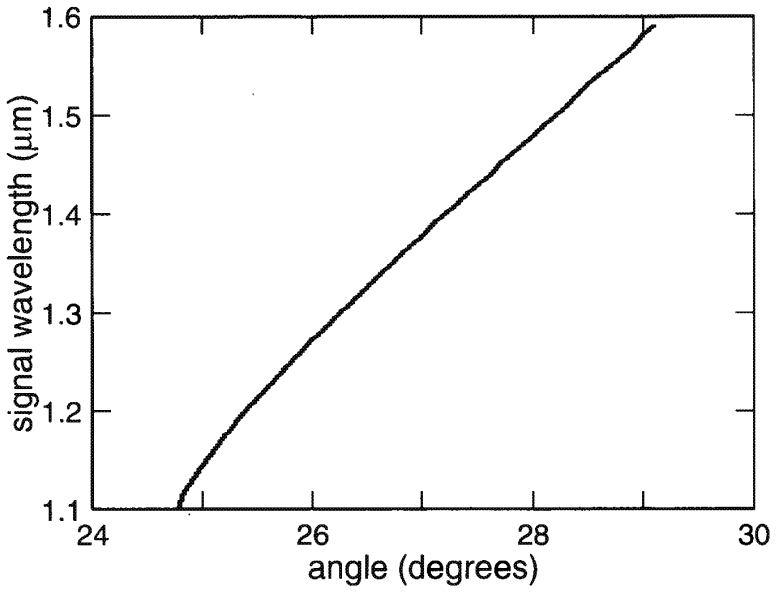


Figure 2.2: Tuning of the OPA signal output wavelength as a function of crystal angle, assuming a pump beam at 800 nm. These values were calculated for type-II phase matching, with the pump beam and idler polarizations extraordinary and the signal polarization ordinary; all the beams propagate collinearly. Our crystal is cut at 26.6°.

same polarization [9].

Figure 2.2 illustrates the phase-matching conditions that determine the tuning of the OPA stage. Phase matching refers to the condition that the output optical wave is in phase with the nonlinear polarization established in the crystal by the input waves. This condition, leading to the highest output power at the desired wavelength, can be achieved by carefully orienting the directions of propagation and polarization of the input beams with respect to the crystal axes (see reference [14] for a thorough discussion). Figure 2.2 shows that wavelengths between 1.1 μm and 1.6 μm are readily achievable in our system.

SIONYX1403000046.0036

SAMSUNG EX. 1002 - 1079/4148

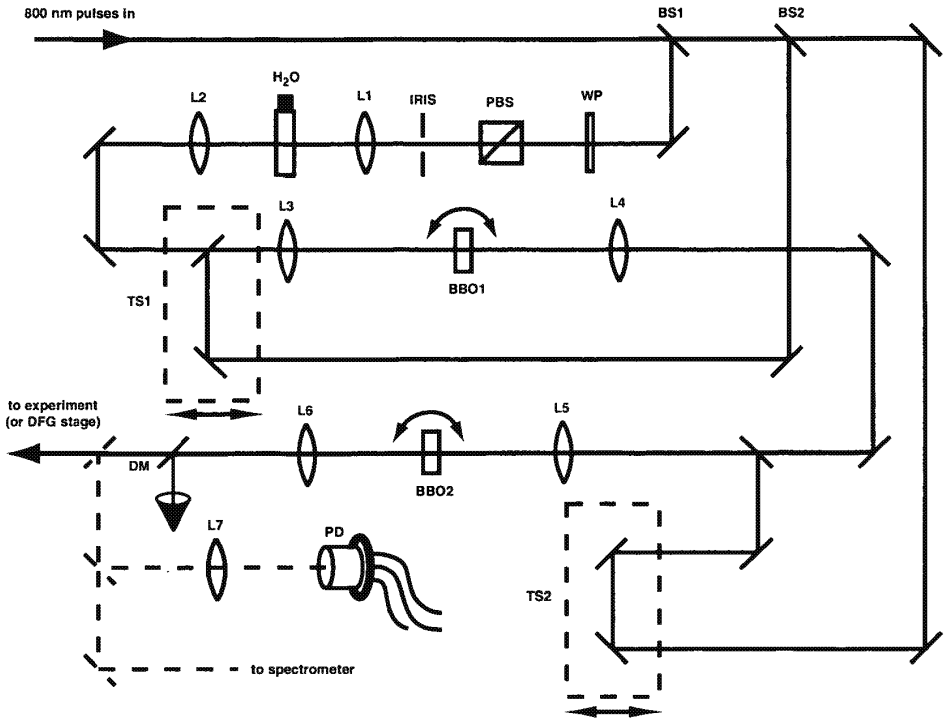


Figure 2.3: Optical parametric amplifier used to convert radiation at 800 nm to infrared radiation with wavelengths 1.1–1.45 μm and 1.8–2.9 μm. Beamsplitters BS1 and BS2 reflect approximately 10% of the 800-nm light. WP is a half-wave plate; PBS is a polarizing beamsplitter cube. The focal lengths of the lenses are as follows: L1, 5 cm; L2, 7.5 cm; L3, 20 cm; L4, 12.5 cm; L5, 40 cm; L6, 40 cm; L7, 7.5 cm. All lenses are fused silica, except L6 and L7, which are uncoated CaF_2. The BBO crystals are both cut for type-II phase matching, at 26.6°. The mirror DM is an 800-nm high reflector on CaF_2 and reflects the pump light into a beamstop while passing the signal and idler beams.

2.2.2 Experimental

Figure 2.3 shows the setup of the optical parametric amplifier. Our OPA consists of two stages, each having one BBO crystal. The first stage creates the infrared signal and idler pulses and the second stage amplifies them.

The laser (not shown) that is used to pump the OPA is a regeneratively amplified

SIONYX1403000046.0037

SAMSUNG EX. 1002 - 1080/4148

Ti:sapphire laser, operating at a wavelength of 800 nm. The laser oscillator is built from a Model TS kit from Kapteyn-Murnane Laboratories and is pumped with a Coherent Verdi V-5 solid-state laser. The amplifier is pumped with a Quantronics 527 Nd:YLF laser. The maximum power output of the laser, after pulse compression, is approximately 430 mW, with a pulse repetition rate of 1 kHz. Typical minimum pulse durations for this system are 100 fs.

The input into the OPA apparatus is 250–300 mW of the 800-nm laser beam. A combination of a half-wave plate (WP), a polarizing beamsplitter cube (PBS), and an iris is used to attenuate a small fraction of the beam, selected by BS1, and rotate its polarization by 90°. Lens L1 focuses this beam into a water cell, generating white light [15]. The white light is then focused into the first β-barium borate (BBO) crystal, where the infrared portion acts as the seed for optical parametric amplification. The translation stage TS1 is used to optimize the temporal overlap between this infrared seed pulse and the 800-nm pump pulse. Note that because of the WP and the PBS cube, the seed and the pump have orthogonal polarizations, as required for type-II phase matching. After collimation by lens L4, the output from the first stage of the OPA is focused by lens L5 into the second BBO crystal, where it now acts as a seed for the amplification stage. The pump for this amplification stage arrives via translation stage TS2, which allows the temporal overlap between it and the infrared beam to be maximized. A dichroic mirror on a CaF_2 substrate reflects most of the 800-nm light into a beam block; the infrared pulses pass through the dichroic mirror and can then be directed either to various diagnostic instruments, such as a power meter or spectrometer, or to the difference frequency generation apparatus.

To optimize the power output of the OPA at a desired wavelength we follow a sequence of steps. First, a narrow-bandwidth optical filter, centered at the desired signal wavelength, is placed in front of the photodiode, along with a sufficient number of neutral density filters to avoid saturating the detector. The white-light output of

SIONYX1403000046.0038

SAMSUNG EX. 1002 - 1081/4148

the water cell is checked to verify that its power output is constant (that is, not flickering) and that its spatial mode is fairly clean (approximately TEM_{00}). If the power output is varying, or the spatial mode is moving in time, these variations are amplified in the OPA and thus the OPA output is extremely unsteady. In order to improve the white-light power or mode stability, the waveplate WP can be rotated to decrease the power going into the water cell, while the iris diameter can be adjusted to give the most constant beam profile. The first crystal BBO1 is placed such that the focus of lens L3 falls behind the crystal, to avoid the damage that would result if the focus were in the crystal. With the pump beam for the second crystal blocked (just after beamsplitter BS2, for example), the power measured at the chosen wavelength on the photodiode is optimized by adjusting both the pointing of the pump beam for the first stage and the timing *via* translation stage TS1. Then, the crystal BBO1 is also rotated and tilted slightly to find the correct phase-matching orientation to yield the highest power output. After any repositioning of the crystal, the pump pointing and the timing are rechecked, and the process is iterated. The output of the first stage is then aligned such that it passes through the center of the second crystal BBO2; the pump for the second crystal is now allowed to pass through and is focused just behind BBO2. The pump pointing and the placement of TS2 are adjusted to maximize the signal on the photodiode. As with the first stage, the tilt and rotation of the crystal BBO2 are optimized and the pump pointing and timing adjusted again. The power and spectrum of the output of the OPA are measured daily.

Narrow bandwidth filters are not always available at the desired signal wavelength; in this event, another method must be used to ensure that each of the stages of the OPA is optimally aligned for that wavelength. We have found two methods to be useful for this optimization. First, a narrow bandwidth filter for a wavelength near the desired one can be used, and the filter tilted by an appropriate, calculated angle with respect to the beam. We have found that this technique works well for

SIONYX1403000046.0039

SAMSUNG EX. 1002 - 1082/4148

tuning by approximately 15 nm or less. Alternatively, the OPA can be optimized at a wavelength near the desired value, and its output directed through the grating spectrometer. With a detector at the spectrometer's output, the spectrometer can be gradually tuned to pass the desired wavelength while the OPA's performance is maximized at each intermediate wavelength value. In this case, the spectrometer essentially acts as a filter with a tunable peak wavelength and bandwidth. This technique is preferable for wavelengths more than approximately 15 nm from the peak wavelength of the closest filter.

2.2.3 OPA performance

Figure 2.4 shows the spectrum of the two infrared beams produced by the OPA. The spectrum varies somewhat from experiment to experiment for two reasons. First, the operating parameters of the laser change over time, shifting the center frequency and spectral width of the pump laser. Second, the daily process of optimization of the power at a given wavelength involves adjustment of the rotation and tilt of the BBO crystals, which changes the output spectrum.

In this particular spectrum, the wavelength of the signal peaked at 1380 nm and the idler at 1950 nm. Note that the frequencies of these two beams sum to 3.7×10^{14} Hz, which corresponds to a wavelength of 808 nm; the spectrum of the initial pump beam shows that it is centered at approximately 800 nm but still has a substantial portion of light at 808 nm. Figure 2.5 summarizes spectra analogous to Fig. 2.4 taken over a number of days. The wavelength of the idler component is plotted as a function of the wavelength of the signal beam. The triangles represent measured values of peak wavelengths, and the curves show calculated values based on three different pump wavelengths, 790 nm, 805 nm, and 820 nm. With a few exceptions, the measured values fall within the range corresponding to pump wavelengths of 790–820 nm, which is roughly the range of the measured pump spectrum.

SIONYX1403000046.0040

SAMSUNG EX. 1002 - 1083/4148

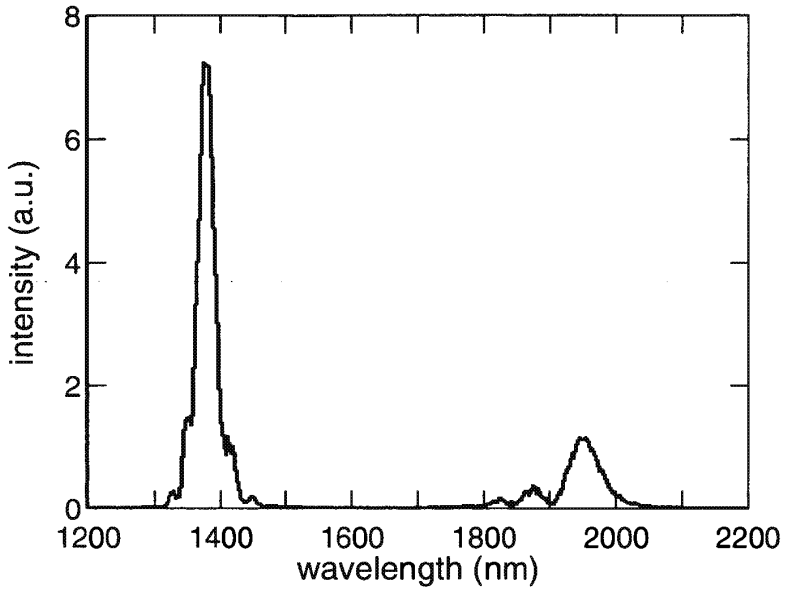


Figure 2.4: Spectrum of output generated by optical parametric amplifier.

Our OPA is most efficient for signal wavelengths in the range of roughly 1.3–1.4 μm, which corresponds to idler wavelengths of approximately 1.9–2.1 μm. Figure 2.6, shows the output power of the OPA (signal plus idler beams) as a function of the wavelength of the signal beam. The peak in efficiency near 1.3–1.4 μm is due, most likely, to the fact that the BBO crystals are cut for optimum phase matching of processes with output wavelengths in this range.

We have measured the duration of the infrared signal pulses using autocorrelation based on second-harmonic generation in a BBO crystal cut for SHG at $\lambda = 1300$ nm [16, 17]. The autocorrelation trace, along with an autocorrelation trace for the 800-nm pump beam, is shown in Fig. 2.7. From pump pulses with a width of approximately 100 fs, we obtain signal pulses with a comparable width at the half-maximum point,

SIONYX1403000046.0041

SAMSUNG EX. 1002 - 1084/4148

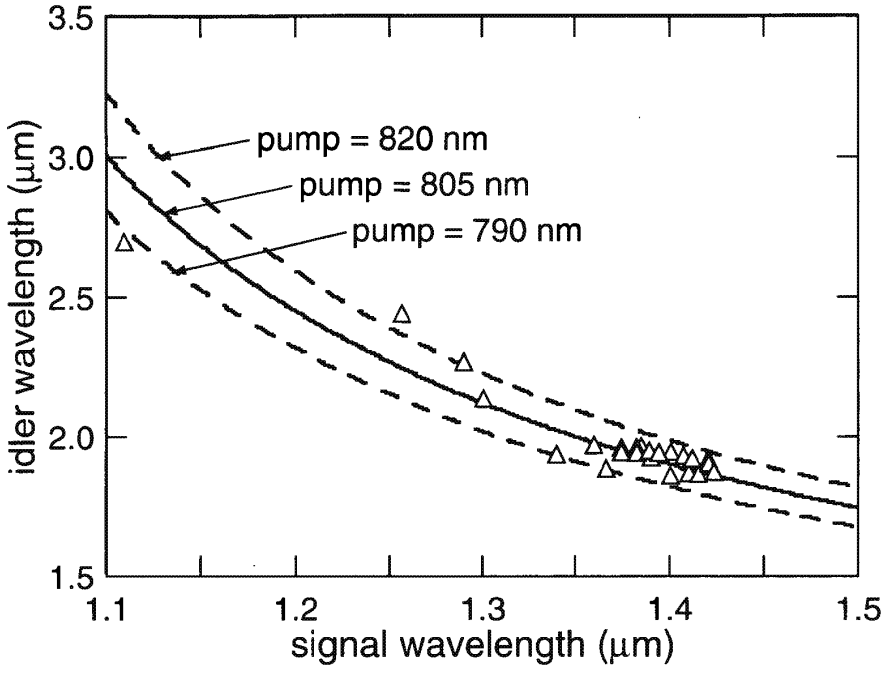


Figure 2.5: Measured peak wavelength of the idler beam *vs.* measured peak wavelength of the signal. The curves show calculated values of the idler wavelength as a function of signal wavelength, calculated for three different values of the wavelength of the pump beam.

but a slightly broader base. We expect that the idler pulsewidth is approximately equal to that of the signal because they are created in the same process.

2.3 Difference frequency generation

To produce photons with energies further into the infrared, the output of the OPA is used as the input to a second frequency conversion apparatus, a difference frequency generation (DFG) stage.

SIONYX1403000046.0042

SAMSUNG EX. 1002 - 1085/4148

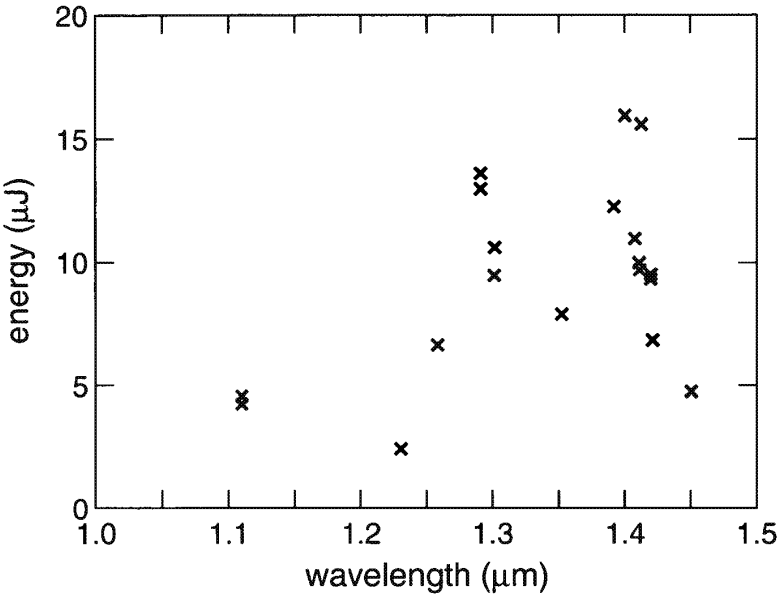


Figure 2.6: Output power of the OPA (signal and idler beams combined) *vs.* wavelength of the signal. The dashed curve is included as a guide to the eye. The different points at a given wavelength correspond to measurements taken on different days, with slightly different operating parameters of the laser and somewhat different alignment of the OPA components.

2.3.1 Background

In the DFG stage, both of the OPA's output beams (the signal and idler) are directed into a nonlinear crystal; light is then produced in the crystal at a frequency equal to the difference between the frequency of the signal and that of the idler. This is called difference frequency generation and occurs via absorption of a signal photon, followed by stimulated emission of a photon with the same frequency as the idler beam. To conserve energy, a "difference photon" must also be emitted, so a new component,

SIONYX1403000046.0043

SAMSUNG EX. 1002 - 1086/4148

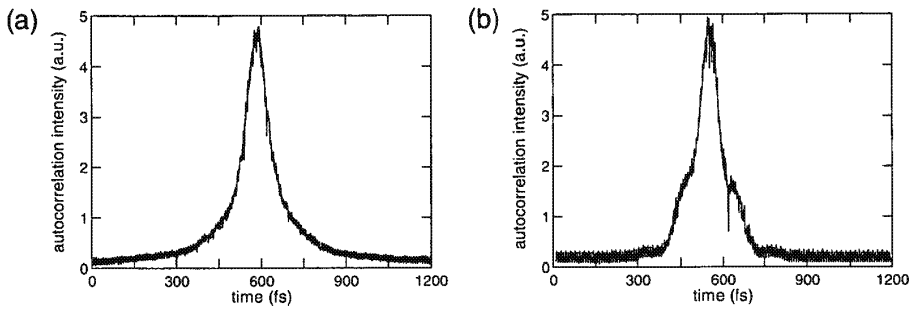


Figure 2.7: Autocorrelations of the (a) pump and (b) signal beams. The signal is not significantly broadened relative to the 100-fs pump pulses.

with wavelength λ_{DFG} is created, where:

$$\frac{1}{\lambda_{signal}} - \frac{1}{\lambda_{idler}} = \frac{1}{\lambda_{DFG}} \tag{2.2}$$

Difference-frequency generation was first observed by Smith and Braslau in 1962 [18]. DFG between the signal and idler beams of an OPA or OPG stage has subsequently become a popular technique for generating radiation in the 6–12-μm wavelength region [19, 20, 21, 22, 23, 24, 25].

The construction of our instrument was influenced most strongly by Golubovic and Reed [24], who investigated type-I and type-II phase matching in $AgGaS_2$. They report continuous tuning in the range of 2.4–12 μm, pulse durations of less than 50 fs, and maximum pulse energies of roughly 24 nJ. It should be noted, however, that some of the parameters of their output pulses, namely the wavelength and pulse duration, were inferred from their signal and idler inputs. The DFG output wavelength is calculated from the signal and idler center wavelengths, using conservation of energy and assuming that all the output power was at the difference frequency. The duration of the output pulses is determined from the cross-correlation of the signal and idler pulses; the duration of the cross-correlation pulse is 48 fs. We suspect,

SIONYX1403000046.0044

SAMSUNG EX. 1002 - 1087/4148

however, that this experiment may have unknowingly suffered from some of the same difficulties we faced in tuning the DFG output (see sections 2.3.2 and 2.3.3 below), so a direct comparison between their reported results and our measured results may not be warranted.

Recently, another group [25] has demonstrated tenfold greater output energy using a similar DFG apparatus, compared to the results of reference [24]. They have shown that pulses with energies as high as 9 μJ can be created in a $HgGa_2S_4$ crystal using signal and idler pulses with energies of 43 μJ and 30 μJ, respectively. They have also found that the use of the $HgGa_2S_4$ crystal in their apparatus gives mid-infrared conversion efficiencies approximately 20% higher than those obtained using $AgGaS_2$. The duration of their DFG output pulses is roughly 200 fs, as determined by cross-correlation using sum-frequency generation. Because the data reported in [25] are measured directly and because this group has obtained the highest conversion efficiency to date, this work represents the best example of what should be achievable using DFG between the signal and idler outputs of an OPA.

Figure 2.8 shows the calculated wavelengths of the output beams (both idler and difference) from the DFG stage, as a function of the wavelength of the signal, assuming that the pump beam has a wavelength of 805 nm. Note that with a range of signal inputs λ_{signal} = 1.1–1.45 μm, and corresponding idlers, the DFG stage should generate wavelengths λ_{DFG} = 1.7–7.5 μm.

2.3.2 Experimental

A schematic diagram of the apparatus used for difference frequency generation between the two output beams of the OPA is shown in Fig. 2.9. The signal and idler beams enter collinearly via a polarization-rotating periscope, then are separated using

SIONYX1403000046.0045

SAMSUNG EX. 1002 - 1088/4148

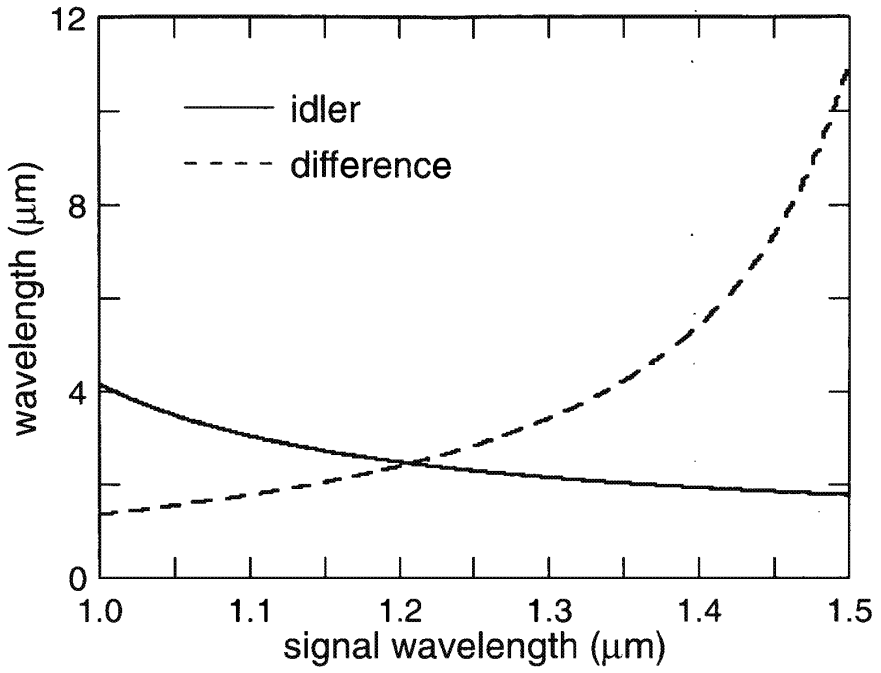


Figure 2.8: Calculated wavelengths of idler and difference beams *vs.* signal wavelength, assuming a pump wavelength of 805 nm.

the dichroic mirror DM1[2]. The signal and idler are then independently directed to the focusing lens, which focuses both just behind the difference-frequency generating crystal. Care must be taken not to focus the beams directly at the surface of the crystal or significant damage occurs from the 800-nm component that copropagates with the signal and possibly with the idler. The crystal is mounted on a rotatable kinematic mount so that it can be optimally placed for good phase matching of the desired wavelength components. We measure the DFG output power using a liquid-nitrogen cooled Hamamatsu P5172 InSb detector.[3] After optimization and power measure-

[2]We are grateful to Murray K. Reed and the Coherent Laser Group, Coherent Inc., for the generous donation of the set of dichroic mirrors.

[3]The detector has a peak in its detectivity ($D^* = 10^{11}$ cmHz$^{1/2}$/W) at approximately $\lambda = 5.3\mu$m, and the detection efficiency falls by approximately one order of magnitude for each additional 500

SIONYX1403000046.0046

SAMSUNG EX. 1002 - 1089/4148

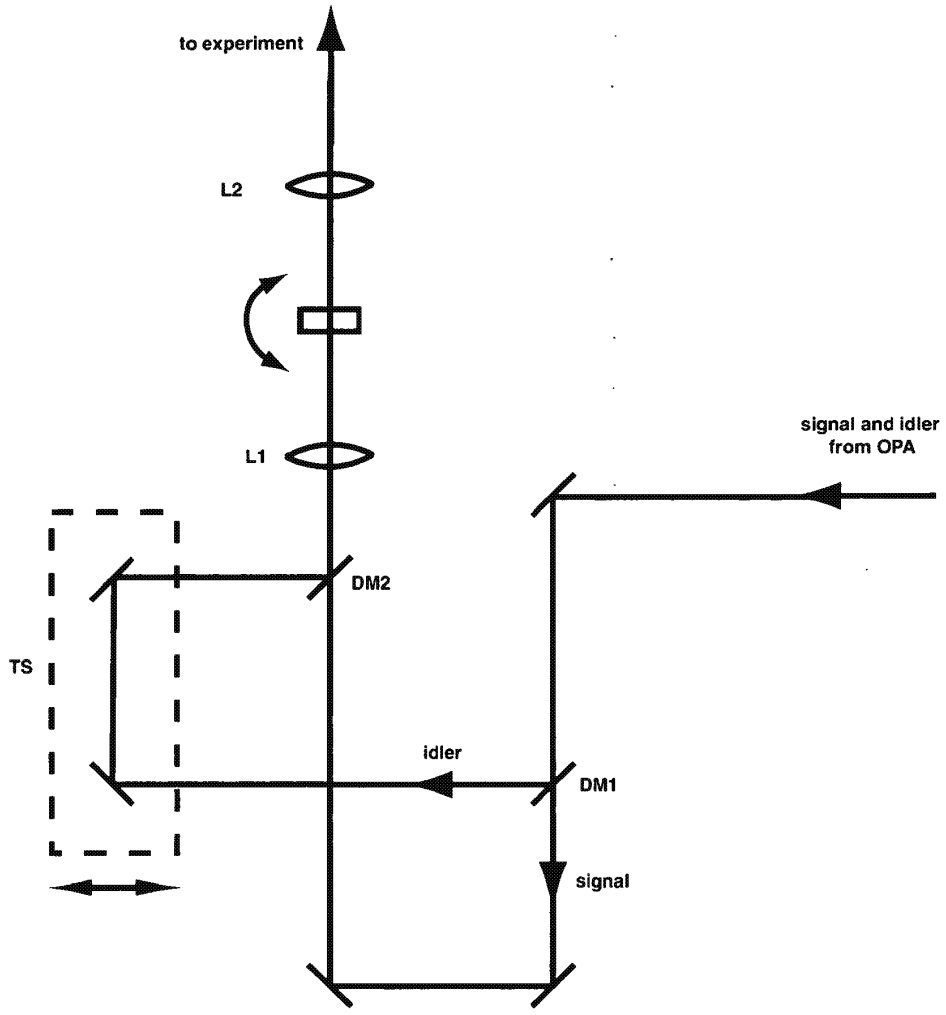


Figure 2.9: Apparatus used for difference frequency generation between the two output beams of the optical parametric amplifier. L1 is an uncoated CaF_2 lens with focal length 100 mm; L2 is a CaF_2 lens with focal length 100 mm, and a broadband anti-reflection coating centered at 3.5 μm. The dichroic mirrors, DM1 and DM2, pass wavelengths in the range of the signal and reflect wavelengths in the range of the idler, separating the two beams.

nm at longer wavelengths. The useful wavelength range for this detector is 1–6 μm, making it much more sensitive in the infrared than our pyroelectric detectors.

SIONYX1403000046.0047

SAMSUNG EX. 1002 - 1090/4148

ment, the output of the DFG stage can then be characterized with a spectrometer or it can be directed into the experiment.

We have found that when operating the DFG apparatus, it is critical to use a narrow-bandwidth optical filter or grating monochromator between the DFG stage and the power meter. This filter selects the desired wavelength before we adjust the optics to maximize the power output. One cannot simply assume that the output of the stage will necessarily be at the difference frequency between the center-frequencies of the signal and idler. Each of the signal and idler are sufficiently spectrally broad that components of their spectra can mix in the crystal to give a broad range of frequencies. Furthermore, nonlinear processes other than DFG can occur, so that if the optical components are aligned within the apparatus simply to maximize power output, without using an optical filter or grating monochromator, the resulting output is not necessarily at the difference frequency expected.

2.3.3 DFG characterization

Our apparatus can generate difference frequencies using a number of different nonlinear crystals. Specifically, we have tried $LiIO_3$ (LIO) and $AgGaS_2$ (AGS) crystals. The spectrum of the output of the DFG stage, when the LIO crystal is used, is shown in Fig. 2.10. With the AGS crystal, the output spectrum shown in Fig. 2.11 is generated. We obtained higher power outputs and wider frequency spectra with the AGS crystal and thus used it for the experiments described below.

The pulsewidth of the infrared output of the DFG is measured with a cross-correlation with 800-nm 100-fs pump pulses using sum-frequency generation in the LIO crystal. The cross-correlation trace is shown in Fig. 2.12. A fit to a sech^2 curve gives a full-width at the half-maximum (FWHM) of 220 fs, which implies a 180-fs FWHM for the DFG output [26].

SIONYX1403000046.0048

SAMSUNG EX. 1002 - 1091/4148

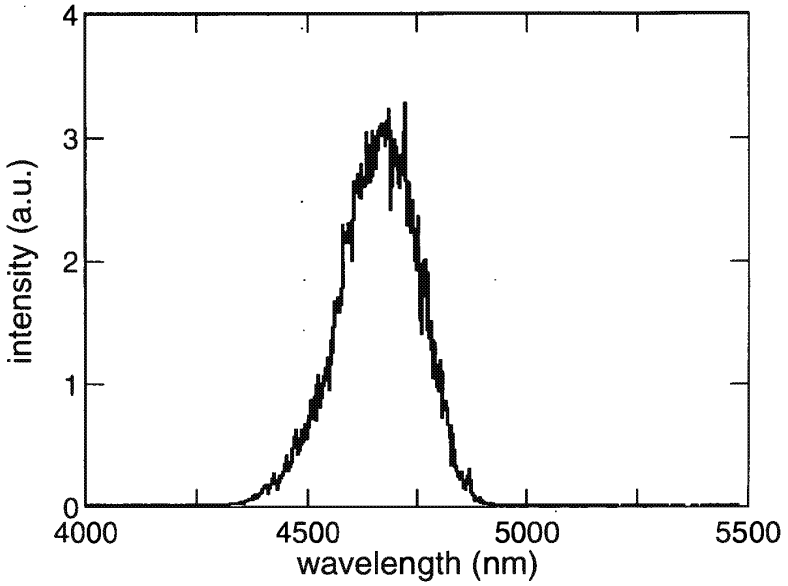


Figure 2.10: Spectrum of the output of the DFG stage using a LIO crystal.

2.4 Application to surface science

We constructed the OPA/DFG apparatus to enable us to perform time-resolved nonlinear optical studies of adsorbates on Pt (111). Specifically, our initial goal was to observe the reaction of CO with O_2 on a Pt surface; we therefore designed the optical instrumentation so that the output pulses of the DFG stage would be resonant with the stretch of the CO molecule. We hoped to use sum-frequency generation between the DFG output in the infrared at $\lambda_{DFG} = 4.9$ μm and the pump beam at $\lambda_{pump} = 800$ nm as a means for detecting CO present on a Pt (111) surface. Our intention was to initiate a reaction between adsorbed CO and O_2 using an ultrashort pulse, and then probe the surface for the presence (or absence) of CO or another species, such as CO_2,

SIONYX1403000046.0049

SAMSUNG EX. 1002 - 1092/4148

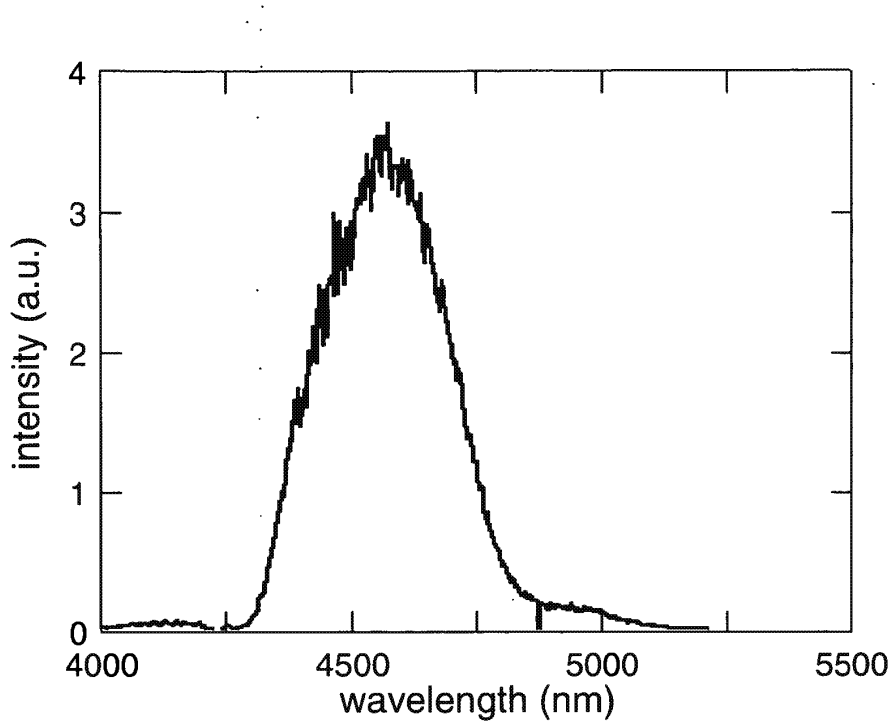


Figure 2.11: Spectrum of the output of the DFG stage using an AGS crystal.

using resonant infrared-visible sum-frequency generation (IR-VIS SFG) generated in a short pulse following the initial pulse by a short, controlled time. This section briefly describes the design of that experiment and explains the procedure followed to obtain the proper alignment and timing of the relevant pulses.

Although our experiment was ultimately unsuccessful because we lacked sufficient power to generate a signal that would be observable with our detectors, many of the techniques we developed and used can be applied to other, similar experiments.

SIONYX1403000046.0050

SAMSUNG EX. 1002 - 1093/4148

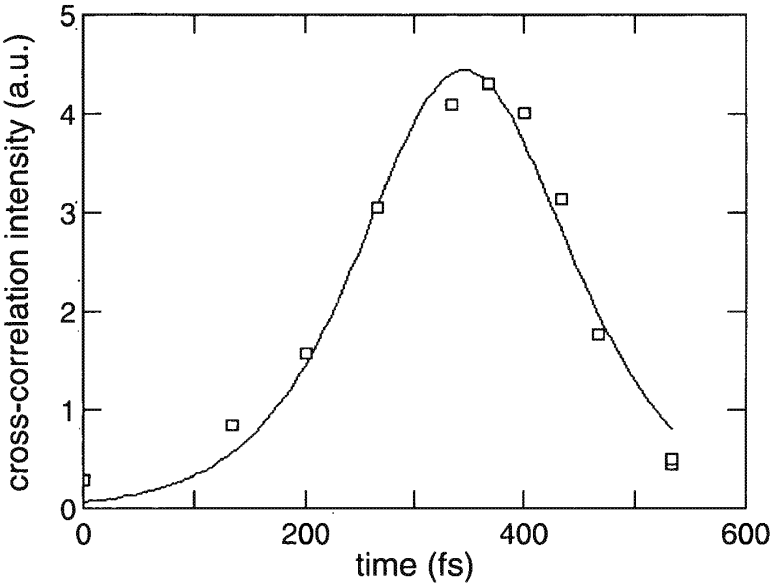


Figure 2.12: Cross-correlation trace of the output of the DFG stage with the 800-nm pump pulse, using SFG in the LIO crystal. The data are fit to a sech^2 profile.

2.4.1 Background

Sum-frequency generation was first observed in 1962 [27], just a few months after (and inspired by) the observation of the first nonlinear frequency conversion process, second harmonic generation [28]. In this first experiment, the two frequencies being mixed were produced by two separate ruby lasers, whose wavelengths differed by only 1 nm. The sum-frequency generation (SFG) process, however, is broadly applicable, not just to closely spaced frequencies; it is currently commonly used for frequency up-conversion [29], for the generation of tunable visible and ultraviolet radiation [14], and for spectroscopy [30]. Here I describe the mixing between one beam in the infrared and one in the visible, generating an output beam that is also in the visible.

SIONYX1403000046.0051

SAMSUNG EX. 1002 - 1094/4148

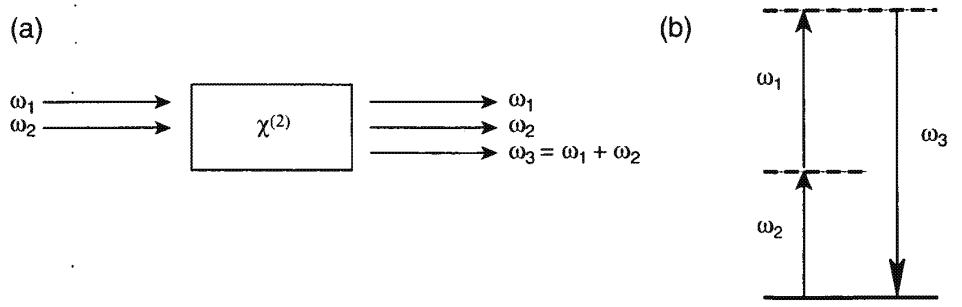


Figure 2.13: Schematic of the sum-frequency generation process; (a) SFG can only occur in materials with a non-zero $\chi^{(2)}$, (b) the dashed levels can be real or virtual states.

SFG is shown schematically in Fig. 2.13. The states in Fig. 2.13 can either be real states or virtual states. Because sum-frequency generation (SFG) is a second-order nonlinear effect, it does not take place in the bulk of materials that possess inversion symmetry [14]. It is thus a surface-specific process for a material such as crystalline Pt, which is centrosymmetric. We can exploit this surface-sensitivity in investigations of adsorbates on Pt (111); the SFG signal is produced entirely by the Pt surface and any adsorbates.

To detect only the SFG signal from the reacting adsorbates, optical resonances of these molecules can be used. SFG can be made very species-sensitive if one of the two frequencies being mixed is tuned to be resonant with either an electronic or vibrational state of a molecule. Here, we tune the infrared beam ω_1 to be resonant with a vibrational transition in the CO molecule adsorbed on Pt (111). The existence of this resonance enhances the second-order optical susceptibility $\chi^{(2)}$ and thus the production of the sum-frequency radiation increases. We expect that the resonant contribution from the adsorbate CO could be made much larger than the nonresonant contribution from the Pt surface, and thus our SFG signal should be largely due to the CO adsorbate.

SIONYX1403000046.0052

SAMSUNG EX. 1002 - 1095/4148

The first infrared-visible sum-frequency generation (IR-VIS SFG) experiment measured the vibrational spectrum of a monolayer of coumarin-504 molecules on the surface of fused quartz. This investigation used a visible Nd:YAG laser with a fixed wavelength and a tunable infrared CO_2 laser, both generating pulses with nanosecond durations [30]. Many later experiments exploited the tuning capabilities of OPA's for similar experiments. In 1993, the infrared output of a DFG stage was used in an IR-VIS SFG study of an air/binary liquid interface [31]. The pulse durations in this experiment were 15–20 ps. Our experiment differs from these earlier studies in that our pulses were sufficiently short (100 fs) to obtain time-resolved information about a reaction taking place on a surface.

2.4.2 Apparatus

The setup for using IR-VIS SFG for the detection of surface species combined our OPA/DFG stages with an ultrahigh vacuum chamber, as is shown schematically in Fig. 2.14.

Ultrahigh-vacuum chamber

The ultrahigh-vacuum chamber incorporates a wide range of surface preparation and analysis apparatus. It was designed by Walter Mieher and others and is described extensively elsewhere [32]. Briefly, the chamber is equipped with a turbo pump, an ion pump, and a Ti sublimation pump, which together evacuate the chamber to a typical operating pressure of 10^{-11}–10^{-10} torr. Instruments for Auger electron spectrometry and low-energy electron diffraction allow us to characterize our Pt crystal. Valves permit the addition of gases, such as neon or O_2, for cleaning purposes, and an ion gun can be used for sputtering the crystal surface. The chamber is also equipped with two capillary-array dosers for adding adsorbates to the Pt surface. A mass spectrometer is used in temperature-programmed desorption studies, to verify the

SIONYX1403000046.0053

SAMSUNG EX. 1002 - 1096/4148

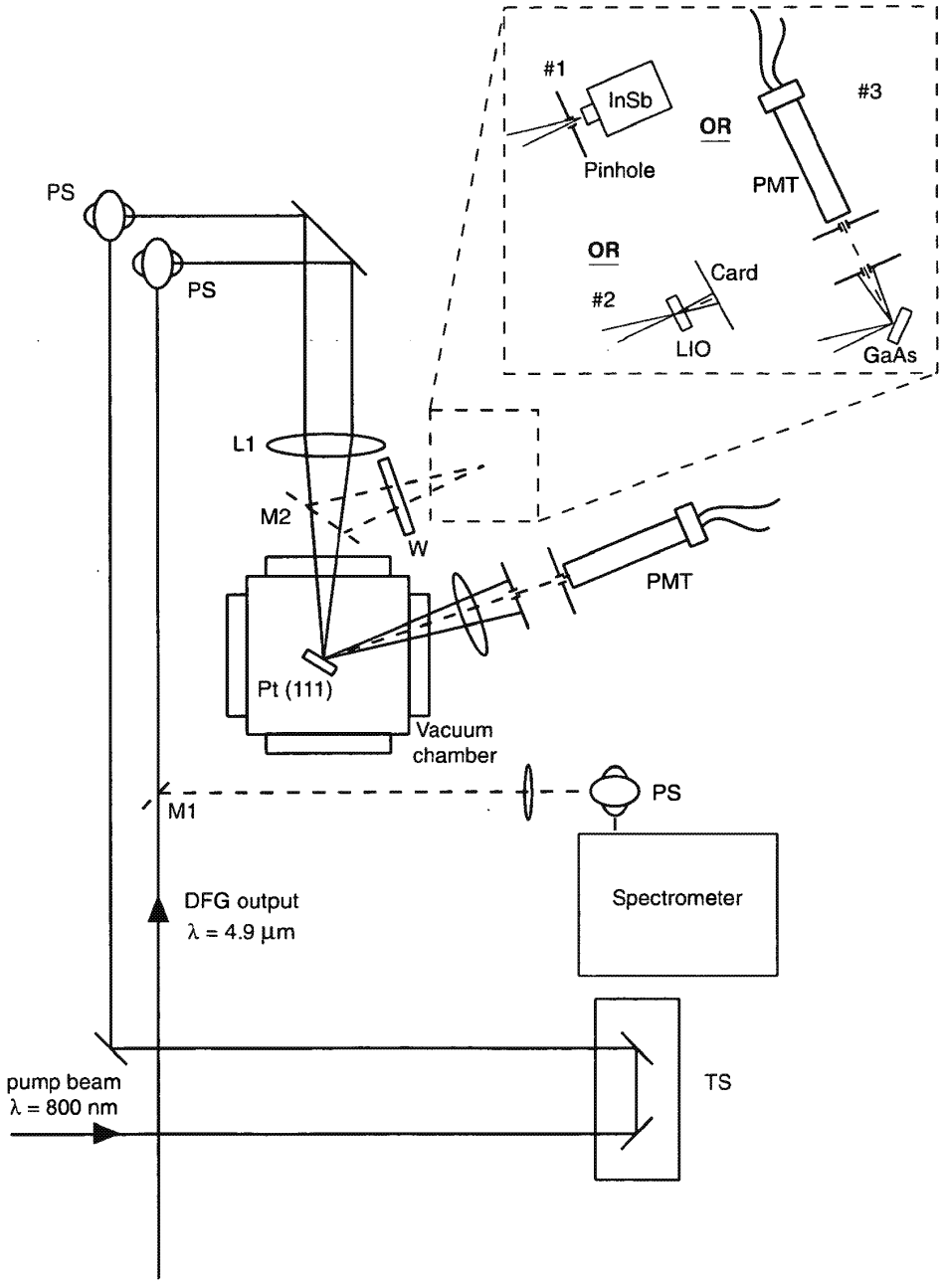


Figure 2.14: Setup for infrared-visible sum-frequency generation at a CO-covered Pt (111) surface. Dashed lines show components or beams that are not always present; inset illustrates three possible diagnostic setups used when mirror M2 is in place. See text for further details.

SIONYX1403000046.0054

SAMSUNG EX. 1002 - 1097/4148

cleanliness of our Pt sample or to assess the coverage of adsorbates.

The 10-mm-diameter sample of crystalline Pt, cut to expose the (111) surface, is mounted on a temperature-controlled manipulation stage with 3-dimensional translational and rotational control. The sample is typically kept at a temperature of approximately 90K, except during cleaning procedures (see section 2.4.5 below).

Optical setup

The mid-infrared beam at $\lambda = 4.9\mu$m is taken from the output of the DFG stage. Mirror M1 can be inserted into the path so that the beam can be sent to the grating monochromator. The power output of the monochromator is measured with an InSb infrared detector (not shown). The SFG's "visible" pump beam at $\lambda = 800$ nm is separated from the main 800-nm beam before the OPA stage.

The pump beam and the output from the DFG stage are directed *via* periscopes (labelled PS) into the UHV chamber and on to the Pt (111) surface. The pump beam is delayed *via* a translation stage so that the pump pulses can arrive at the Pt crystal simultaneously with the DFG pules. An anti-reflection coated CaF_2 lens focuses both beams onto the crystal.

Mirror M2 can be inserted to intercept the focusing beams and direct them through a CaF_2 window, W, to one of three possible diagnostic apparatuses. Diagnostic #1 consists of a pinhole with a diameter of approximately 100 μm and an InSb infrared detector. Diagnostic #2 features a lithium iodate (LIO) crystal, 3-mm thick, and a white card for imaging. In diagnostic #3, a GaAs crystal, two irises and a photomultiplier tube, labelled PMT, are used. Diagnostic #1 is used to achieve rough spatial overlap between the visible and infrared beam; the overlap is improved using sum-frequency generation in diagnostics #2 and #3, as described below.

In the absence of mirror M2, the infrared and visible beams pass into the vacuum chamber through a CaF_2 window and focus on the Pt (111) surface. The reflected

SIONYX1403000046.0055

SAMSUNG EX. 1002 - 1098/4148

beams, as well as any SFG beam, exit the chamber through a different window. The two reflected beams are blocked by irises, but any beam passing between them (such as the SFG beam) is focused onto the photomultiplier tube, the output of which is amplified and then displayed on an oscilloscope.

2.4.3 Alignment procedures for experiments in vacuum

Irises are first placed on the table to define parallel beam paths to lens L1, so that the infrared and visible beams will focus to the same point. Although the pump beam can be aligned onto the various optical components using only an IR-sensitive card or viewer, the DFG output beam is too far into the infrared to be visible with either cards or viewers. However, if the OPA and the DFG stage have all been aligned properly, such that the seed and pump in each crystal are collinear, there should be an 800-nm component, as well as some light at the signal and idler wavelengths, travelling collinearly with the DFG output. The first step in aligning the DFG output is therefore to align the shorter-wavelength signal beam along the path the DFG output is meant to follow.

For a more careful alignment, mirror M2 is inserted, along with the diagnostic setup #1 shown in Fig. 2.14. The pinhole is placed where the focus of the two beams is assumed to be, and the transmission of the 800-nm and 4.9-μm beams through the pinhole, as measured on the InSb detector, is maximized. When mirror M2 is removed, the two beams will focus at the same point somewhere inside the chamber. The focus cannot be imaged on the Pt crystal itself, since the Pt is too well-polished for any scatter of the beams to be seen. Instead, we position the sample holder so that the tantalum support just next to the Pt sample is at the focal point. The sample mount can then be moved in the direction transverse to the beams' propagation so that the Pt surface is at the focal point.

SIONYX1403000046.0056

SAMSUNG EX. 1002 - 1099/4148

2.4.4 Overlapping the infrared and visible pulses in time

It is critical that the two input pulses for SFG arrive simultaneously, and because the surface signal from the CO monolayer in vacuum was expected to be very small, we did not anticipate being able to adjust the timing by looking for this signal to appear. We developed an alternate technique that allowed us to set the timing correctly outside the chamber.

In the first step, the signal beam, which is at $\lambda_{SFG} = 1.4\mu$m and is copropagating with the DFG beam, is aligned to overlap spatially with the 800-nm pump, as described above in section 2.4.3. Leaving mirror M2 in place, diagnostic setup #2, as shown in Fig. 2.14 is added. The LIO crystal, mounted on a rotation stage, is carefully positioned at the focus of the two beams, and a plain white card is held behind it. A window of CaF_2, W, with the same thickness as the vacuum window is placed in the beam paths to mimic the effect of the window. By iterating slight changes in the position of the translation stage TS and the orientation of the crystal, we are able to produce sum-frequency generation inside the LIO. The SFG beam due to the signal and the 800-nm pump is at approximately $\lambda_{SFG} = 510$ nm and thus is easily seen by eye. When SFG is produced, the timing is quite close. The DFG output is then aligned such that its focus overlaps the 800-nm beam's focus, as described in section 2.4.3, and SFG between the 4.9-μm IR beam and the 800-nm pump is observed in the LIO bulk. We adjust the position of the translation stage to maximize the SFG signal at approximately $\lambda_{SFG} = 688$ nm.

In order to further improve the overlap of the two pulses in time and space, such that the probability of detecting a surface signal is maximized, we then use diagnostic setup 3. In this configuration, the LIO crystal is replaced with a small piece of GaAs, positioned so that the focus of the two beams is on the polished front surface of the GaAs. We then use two irises to block the reflected 800-nm and 4.9-μm light, and

SIONYX1403000046.0057

SAMSUNG EX. 1002 - 1100/4148

detect the SFG coming off the surface. Very small adjustments in the pointing of the beams and the timing are made in order to maximize the SFG signal. Because there is no contribution to the SFG from the GaAs bulk, the signal comes entirely from the surface. This gives us a way to maximize the overlap of the two beams in both the transverse and longitudinal directions, such that the overlap at the surface is highest. We can then remove mirror M2 and allow the overlapping beams to hit the Pt (111) surface in vacuum.

As discussed above in section 2.4.1, SFG is not possible in centrosymmetric materials such as Pt. Thus, we do not see a signal from the Pt bulk. With sufficiently high input powers, however, we can see an SFG signal from the Pt (111) surface. We are limited in the power of our input beams by two factors. First, we must keep the fluence low enough that we do not damage the Pt crystal itself (approximately 1 mJ/mm^2). Second, and most importantly, we must keep the fluence below the desorption threshold. For experiments involving CO adsorbed on Pt (111) the desorption threshold is 10 $\mu J/mm^2$. For alignment purposes, we illuminate the crystal with the maximum output infrared power obtainable with the signal from the OPA, as well as all the residual 800-nm radiation we have available. The fluence in this case is below the damage threshold for Pt, but above the CO-desorption threshold. We can then use the observed SFG off of the clean Pt in vacuum to help us to more carefully position the beams, as well as the sample, to maximize the detected SFG signal. In addition to now replacing the signal beam with the 4.9 μm infrared beam, the power in the 800-nm beam must then be attenuated before attempting to see SFG off of the CO-covered surface.

2.4.5 Preparation of the CO/Pt(111) surface

Prior to CO adsorption, the Pt (111) surface must be carefully cleaned. The surface is cleaned following a routine procedure consisting of: (1) annealing in 5×10^{-8} torr

SIONYX1403000046.0058

SAMSUNG EX. 1002 - 1101/4148

of O_2 for 5 minutes at 1000K , (2) sputtering with neon ions for 10 minutes at 600K, (3) annealing in vacuum for 5 minutes at 1100K, (4) annealing in 5×10^{-8} torr of O_2 for 10 minutes at 500K, and (5) annealing in vacuum for 6 seconds at 1100K.[4]

The clean sample is dosed with CO through a 12-mm diameter tube, less than 5 mm from the Pt sample face. We dosed to saturation coverage, as verified with a temperature programmed desorption.

2.4.6 Results of experimental trials

Despite our ability to observe IR-VIS SFG between 800-nm and 1.3-μm light on clean Pt (111) in the vacuum chamber, we were never able to detect enough signal from the mid-IR beam and the CO-covered Pt surface to make this experiment viable. Our main limitation was that the incident powers necessary to produce an observable signal were sufficient to desorb the CO from the surface.

We compared the output SFG signal we obtained on the clean Pt surface from the signal and pump beams with the signal we would expect to produce with the 4.9-μm mid-IR beam and the attenuated pump beam. With the highest SFG signal we could generate between 1.3-μm and 800-nm light, we began adding neutral-density filters to the paths of both the visible and infrared beams. Taking into consideration that we expected a resonant enhancement of at least a factor of 10–100 in the SFG output for the portion of the infrared beam within the band of the CO-stretch, we demonstrated that decreasing our input powers to the levels that would be necessary for doing this experiment led to an output SFG that was below what we could detect.

[4]Annealing in oxygen is necessary for the removal of contaminants such as silicon and carbon. Sputtering is used to dislodge these oxidized contaminants, as well as other impurities present at the surface. Annealing in vacuum can eliminate some of the structural defects caused by the sputtering. This procedure has previously been found to produce a clean surface, as judged with temperature programmed desorption of oxygen [33].

SIONYX1403000046.0059

SAMSUNG EX. 1002 - 1102/4148

2.4.7 Future work

This experiment was limited by the total infrared output we were able to obtain from the OPA/DFG stage. It is important to note that the intensity of the SFG output light that would be created by the CO layer is dependent on the product of the intensity of the infrared beam and the intensity of the visible beam. In our case, the visible beam is at least 3 orders of magnitude more intense than the infrared beam. The damage of the surface or the desorption of CO, however, depends on the sum of the two intensities, which in this case is approximately equal to the intensity of the visible component. Thus, if we limit the fluence of the visible beam to a level just below the desorption threshold, we could, in principle, increase the SFG signal by increasing the infrared fluence.

Possible avenues for increasing the infrared light output by the DFG setup include implementing some of the recommendations in reference [25]. It is also possible that an improvement in the detection scheme would be beneficial. A cooled detector or perhaps lock-in detection might be helpful in the effort to reduce the noise to below the detected SFG output level.

We have also considered using a molecule other than CO for the first, proof-of-principle experiment. If a molecule could be found with a larger $\chi^{(2)}$ and with a resonance within the range of the tuning of our infrared source, a larger output signal might also be generated. It may then be possible to observe the time-resolved dynamics of a reaction between adsorbates using IR-VIS SFG.

SIONYX1403000046.0060

SAMSUNG EX. 1002 - 1103/4148

Chapter 3

Formation of silicon microstructures

3.1 Introduction

We observe that irradation of silicon by subpicosecond-duration laser pulses in the presence of halogen-containing ambient gases leads to the formation of micron-scale conical structures on the surface of the silicon (see Fig. 3.1) [34, 35, 36, 37]. The microstructures develop upon irradiation with hundreds of pulses and form without the use of masks. We have also created silicon microstructures in the presence of 100-fs laser pulses and non-halogen-containing gases, such as N_2 or air, but these structures tend to be less conical and more blunt and irregular in shape. Similar structures have also been created by others using longer-duration pulses and a variety of background gases [38, 39, 40, 41, 42, 43].

In this chapter I describe the apparatus used and procedure followed to form microstructures on the surface of silicon using 100-fs laser pulses. The experimental information contained here also pertains to the microstructured samples described

SIONYX1403000046.0061

SAMSUNG EX. 1002 - 1104/4148

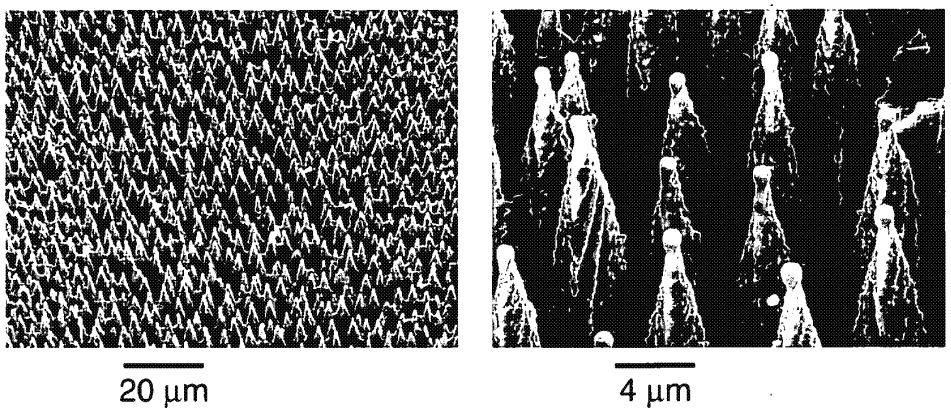


Figure 3.1: Conical silicon microstructures made by irradiating a silicon surface with a train of 100-fs pulses in the presence of 500 torr of SF_6. Scanning electron micrographs at two different magnifications are shown.

in later chapters. I discuss the development of the microstructures over time during formation, and we present some possible explanations for the shapes of the structures. I also describe the variation in morphology of the microstructures with ambient gas species and laser fluence.

3.2 Background

Structures similar to those we fabricated can be formed using a variety of maskless processes. For example, rippled patterns and "sputter cones" are formed by ion bombardment of surfaces [44]. Structures with both one- and two-dimensional periodicity also form on surfaces under irradiation with nanosecond- or picosecond-duration laser pulses [45]. Understanding the formation of these other patterns may help in elucidating the mechanisms responsible for the creation of conical structures on silicon irradiated with femtosecond laser pulses in the presence of reactive background gases. Specifically, in this section we hope to use what is known about structures made using

SIONYX1403000046.0062

SAMSUNG EX. 1002 - 1105/4148

other techniques to help us answer the following questions: What is the origin of the typical periodicity of our structures? What is the effect of using an ultrashort laser pulse, as compared with a longer-duration pulse? What is the role of the ambient gas and the role of the plasma formed by the laser? Are the cones formed purely by material removal or are growth processes also involved? What is the origin of the rounded tip seen on some of the cones? What is the origin of the submicrometer-scale features along the walls of some cones? These questions will be addressed in section 3.9 as well.

3.2.1 Structures formed with ion-bombardment

Solid surfaces can develop a wide range of topological features upon bombardment with ions. Some of the most frequently observed features include etching pits, droplets, ripples, cones, pyramids, and whiskers. The theory describing the formation of these features is currently incomplete: no single model predicts the features that form under the full range of possible parameters such as surface species, crystal orientation, sputtering ion, and beam energy [44]. An exhaustive description of the theories developed to explain various surface modifications is thus beyond the scope of this thesis; however, a brief discussion of some of the most relevant work is offered.

Periodic ripple patterns

Ion bombardment has often been observed to cause a ripple-like pattern on solid surfaces. Typical periodicities of these features are 0.01–1 μm. Generally, this phenomenon is an undesirable side-effect of etching or planarization processes and much attention has been devoted to minimizing such surface ripples. It has been suggested, however, that the surface patterning that results from ion bombardment could have practical applications in making diffraction gratings [46] or in texturing optical devices, such as solar cells, or templates for heteroepitaxial growth [47].

SIONYX1403000046.0063

SAMSUNG EX. 1002 - 1106/4148

The standard theoretical treatment of sputter rippling has sought to explain the typical wavelengths of the observed ripples, as well as their dependence on sputtering parameters such as the flux of the ion beam and the angle of incidence of the beam with respect to the surface normal. Bradley and Harper [46] attribute the rippling to a combination of ion-induced surface roughening, which makes the surface unstable against sinusoidal perturbations, and surface self-diffusion. The rate of material removal by sputtering varies proportionately with the local curvature of the surface in such a way that troughs erode faster than crests[46, 48]; sputtering therefore tends to increase the amplitude of all periodic surface perturbations. Self-diffusion, which is temperature-dependent, then acts to counteract the roughening effect and determines the resulting wavelength of the surface structure. This model predicts that ripples form parallel to the ion beam's direction for grazing incidence and perpendicular for angles close to normal [46]. Later work modified this theory to help describe the evolution of surface structures for long sputtering times [47]. Limits to the ultimate sizes of the ripples are explained by a physical mechanism called "terrace pinch off" [47]. In this mechanism, thermal fluctuations at the horizontal boundaries near a ripple's crest can lead the boundaries to intersect and "pinch off," particularly near a curve in the ripple; the relaxation of the resulting islands limits the ripple's height.

Ripples have been found to form or not form depending sensitively on details of the given experiment. Ripples have been observed on a wide variety of materials, including amorphous insulators, such as SiO_2 [49]; metals, including Cu [50] and Ag [51]; and semiconductors, including Ge [52] and Si [53, 54, 55]. Noble gas ions are the most common species used for sputtering, and ripples have been made in silicon using Ar^+ [53, 47] and Xe^+. Other studies have shown, however, that beams of Ar^+ with different operating parameters do not create ripples [56], and Ne^+ and Ar^+ can also be used to smooth out rough or rippled surfaces [57]. Bombardment of silicon with oxygen ions has been shown to form surface ripples [55]; however, irradiation of

SIONYX1403000046.0064

SAMSUNG EX. 1002 - 1107/4148

silicon surfaces with silicon ions does not [58]. These experiments illustrate that fairly small changes in experimental parameters can have substantially different effects on the modifications to the surface. The reasons for some of these differences are not currently known.

Sputter cones

Cones have been formed on a wide variety of materials under many sputtering conditions.[1]

One of the most commonly observed cone-formation mechanisms is the etching of material around impurity islands: the formation of so-called seed cones. In this case, the surface on which the cones are to be formed is bombarded with ions in the presence of another material, the sputtering of which introduces impurities into the cone surface. For example, cones on the order of 1 μm in size are formed on silicon sputtered with 3 keV Ar^+ ions in the presence of a Ni [59] or Mo [60] wire, which acts as the seed source. The impurity atoms seed the cone formation if they have a higher melting point or a lower sputter yield than the surrounding surface [44]. As the impurity atoms accumulate, they can form clusters as the surrounding material sputters away. The resulting protrusion on the surface forms the initial top of the cone. A cone then results as the sputter yield depends on the angle of the ion beam with respect to the local normal. The cones point in the direction of the incoming ion beam and generally decrease in size as the seed material is etched away, provided there is not a continuous source of impurities.

Seeding is not necessary for the formation of cones; one group has found that the formation of cones on their silicon surfaces upon bombardment with 30 keV Ar^+ ions is independent of the presence of high-melting-point W seed atoms [61]. Even in these cases, the dependence of the sputter yield on the ion-impinging angle is

[1] For a summary of some of the diverse experimental results, see [44] and references therein.

SIONYX1403000046.0065

SAMSUNG EX. 1002 - 1108/4148

typically thought to be a major contributor to the formation of the sloped sides of the cones [62]. Cone formation is often affected by the sample temperature, implying that the mobility of surface atoms is important, and that growth, as well as etching, is taking place [44]. Cones are typically surrounded by shallow trenches or grooves, due to enhanced sputtering by the ions reflected off the walls of the cones or by atoms sputtered off of the sides of the cones [62].

Other microstructures

Pyramids, somewhat similar to cones, form on some surfaces upon ion bombardment. Their distinguishing features are that they do not protrude above the initial surface of the substrate, their sides are specific crystal facets, and they are not generally thought to be the result of any seed process or growth mechanism [44].

Formations described as "whiskers" also grow upon ion bombardment, but they do not appear to align themselves either with particular crystal planes, as is the case with pyramids, or with the direction of the incident beam, as is the case with cones [62]. The whiskers have been described as forming the basis for cone growth, however [62], but this may occur only in isolated cases, where these cones serve the same function as the clusters of seed impurities described above [44].

3.2.2 Vapor-liquid-solid growth of silicon whiskers

The vapor-liquid-solid (VLS) method is frequently used for the growth of whisker-like structures, particularly in SiC [63]. The VLS technique was first discovered in 1964 by Wagner and Ellis [64], and is the topic of a review by Wagner [65].

The basic process for VLS whisker growth is as follows [63]. The substrate is covered with a layer of catalyst particles, which are then melted to form catalyst droplets. A gas containing the species from which the whiskers will be composed is passed over the catalyst droplets, which extract the whisker species. The droplet of catalyst can

SIONYX1403000046.0066

SAMSUNG EX. 1002 - 1109/4148

become supersaturated with the whisker species, such that they precipitate out of the catalyst droplet to form a long, thin, crystalline "whisker" on the substrate, capped with the spherical catalyst droplet. This technique can be used for both compound and elemental whiskers, and the catalyst must be chosen depending on the species.

The mechanism of whisker growth by VLS is believed to be [66]: (1) Vapor-phase whisker material is transported to the vapor-liquid interface at the surface of the droplet of molten alloy catalyst; generally the gaseous species flows over the catalyst at high pressure. (2) Chemical reaction between the whisker species and the catalyst material occurs at the interface; the molten droplet of catalyst provides sites that are preferred for deposition, relative to sites on a solid; the reaction occurs more readily on the surface of the liquid than in the vapor phase. (3) The whisker species dissolves into the liquid alloy droplet. (4) Precipitation of the whisker species at the liquid-solid interface is facilitated by the catalyst droplet; the alloy reduces the activation energy and the surface of the droplet provides a preferred path for surface diffusion.

The morphology of whiskers depends very sensitively on experimental parameters [65]. Typical size scales for whiskers formed using VLS are on the order of $1 - 100\mu$m in diameter, and up to 10 mm in length, depending on the chemical composition of the whisker. With the proper choice of catalyst, whiskers can be grown along a preferential direction. Gold is a commonly used catalyst, for example, to grow oriented silicon whiskers along the $\langle 111 \rangle$ direction.

3.2.3 Laser interactions with solids

In the interaction of a laser beam with a solid, damage or modification of the solid surface or bulk may occur in two ways: as a result of the deposition of large amounts of energy, in the form of heat, or as a result of the plasma that can form in an intense laser field. This damage is often an unintentional result, as in many of the earliest observations of these effects, when ruby lasers were seen to damage some of the optical

SIONYX1403000046.0067

SAMSUNG EX. 1002 - 1110/4148

elements with which they were used. There have also been many advances, however, in the deliberate use of such damaging processes for laser cutting, welding, etching, or other machining uses. The processing of solid materials with lasers has developed into a vibrant field, and a number of excellent texts exist [67, 68, 69, 70].

Melting and ablation

Two of the most commonly observed damage mechanisms for solid surfaces are melting and ablation. The nature of the surface damage and its extent depend sensitively on the material (for example, its transparence or opacity, and its thermodynamic properties) and on the parameters of the laser radiation, such as the pulse duration and the wavelength. Here I consider the specific case of the melting and/or ablation of a solid silicon surface with ultrashort laser pulses with duration of approximately 100 fs. This case has been recently explored, both theoretically and experimentally, by Cavalleri *et al.* [71] and references therein. A more detailed discussion of laser-induced ablation and melting in the regimes relevant to our experiment is also given in Wu [37] and references therein.

Cavalleri *et al.* describe four distinct fluence intervals, in which different physical effects dominate [71]: (1) Below 1.5 kJ/m^2, the sample does not melt; photoexcited carriers relax via carrier-carrier and carrier-phonon scattering. Most of the absorbed energy is transferred to the lattice in the form of heating, on the timescale of picoseconds. (2) For fluences greater than 1.5 kJ/m^2, the lattice reaches temperatures exceeding the melting temperature of silicon, 1685 K, and a molten liquid layer develops. (3) Higher fluences can induce ultrafast, non-thermal melting, wherein the lattice melts on a timescale (approximately 1 ps) shorter than the equilibration time. (4) Above 300 kJ/m^2, the ablation threshold, substantial material removal occurs from the surface and ablation damage becomes observable.

SIONYX1403000046.0068

SAMSUNG EX. 1002 - 1111/4148

Laser-assisted chemical etching

It has been shown that many chemical reactions between etchants, both in gaseous and solution form, and solid surfaces can be initiated or enhanced by laser irradiation.[2] A wide variety of surface species have been etched with laser-induced chemical etching, including semiconductors, metals, insulators, magnetic and ceramic materials, and organic polymers [72]. The discussion here is restricted to the processing of silicon. In the cases of laser-induced etching of silicon surfaces by gaseous reactants, the most studied etchants are halogen-containing compounds, including Cl_2, SF_6, and XeF_2 [72].

There are a number of possible ways that laser-assisted chemical etching can take place. Consider the example of SF_6-etching of silicon surfaces. At room temperature, SF_6 and silicon do not react; however, heating to approximately 1000°C initiates a thermal reaction [75]. Thus, laser heating alone could, in principle, drive the process. A plasma of SF_6 also readily etches silicon; in fact, plasmas of halogen-containing compounds, including SF_6, Cl_2, Cl_2/C_2F_6, and ClF_3, are some of the most commonly used dry etches for silicon [76]. When intense femtosecond laser pulses are used, the components of the resulting plasma, especially the halogen ions and radicals, etch the silicon. The expected products are the same as the volatile products formed in conventional reactive ion etching: SiF_4 is the prevalent product for etching silicon with fluorine ions [76].

One also expects that excitation of the gas molecules or the substrate by the laser can increase their reactivity. In studies of silicon irradiated with 50 ns infrared (λ = 9–11 μm) pulses from a CO_2 laser in the presence of SF_6, the vibrationally excited SF_6^* molecules are very reactive with solid silicon [77, 78]. The dominant products of this reaction are SiF_4 and SF_4. Etching results because of the volatility of the SiF_4 product. Furthermore, the reaction of excited SF_6^* with silicon is enhanced if

[2] See reviews by Chuang [72, 73] and Ehrlich *et. al.* [74], and references therein.

SIONYX1403000046.0069

SAMSUNG EX. 1002 - 1112/4148

the silicon is irradiated with laser light, in addition to just the radiation required for vibrational excitation of the gas molecules. This suggests that direct excitation of the substrate, perhaps followed by thermal activation, enhances the reaction [72]. Following etching with SF_6^* molecules, the silicon surface is covered with a fluorinated layer, similar to SF_2, suggesting a possible intermediate [78]. The proposed reactions proceed as follows [78]:

$$SiF_2(ads) + SiF_2(ads) \xrightarrow{h\nu} Si + SiF_4(ads) \tag{3.1}$$

$$SiF_4(ads) \longrightarrow SiF_4(g) \uparrow \tag{3.2}$$

The SiF_2 can be formed in a number of ways, as discussed above, including through the vibrationally excited SF_6^* chemisorbed on the silicon surface [78]:

$$SF_6^*(g) + Si(s) \longrightarrow SF_6^* - Si(ads) \tag{3.3}$$

$$SF_6^* - Si(ads) \longrightarrow SiF_2(ads) + SF_4(g) \uparrow \tag{3.4}$$

It is also likely that the vibrationally excited SF_6^* reacts directly with the fluorinated adsorbate [78]:

$$SF_6^*(g) + SiF_2(ads) \longrightarrow SiF_4(ads) + SF_4(g) \uparrow \tag{3.5}$$

In the reaction of silicon with Cl_2, 10 ns excimer laser pulses (λ = 308 nm and 248 nm) induce etching, yielding Si, SiCl, $SiCl_2$, and $SiCl_3$ as the dominant reaction products [79]. The proposed mechanism involves Cl_2 dissociatively adsorbed on the silicon surface. The resulting SiCl layer then absorbs the radiation and thermal desorption results. Because these experiments were done at a low pressure (10^{-6} – 10^{-4} torr), dissociation of gaseous Cl_2 was neglected; dissociated Cl contributes to the etching at higher background pressures, however [80]. It was found that the roughness of the surface has a significant impact on the etching rate, thus all experiments were performed on a roughened surface to maximize the reaction rate.

SIONYX1403000046.0070

SAMSUNG EX. 1002 - 1113/4148

Generation of particulates

The formation of particulates with sizes on the order of 10 nm to 1 μm is a common occurence during laser ablation and is generally considered a nuisance in the attempts to create thin films with pulsed laser deposition (see the review by Chen [81], and references therein). Particulates have been produced by Lubben *et. al.* upon the irradiation of silicon and germanium targets with 15 ns excimer laser pulses [82]. According to the authors, particulate formation is a result of superheating of the subsurface region before the vaporization temperature is reached at the surface. The particles, approximately 1 μm in size, are collected on a substrate oriented opposite the target, along with ions and neutrals that are evaporated off the target during the laser irradiation. In these experiments, most of the material transferred from the target to the substrate is in the form of ions or neutral atoms, rather than as particulates; furthermore, the velocity of the particulates in the chamber is much smaller than that of the emitted ions and atoms. The number of particulates accumulating on the substrate is also substantially decreased (factor of 5) when the substrate is biased with a negative voltage: evidently, the particles accumulate a negative charge as a result of their transit through the plasma near the target surface [82].

3.2.4 Laser-induced periodic structures

Laser-induced pattern formation on the surface of a solid was first seen when ruby laser irradiation caused a ripple or groove structure to develop on Ge [83]. In this process, the structures formed on the surfaces show a characteristic period that is smaller than the spot size of the laser and larger than the wavelength of the radiation used; the pattern forms spontaneously without the use of masks. The rippling phenomenon was later seen on a variety of materials, including metals, semiconductors, and dielectrics, under a wide range of laser irradiation conditions. These

SIONYX1403000046.0071

SAMSUNG EX. 1002 - 1114/4148

laser-induced periodic surface structures are the subject of a theoretical treatment by Young, *et. al.* [84].

The formation of cones under laser irradation was seen on the surface of Al_2O_3 [85]. These first conical structures were attributed, like the early ripple patterns, to diffraction effects in the laser beam. Later, cones were shown to form in a wide variety of materials [45]. Foltyn, in [45], notes that in the majority of the cases, the cones "are formed as surrounding material is removed by successive laser pulses, and as a result of this erosional formation process, they grow in length as laser exposure increases, and they point in the direction of incoming laser radiation." Furthermore, it is seen that, for laser spots with Gaussian intensity profiles, the laser-induced cones often form in the central portion of the spot, and ripples form around the periphery, indicating that the morphology of the surface modification is dependent on, among other factors, the laser intensity.

Conical structures have been formed on silicon and germanium after irradiation in vacuum with 100–400-fs pulses at a wavelength of 248 nm [86]. The cones grow in height and their separation becomes larger with successive pulses. One interesting effect noticed in this experiment is that the structures formed are substantially "improved" when the sample is electrically grounded during irradiation: the area of damage outside the irradiated region is decreased by about half relative to that when the sample is electrically isolated. The authors also note that they believe that reflective focusing of the laser light off of the sides of the cones leads to an increase in intensity by an order of magnitude at the base of the structures, relative to their peaks, assuming that the radius of the cones increases threefold from the peak to the base. They assert that this increase in intensity, for their operating parameters, leads to non-thermal ejection of material from the cavities between cones [86].

SIONYX1403000046.0072

SAMSUNG EX. 1002 - 1115/4148

3.3 Apparatus

Figure 3.2 shows the apparatus that we used for texturing the surface of silicon samples.

The vacuum system in which the silicon is microstructured is constructed primarily of 2 3/4" Conflat hardware. An Edwards two-stage roughing pump, filled with Fomblin oil, is used to pump the chamber to a pressure of approximately 10^{-4} torr. Two gauges can be used to measure the pressure: the diaphragm gauge for high pressures (1 torr and above), and the convectron gauge for lower pressures (10 torr – 10^{-4} torr). Any of a variety of different background gases can be admitted into the chamber via a gas-handling system made of stainless steel tubing. The silicon sample, typically 10 mm × 10 mm, is mounted using conductive carbon tape to a stainless steel rod, which is supported in vacuum by a flange mounted to a Huntington stage with two orthogonal directions of translation. The stage is driven by two motorized, computer-controlled actuators. The sample is positioned approximately 10 mm from a quartz window with a diameter of approximately 70 mm.

The laser used is a regeneratively amplified Ti:sapphire laser, with a wavelength of 800 nm, a typical pulse duration of 100 fs, and a repetition rate of 1 kHz. The optical apparatus consists of mirrors to direct the laser beam into the chamber and a focusing lens. A white-light fiber lamp illuminates the surface of the silicon sample during laser irradiation. The white light reflected off the silicon is collected by a CCD camera, so that an image of the silicon surface and any patterned regions can be displayed on a monitor.

SIONYX1403000046.0073

SAMSUNG EX. 1002 - 1116/4148

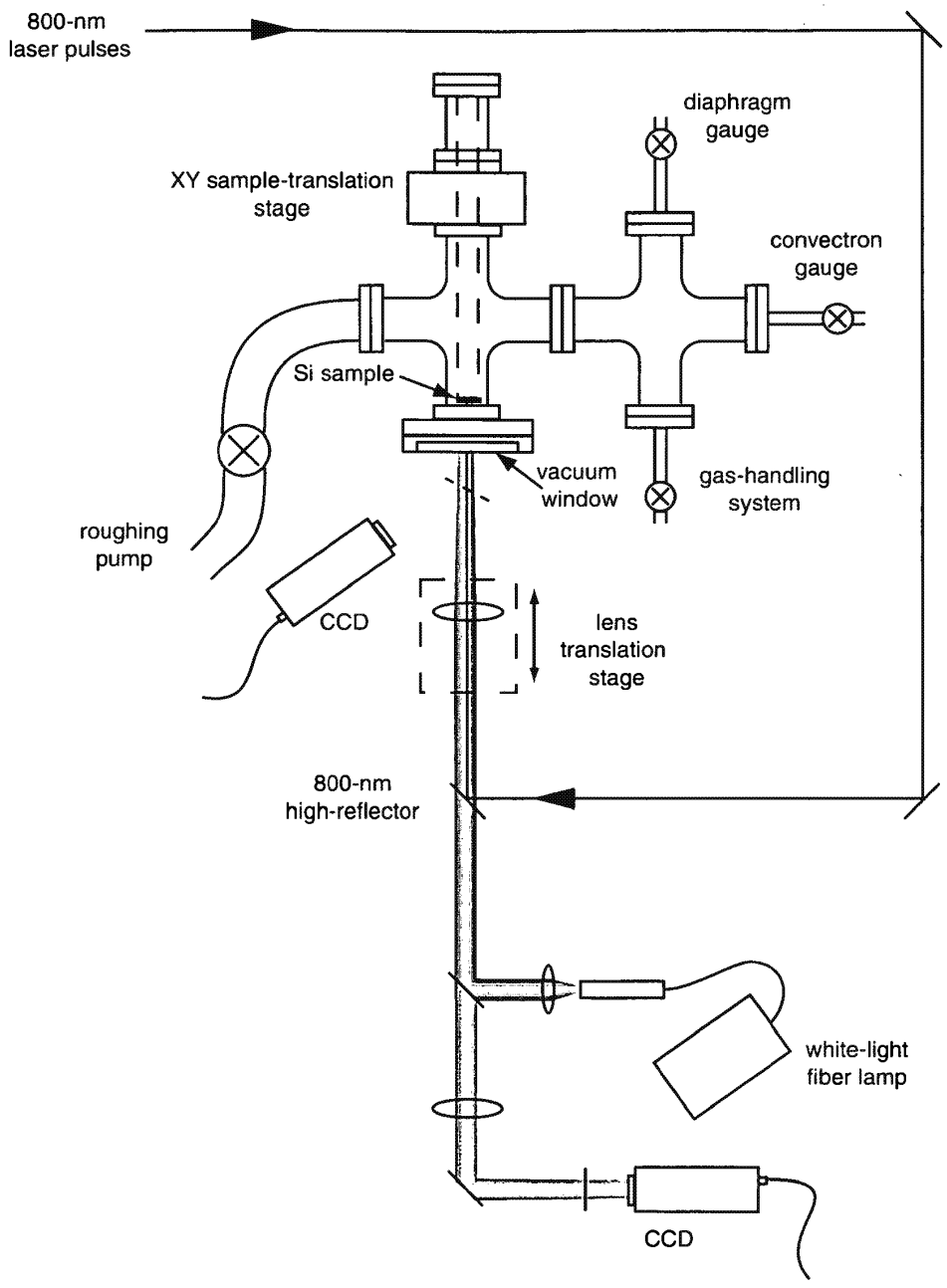


Figure 3.2: Apparatus for creating microstructures on the surface of silicon using 100-fs laser pulses in the presence of a background gas. The optical setup includes components for directing and focusing the beam onto the silicon sample as well as an imaging apparatus.

SIONYX1403000046.0074

SAMSUNG EX. 1002 - 1117/4148

3.4 Procedure for making microstructured silicon

The silicon samples that are used in our microstructuring studies are typically cut from 3- or 4-inch wafers[3] into 10 mm × 10 mm squares. They are soaked in a bath of trichloroethylene for 15 minutes, then cleaned in an ultrasonic cleaner, first for 10 minutes in acetone and then for 10 minutes in methanol. They are rinsed with methanol and dried with air if they are to be used immediately. Otherwise, the cleaned samples are stored in a covered beaker of methanol for future use.

To pattern a sample, a square piece of silicon is mounted into the chamber after the chamber's window is cleaned by wiping it with a lint-free cloth and acetone or, when necessary, by scrubbing it with a cloth and a suspension of alumina in water. Care must be taken to mount the sample such that its edges are parallel to the direction of the translation of the vacuum xy-translation stage; this insures that the entire sample can be accessed using the translation stage. The chamber is evacuated to a base pressure of about 10^{-4} torr, and the desired background gas is admitted. Typically a gas pressure of 500 torr is used, although lower pressures were occasionally used in studies of the effects of different partial pressures on the morphology of the resulting microstructures (see section 3.7.2).

The laser is aligned so that it is incident normal to the silicon sample. The laser spot size is measured using the following steps. A mirror is inserted via a flipper mount between the focusing mirror and the window on the vacuum chamber. A CCD camera is placed such that the path from the focusing lens to the CCD is equal in length to the path from the focusing lens to the sample (see Fig. 3.2). The size of the laser spot on the CCD is measured and the position of the focusing lens is adjusted to give the desired spot size. The spot size at the sample is then equal to the size measured on the CCD. For most experiments, a laser spot diameter of approximately

[3]Data shown here are for n-Si (111), 260 μm thick, with resistivity ρ = 8–12 Ωm. Microstructures also form on silicon surfaces in other orientations or with different dopant levels.

SIONYX1403000046.0075

SAMSUNG EX. 1002 - 1118/4148

150 μm is used.

The laser power is measured directly in front of the chamber window. Typical powers are 300 mW, although the power can be varied, along with the beam size and pulse duration, to change the characteristics of the microstructures formed. The typical fluence is therefore 10 kJ/m^2.

The laser beam is allowed to pass into the chamber and the dark spot left on the sample as a result of the laser-assisted texturing is visible on the imaging monitor. Exposures can either be spot exposures, where the sample is not translated during irradiation and a given spot is exposed to a specific number of laser pulses (generally 500 or fewer), or they can be large area exposures, where the vacuum translation stage is used to raster the sample across the laser beam such that the sample can be irradiated in closely-spaced rows, achieving a rectangular patterned area of up to 10 mm $\times$ 10 mm. The translation speed for the stage is typically 100–300 μm/sec, with a row spacing of 50–75 μm, depending on the size of the desired structrures. For samples that will be used in optical studies, the patterned area is generally 10 mm $\times$ 10 mm, and for field-emission studies, the patterned area is generally 2 mm $\times$ 2 mm, or 3 mm $\times$ 3 mm.

Following the laser-induced microstructuring, we typically do not perform additional processing steps on our samples. We consider this a positive aspect of our technique: the process consists of very few steps.

3.5 Evolution of microstructures during laser irradiation

Figure 3.3 shows scanning electron micrographs (SEM) of 4 different spots irradiated with varying numbers of pulses in a background of 500 torr of SF_6. After each spot has been exposed to just a few pulses, small pits are visible on the surface, accompanied

SIONYX1403000046.0076

SAMSUNG EX. 1002 - 1119/4148

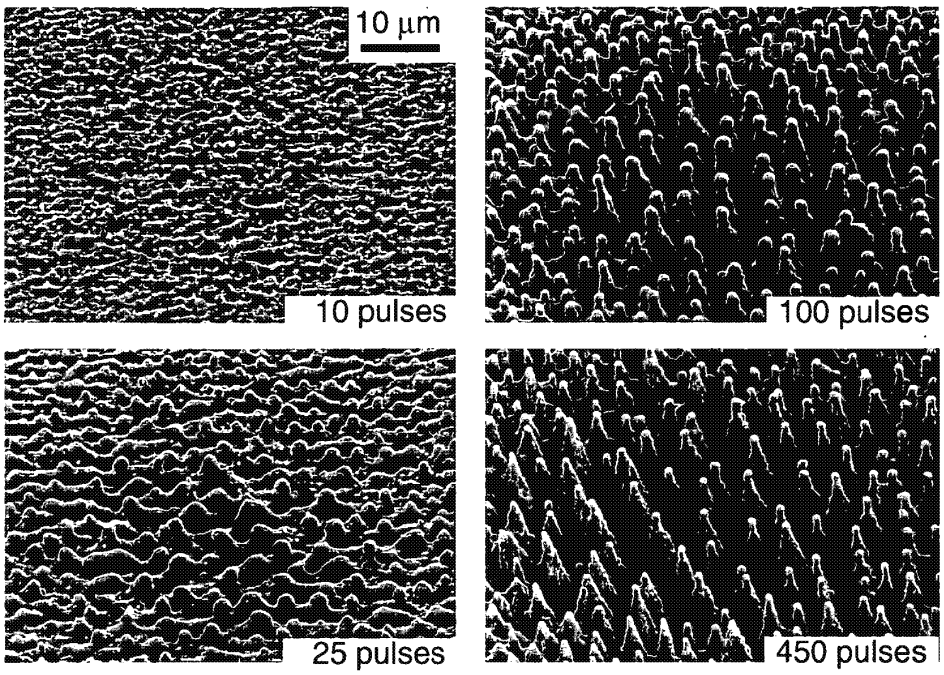


Figure 3.3: SEM images of microstructures formed in a background of 500 torr of SF_6 upon irradiation with the given number of pulses.

by bits of debris. After roughly ten pulses, a ripple-like pattern develops, with a characteristic separation of a few micrometers. As the number of pulses increases, the one-dimensional pattern changes to a two-dimensional pattern of small bumps with rounded tips. Beyond approximately 100 pulses, these microstructures increase in height as the surrounding material is etched away. At 450 pulses, as shown in Fig. 3.3, the structures are separated by several micrometers and are typically more than 10 μm high.

We see that the laser-induced cones grow in height when they are exposed to increasing number of pulses, as surrounding material is removed, in agreement with Foltyn's reports [45]. Cleavage of the silicon sample on which the structures are formed, and viewing from the side shows that the tips of the structures are all be-

SIONYX1403000046.0077

SAMSUNG EX. 1002 - 1120/4148

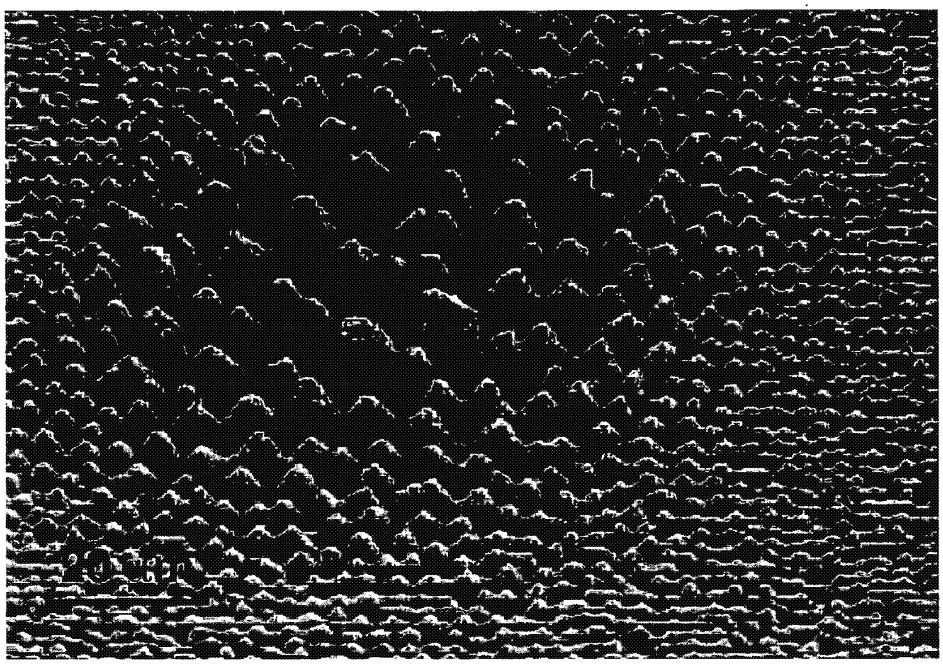


Figure 3.4: Scanning electron micrograph of silicon microstructures made in air by irradiating silicon with 500 pulses, with 245 mJ per pulse, without translating the laser beam. Note the ripple-like structure around the periphery of the patterned area.

low the original height of the flat surface. This suggests that etching, rather than deposition, is the primary means of cone formation.

We also observe that the cones point in the direction of the incoming laser. When microstructures are formed with the laser aligned at various angles to the normal of the surface, the cone orientation is determined solely by the wavevector of the laser and not by the crystal orientation of the silicon wafer or by the surface orientation.

Additionally, we see, as in other cases [45], that exposures to beams with Gaussian profiles leads to the formation of roughly circular areas of tall conical structures, with smaller bumps surrounding the tall cones, and ripples reminiscent of laser induced periodic surface structures around the exterior (see Fig. 3.4).

The microstructures on samples made with large-area exposures, rather than

SIONYX1403000046.0078

SAMSUNG EX. 1002 - 1121/4148

single-spot exposures, typically have a similar overall conical shape to those formed after 450 shots and shown in Fig. 3.3. They do, however, generally show greater nanometer-scale roughness along the sides of the cones. The origin of this surface roughness is not known but may be due to debris accumulating on formed cones as a nearby region is irradiated. The structures made in large-area exposures (see, for example, Fig. 3.5a) also typically lack the spherical tip seen on the ends of cones made with spot-exposures, like those shown in Fig. 3.3, formed with 450 pulses in SF_6.

3.6 Properties of microstructures

We investigated the chemical and structural properties of microstructured silicon using a number of techniques[36]. Previous studies using secondary ion mass spectrometry (SIMS) have shown that microstructures made in SF_6 contain a high concentration of both sulfur (one part in 10^3) and fluorine (one part in 10^6). Both the sulfur and fluorine concentrations are highest just below the surface and decrease with depth into the sample. Annealing in vacuum for 3 hours at 1200 K decreases the sulfur and fluorine signals in SIMS by a factor of approximately 2. The structural properties of the textured surfaces were examined with electron backscattering and ion channeling: both methods indicate that the microstructures crystalline but most likely have a high density of defects. The crystalline structure is not changed after the sample is annealed in vacuum for 3 hours at 1200 K.

We also performed a temperature-programmed desorption (TPD) study of a 10 mm × 10 mm sample of microstructures formed in SF_6. The procedure for TPD studies with our apparatus is described in detail elsewhere [87, 33]. Briefly, the sample is clamped to a resistive heater within a vacuum chamber with a base pressure of 10^{-11}–10^{-10} torr. The sample is placed approximately 10 mm from the entrance aperture for a UTI

SIONYX1403000046.0079

SAMSUNG EX. 1002 - 1122/4148

quadrupole mass spectrometer, which measures the concentration of desorbed species with various masses as the temperature of the sample is increased.

Because of the high concentration of S observed in SIMS, we tuned the mass spectrometer to detect species with a mass of 32 atomic mass units (amu) during the TPD. We also tuned to detect Fl (19 amu), Si (28 amu), C (12 amu), and O (16 amu).[4] Species with a mass of 104 amu, corresponding to SiF_4, were also included in the TPD, as one possible volatile compound that could be created upon heating.

The TPD covered the temperature range 100–1100 K. The major components desorbed were masses 28 amu, 12 amu, and 16 amu, corresponding, most likely, to CO, C, and O. We expect the CO signal is probably due to CO that adsorbs on the sample during exposure to atmosphere or CO present in the vacuum chamber. We are not able to detect any sulfur that is clearly distinguishable from the effects of the CO signal saturating the detector. We do however, see a peak corresponding to the desorption of fluorine at approximately 500 K. Furthermore, there is a broad but very large 28-amu peak at $750 - 1000$ K, which is not accompanied by corresponding carbon or oxygen peaks. This may be silicon, or it could be N_2.

The TPD results are interesting because they provide information about the surface composition that was not available from SIMS alone. We are currently further pursuing these TPD studies. We would like to try again to detect S on the surface, as well as to understand the origin of the CO signal.

[4] Atomic oxygen was included because any mass 32 detected could be either atomic S or molecular O_2. Detecting atomic O should help distinguish the two. Carbon was included to help us distinguish the quantity of mass 28 that was due to Si from that due to CO.

SIONYX1403000046.0080

SAMSUNG EX. 1002 - 1123/4148

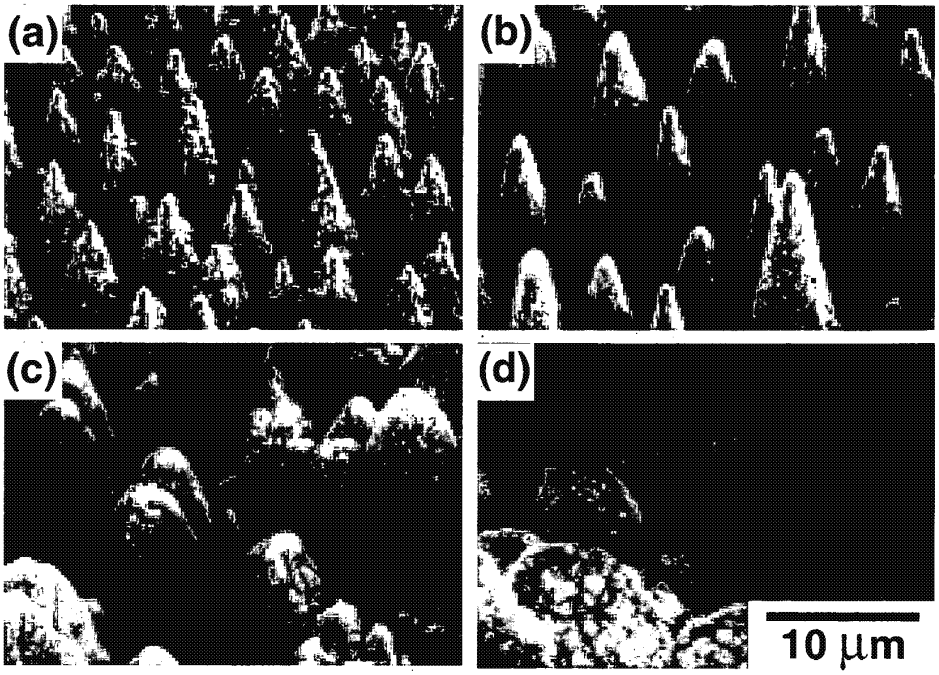


Figure 3.5: SEM images of microstructures formed in four different ambient gases: (a) SF_6, (b) Cl_2, (c) N_2, and (d) air.

3.7 Dependence of morphology on ambient gas species

The morphology of the laser-induced silicon microstructures depends on the gas in which they are formed. We investigated, specifically, the effects of two halogen-containing gases, SF_6 and Cl_2, as well as N_2 and air. Figure 3.5 shows SEM images of 4 samples of microstructures, each formed in a different ambient gas, at a pressure of 500 torr. The laser and translation parameters in each case were chosen to give microstructures with heights of approximately 10–15 μm.

SIONYX1403000046.0081

SAMSUNG EX. 1002 - 1124/4148

3.7.1 Shapes of microstructures

Use of SF_6 or Cl_2 leads to sharp-tipped conical structures with a radius of curvature of approximately 500 nm. The cones made in SF_6 have more surface roughness than those prepared in Cl_2. The dendritic formations on the SF_6-formed cone surface have a characteristic length scale of 100–200 nm.

Structures made in air or N_2 are much more rounded than those made in the halogen-containing gases; the radius of curvature of their tips is approximately 2–3 μm. Additionally, the structures made in air show substantial surface roughness compared to the N_2-prepared structures. This roughness appears less dendritic than the roughness on the SF_6-prepared cones.

We also examined the dependence of the shapes of the structures on the partial pressures of the background gases. With no reactive background gas present, the chamber pressure is roughly 10^{-4} torr during the laser irradiation. Under these conditions, rounded structures similar to the blunt structures formed in 500 torr of N_2 develop. As the pressure of a reactive background gas, such as Cl_2 or SF_6, is increased, the structures become sharper and more conical. For all pressures of Cl_2 up to 500 torr, the cones show very little surface roughness; for cones made in SF_6, however, increased pressure leads to an increase in the rounghness along the sides of the cones.

3.7.2 Microstructure number density

The number density of conical structures on the surface also depends on the ambient gas species, with higher densities achieved using halogen-containing gases. Surfaces prepared with SF_6 give the greatest number density, followed by Cl_2. The number densities produced with N_2 and air are approximately equal and are roughly a factor of two less than for the SF_6-prepared surfaces.

We investigated the variation of the number density of the microstructures with

SIONYX1403000046.0082

SAMSUNG EX. 1002 - 1125/4148

the partial pressure of the ambient gas. For both SF_6 and Cl_2, we measured the number density of the structures for surfaces patterned in either the halogen-containing gas alone or in a mixture of the halogen-containing gas and N_2. We made spot samples of microstructures in background pressures of 0–500 torr of the reactive halogen-containing gas. We then made similar spot samples while varying the partial pressure of the halogen-containing gas, but keeping the total pressure constant at 500 torr by adding N_2.[5]

Figure 3.6 shows the number of conical microstructures formed within a circle of diameter 100 μm for the various gas parameters. The number density is measured by examining a scanning electron micrograph of the spot sample. The number of structures within the 100-μm-diameter circle for each SEM micrograph is counted by hand. Each data point represents an average over four samples, with a typical range of 30–40 counts, made with the same gas parameters.

In the cases of both SF_6 and Cl_2, the number density of microstructures increases with the partial pressure of the reactive gas. A plateau is reached in each case; the maximum number density is reached at roughly 100 torr of Cl_2, or 400 torr of SF_6. For both gases, the exposures done with N_2 added to increase the total pressure to 500 torr yield slightly higher number densities, but this effect is small. We conclude from this that collisions of etching reactants or accumulating products with the background gas play a role in determining the microstructure shape. Collisions could act to confine reactive species close to the Si surface or could direct Si-rich products back onto the developing conical structures.

[5]Gases are admitted through valves in the gas-handling system. For spot exposures with a constant total pressure of 500 torr and different partial pressures of the halogen-containing gas, the chamber is evacuated between exposures. The desired partial pressure of the halogen-containing gas is admitted, followed by N_2 to bring the total pressure to 500 torr.

SIONYX1403000046.0083

SAMSUNG EX. 1002 - 1126/4148

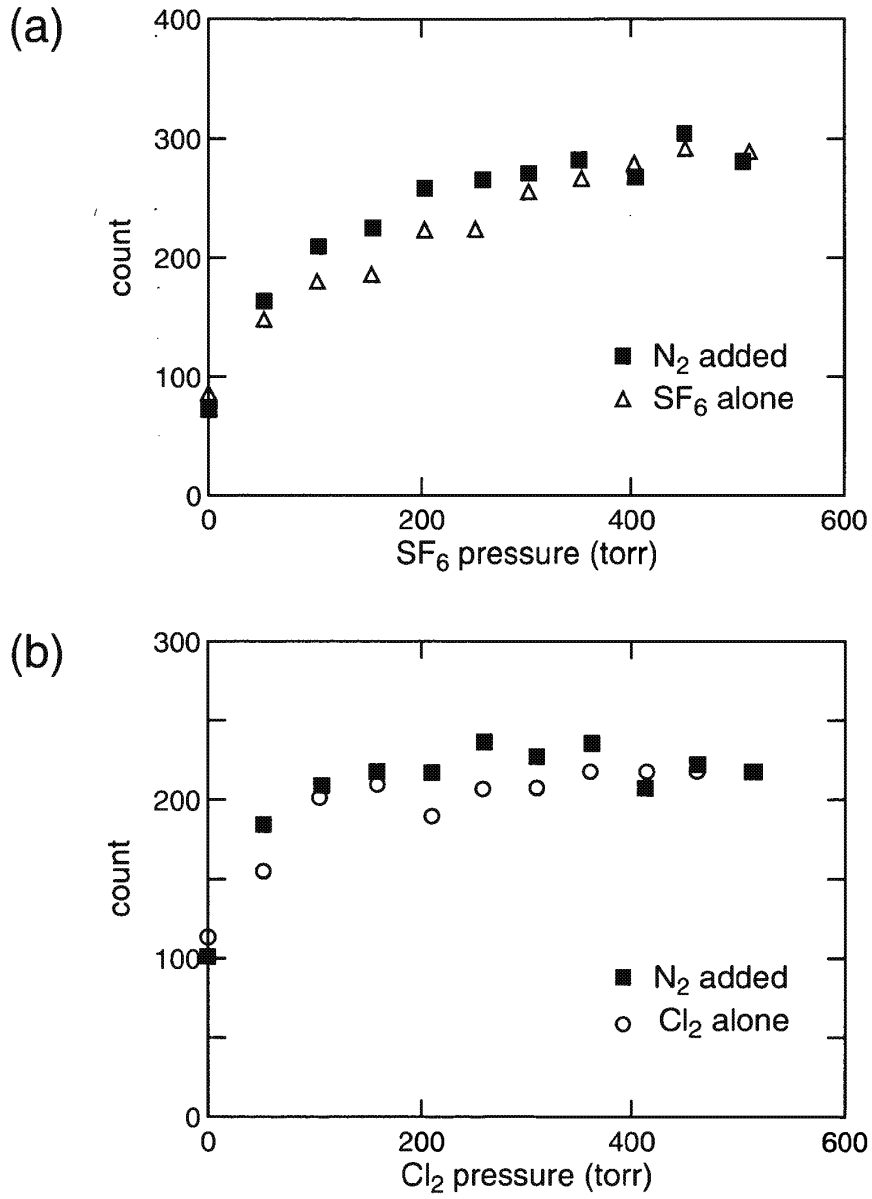


Figure 3.6: Dependence of number of conical structures formed in a circular area with diameter 100 μm on partial pressure of reactive gases (a) SF_6 and (b) Cl_2. The hollow markers refer to processing in the halogen-containing gas alone; the filled markers refer to samples processed in the indicated partial pressure of the gas, but with added N_2, to give a total background pressure of 500 torr.[7]

SIONYX1403000046.0084

SAMSUNG EX. 1002 - 1127/4148

3.8 Microstructures formed with low fluence

Previous work has demonstrated the relationship between intensity and microstructure height for spots irradiated with a fixed number (500) of pulses [88]. In these experiments, samples were irradiated with laser pulses with Gaussian intensity profiles and high fluence (10 kJ/m^2). The size of the microstructures as a function of their distance from the center of the Gaussian profile reveals the dependence of microstructure size on laser intensity.

We further investigated the effects of intensity by creating samples of microstructures using low-energy pulses (approximately 1 kJ/m^2 or less at the center of the laser spot). We prepared a wide variety of samples in vacuum, N_2, and air, with a range of pulse energies and numbers of shots. Figure 3.7 shows SEM images of four samples made upon irradiation with low-energy pulses. The laser spot was approximately 150 μm in diameter; the repetition rate of the laser was 1 kHz. In order to induce structures on the silicon surface that are visible under SEM with the pulse energies used (25 or 40 μJ per pulse), it was necessary to use more than the 500 pulses normally used. Figure 3.7a shows the structures that result from an exposure to 2000 40-μJ pulses in vacuum. The surface has a distinctly rippled appearance; the period is roughly 1 μm. For lower pulse energies in vacuum, longer exposures are necessary in order to pattern an area comparable to that shown in the micrograph. Figure 3.7b shows a spot irradiated with 10^5 25-μJ pulses in vacuum. The rippling pattern seen with larger fluences is still present, but the period here is approximately 300 nm. Low-fluence exposures made in the presence of background gases show the creation of the dendritic nanoscale particles that are seen to accumulate on the sides of some of the microstructures made with higher fluence. A spot exposed to 2000 25-μJ pulses in the presence of 500 torr N_2 is shown in Fig. 3.7c. Ripples with a period of several hundred nm are formed, as well as clusters of nanoparticles, which show

SIONYX1403000046.0085

SAMSUNG EX. 1002 - 1128/4148

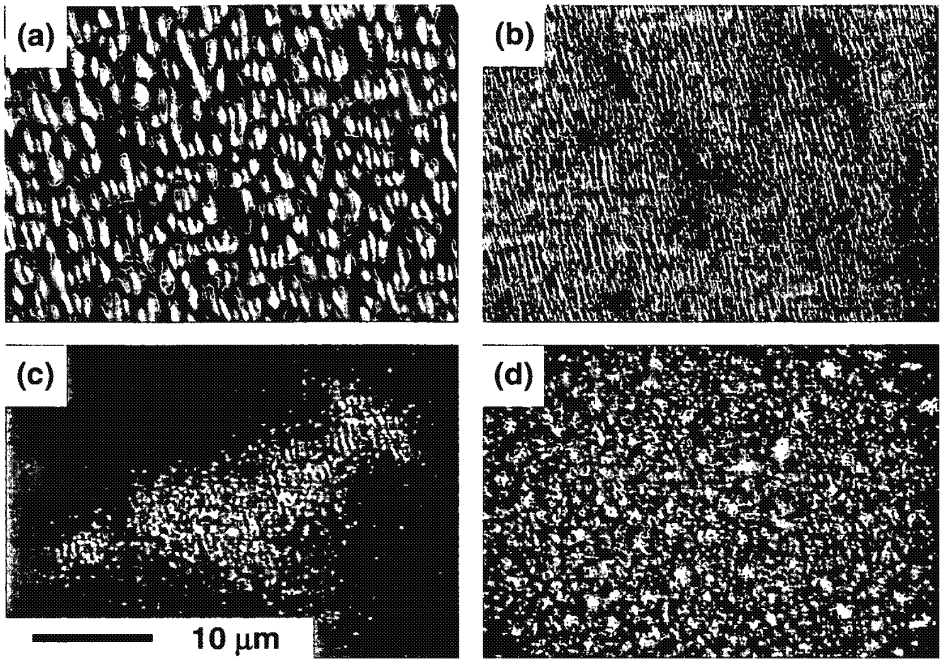


Figure 3.7: SEM images of 4 spot samples made with low-fluence exposures: (a) irradiated with 2000 pulses, 40 μJ per pulse, vacuum (10^{-3} torr); (b) 10^5 pulses, 25 μJ per pulse, vacuum; (c) 120 pulses, 25 μJ per pulse, 500 torr N_2; (d) 10^5 pulses, 25 μJ per pulse, 500 torr air. All four images were taken at normal electron-beam incidence.

up in the micrograph as bright features. In the presence of 500 torr of air, exposure to 10^5 25-μJ pulses leads to the formation of many more of these clusters, as shown in Fig. 3.7d. Rippling is faintly visible underneath the clusters of nanoparticles, but the clusters are clearly the dominant feature here.

3.9 Discussion

One of the most significant open questions related to the silicon microstructures induced with femtosecond laser pulses is the mechanism by which such features are

SIONYX1403000046.0086

SAMSUNG EX. 1002 - 1129/4148

formed. This mechanism should explain not just the formation of the cones, but the dependence of their shapes, sizes, and separation on such parameters as ambient gas, laser pulse duration and fluence, and other parameters. We can refer to the mechanisms already put forth for the formation of similar structures using other techniques (see section 3.2) for clues as to the possible processes taking place.

3.9.1 Formation mechanisms

In attempting to elucidate the mechanism for subpicosecond laser-induced microstructure formation, we can compare them to similarly shaped features formed by other groups using nanosecond pulse irradiation [38, 39, 40, 41, 42, 43, 89, 90]. Of work done regarding cone-formation mechanisms, this work most closely resembles ours in terms of the experimental parameters and the structures formed.

Experiments in other groups using nanosecond laser pulses and various background gases have lead to the creation of column-shaped structures, the tips of which protrude above the height of the original surface[8] [39, 41, 43]. This observation strongly suggests that some sort of redeposition process is present during the formation with nanosecond pulses; ablation and material removal alone could clearly not explain such protrusions. The authors of that work state that several competing processes take place simultaneously: ablation, chemical-assisted etching, melting, and redeposition. The redeposition mechanism is hypothesized to be essentially the same as that in VLS whisker growth (see section 3.2.2). In the work by Pedraza *et. al.* [39, 42, 41], Lowndes *et. al.* [40], Fowlkes *et. al.* [43], and Sanchez *et. al.* [89, 90], the comparison of the silicon microstructure formation mechanism to VLS growth is strengthened by

[8]The evidence for the protrusion of the silicon microstructures above the surface, in these cases, comes from profilometry scans over several mm. It is unclear whether the authors compensated for the tendency of uncalibrated profilometers to show curvature where none exists. Furthermore, profilometry data may also show the curvature of the wafer, particularly when scans are performed over large areas, as in this experiment. Extraction of quantitative conclusions from this profilometry data should perhaps be done with caution.

SIONYX1403000046.0087

SAMSUNG EX. 1002 - 1130/4148

the similarity in appearance of the laser-formed structures to the VLS whiskers: both kinds of structures are capped with an essentially spherical tip, and there is often a groove seen between the spherical tip and the rest of the column or cone.

The nearly spherical tips of cones made by repeatedly irradiating the same spot on the sample without translating the laser beam have been explained as the result of the resolidification of a molten droplet. Some authors have described similar spherical features, formed with ns pulses and observed without the underlying cone, as "emerging [liquid] material in isolated points," and have named them "mushrooms" [90]. These droplets appear on the tips of columns that protrude tens of microns above the original silicon surface and thus have been attributed to "hydrodynamical" growth, rather than to material removal [89]. The spherical tips are not just seen on silicon, but were first reported on gold irradiated in air with ns pulses and were described as droplets in the process of being emitted from the molten surface [91]. The presence of resolidified molten droplets at the tips of our silicon microstructures opens the possibility that a VLS growth mechanism, like that seen for nanosecond-duration pulses, is at work in our experiments with fs pulses as well.

Because the reactants and products present in our femtosecond-pulse experiments are most likely the same as those present during microstructure formation with nanosecond pulses and because the structures made in the two processes show many qualitative similarities, we believe a similar set of processes are probably present in the formation of our microstructures as are seen in the formation of structures using nanosecond-duration pulses. It seems clear, however, that the balance between these processes is different in the case of femtosecond-pulse irradiation than in the case of nanosecond-pulse irradiation. For example, the fact that the structures made with femtosecond pulses have not been seen to protrude above the surrounding silicon surface suggests that ablation or removal of silicon by chemical etching, in this case, is dominant over redeposition.

SIONYX1403000046.0088

SAMSUNG EX. 1002 - 1131/4148

Table 3.1: Boiling points of compounds produced in etching of Si.

Gas	SiH_4	SiF_4	Si_2H_6	$SiHCl_3$	$SiCl_4$	Si_2OCl_6	Si_2Cl_6
BP (° C)	-111.6	-95.7	-15	31.7	56.7	135.5	147

3.9.2 Effects of ambient gas

Etching properties of gases used

SF_6 and Cl_2 are routinely used, among other halogen-containing compounds, in a wide variety of dry etching processes for several reasons. First, compounds of silicon and chlorine or fluorine are among the most volatile silicon compounds; listed in Table 3.1 are some of the compounds created in the etching of silicon, along with their boiling points [76].

As discussed previously in section 3.9.2, the halogen-containing gases have been used in laser-assisted etching in previous work. In our experiments there is a very clear qualitative difference between microstructures formed in the halogen-containing gases and those made in air or N_2: only in the halogen-containing gases are sharp conical structures formed. We hypothesize that strong laser-assisted chemical etching is necessary for the creation of sharp cones, whereas the blunt and rounded structures formed in N_2 and air may be the result of ablation and melting processes alone.

Dendritic nanoscale features

The nanoscale roughness on the sides of the structures also depends on the ambient gas used. For samples that display roughness on the sides of the cones a heavy etching plume is visible during laser irradiation. The material that composes the plume coats not only the microstructures but also the unpatterned area of the silicon sample, the sample holder, and the vacuum window. We collected and analyzed some of the

SIONYX1403000046.0089

SAMSUNG EX. 1002 - 1132/4148

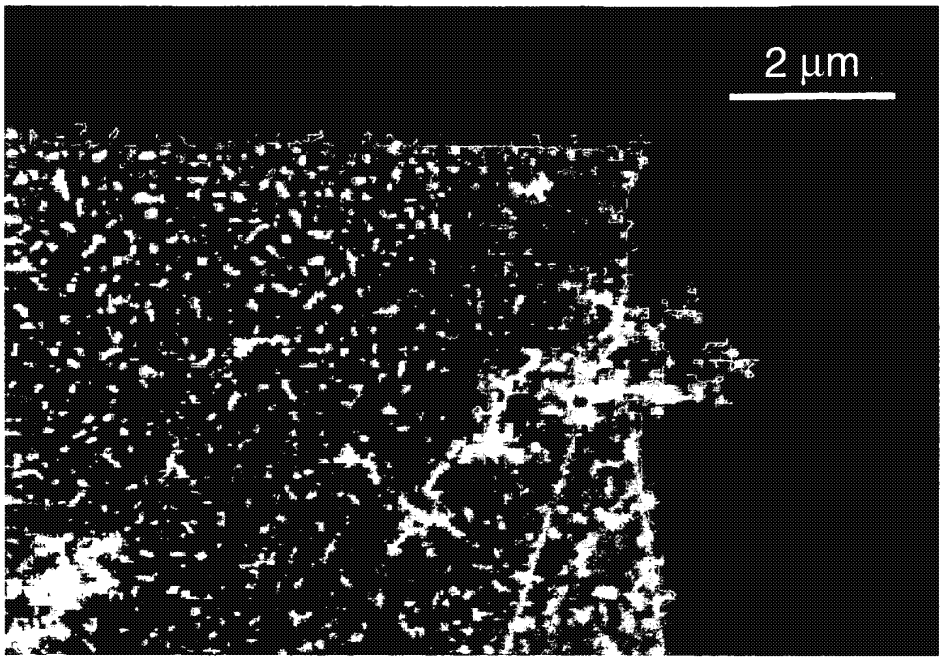


Figure 3.8: SEM image of debris collected from etching plume during the creation of silicon microstructures in SF_6. Note the protrusion of dendritic formation off the edge of the silicon sample used for collection (right side).

redeposited material that accumulates on the inside of the chamber. Figure 3.8 shows an SEM image of the corner of a flat silicon sample that was placed in the chamber along the inside of the window (see Fig. 3.2) during the preparation of a sample of conical microstructures in SF_6. The figure shows many small granules, with a size of approximately 100 nm. Along the right edge of the sample, a dendritic structure has also formed; it protrudes more than 1 μm off the edge of the silicon.

There is a high density of these granules deposited on non-irradiated areas of the sample, adjacent to the laser-irradiated regions, with the number of granules decreasing with distance from the laser spot. The granules are readily removed with wiping or rinsing with solvents. The nanoscale roughness on the sides of the cones can also be substantially reduced with cleaning, especially using an ultrasonic cleaner;

SIONYX1403000046.0090

SAMSUNG EX. 1002 - 1133/4148

the overall shape of the underlying cone, however, remains intact.

Given that the collected material shows a size scale and typical shape that closely resembles the nanoscale roughness on the sides of the cones formed in SF_6, we conclude that the roughness must be due to redeposited material from the etching plume. Furthermore, the fact that the redeposited material can form into dendritic structures more than a micrometer in size suggests that this regrowth may form a substantial contribution to the creation of cones.

3.10 Future work

Many experiments remain to be done to elucidate the mechanism for the creation of conical microstructures using femtosecond laser pulses. The mechanism will be instructive not just in clarifying the underlying physics, but should also help us to tailor our process to fabricating structures with desired characteristics, such as sharp tips or rough or smooth sidewalls.

Recently, an *in situ* UV spectroscopic technique, dubbed light scattering spectroscopy, or LiSSp, has been used to observe the typical lengthscales of ripple patterns that form during ion bombardment [92]. Features 200–2000 nm in size can be measured with this technique [53], suggesting that it could be appropriate for *in situ* observation of the periodicity of the structures that evolve under laser irradiation. This technique might provide an efficient way to investigate the dependence of the sizes of microstructures on factors such as laser fluence, pulse duration, or gas parameters quickly, without having to make sets of structures and then image each set separately with electron microscopy.

To examine further the effects of non-reactive background gases, following Fig. 3.6, a non-reactive gas with a molecular weight closer to the weight of the halogen-containing molecule could be chosen. Specifically, Xe could be used in conjunction

SIONYX1403000046.0091

SAMSUNG EX. 1002 - 1134/4148

with the reactive Cl_2 or SF_6.

Investigations of conical structures cut to reveal cross-sections should give information about the structure and chemical composition of the surface and interior of the cones. Previous studies of laser cones formed on YBCO films using electron microprobe analysis have shown phase separation in the first several microns of depth in the cones, with the interior of the cone undisturbed [93]. A similar study of our microstructures should show the depths to which the S, O, or other impurities are present within the cones. We are also pursuing using transmission electron microscopy (TEM) as a means for determining the structure of the cones.[9]

[9]Cross-sectional TEM has been performed on samples of cones formed on silicon upon bombardment with Ar^+ ions in the presence of Mo. A focused ion-beam is used to thin the samples of cones to make them suitable for TEM studies, which reveal the crystalline and amorphous regions within the cones [60]. Similar experiments should be possible with equipment available at Harvard.

SIONYX1403000046.0092

SAMSUNG EX. 1002 - 1135/4148

Chapter 4

Optical Properties of Microstructured Surfaces

4.1 Introduction

The optical properties of silicon surfaces patterned with femtosecond laser pulses are striking. Even upon the most cursory comparison with non-irradiated Si (111) surfaces, an increase in absorption of visible light by the patterned silicon surface is apparent: laser irradiation changes the surface from shiny grey to matte black. Furthermore, the absorption of not only visible but also infrared light by the patterned surface, as well as the photocarrier production, are larger than for flat silicon.

In this chapter I describe the measurements of the optical properties of large areas of femtosecond-laser-induced silicon microstructures. Structures formed in a variety of gases are investigated, and the differences in properties between surfaces patterned in the various gases are explained. Possible applications for devices fabricated using our surface texturization technique are also discussed, along with an outline of the future work that would be necessary to make these applications practical.

SIONYX1403000046.0093

SAMSUNG EX. 1002 - 1136/4148

4.2 Background

Crystalline silicon is the most widely used substrate in semiconductor electronic devices, but its band structure limits its usefulness in optoelectronic devices. Ordinary crystalline silicon has a band gap of 1.07 eV, corresponding to light with a wavelength of approximately 1.1 μm. As a result, ordinary silicon does not absorb light with wavelengths longer than 1.1 μm. This restricts the use of silicon in optoelectronic devices to only those devices that detect visible light. Furthermore, flat silicon is fairly reflective even in the visible wavelength range, limiting the sensitivity of silicon photodetectors and the efficiency of silicon solar cells. Increasing the wavelength range wherein silicon devices are useful and decreasing their reflectivity in the visible are therefore issues of technological interest, particularly given the low cost of silicon, its ubiquity in existing electronic devices, and the wealth of knowledge that already exists regarding silicon processing and fabrication techniques.

Surface texturing is a well-known method for reducing reflection from many types of surfaces. Anechoic acoustic surfaces can be made this way, and naturally ocurring textured surfaces that reduce optical reflections can be found, for example, in the corneal lenses of some nocturnal insects [94], and on the petals of some flowers [95]. A number of surface texturization processes have been used in the past to reduce the reflectivity of silicon to just a few percent. These include anisotropic wet etching [96, 97, 98], reactive ion etching [99, 100], electron beam lithography followed by etching [101], and the use of porous silicon films [96, 102]. Laser-induced microstructuring of silicon offers a technique for surface texturization that has advantages over methods currently in use.

Reducing the reflection of visible light increases the visible absorptance of silicon, making these surface texturing processes potentially useful for improving the efficiency of optical devices, such as solar cells, that operate in the wavelength range $\lambda < 1.1$ μm.

SIONYX1403000046.0094

SAMSUNG EX. 1002 - 1137/4148

In the wavelength range $\lambda > 1.1$ μm, however, a reduction in reflectance results in an increase in transmittance, rather than absorptance, because the bandgap ultimately limits the absorptance of infrared radiation. In order to increase the below-band gap absorptance of silicon, one must therefore alter the band structure of silicon, as this method of laser irradiation does (see section 4.5.2).

Femtosecond laser irradiation of silicon in the presence of ambient gases introduces impurities into the silicon; the presence of these impurities appears to strongly affect the optical and optoelectronic properties of the silicon, most likely via the impurity photovoltaic effect. The impurity photovoltaic effect refers to the intentional incorporation of impurities or other defects into a crystal in order to allow photocarrier production via impurity levels within the bandgap of a semiconductor [103]. First suggested in 1960 [104] as a means for increasing the efficiency of photovoltaic solar cells, this technique has been investigated both theoretically [103] and experimentally [105, 106].

4.3 Experimental

Our primary means for characterizing the optical properties of patterned silicon samples is measuring the samples' reflectance and transmittance using a Hitachi U-4001 spectrophotometer. The setup for measuring reflectance is shown in Fig. 4.1a and for transmittance in Fig. 4.1b.

The morphology of the microstructured silicon samples requires the use of a non-standard detector configuration. Because the laser-patterned sides of our samples are corrugated and the back sides are not polished, it is likely that some of the incident light from the source in the spectrophotometer is scattered diffusely and that some emerges from the backs of the samples at angles other than that at which it entered (it undergoes "diffuse transmission"). In order to detect scattered as well

SIONYX1403000046.0095

SAMSUNG EX. 1002 - 1138/4148

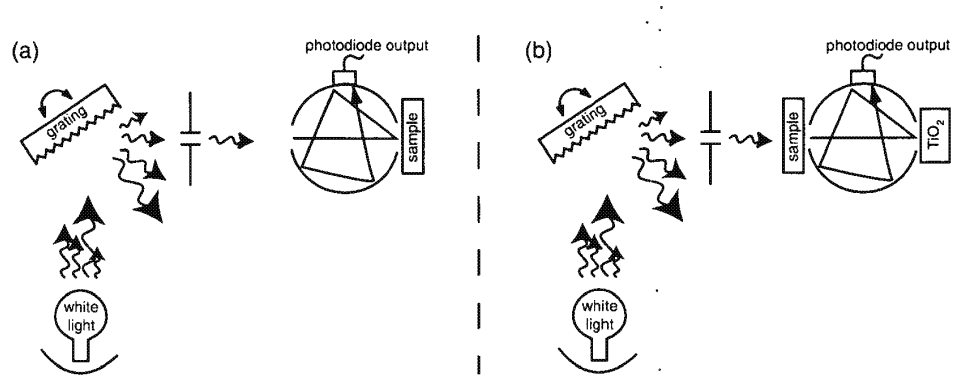


Figure 4.1: Schematic of measurements of optical properties of microstructured silicon samples using Hitachi U-4001 spectrophotometer: (a) configuration for measuring reflectance, (b) configuration for measuring transmittance.

as specularly reflected and transmitted light, we incorporated the detector into an integrating sphere. The interior of the sphere is painted white so that light striking any part of the inside of the sphere is scattered. The detector mounted on the top of the sphere then collects the light that scatters off the inside of the sphere. For reflectance measurements, the sphere collects all light that is reflected or scattered from the front of the sample, and for transmittance measurements, it collects the light that passes through the sample at any angle.

Our samples are all smaller than the open aperture of the integrating sphere, so they must be mounted on another substrate in order to hold them in place. A CaF_2 window is used as a supporting substrate because the reflectance of CaF_2 is low (approx. 6%) and the optical absorptance is negligible for the entire range of wavelengths at which our spectrophotometer operates, 250 nm $< \lambda <$ 2.5 μm. A 10 mm $\times$ 10 mm sample of microstructured silicon is mounted on the CaF_2 window using a tiny sliver (less than 1 mm on each side) of black carbon tape. As little of the silicon is obstructed by the tape as possible. The CaF_2 window is mounted in a standard 1-inch lens mount, which is then held in place against the integrating sphere

SIONYX1403000046.0096

SAMSUNG EX. 1002 - 1139/4148

with a clamp and paper tape.

For reflectance measurements (see Fig. 4.1a), the silicon sample is placed behind the integrating sphere. At this position, the spectrophotometer source's beam is almost as large as the silicon sample, so care must be taken to position the sample properly to obtain an accurate measurement. To do this, we fix the wavelength of the spectrophotometer source to a value in the visible using the spectrophotometer's grating monochrometer; the silicon sample and its supporting window are then placed such that the sample intercepts as much of the beam as possible.

For transmittance measurements (see Fig. 4.1b), the silicon sample is placed in front of the integrating sphere and a block of TiO_2 blocks the opening at the back of the sphere. In this position, the silicon sample can easily be placed such that all the incident light is directed on to the sample.

We measure the reflectance and transmittance of each sample over the entire wavelength range of the spectrophotometer, 250 nm $< \lambda <$ 2.5 μm. The absorptance (A) of each sample as a function of wavelength is then calculated from the reflectance (R) and transmittance (T) by:

$$A(\lambda) = 1 - R(\lambda) - T(\lambda) \tag{4.1}$$

4.4 Results

We measured the optical properties of samples of microstructures made in a variety of conditions, as described below. The parameters influencing optical absorptance are the heights of the microstructures and the gases in which they were formed.

4.4.1 Unmodified Si(111)

We characterized the optical properties of flat, crystalline silicon for comparison with our laser-irradiated samples. Reflectance and transmittance were measured for a

SIONYX1403000046.0097

SAMSUNG EX. 1002 - 1140/4148

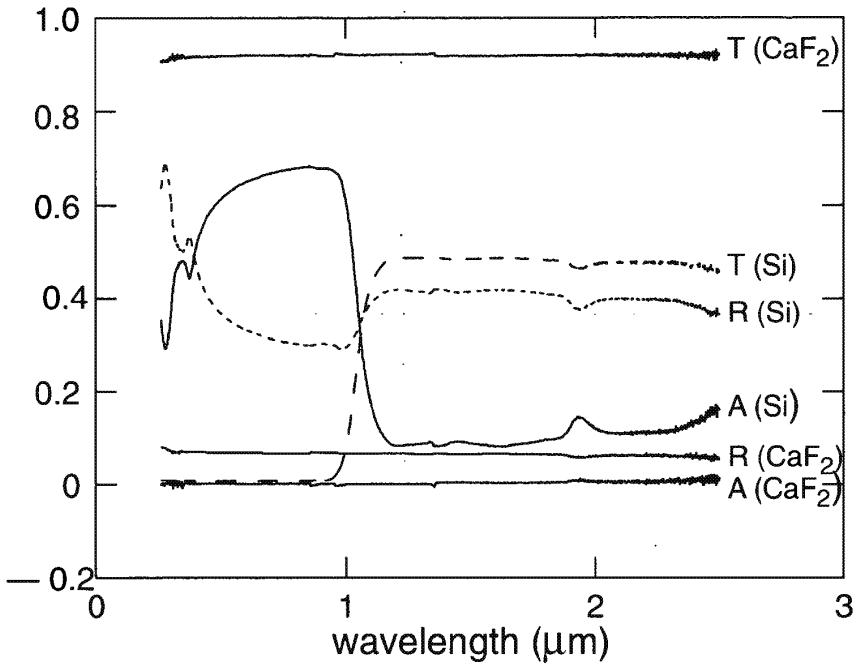


Figure 4.2: Reflectance (R), transmittance (T), and absorptance (A) for both a flat, unmodified sample of Si (111) and the supporting CaF_2 window alone. Note that the absorptance of CaF_2 is < 0.01 for the wavelength range shown. The dip shown in R and T measurements for Si at $\lambda \approx 2\mu$m (also appearing as a bump in A) is believed to be an artifact of our measurement apparatus.

piece of flat, unmodified Si (111) that was cut and cleaned in the same manner as our patterned silicon pieces (see Section 3.4). The results, along with the calculated absorptance spectrum, are shown in Fig. 4.2. The absorptance of unmodified silicon is roughly 0.70 for light with wavelengths between 750 nm and 950 nm. The band edge at $\lambda = 1.1$ μm is evident, and the absorptance beyond this edge drops as low as 0.08. For longer wavelengths, the absorptance increases, but it is nevertheless only 0.16 at $\lambda = 2.5$ μm, at the end of our spectrophotometer's useful range.

To demonstrate that the CaF_2 window makes only a very minor contribution to

SIONYX1403000046.0098

SAMSUNG EX. 1002 - 1141/4148

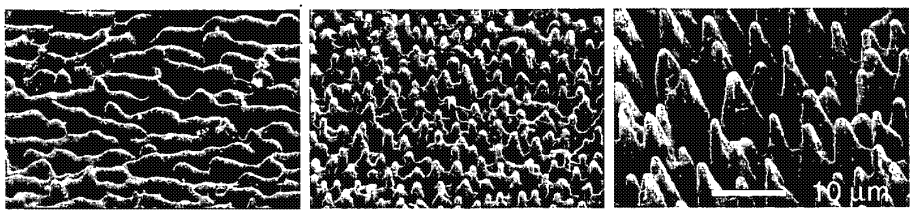


Figure 4.3: Three samples laser-patterned in SF_6, each with microstructures of a different height. The height of the structures on a given sample is determined by the laser fluence and the speed of translation of the laser spot across the sample as the structures are formed.

the results, Fig. 4.2 also shows the reflectance, transmittance and absorptance of the CaF_2 window alone. The reflectance of the CaF_2 window is approximately 0.06 for the wavelength region shown. Because the transmittance is approximately 0.94, the absorptance of the window is less than 0.01, or less than 1% of the incident light.

4.4.2 Surfaces patterned in SF_6

We measured the optical properties of samples prepared in SF_6 using various translation speeds and laser fluences and thus having microstructures of various heights. We compared the properties of samples with three different microstructure heights: 1–2 μm, 4–7 μm, and 10–12 μm (see Fig. 4.3). The reflectance spectra of these three samples are shown in Fig. 4.4, and the transmittance spectra in Fig. 4.5. Figure 4.6 shows the absorptance of these three samples.

Even for areas patterned with the smallest microstructures, only 1–2 μm tall, the optical absorptance over the wavelength range 250 nm $< \lambda <$ 2.5 μm is substantially greater than that of flat, crystalline silicon. For wavelengths between 500 nm and 1.1 μm, the absorptance for these small microstructures is as high as 0.9. The absorptance drops at the band edge, as it does for flat silicon, but even for these longer

SIONYX1403000046.0099

SAMSUNG EX. 1002 - 1142/4148

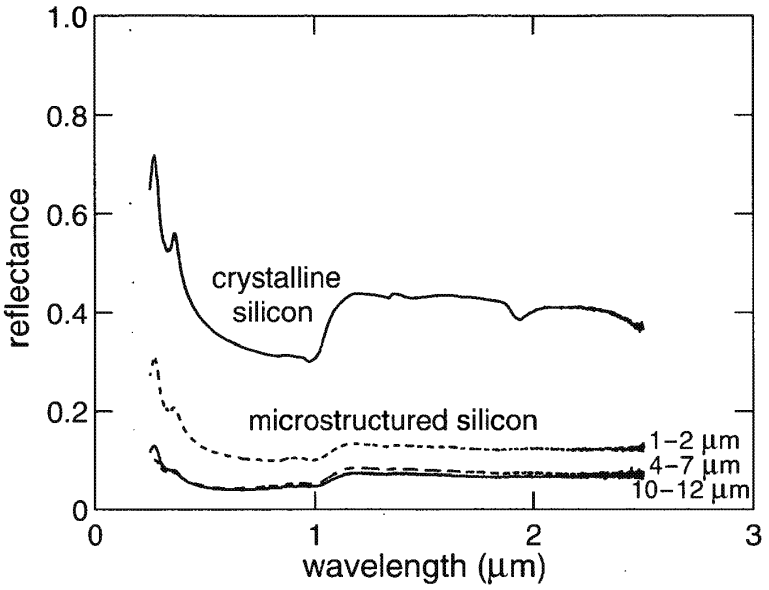


Figure 4.4: Reflectance of samples prepared with three different translation speeds, and thus having three characteristic microstructure sizes, versus wavelength. The reflectance of flat, crystalline silicon is included for comparison.

wavelengths, $\lambda > 1.1$ μm, the absorptance is greater than 0.8, or more than five times the absorptance of the flat, crystalline silicon.

As the heights of the structures increases, so does the optical absorptance, both below and above the band gap. For the tallest microstructures studied, with heights of 10–12 μm, the absorptance is approximately 0.9 or greater across the entire wavelength region investigated. This represents a remarkable increase in absorptance compared with flat silicon, especially for infrared wavelengths 1.1 μm $< \lambda <$ 2.5 μm.

SIONYX1403000046.0100

SAMSUNG EX. 1002 - 1143/4148

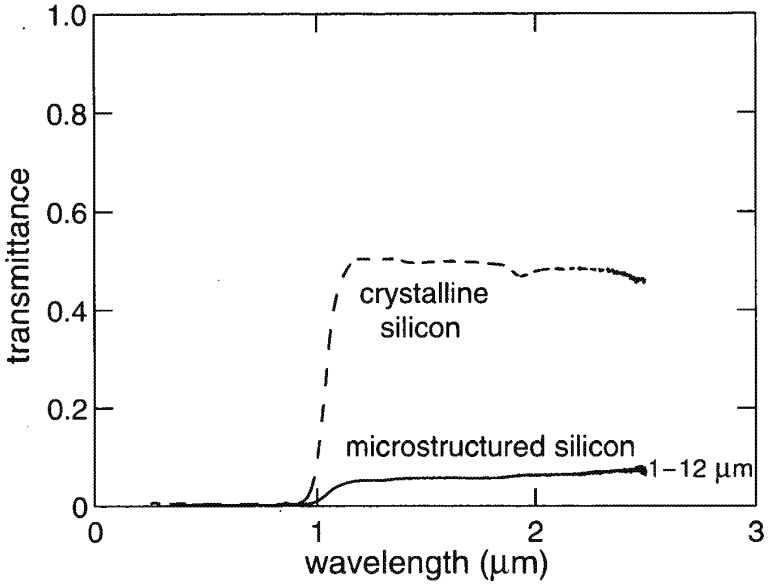


Figure 4.5: Transmittance of samples prepared in SF_6 versus wavelength. The traces for samples with microstructure heights in the range of 1–12 μm are indistinguishable on this scale. The transmittance of flat, crystalline silicon is included for comparison.

4.4.3 Surfaces patterned in other gases

We investigated the optical properties of microstructured silicon surfaces prepared in a number of gases in addition to SF_6.

The reflectance of samples prepared in SF_6, Cl_2, N_2, and air is shown in Fig. 4.7. Figure 4.8 shows the transmittance of these samples. The reflectance and transmittance are lowest for the structures formed in halogen-containing gases. For samples prepared in either SF_6 or Cl_2, the reflectance and transmittance are lower than those for flat, crystalline silicon across the entire 1.2–2.5-μm wavelength range, with the reflectance and transmittance lowest for the surfaces prepared in SF_6. Samples made

SIONYX1403000046.0101

SAMSUNG EX. 1002 - 1144/4148

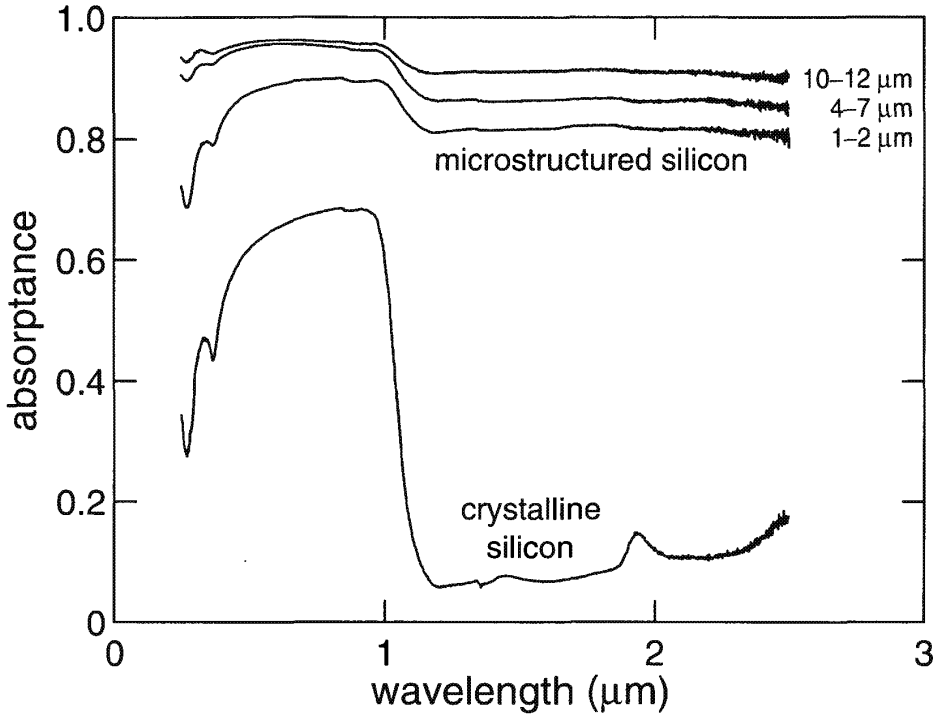


Figure 4.6: Absorptance of samples prepared with three different translation speeds, and thus having three characteristic microstructure sizes, versus wavelength. The absorptance of flat, crystalline silicon is included for comparison.

in air or N_2 show decreased transmittance relative to flat silicon as well as decreased reflectance in the short-wavelength region ($\lambda < 1.5$ μm for air, $\lambda < 1.77$ μm for N_2).

Figure 4.9 shows the absorptance of the silicon samples, as calculated from the reflectance and transmittance, for structures made in the four gases. The drop in reflectance is accompanied by an increase in absorptance in the visible wavelength region for all gases used. Although samples fabricated in any of the gases show an increase in infrared absorption over ordinary crystalline silicon, the effect is strongest for structures formed in the presence of SF_6: the absorptance is approximately 0.9 in the wavelength region 1.2-2.5 μm. Structures made in Cl_2 show an absorptance

SIONYX1403000046.0102

SAMSUNG EX. 1002 - 1145/4148

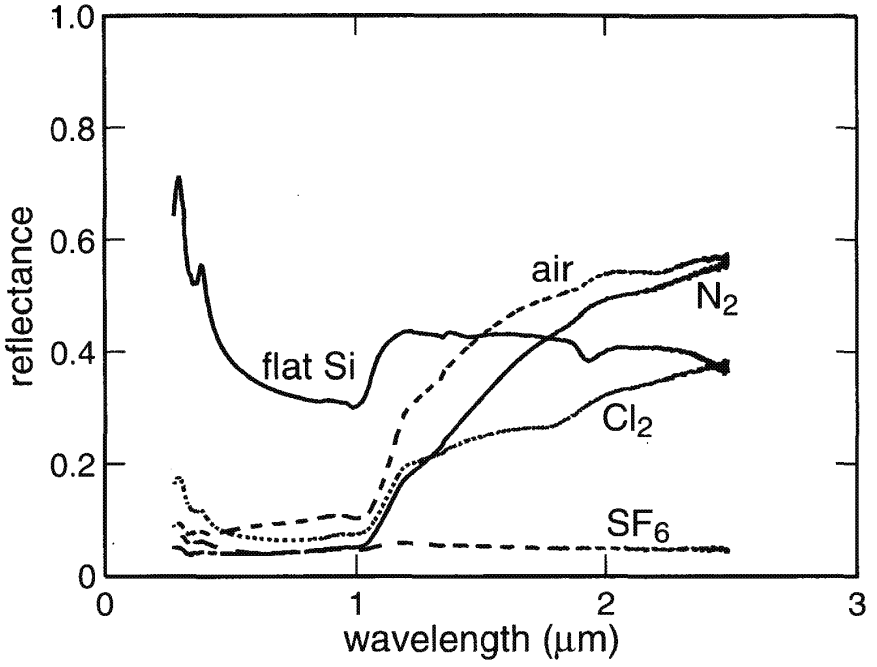


Figure 4.7: Reflectance of samples prepared in four different ambient gases is shown versus wavelength. The reflectance of flat, polished silicon is included for comparison.

of 0.3–0.9 in this wavelength region, while for unmodified silicon, the absorptance at these infrared wavelengths is less than 0.2. Surfaces structured in air or N_2 are less effective absorbers than those made in halogen-containing gases in the wavelength range $\lambda > 0.5$ μm for air and $\lambda > 1.3$ μm for N_2. Furthermore, they show lower infrared absorptance than flat silicon for long wavelengths ($\lambda > 1.9$ μm for air and $\lambda > 2.2$ μm for N_2).

SIONYX1403000046.0103

SAMSUNG EX. 1002 - 1146/4148

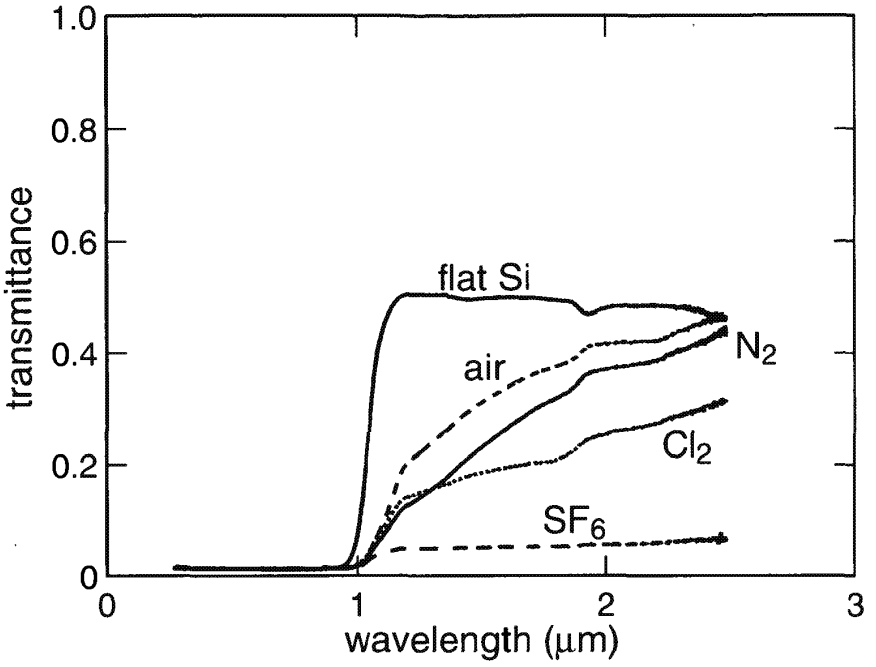


Figure 4.8: Transmittance of samples prepared in four different ambient gases versus wavelength. The transmittance of flat, polished silicon is included for comparison.

4.5 Discussion

We would like to understand why silicon patterned with femtosecond laser pulses exhibits different optical properties than flat silicon. In particular, we are interested in learning the role of the shape of the structures and in understanding the importance of the ambient gas used during laser irradiation.

4.5.1 Multiple reflections

We believe that the increase in absorptance by all of the structures in the visible ($\lambda < 1.1$ μm) wavelength range is at least partly due to geometric factors. Simply

SIONYX1403000046.0104

SAMSUNG EX. 1002 - 1147/4148

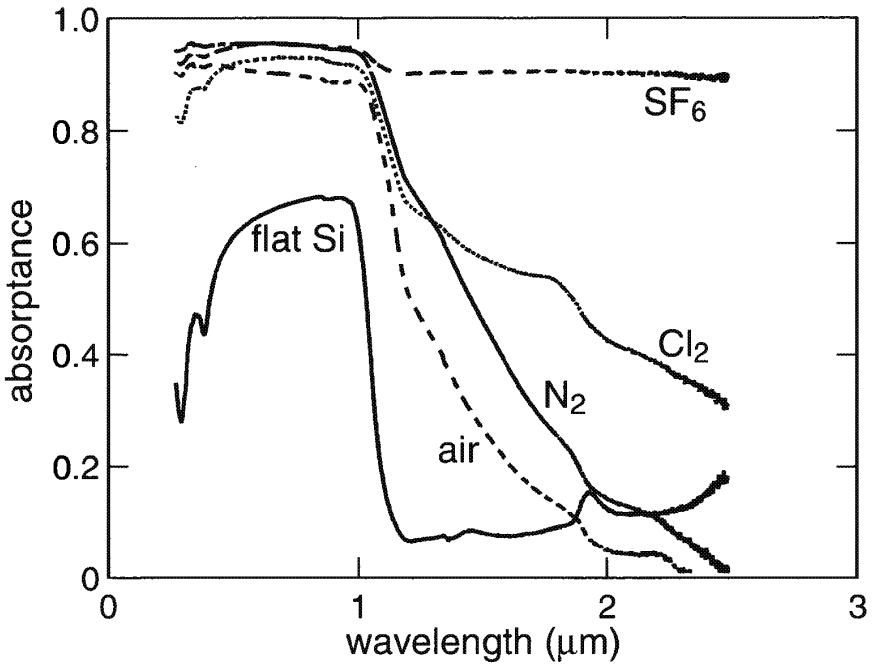


Figure 4.9: Wavelength dependence of the optical absorptance of silicon surfaces for four different ambient gases present during the microstructure formation. The absorptance spectrum of an unmodified Si(111) surface is included for reference. Microstructured surfaces exhibited a marked increase in absorptance above the band edge of silicon (1.1 μm).

increasing the surface area of the silicon sample ought to provide an increase in absorptance, as would creating structures with steep slopes along their sides, leading to multiple reflections.

We can compare the multiple reflections in our silicon cones with the reflections in surface structures introduced using standard etching techniques designed to produce antireflective layers. The advantages of the steeper slopes in the laser-induced cones are clear. Figure 4.10a shows the path followed by a ray incident normally on a corrugated surface, such as the cones formed in SF_6. This figure assumes each cone

SIONYX1403000046.0105

SAMSUNG EX. 1002 - 1148/4148

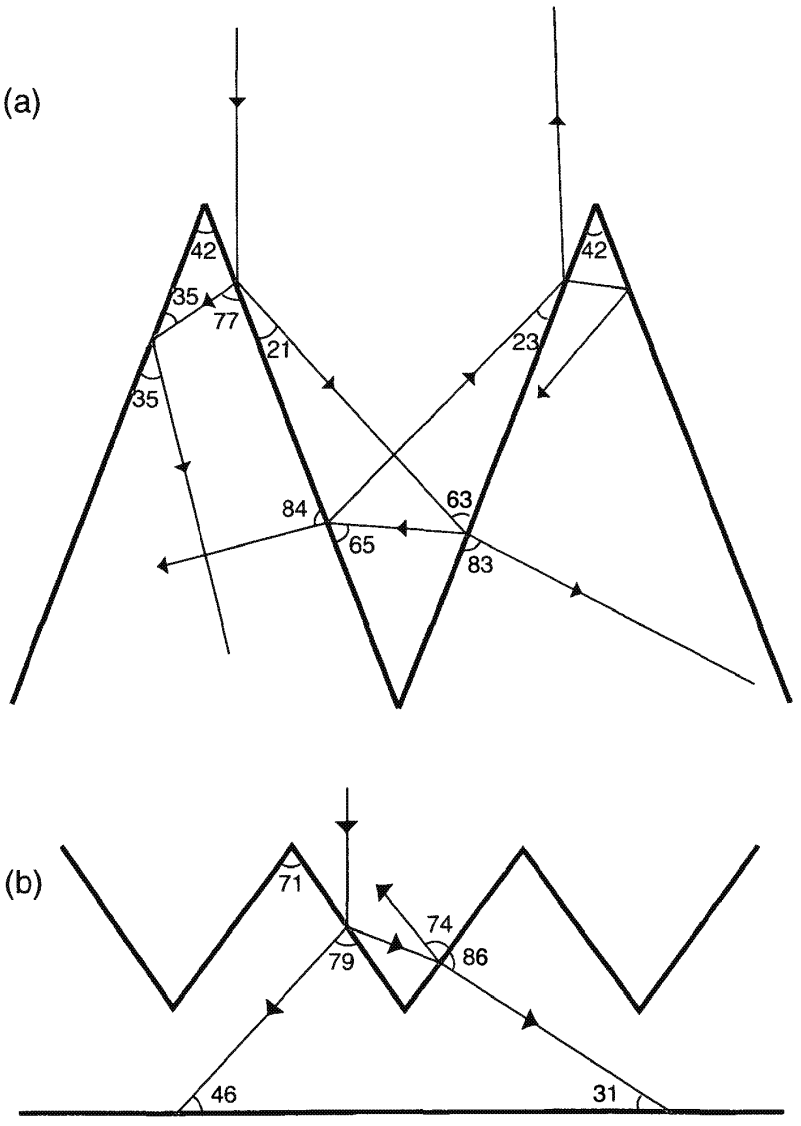


Figure 4.10: Illustration of the optical path of light incident on microstructured silicon surface: (a) Our laser-textured surfaces, with cones subtending 42°, (b) Textured silicon surface of inverted pyramids made using anisotropic etching, after [107]. Angles are labelled in degrees.

SIONYX1403000046.0106

SAMSUNG EX. 1002 - 1149/4148

subtends an angle of 42°, which is the average subtended angle for the twelve cones in the center portion of Fig. 3.5a.[1] We further assume that the textured silicon surface maintains the index of refraction of ordinary silicon, approximately 4 for $\lambda = 600$ nm. From the figure, it is clear that each ray reflects several times off the sides of the structures before escaping. Furthermore, once a ray enters the microstructure, the angle for total internal reflection is approximately 14° from the local normal, so that essentially all rays are trapped inside the cones. Figure 4.10b shows the optical path for rays incident normally on a silicon surface with the morphology of an array of inverted pyramids, like the structures made using anisotropic etching [107]. Such surface texturing is currently commonly used in silicon-based optoelectronic devices for the reduction of reflections; a demonstrated reduction in the reflection of sunlight from 35% to 10% has been reported. The subtended angle of the features in these devices is determined by the crystalline structure of silicon: etching of a (100) surface using NaOH reveals the (111) planes and forms internal angles of 70.5°. In this case, an incident ray will undergo 2 reflections before leaving the surface. The greater number of reflections in the laser-induced cones should lead to higher optical absorption.

4.5.2 Introduction of states into the band gap

Simply changing the geometry of the surface of silicon, whether through laser processing or more conventional means, cannot increase the absorptance of sub-band gap radiation as dramatically as we see for laser-induced microtexturing. For samples patterned in SF_6, we believe states, or perhaps bands of states, have been introduced within the silicon band gap. Sulfur is known to contribute impurity states in silicon

[1]The subtended angle of 42° is measured from the scanning electron micrograph taken at an angle of 45° with respect to the normal. The cones are actually sharper than they appear in the SEM from this angle, making the effect of multiple reflections even more pronounced than shown in Fig. 4.10.

SIONYX1403000046.0107

SAMSUNG EX. 1002 - 1150/4148

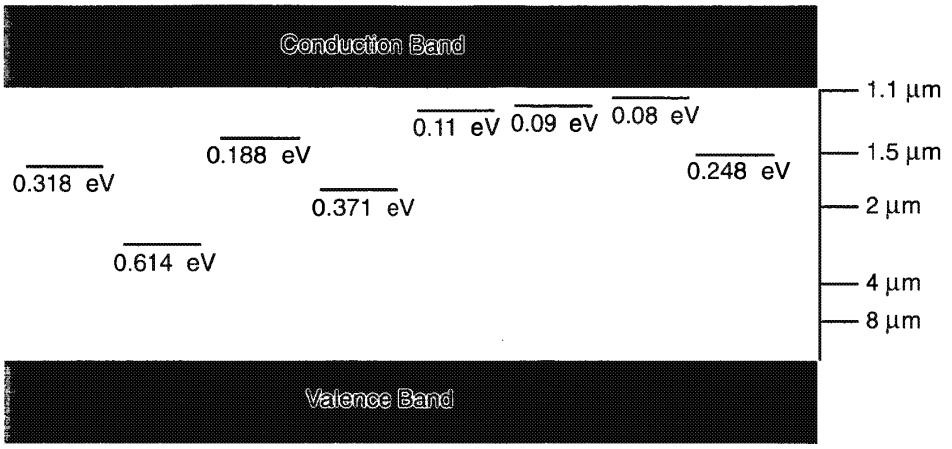


Figure 4.11: The impurity states within the silicon band gap contributed by sulfur. The energy of each state is noted, relative to the bottom of the conduction band (after Janzén et al. [108]). The wavelength scale from the top of the valence band is given along the right side.

[108], as shown in Fig. 4.11. For high concentrations of sulfur, such states could effectively introduce an impurity band into the gap.

In previous work in our group [36], secondary ion mass spectrometry (SIMS) was used to characterize the chemical species present on the surface of the cones formed in SF_6; sulfur was detected at a concentration of about 1 part in 10^3. After the sample is annealed in vacuum, the sulfur signal in the SIMS measurement decreases by approximately a factor of 2 and the small grains on the walls of the cones are no longer present. At the same time, the absorptance in the $1.2-2.5$-μm range decreases by approximately half. This result suggests that the sulfur impurities, whether in the cones themselves or in the rough features on the walls of the cones, play a role in inducing the particularly high absorptance of the microstructures formed in SF_6.

Further evidence that the increased optical absorptance of SF_6-patterned surfaces compared with flat silicon cannot be due solely to geometrical contributions is found on comparison of the absorptance of samples irradiated in SF_6 with those irradiated

SIONYX1403000046.0108

SAMSUNG EX. 1002 - 1151/4148

in Cl_2. The microstructures are very similar in size and overall conical shape for the two gases, but the absorptances (see Fig. 4.9) are very different in the infrared. We attribute the infrared absorption properties, therefore, not only to geometry but also to the presence of impurities introduced during fabrication.

For structures made in air or N_2, the rounded shapes of the structures are sufficiently different from the conical shapes of the microstructures made in the halogen-containing gases that geometry, and not just the presence of different impurities, may well influence their absorptance. Possible explanations for a geometrical contribution to the absorptance include a dependence of the absorptance on total surface area of the patterned silicon, as well as the number of reflections of light from the surfaces of the structures.

4.6 Applications

Demonstration of an absorptance of approximately 0.9 across the wavelength range 250 nm $< \lambda <$ 2.5 μm prompts interest in using silicon microstructured in this way to improve the efficiency, sensitivity, and wavelength-range of inexpensive silicon optoelectronic devices. In order to be useful, however, the textured samples must demonstrate that increased optical absorption leads to increased photocarrier production, and not just to heating.

Significantly enhanced photocarrier production was recently demonstrated in our group in microstructured silicon at infrared wavelengths near and below the band gap [36]. Half of the light collection area of ordinary silicon avalanche photodiodes was microstructured in SF_6, and half was left unaltered. With no further processing of the devices, the response (photocurrent) of both areas to illumination from the 1.064 μm line of a Nd:YAG pulsed laser and from a 1.310 μm diode laser (cw, chopped at 100 Hz) was measured. Illuminating the microstructured area generates a response at

SIONYX1403000046.0109

SAMSUNG EX. 1002 - 1152/4148

bias voltage 500 V and higher, whereas the unstructured area shows no measurable response for bias voltage less than 900 V. For a bias of 900 V or greater, at both 1.064 μm and 1.310 μm, photocarrier production from the microstructured area is at least three times that from the unstructured area. There is no detectable difference in noise from the two areas. The increased photocarrier production relative to flat silicon could have applications in silicon solar cells and detectors.

4.6.1 Silicon solar cells

The first silicon solar cell was demonstrated at Bell Laboratories in 1953. This device exhibited a conversion efficiency (4%) that was approximately 5 times higher than that for the Se solar cells that had previously been demonstrated [109]. The following year, the first practical device was fabricated, with an efficiency of 6% [110]. Since then, solar cells have enjoyed an expanding niche in the electrical energy business. Although the total amount of solar power used is still small relative to the world's net energy consumption, solar cells do show substantial advantages in a number of specialized applications. For example, satellites in space are commonly solar-powered, as are many ground-based signal stations, homes in rural areas, and some small consumer electronic devices (pocket calculators, wristwatches, *etc.*). There is also speculation that solar power may find applications in the growing market of the Third World [107]. In year 2000, the photovoltaic industry increased production by 29 percent in the United States and 39 percent worldwide [111].

The use of silicon in solar cells offers a number of advantages over other materials, specifically, the low cost of silicon and the ability to exploit the extensive knowledge base for silicon device fabrication techniques. Furthermore, photovoltaics made from crystalline silicon exhibit excellent long-term stability [107]. In 1995, crystalline silicon solar cells accounted for 85% of photovoltaics produced [112].[2] Three ma-

[2]Amorphous silicon is also used in solar cells; see the review by Rech and Wagner [113].

SIONYX1403000046.0110

SAMSUNG EX. 1002 - 1153/4148

jor types of crystalline devices are common: single-crystal, cast polycrystalline, and polycrystalline ribbon.

Much of the current work in improving solar cells is directed toward increasing their efficiency [107, 109, 112, 114]. Loss mechanisms in solar cells are either optical or electrical; reflection, shadowing, and poor absorption of long-wavelength radiation comprise the reasons for optical losses [107].[3] A overall efficiency of 23–24% has been demonstrated in the laboratory; device with efficiencies of 16–18% are available commercially [115].

Microstructuring silicon with femtosecond laser pulses could contribute several advantages to current silicon solar cells. First, an increase in visible absorption, most likely due to the decreased reflectance because of the surface texture, could increase the efficiency of solar cells. Furthermore, from Fig. 4.12, it is clear that although the bulk of solar radiation is at wavelengths shorter than 1.1 μm, there is nevertheless a sizable component with wavelengths further in the infrared, for the distributions of both extraterrestrial and terrestrial radiation. The below-band gap absorption observed for microstructured silicon should also increase the efficiency of solar cells in the infrared.

The cost of constructing a solar array has four major components [107]: (1) land, and land preparation, approximately 35% of the total cost, (2) module manufacturing, including frames but not including solar cells, approximately 25%, (3) silicon wafers, approximately 20%, and (4) processing of the silicon into a solar cell, approximately 20%. Each of these costs is roughly proportional to the area of the array. The cost of the array is therefore approximately inversely proportional to the efficiency of the solar cells [107]. The financial incentive for increasing the efficiency of solar cells is great, even if, as would be the case for femtosecond-laser patterning, the processing

[3]Shadowing refers to the fact that the effective absorbing area of a solar cell is smaller than the actual size of the cell by about 2% due to the presence of the finger grid that makes electrical contact with the top surface of the cell.

SIONYX1403000046.0111

SAMSUNG EX. 1002 - 1154/4148

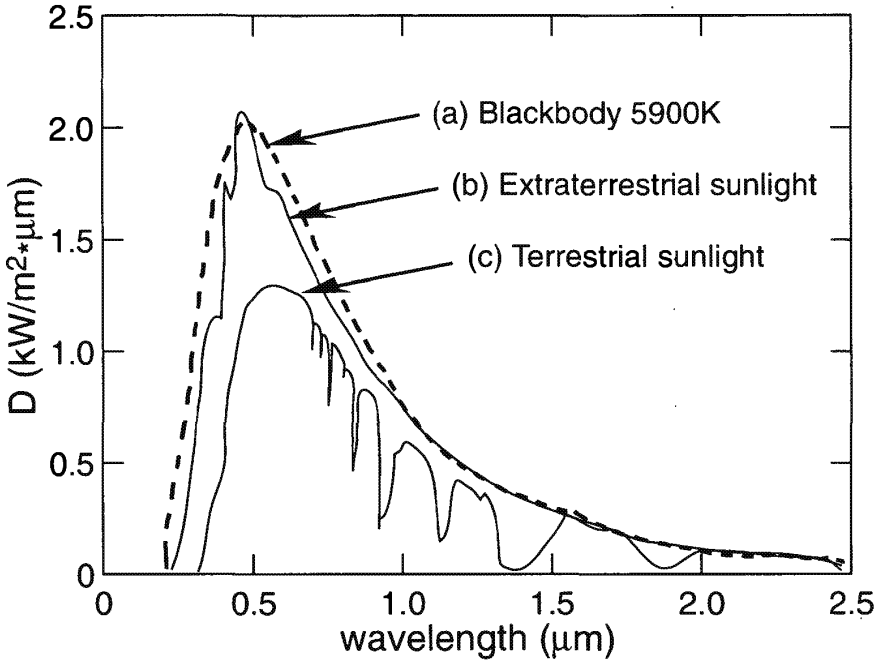


Figure 4.12: Distribution of solar radiation: (a) ideal blackbody radiation at 5900K, (b) extraterrestrial radiation, applicable to satellites, (c) terrestrial sunlight, through an air mass 1.5 times greater than the vertical thickness of the atmosphere, corresponding to the sun 41.8° above the horizon. Dips in the terrestrial curve are due to absorption by O_2, H_2O, and CO_2 in the atmosphere. After Goetzberger, Knobloch, and Voss [107].

costs may be substantial.

4.6.2 Silicon photodetectors

Commercially available silicon photodetectors are sensitive in the wavelength range 200–1100 nm, corresponding to the range in which crystalline silicon is absorptive (see Fig. 4.2). Infrared-sensitive Schottky-barrier photodetectors based on porous

SIONYX1403000046.0112

SAMSUNG EX. 1002 - 1155/4148

silicon have also been demonstrated in the laboratory; a quantum efficiency of 14.4% has been shown at $\lambda = 1.55$ μm [116].[4] The response of detectors patterned with laser-induced microstructures has not been measured at wavelengths longer than 1.3 μm, but the high optical absorptance for wavelengths as long as 2.5 μm suggests that laser patterning may be useful in increasing the efficiencies of photodetectors beyond the bandgap and perhaps beyond the useful range of porous silicon detectors.

4.7 Future Work

Surfaces textured using femtosecond pulses in the presence of reactive gases, particularly SF_6, hold promise for applications in photodetectors and solar cells. There is a great deal of work that remains to be done, however, if this technique is to be practical for device fabrication.

First, it is important to establish with certainty the mechanism for increased optical absorptance, both in the visible and in the infrared wavelength ranges. Our current processing steps, while relatively straightforward, are time-consuming relative to other steps in the fabrication of photodetectors and solar cells. If we can confirm which parts of our process are necessary for the increased absorption, we can tailor the technique so that we avoid any steps that are not crucial, or which contribute time and complexity to the process out of proportion to the improvements they make. We have already learned, for example, that while taller microstructures absorb more visible radiation than the 1–2-μm high structures (see Fig. 4.6), the extra time taken, a factor of approximately 4, in making the tall structures may make the smaller structures preferable.

We are investigating the degree to which patterning in the presence of other gases leads to enhanced photocurrent of modified versus unmodified silicon surfaces. This

[4] Data are not available for the porous silicon detector beyond $\lambda = 1.7$ μm because of the limitations of the measurement system [116].

SIONYX1403000046.0113

SAMSUNG EX. 1002 - 1156/4148

should improve our understanding of the role that sulfur impurities play in altering the band structure of the material (see Fig. 4.11). We are also interested in fabricating structures similar to our structures formed in SF_6, but using a different technique, in order to establish which characteristics of the surface enhance its optical properties. If, for example, conical structures with similar aspect ratios and dopant levels to the ones shown here could be made using processing tools already integrated into the manufacturing of devices, that might be more attractive to industry than the use of femtosecond laser systems.

Second, we are pursuing integrating our textured surfaces into established device-manufacturing processes. For example, we are currently collaborating with a manufacturer of solar cells to make a prototype solar cell using our microstructured silicon. We will compare the efficiency of the microstructured device to that of a standard polycrystalline silicon solar cell, with or without surface texture introduced with the standard anisotropic etching technique, in both the visible and infrared regions of the spectrum. We will also need to determine whether, in addition to the decrease in optical loss of patterned silicon solar cells, there might be a change in other loss mechanisms, such as ohmic loss or recombination loss.

We would also like to investigate the degree to which processing steps that are necessary for fabricating other portions of the device might decrease the absorptance of a microstructured surface. For example, many processing techniques involve heating the device; as noted previously, we have established that annealing for 3 hours at 1200 K in vacuum decreases the absorptance of patterned samples by a factor of two. We are presently investigating the effects of heating to lower temperatures or for shorter times.

SIONYX1403000046.0114

SAMSUNG EX. 1002 - 1157/4148

Chapter 5

Field emission by laser-induced conical microstructures

5.1 Introduction

The conical silicon microstructures described in chapter 3 show great potential as field emitters. Their sharp tips, as well as their altered work function due to introduced impurities, give them field-emission properties that rival those of some of the best devices currently under development. Furthermore, the technique used to fabricate these laser-induced silicon structures is fairly simple, relative to the process used in the creation of some other field emitters, because they do not require further processing steps beyond laser irradiation.

In this chapter I discuss the use of conical silicon microstructures as field emitters. I briefly review the theory of field emission from metals and from semiconductors. I describe the apparatus and procedure for measuring the current emitted from our structures as a function of the applied voltage and present the data from our measurements. These data show certain important features, which are noted, and the data

SIONYX1403000046.0115

SAMSUNG EX. 1002 - 1158/4148

are compared with results from other types of emitters. I then suggest some further experiments, as well as possible avenues for improving the field-emitting properties of the laser-induced silicon microstructures.

5.2 Background

Field emission refers to the emission of electrons from a solid cathode (generally in the shape of a sharp tip) into vacuum under the influence of a strong electric field [117]. The electric field is the result of biasing the cathode with respect to a nearby anode; the pointed or conical shape of the cathode strongly enhances the electric field at the tip [118]. Field emission occurs when electrons tunnel through the potential energy barrier at the interface between the cathode and the vacuum. This is in contrast with the more familiar phenomenon of thermionic emission, wherein electrons are emitted from a cathode when they have sufficient thermal energy to pass over the potential barrier.

I will review the fundamental theory describing field emission, presented in the classic work by Gomer [117] and subsequently discussed by Schwoebel and Brodie [119]. The reader is referred to these works for further detail.

5.2.1 Field-emission from a metal

We first consider the case of field emission from a metallic tip. The relevant energy-level diagrams are shown in Fig. 5.1. Figure 5.1a shows the potential energy as a function of position for an electron near a metallic surface. Within the metal, energy states up to the Fermi energy ϵ_F are occupied. In the vacuum, the lowest accessible level is at an energy $\epsilon_F + \phi$, where ϕ is the work function of the metal. To induce field emission, an electric field F is applied. The resulting potential energy is shown in Fig. 5.1b. The potential energy on the vacuum side is altered by the presence of

SIONYX1403000046.0116

SAMSUNG EX. 1002 - 1159/4148

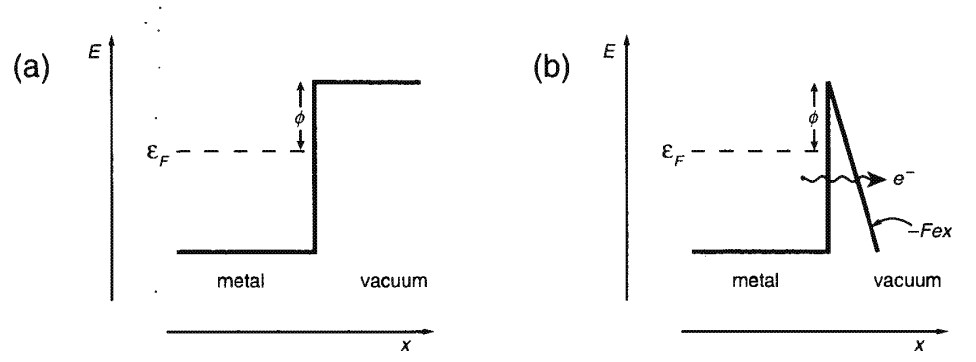


Figure 5.1: Potential energy, E, of an electron *vs.* position, (a) near a metal surface, or (b) near a metal surface in the presence of an applied electric field F. The work function is ϕ; the Fermi energy is ϵ_F.

the field; the potential energy in the vacuum is now a linear function of distance from the metal-vacuum interface. As the electric field is increased, the potential barrier narrows and thus the probability of the electron tunneling from the metal to the vacuum increases.

A qualitative understanding of the tunneling phenomenon can be gained from the Heisenberg uncertainty principle. An electron within the metal, with a kinetic energy of E_x due to its velocity in the x-direction, experiences a potential barrier at the metal-vacuum interface with height $\epsilon_F + \phi - E_x$ and width $(\epsilon_F + \phi - E_x)/Fe$. From the uncertainty principle, for an electron to have a position uncertainty Δx equal to the width of the potential barrier, its momentum uncertainty is:

$$\Delta p \geq \hbar/\Delta x = \hbar eF/(\epsilon_F + \phi - E_x). \tag{5.1}$$

If we consider an electron with an energy near the Fermi energy, then

$$\Delta p \geq \hbar eF/\phi. \tag{5.2}$$

For this energy uncertainty to result in a kinetic energy that equals the barrier height,

SIONYX1403000046.0117

SAMSUNG EX. 1002 - 1160/4148

the corresponding momentum uncertainty is

$$\Delta p = (2m\phi)^{1/2}. \tag{5.3}$$

Setting these two expressions for Δp to be equal, the threshold condition for field emission is:

$$1 \approx \frac{(2m)^{1/2}\,\phi^{3/2}}{\hbar F e}. \tag{5.4}$$

Alternately, we can consider field emission using the semiclassical description of tunneling due to Wentzel, Kramers, and Brillouin (WKB). The WKB theory can be used to calculate the probability $D(E,P)$ that an electron with potential energy P and kinetic energy E will tunnel through a barrier extending from $x = 0$ to $x = \ell$:

$$D(E,P) = f(E,P)\,exp\left[-2\left(\frac{2m}{\hbar^2}\right)^{1/2}\int_0^{\ell}(P-E)^{1/2}\,dx\right]. \tag{5.5}$$

Here, $f(E,P)$ is an insensitive function of E and P that can generally be approximated by a constant.

Equation 5.5 can be qualitatively explained in the following way. Consider the wave function ψ describing the electron. The probability of transmission through the barrier is approximately equal to the ratio of the probability of finding the electron on the right side of the barrier, at $x = \ell$, to the probability of finding the electron on the left side, at $x = 0$:

$$D(E,P) \cong [\psi(\ell)/\psi(0)]^2. \tag{5.6}$$

For small distances, such that P is roughly constant,

$$\psi(x) \cong e^{ikx}, \tag{5.7}$$

where

$$k = p/\hbar = \left[\frac{2m}{\hbar^2}(E-P)\right]^{1/2}. \tag{5.8}$$

SIONYX1403000046.0118

SAMSUNG EX. 1002 - 1161/4148

This implies

$$\psi(x+dx)/\psi(x) = exp\left[-\left(\frac{2m}{\hbar^2}\right)^{1/2}(P-E)^{1/2}\,dx\right] \tag{5.9}$$

$$\psi(\ell)/\psi(0) = exp\left[-\left(\frac{2m}{\hbar^2}\right)^{1/2}\int_0^{\ell}(P-E)^{1/2}\,dx\right]. \tag{5.10}$$

The resulting transmission probability is then:

$$D(E,P) \cong exp\left[-2\left(\frac{2m}{\hbar^2}\right)^{1/2}\int_0^{\ell}(P-E)^{1/2}\,dx\right]. \tag{5.11}$$

The integral in Eqn. 5.11 can be approximated by the area of a triangle with a base of $\ell = (\epsilon_F + \phi - E_x)/Fe$ and a height of $(\epsilon_F + \phi - E_x)^{1/2}$. Therefore,

$$D(E,P) \cong exp\left[-\left(\frac{2m}{\hbar^2}\right)^{1/2}\frac{(\epsilon_F+\phi-E_x)^{3/2}}{Fe}\right]. \tag{5.12}$$

A more rigorous calculation has been performed by Fowler and Nordheim [120], yielding very similar results:

$$D(E_x) = \frac{4\left[E_x\left(\epsilon_F+\phi-E_x\right)\right]^{1/2}}{\epsilon_F+\phi}\,exp\left[-\frac{4}{3}\left(\frac{2m}{\hbar^2}\right)^{1/2}\frac{(\epsilon_F+\phi-E_x)^{3/2}}{Fe}\right]. \tag{5.13}$$

The emitted current density is found by multiplying this tunneling probability by the rate of arrival at the barrier of electrons with energy E_x, and then integrating over the energy range $0 \leq E_x \leq \epsilon_F$. The result is known as the Fowler-Nordheim equation [120]:

$$J = A\,(\beta V)^2\,exp\left(-\frac{B\phi^{3/2}}{\beta V}\right). \tag{5.14}$$

Here, V is the applied potential difference between the cathode and anode and β is a geometrical factor describing the field enhancement at the sharp tip; the electric field is $F = \beta V$. A is a function of ϕ, and B is a constant.

The Fowler-Nordheim equation is a useful tool for evaluating whether a given emission current is due to field emission or, for example, thermionic emission or

SIONYX1403000046.0119

SAMSUNG EX. 1002 - 1162/4148

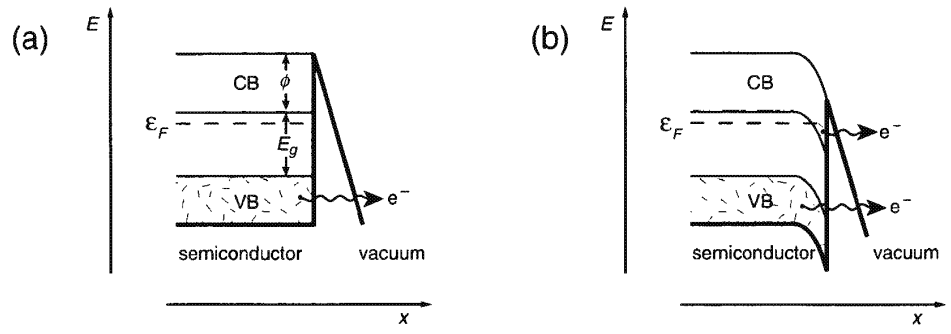


Figure 5.2: Potential energy, E, of an electron *vs.* position near a semiconductor surface (a) in the presence of an applied electric field, and (b) with the penetration of the field into the surface taken into account. The work function is ϕ, the Fermi energy is ϵ_F, and the bandgap is E_g. The valence band is labelled VB and the conduction band is CB.

photo-emission. During field emission, the current emitted from the cathodes follows the V-dependence described in Equation 5.14. Thus, we can plot $ln(I/V^2)$ *vs.* $1/V$ and expect a linear relation if the current I is the result of field emission. The constants A and B can also be extracted from the slope and y-intercept of the linear Fowler-Nordheim plot.

5.2.2 Field-emission from a semiconductor

Field-emission from a semiconductor is described by a very similar theory to that for the field emission from a metal, as summarized above in the Fowler-Nordheim equation, but the more complicated energy bandstructure in a semiconductor leads to a few important modifications.

Figure 5.2 shows the energy states of the semiconductor near the semiconductor-vacuum interface. In Fig. 5.2a, the penetration of the applied electric field is neglected. In this case, tunneling can occur from the valence band if the applied field is sufficiently intense. The current then obeys Fowler-Nordheim behavior, but with

SIONYX1403000046.0120

SAMSUNG EX. 1002 - 1163/4148

an effective work function $\phi_{effective} = \phi + E_g$, where E_g is the bandgap of the semiconductor. If the conduction band is thermally occupied, tunneling also takes place from the conduction band, but this is not usually the case.

If we take into account the penetration of the applied electric field into the semiconductor, the picture becomes somewhat more complicated. The electric field deforms the potential experienced by the electrons, as shown in Fig. 5.2b. If the deformation is strong enough, the bottom of the conduction band is at a lower energy than the Fermi energy on the semiconductor side of the interface, and electrons accumulate in the dip in the conduction band. We must then consider tunneling, and hence field emission, from two distinct groups of electrons, those in the valence band and those in the dip in the conduction band. Field emission due to the conduction band electrons follows Fowler-Nordheim behavior with an effective work function $\phi_{effective} = \phi - (\epsilon_F - V_0)$, where V_0 is the energy by which the bottom of the conduction band is shifted in the presence of the applied field. Clearly, the electrons in the altered conduction band can be induced to tunnel through the barrier by a lower electric field than must be used to induce tunneling by the valence-band electrons. Thus, in some cases, two regimes of field-emission are seen for two regimes of applied field strength.

In evaluating the emission from our laser-induced silicon microstructures, we will compare the current emitted as a function of applied voltage to the behavior predicted by the Fowler-Nordheim equation.

5.3 Apparatus and procedure

The current produced by a sample of our silicon microstructures in response to a given bias voltage is measured using the setup shown in Fig. 5.3. The microstructures are formed on a piece of silicon wafer, the back of which has been coated with 40 nm of gold to allow good electrical contact to the sample. The procedure for creating the

SIONYX1403000046.0121

SAMSUNG EX. 1002 - 1164/4148

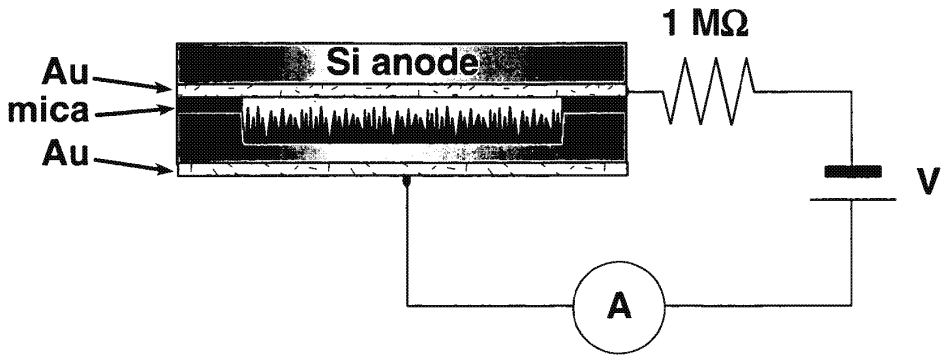


Figure 5.3: Apparatus used to measure field emission from silicon microstructures.

microstructures is otherwise the same as is outlined in Chapter 3. We typically use a patterned area of 2 mm × 2 mm or 3 mm × 3 mm for field-emission measurements.

The sample of microstructures is clamped to another gold-coated silicon wafer, which acts as the anode, with a pair of thin mica spacers between the two wafers. The mica spacers are made by carefully cleaving sheets of mica using the tip of a razor blade. The mica preferentially cleaves into layers that are 20–25 μm thick. Thus, we can make spacers with uniform thickness (typically 20–60 μm) over their area of several square millimeters. The microstructures and anode are placed in a small vacuum chamber, constructed primarily of 2 3/4" Conflat hardware and featuring a vacuum electrical feedthrough. The chamber is evacuated to a pressure of approximately 10^{-6} torr using a small Varian turbo pump.

Electrical connections to the external circuit are made via the vacuum feedthroughs. A Stanford Research Systems PS310 high-voltage power supply is used to apply a potential difference between the microstructured sample and the anode. A Keithley 486 picoammeter and a protection resistor (typical resistance 1 MΩ) are connected in series with the field-emission setup.[1] The current is measured with the picoammeter for

[1]The purpose of the protection resistor is to limit the current passing through the ammeter in

SIONYX1403000046.0122

SAMSUNG EX. 1002 - 1165/4148

various bias voltages, up to approximately 1000 V, depending on the microstructured sample used.

The microstructured sample is destroyed if excessive currents pass through it. A short between the patterned silicon microstructure sample and the anode, due to incorrect placing of the mica spacers, usually ruins the field emitters when high voltages are applied. Another failure mechanism is breakdown of the air between the emitters and the anode if the chamber is not adequately evacuated.

5.4 Field emission results

Figure 5.4 shows the field emission current measured as a function of applied bias voltage for a 2 mm × 2 mm sample of conical microstructures formed in SF_6. The separation between the structured sample and the anode was 20 μm. The low-voltage region shown in Fig. 5.4a clearly shows the exponential increase in current (I) as a function of bias voltage (V). For the higher-voltage region ($V > 100$ V), Fig. 5.4b shows that the relationship becomes linear. That is, for high bias voltages, the response of the circuit becomes ohmic, with the slope of the I-V graph equal to the reciprocal of the resistance of the protection resistor.

The Fowler-Nordheim plot for this device is shown in Fig. 5.5. Two linear regimes are observed for low biases (seen on the right hand side of the graph). For higher biases (on the left hand side of the graph), the data deviate from linear, showing that the current is no longer due to ideal field emission.

the event that the microstructure sample shorts to the anode, which happens if the mica spacers become dislodged, for example.

SIONYX1403000046.0123

SAMSUNG EX. 1002 - 1166/4148

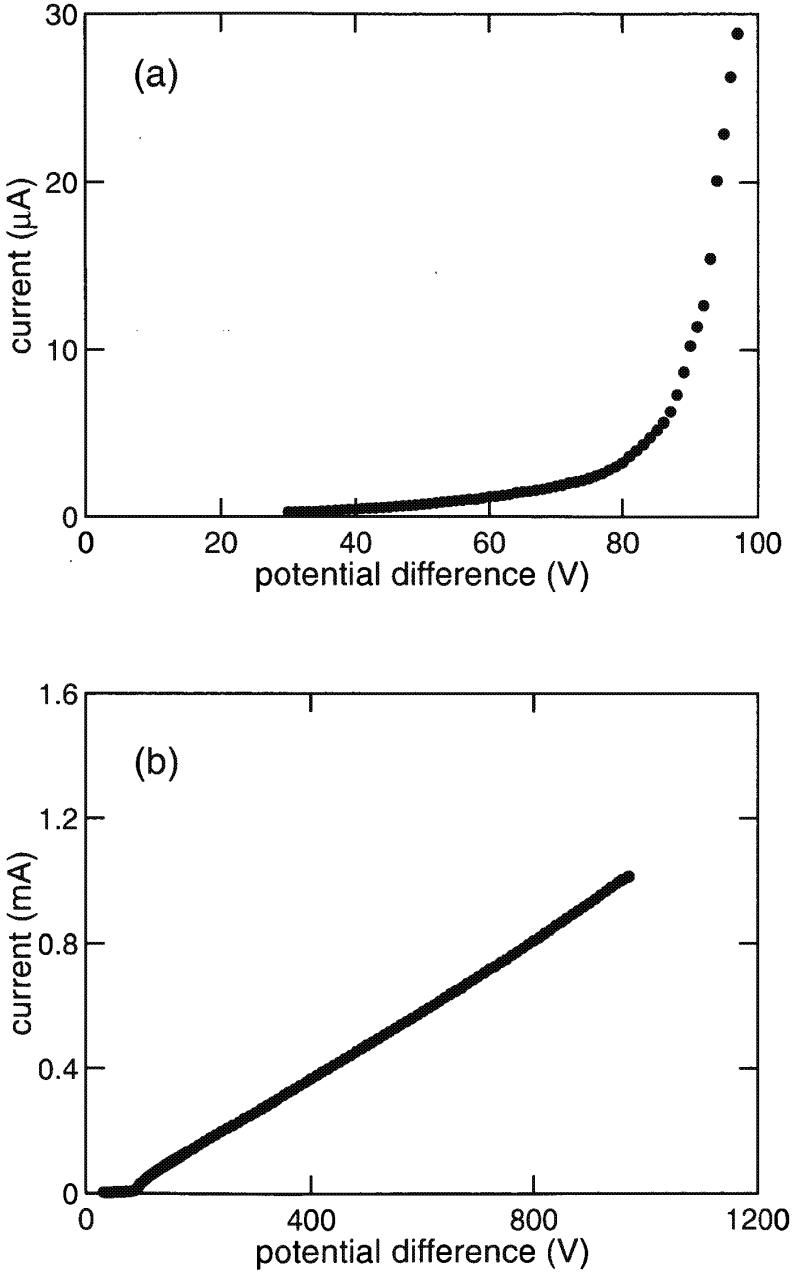


Figure 5.4: Measurements of field emission current as a function of applied bias voltage for a sample of microstructures made in SF_6. The low-voltage regime is shown in (a), and the higher-voltage regime in (b). Note the difference in scale of the two y-axes.

SIONYX1403000046.0124

SAMSUNG EX. 1002 - 1167/4148

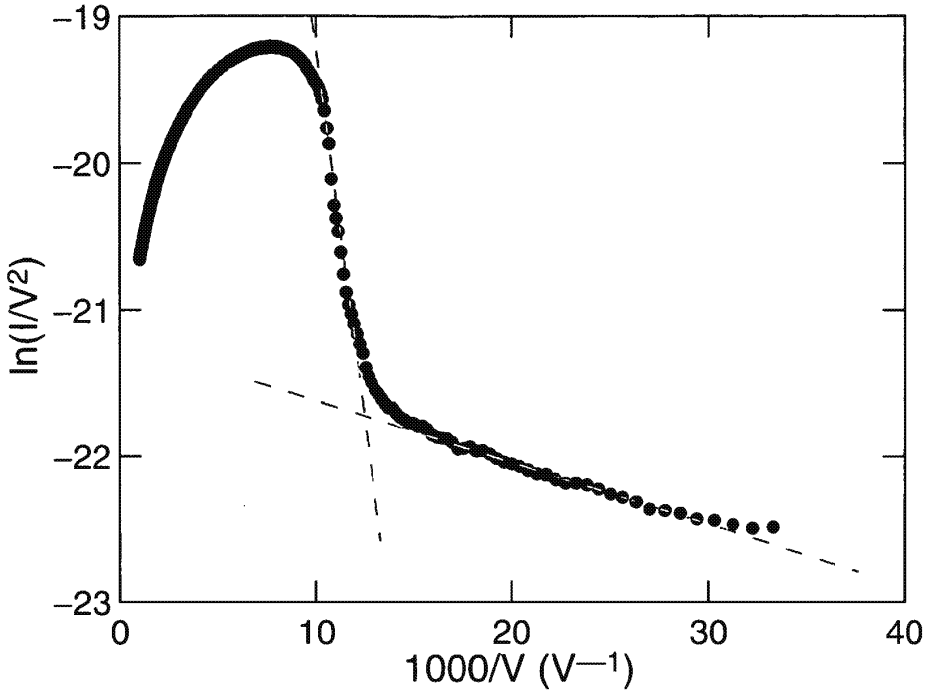


Figure 5.5: Fowler-Nordheim plot of data shown in Fig. 5.4. The dashed lines indicate the two linear regimes of field emission.

5.5 Discussion

Field emitters are often characterized by the field needed to create measurable emission current (the "turn-on field") and the field needed to create a substantial emission current (the "threshold field"). For our devices, the turn-on field, defined as the electric field (bias voltage divided by the tip-to-anode spacing) for which a current density of 0.01 μA/mm^2 is observed, is 1.3 V/μm. The threshold field, defined as the field at which a current density of 0.1 μA/mm^2 is produced, is 2.15 V/μm.

Our devices compare well with some currently in use; however, other techniques have been used to make field emitters with lower turn-on and threshold fields. For example, Huq *et al.* have created silicon tips using conventional electron-beam lithog-

SIONYX1403000046.0125

SAMSUNG EX. 1002 - 1168/4148

raphy and dry etching [121]. An array of 40 × 40 tips, spaced by 7 μm, gives an output current of 50 μA for an applied field of 2.25 V/μm. When these tips are coated with a layer of amorphous diamond, the output increases dramatically: for an applied field of 1.5 V/μm, the field-emission current is 1.4 mA. Many other implementations of field-emission technology feature gate electrodes in the shape of a plane with a hole placed close (< 1 μm) to the tip [122]. Comparison of the operation of gated emitters with our emitters is difficult because their operation relies on different parameters.

The Fowler-Nordheim plot presents the easiest way to compare emission from our laser-induced microstructures to ideal field emission. We are particularly interested in the two linear regions of the Fowler-Nordheim plot, as well as the non-linear region corresponding to high (> 100 V) bias voltages.

5.5.1 Two field-emission regimes

The two distinct linear regions shown in Fig. 5.5 can be explained by the semiconducting nature of the silicon tips. With low bias voltages, electrons from the conduction band begin tunneling across the barrier. This may be enhanced by the presence of additional states near the bottom of the conduction band, introduced by the sulfur impurities. For higher bias voltages, electrons can be removed from the valence band; the slope of the Fowler-Nordheim plot showing this tunneling is different from the case of tunneling from the conduction band because of the different effective work function. This is exactly what we observe in Fig. 5.5.

5.5.2 Ohmic response for high biases

As the bias voltage is increased and the current passing through the field-emission device increases, the potential drop across the protection resistor increases. Eventu-

SIONYX1403000046.0126

SAMSUNG EX. 1002 - 1169/4148

ally, the potential drop across the resistor is sufficiently high that it limits the current passing through the circuit. In this case, the total effective impedance in the circuit is approximately equal to just the resistance of the protection resistor and thus the *I-V* curve (see Fig. 5.4b) is linear, with a slope equal to the resistance of the protection resistor.

5.6 Applications of field emitters

During the last fifty years, thermionic vacuum tubes have been replaced with solid-state microelectronic devices in the majority of their applications. Thermionic devices are now used in only a few types of devices, most notably cathode-ray displays and microwave sources. Field-emitter technology, or "vacuum microelectronics," offers some of the advantages of conventional vacuum tube devices and some of the advantages of solid-state microelectronics and thus may be well-suited to replace thermionic vacuum tubes in some of these last remaining applications [123].

Devices based on field-emission feature many desirable characteristics [124]. Field emitters can produce electron beams with high brightness and current density while operating at low voltages and consuming relatively little power. They can be integrated into small, lightweight devices and can be operated with high pulse-repetition rates due to their rapid on/off switching speed. Furthermore, fabrication of semiconductor field-emission arrays can take advantage of the existing wealth of knowledge of semiconductor processing techniques.

A number of applications take advantage of the field emission current from a single sharp tip or an array of tips. In the current implementation of our microstructure-fabrication technique, we make arrays of microstructures. However, modifications may be possible that allow the creation of single tips. A few of the most important applications of single tips and arrays are discussed here, including displays and mi-

SIONYX1403000046.0127

SAMSUNG EX. 1002 - 1170/4148

crowave sources. The reader is referred to excellent reviews by Temple [125] and by Brodie and Schwoebel [123] for further details on applications of emitter arrays.

5.6.1 Flat panel displays

The use of arrays of field emitters in flat panel displays, as an alternative to liquid crystals, is the application currently receiving the most attention in industry. In a field emission display, as in a conventional cathode-ray tube (CRT), an electron beam impinges upon a phosphor screen to create an image. Unlike in the CRT, however, the field-emission beam need not raster across the screen in order to generate the entire image. Rather, an individual pixel in the image is defined by a small region of tips within one square of a grid of electrodes. Tips within the pixel are induced to emit electrons by the application of a bias voltage to the adjacent electrodes that define that square within the grid. Figure 5.6 is a schematic representation of a flat-panel display using field emitters.

A display based on field-emission has the benefit of similar brightness and picture quality to a CRT display, but allows a much smaller device size and lower power consumption [119]. Much work is currently devoted to improving the field-emission display, particularly to make it more reliable and to improve the lifetime and current stability.

5.6.2 Microwave sources and electron beams

The use of field-emitter arrays in plasma and microwave source applications is reviewed by Jensen [124]. The high current density that is achievable at ambient temperatures using field-emission technology opens the possibility for using these devices in microwave tubes, to produce or amplify radio-frequency power [123]. One technique for implementing field emitters into microwave tubes is to simply replace the electron

SIONYX1403000046.0128

SAMSUNG EX. 1002 - 1171/4148

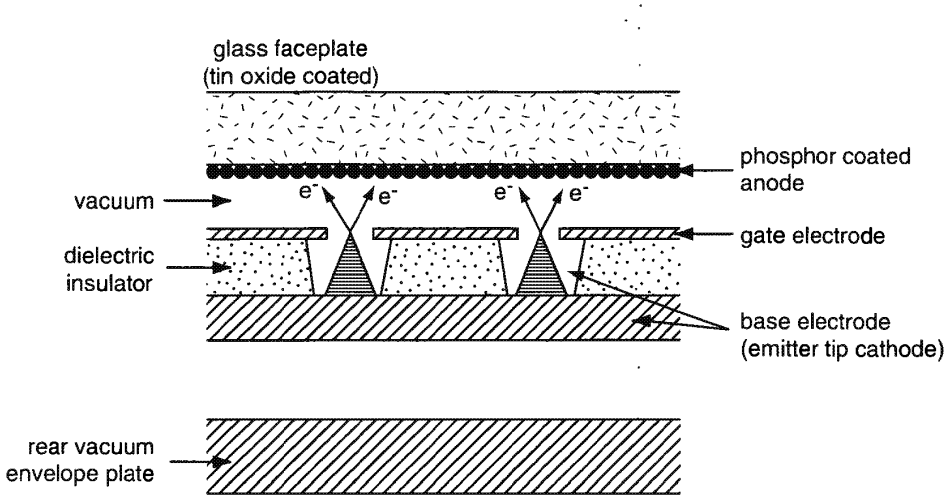


Figure 5.6: Schematic of a flat-panel display based on field emission. Redrawn from Schwoebel and Brodie [119].

gun in a conventional tube with a field-emission source. Another method is to modulate the tip-to-anode bias voltage at a microwave frequency equal to the frequency of the desired output; the electrons are then emitted from the tips in bunches. The bunched electrons then interact with a cavity, which serves as a source of microwaves that are resonant with the cavity modes.

The high current density of field-emission cathodes are also of use in electron guns [123]. Arrays of emitters and single-tip cathodes both exhibit very fast switching times. Furthermore, single-tip cathodes have the advantage of producing high currents with low applied voltages, which is necessary in applications where high-energy electrons are undesirable, such as in some electron microscopes or some electron-beam lithography systems where high-energy electrons might damage the sample.

SIONYX1403000046.0129

SAMSUNG EX. 1002 - 1172/4148

5.6.3 Other applications

A few other niche applications have been suggested for field-emission arrays. For example, the thermionic emission from a filament could be replaced with field emission in devices such as Bayard-Alpert and other 'ion' pressure gauges or in mass spectrometers [125]. Replacing a hot filament with a cold cathode would prevent some undesirable processes, such as the cracking of molecules on the filament, outgassing of the filament, and thermal reaction on the filament and adjacent areas. A cold cathode would also consume less power and could be made smaller, and the effects of stray light would be avoided.

Another possible set of applications exploits the dependence of field emission current on applied electric field, which is highly dependent on the tip-to-anode spacing [125]. If the anode is made of a deformable diaphragm material, the field-emission current can be used as a measure of pressure on the diaphragm, acoustic intensity, or displacement.

5.7 Future work

In light of the encouraging preliminary results regarding the utility of laser-induced silicon microstructures in field-emission applications, a number of experiments should be performed to further examine the field-emitting properties of these structures and how they might be improved or integrated into useful devices.

5.7.1 Apparatus modifications

The current experimental apparatus suffers from a number of problems. The technique for measuring the current passing through the conical tips as a function of bias voltage uses thin mica spacers that are dificult to cleave and that cause shorts if not

SIONYX1403000046.0130

SAMSUNG EX. 1002 - 1173/4148

carefully placed (see section 5.3). Furthermore, this method of "sandwiching" the two electrodes together prior to pumping out the chamber necessarily leads to a higher gas pressure at the site of the microstructures than is measured at the gauge. Long pumping times (> 1 hour) are needed to reduce this pressure to the level where the bias voltage does not induce breakdown in the air between the electrodes.

Several modifications to the experimental setup will make taking data easier, faster, and less likely to damage the samples. A better method for separating the microstructures from the opposite electrode is to mount the patterned sample on a linear translation stage, with the sample initially placed fairly far (more than 1 cm) from the anode. After the chamber is evacuated to the desired pressure, the sample could be translated into position, tens of microns from the surface of the anode. The anode-sample spacing could be fixed by first translating the sample until it just contacts the anode, then backing it away by the desired separation. This has the advantage of more flexibility in the tip-to-anode spacing, as well as the guarantee that the two electrodes do not come into accidental electrical contact. With no possible short and a lower pressure in the vicinity of the microstructures, testing would be less likely to damage the patterned sample.

5.7.2 Structures made with different gases

As discussed in chapter 3, microstructures made in gases other than SF_6 exhibit morphology different from those made in SF_6. Furthermore, the impurities introduced into these microstructures during processing is dependent on the gas species present during irradiation. We are interested in investigating the degree to which different shapes and different impurities affects the field-emission properties of laser-induced conical microstructures. Specifically, we would like to measure the I-V characteristics of samples patterned in Cl_2, as these show similar morphology to the samples made in SF_6 that show high field-emission currents. This would give us some evidence as

SIONYX1403000046.0131

SAMSUNG EX. 1002 - 1174/4148

to the importance of overall shape versus the presence of S impurities in determining field-emission properties. It is unlikely that structures made in N_2 or air would show the high field-emission currents that the sharp structures made in SF_6 exhibit, but this should be confirmed.

5.7.3 Chemical modification of microstructured surfaces

As described in section 5.2, the work function of the surface is a key parameter in determining a structure's field-emission properties. We are currently pursuing experiments to chemically modify the surface of our microstructures following their creation, thereby altering the work function of the material. Of particular interest is the possibility of adding a carbon-rich layer. Carbon-rich silicon tips, in the form of solid SiC structures [126] or silicon tips with a diamond coating [121] or a thin SiC layer [127] also have the advantage of lower chemical reactivity than a silicon emitter, and thus potentially extended lifetimes and more stable emission currents.

In previous work silicon tips grown using a vapor-liquid-solid technique, as described in chapter 3, have been coated with SiC layers to improve their field-emission properties [127]. The SiC layers are 2 to 500 nm thick and are formed by heating the single-crystal silicon tips to $850 - 950°$ C in the presence of ethylene gas. In this process, the SiC layer forms as silicon from the substrate diffuses through the SiC and reacts with the ethylene molecules as they adsorb on the surface. The SiC layer grows thicker and hydrogen is released. A Fowler-Nordheim plot for the modified tips has a slope nearly twice the slope of a Fowler-Nordheim plot for a similar but unmodified silicon tip. Field-emission currents in excess of 12 μA are observed from a single tip.

We are also investigating forming a thin carbon coating on our silicon microstructures by covering them with approximately one monolayer of propylene and heating them. We expect heating to cause the desorption of some intact propylene molecules, but carbon-containing fragments should also remain on the silicon surface [128, 129].

SIONYX1403000046.0132

SAMSUNG EX. 1002 - 1175/4148

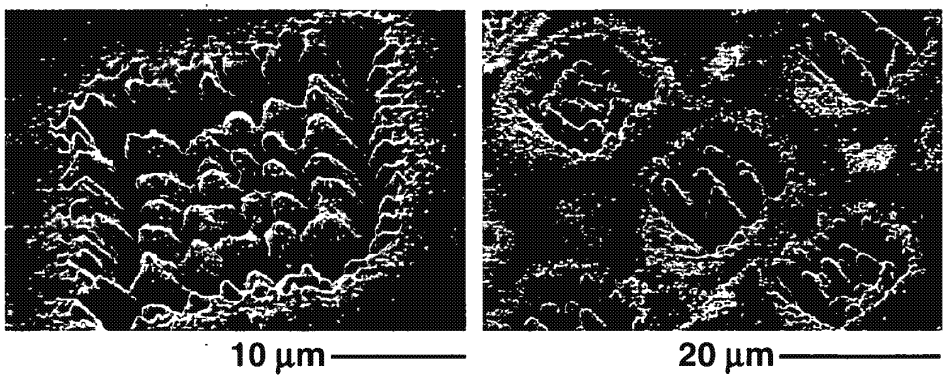


Figure 5.7: Square arrays of microstructures made by irradiating through masks with square holes.

The field-emission properties of these altered tips will be measured in the near future.

5.7.4 Controlled placement of microstructures

For the practical use of field emitters in devices such as displays, it is necessary to have a means for addressing only a small area of the patterned surface, to define one pixel, for example. We have recently observed that microstructures can be formed in areas as small as 15 μm $\times$ 15 μm.

Fig. 5.7. shows microstructures formed upon irradiation of a Si sample through a copper grid with square openings. The fluence used to make these samples was 5 kJ/m^2, which is approximately half the fluence used to make the sharp microstructures used in our investigations of field-emission properties. These structures are therefore quite blunt and thus may not show the high field-emission currents seen with the sharp structures. However, this result does suggest a possible technique for arranging microstructures into deliberately placed arrays, as would be necessary for defining pixels in a display.

SIONYX1403000046.0133

SAMSUNG EX. 1002 - 1176/4148

Chapter 6

Summary and Conclusions

This thesis addresses a few of the myriad ways that ultrashort optical pulses can be used. Nonlinear processes in solids are used to create a tunable source of laser pulses that can permit ultrafast studies of chemical or physical processes. The intense fields generated by the ultrashort pulses can permanently modify materials in novel and useful ways.

In our first set of experiments, we constructed a set of optical apparatus for use in surface studies. Our optical parametric amplifier and difference frequency generation stage can create laser pulses with wavelengths essentially anywhere between 550 nm and 7.3 μm. We used these instruments in an infrared-visible sum-frequency generation experiment, in an attempt to time-resolve the reaction between CO and O_2 on the surface of Pt (111). Although we lacked sufficient infrared power at the appropriate wavelength to observe the SFG, we developed techniques that can be applied to other, future optical studies of adsorbates on surfaces.

The second set of experiments investigated the creation and applications of surface texturing induced with ultrashort laser pulses. We formed arrays of conical microstructures on the surface of silicon by irradiating it with a train of ultrashort laser pulses in the presence of a reactive background gas. The microstructures evolve

SIONYX1403000046.0134

SAMSUNG EX. 1002 - 1177/4148

over exposure to hundreds of laser pulses and exhibit a typical size and spacing dependent on the identity and pressure of the background gas and on the laser parameters. Halogen-containing ambient gases lead to structures with sharp tips, while nitrogen or air lead to blunt, rounded structures. The mechanism leading to the microstructure formation most likely involves melting, ablation, laser-assisted chemical etching, and possibly redeposition. The structures exhibit shapes and chemical compositions that may make them useful in a number of applications.

The optical properties of the microstructures are very different from the optical properties of flat, crystalline silicon. The optical absorptance in the wavelength range 250 nm to 2.5 μm is approximately 0.9 for the tallest structures fabricated in SF_6. Smaller structures and structures made in other gases absorb less, particularly in the infrared. The increased absorptance is most likely due to a combination of geometrical effects and impurities. The geometry of conical structures leads to multiple reflections off of the steep walls. Sulfur impurities introduced during fabrication create states within silicon's band gap that lead to below band gap optical absorption. The high optical absorptance and simple fabrication technique of the laser-induced silicon microstructures make them well-suited for applications in optoelectronic devices such as solar cells and infrared detectors.

The microstructures also show strong field emission. We measured the field-emission current for arrays of microstructures formed in SF_6 and observed a turn-on field of 1.3 V/μm and a threshold field of 2.15 V/μm. A Fowler-Nordheim plot of the data shows two regions of field-emission, as well as a region of ohmic behavior for high bias voltages. We believe the two distinct field-emission regions follow from the two bands of electron energy states in the semiconductor. Future work will help to clarify the field-emission mechanism, and will help us to improve the field-emitters and optimize the fabrication process to make the microstructures compatible with various applications.

SIONYX1403000046.0135

SAMSUNG EX. 1002 - 1178/4148

In this thesis, I have touched on just a few ways we can use ultrafast laser pulses as tools in nonlinear optics, ultrafast spectroscopy, and material modification. Judging from progress in ultrafast optics thus far, this rich and interesting branch of research will contribute to our scientific understanding and technological advancement in the future in ways we cannot even imagine.

SIONYX1403000046.0136

SAMSUNG EX. 1002 - 1179/4148

References

[1] C. C. Wang and G. W. Racette, Appl. Phys. Lett. **6**, 169 (1965).

[2] J. A. Giordmaine and R. C. Miller, Phys. Rev. Lett. **14**, 973 (1965).

[3] R. L. Byer and R. L. Herbst, in *Nonlinear Infrared Generation*, edited by Y.-R. Shen (Springer Verlag, Berlin, 1977).

[4] A. Yariv, *Quantum Electronics* (Wiley, New York, 1989), 3rd ed.

[5] W. R. Bosenberg and R. C. Eckhardt, eds., feature on optical parametric devices, J. Opt. Soc. Am. B **12**, 2084 (1995).

[6] R. Danielius, A. Piskarskas, A. Stabinis, G. P. Banfi, P. D. Trapani, and R. Righini, J. Opt. Soc. Am. B **10**, 2222 (1993).

[7] A. Shirakawa and T. Kobayashi, Appl. Phys. Lett. **72**, 147 (1998).

[8] M. K. Reed, M. K. Steiner-Shepard, and D. K. Negus, Opt. Lett. **19**, 1855 (1994).

[9] M. Nisoli, S. DeSilvestri, V. Magni, O. Svelto, R. Danielius, A. Piskarskas, G. Valiulis, and A. Varanavicius, Opt. Lett. **19**, 1973 (1994).

[10] V. V. Yakovlev, B. Kohler, and K. R. Wilson, Opt. Lett. **19**, 2000 (1994).

[11] F. Seifert, V. Petrov, and F. Noack, Opt. Lett. **19**, 837 (1994).

SIONYX1403000046.0137

SAMSUNG EX. 1002 - 1180/4148

[12] V. Petrov, F. Seifert, and F. Noack, Appl. Phys. Lett. **65**, 268 (1994).

[13] A. Shirakawa, I. Sakane, and T. Kobayashi, Opt. Lett. **23**, 1292 (1998).

[14] R. W. Boyd, *Nonlinear Optics* (Academic Press, San Diego, 1992).

[15] R. R. Alfano, ed., *The Supercontinuum Laser Source* (Springer Verlag, New York, 1989).

[16] E. P. Ippen and C. V. Shank, Appl. Phys. Lett. **27**, 488 (1975).

[17] E. N. Glezer, in *Spectroscopy and Dynamics of Collective Excitations in Solids*, edited by B. D. Bartolo (Plenum, NATO ASI series, 1996).

[18] A. W. Smith and N. Braslau, IBM J. Res. **6**, 361 (1962).

[19] H. J. Krause and W. Daum, Appl. Phys. B **56**, 8 (1993).

[20] A. Lohner, P. Kruck, and W. W. Ruhle, Appl. Phys. B **59**, 211 (1994).

[21] F. Seifert, V. Petrov, and M. Woemer, Opt. Lett. **19**, 2009 (1994).

[22] J. D. Kafka, M. L. Watts, J. W. Pieterse, and R. L. Herbst, Appl. Phys. B **60**, 449 (1995).

[23] M. K. Reed and M. K. Steiner-Shepard, IEEE J. Quantum Electron. **32**, 1273 (1996).

[24] B. Golubovic and M. K. Reed, Opt. Lett. **23**, 1760 (1998).

[25] F. Rotermund, V. Petrov, and F. Noack, in *Conference on Lasers and Electrooptics* (2001), p. 165.

[26] A. Yariv, *Optical Electronics* (Saunders College Publishing, Philadelphia, 1991), 4th ed.

SIONYX1403000046.0138

SAMSUNG EX. 1002 - 1181/4148

[27] M. Bass, P. A. Franken, A. E. Hill, C. W. Peters, and G. Weinreich, Phys. Rev. Lett. **8**, 18 (1962).

[28] P. A. Franken, A. E. Hill, C. W. Peters, and G. Weinreich, Phys. Rev. Lett. **7**, 118 (1961).

[29] R. W. Boyd and C. H. Townes, Appl. Phys. Lett. **31**, 440 (1977).

[30] X. D. Zhu, H. Suhr, and Y. R. Shen, Phys. Rev. B **35**, 3047 (1987).

[31] D. Zhang, J. H. Gutow, K. B. Eisenthal, and T. F. Heinz, J. Chem. Phys. **98**, 5099 (1993).

[32] J. R. Goldman, *Laser studies of energy- and charge-transfer dynamics*, Ph.D. thesis, Harvard University (1994).

[33] R. Finlay, *Femtosecond-laser-induced reactions at surfaces*, Ph.D. thesis, Harvard University (1998).

[34] T.-H. Her, R. J. Finlay, C. Wu, S. Deliwala, and E. Mazur, Appl. Phys. Lett. **73**, 1673 (1998).

[35] T. H. Her, R. J. Finlay, C. Wu, and E. Mazur, Appl. Phys. A **70**, 383 (2000).

[36] C. Wu, C. H. Crouch, L. Zhao, J. E. Carey, R. Younkin, J. A. Levinson, E. Mazur, R. M. Farrell, P. Gothoskar, and A. Karger, Appl. Phys. Lett. **78**, 1850 (2001).

[37] C. Wu, *Femtosecond laser-gas-solid interactions*, Ph.D. thesis, Harvard University (2000).

[38] A. J. Pedraza, J. D. Fowlkes, and D. H. Lowndes, Appl. Phys. A **69 [Suppl.]**, S731 (1999).

SIONYX1403000046.0139

SAMSUNG EX. 1002 - 1182/4148

[39] A. J. Pedraza, J. D. Fowlkes, and D. H. Lowndes, Appl. Phys. Lett. **74**, 2322 (1999).

[40] D. H. Lowndes, J. D. Fowlkes, and A. J. Pedraza, Appl. Surf. Sci. **154-155**, 647 (2000).

[41] A. J. Pedraza, J. D. Fowlkes, S. Jesse, C. Mao, and D. H. Lowndes, Appl. Surf. Sci. **168**, 251 (2000).

[42] A. J. Pedraza, J. D. Fowlkes, and D. H. Lowndes, Appl. Phys. Lett. **77**, 3018 (2000).

[43] J. D. Fowlkes, A. J. Pedraza, and D. H. Lowndes, Appl. Phys. Lett. **77**, 1629 (2000).

[44] L. S. Dake, D. E. King, J. R. Pitts, and A. W. Czanderna, in *Beam effects, surface topography, and depth profiling in surface analysis*, edited by A. W. Czanderna, T. E. Madey, and C. J. Powell (Plenum Press, New York, 1998).

[45] S. R. Foltyn, in *Pulsed Laser Deposition of Thin Films*, edited by D. B. Chrisey and G. K. Hubler (Wiley-Interscience, New York, 1994).

[46] R. M. Bradley and J. M. E. Harper, J. Vac. Sci. Technol. A **6**, 2390 (1988).

[47] J. Erlebacher, M. J. Aziz, E. Chason, M. B. Sinclair, and J. A. Floro, J. Vac. Sci. Technol. A **18**, 115 (2000).

[48] P. Sigmund, J. Mater. Sci. **8**, 1545 (1973).

[49] T. M. Mayer, E. Chason, and A. J. Howard, J. Appl. Phys. **76**, 1633 (1993).

[50] G. Carter, M. J. Nobes, I. V. Katardjiev, and J. L. Whitton, Defect Diffusion Forum **57**, 97 (1988).

SIONYX1403000046.0140

SAMSUNG EX. 1002 - 1183/4148

[51] S. Rusponi, C. Baragno, and U. Valbusa, Phys. Rev. Lett. **78**, 2795 (1997).

[52] E. Chason, T. M. Mayer, B. K. Kellerman, D. T. McIlroy, and A. J. Howard, Phys. Rev. Lett. **72**, 3040 (1994).

[53] J. Erlebacher, M. J. Aziz, E. Chason, M. B. Sinclair, and J. A. Floro, Phys. Rev. Lett. **82**, 2330 (1999).

[54] G. Carter and V. Vishnyakov, Phys. Rev. B **54**, 17647 (1996).

[55] Z. X. Jiang and P. F. A. Alkemade, Appl. Phys. Lett. **73**, 315 (1998).

[56] J. J. Vajo, R. E. Doty, and E.-H. Cirlin, J. Vac. Sci. Technol. A **14**, 2709 (1996).

[57] V. Vishnyakov and G. Carter, Nucl. Instrum. Meth. Phys. Res., Sect. B **106**, 174 (1995).

[58] V. Vishnyakov, G. Carter, D. T. Goddard, and M. J. Nobes, Vacuum **46**, 637 (1995).

[59] Y. Fujimoto, M. Nozu, and F. Okuyama, J. Appl. Phys. **77**, 2725 (1995).

[60] A. Imai, C. Kamiya, Y. Fujimoto, and F. Okuyama, Surf. Sci. **461**, L515 (2000).

[61] T. K. Chini, S. R. Bhattacharyya, D. Ghose, and D. Basu, Jpn. J. Appl. Phys. **30**, 2895 (1991).

[62] G. K. Wehner, J. Vac. Sci. Technol. A **3**, 1821 (1985).

[63] A. Parvizi-Majidi, in *Structure and Properties of Composites*, edited by T. W. Chou (Weinheim, New York, 1993), Materials Science and Technology: A Comprehensive Treatment.

[64] R. S. Wagner and W. C. Ellis, Appl. Phys. Lett. 4, 89 (1964).

SIONYX1403000046.0141

SAMSUNG EX. 1002 - 1184/4148

[65] R. S. Wagner, in *Whisker Technology*, edited by A. P. Levitt (Wiley-Interscience, New York, 1970).

[66] H. Wang and G. S. Fischman, J. Appl. Phys. **76**, 1557 (1994).

[67] A. W. Johnson, D. J. Ehrlich, and H. R. Schlossberg, eds., *Laser-Controlled Chemical Processing of Surfaces* (North-Holland, New York, 1984).

[68] R. Singh, D. Norton, L. Laude, J. Narayan, and J. Cheung, eds., *Advanced Laser Processing of Materials– Fundamentals and Applications* (Materials Research Society, Pittsburgh, 1996).

[69] R. K. Singh, D. H. Lowndes, D. B. Chrisey, E. Fogarassy, and J. Narayan, eds., *Advances in Laser Ablation of Materials* (Materials Research Society, Warrendale, 1998).

[70] D. B. Chrisey and G. K. Hubler, eds., *Pulsed Laser Deposition of Thin Films* (John Wiley and Sons, New York, 1994).

[71] A. Cavalleri, K. Sokolowski-Tinten, J. Bialkowski, M. Schreiner, and D. von der Linde, J. Appl. Phys. **85**, 3301 (1999).

[72] T. J. Chuang, in *Laser-Controlled Chemical Processing of Surfaces*, edited by A. W. Johnson, D. J. Ehrlich, and H. R. Schlossberg (North-Holland, New York, 1980).

[73] T. J. Chuang, Surface Science **178**, 763 (1986).

[74] D. J. Ehrlich and J. Y. Tsao, J. Vac. Sci. Technol. B **1**, 969 (1983).

[75] L. J. Stinson, J. A. Howard, and R. C. Neville, J. Electrochem. Soc. **123**, 551 (1976).

[76] M. Köhler, *Etching in Microsystem Technology* (Wiley-VCH, Weinheim, 1999).

SIONYX1403000046.0142

SAMSUNG EX. 1002 - 1185/4148

[77] T. J. Chuang, J. Chem. Phys. **72**, 6303 (1980).

[78] T. J. Chuang, J. Chem. Phys. **74**, 1453 (1981).

[79] T. Baller, D. J. Oostra, A. E. de Vries, and G. N. A. van Veen, J. Appl. Phys. **60**, 2321 (1986).

[80] Y. Horiike, M. Sekine, K. Horioka, T. Arikado, and H. Okano, *Extended abstracts of the 16th (1984 International) conference on solid state devices and materials* (Japan Soc. Appl. Phys., Tokyo, Japan, 1984).

[81] L.-C. Chen, in *Pulsed Laser Deposition of Thin Films*, edited by D. B. Chrisey and G. K. Hubler (John Wiley and Sons, New York, 1996).

[82] D. Lubben, S. A. Barnett, K. Suzuki, S. Gorbatkin, and J. E. Greene, J. Vac. Sci. Technol. B **3**, 968 (1985).

[83] M. Birnbaum, J. Appl. Phys. **36**, 3688 (1965).

[84] J. F. Young, J. E. Sipe, and H. M. van Driel, Phys. Rev. B **30**, 2001 (1984).

[85] J. E. Rothenberg and R. Kelly, Nucl. Instrum. Meth. Phys. Res. **B1**, 291 (1984).

[86] G. Herbst, M. Steiner, G. Marowsky, and E. Matthias, in *Advanced Laser Processing of Materials- Fundamentals and Applications*, edited by R. Singh, D. Norton, L. Laude, J. Narayan, and J. Cheung (Materials Research Society, Pittsburgh, 1996).

[87] S. M. Deliwala, *Time-resolved Studies of Molecular Dynamics Using Nano- and Femto-second Laser Pulses*, Ph.D. thesis, Harvard University (1995).

[88] T.-H. Her, *Femtochemistry at gas/solid interfaces*, Ph.D. thesis, Harvard University (1998).

SIONYX1403000046.0143

SAMSUNG EX. 1002 - 1186/4148

[89] F. Sanchez, J. L. Morenza, R. Aguiar, J. C. Delgado, and M. Varela, App. Phys. Lett. **69**, 620 (1996).

[90] F. Sanchez, J. L. Morenza, R. Aguiar, J. C. Delgado, and M. Varela, App. Phys. A **66**, 83 (1998).

[91] R. Kelly, J. J. Cuomo, P. A. Leary, J. E. Rothenberg, B. E. Braren, and C. F. Aliotta, Nucl. Instrum. Methods B **9**, 329 (1985).

[92] E. Chason, M. B. Sinclair, J. A. Floro, J. A. Hunter, and R. Q. Hwang, Appl. Phys. Lett. **72**, 3276 (1998).

[93] S. R. Folytn, R. C. Dye, K. C. Ott, E. Peterson, K. M. Hubbard, W. Hutchinson, R. E. Muenchausen, R. C. Estler, and X. D. Wu, Appl. Phys. Lett. **59**, 594 (1991).

[94] C. G. Bernhard, Endeavour **26**, 79 (1967).

[95] K. Noda, B. J. Glover, P. Linstead, and C. Martin, Nature **369**, 661 (1994).

[96] E. S. Kolesar, V. M. Bright, and D. Sowders, Thin Solid Films **270**, 10 (1995).

[97] E. S. Kolesar, V. M. Bright, and D. Sowders, Thin Solid Films **290-291**, 23 (1996).

[98] J. Zhao, A. Wang, M. Green, and F. Ferrazza, Appl. Phys. Lett. **73**, 1991 (1998).

[99] H. G. Craighead, R. E. Howard, and D. M. Tennant, Appl. Phys. Lett. **37**, 653 (1980).

[100] J. I. Gittleman, E. K. Sichel, H. W. Lehmann, and R. Widmer, Appl. Phys. Lett. **35**, 742 (1979).

SIONYX1403000046.0144

SAMSUNG EX. 1002 - 1187/4148

[101] E. Chen and S. Chou, Appl. Phys. Lett. **70**, 753 (1980).

[102] J. P. Zheng, K. L. Jiao, W. P. Shen, W. A. Anderson, and H. S. Kwok, Appl. Phys. Lett **61**, 459 (1992).

[103] M. J. Keevers and M. A. Green, J. Appl. Phys. **75**, 4022 (1994).

[104] M. Wolf, Proc. IRE **48**, 1246 (1960).

[105] M. J. Keevers and M. A. Green, Solar Energy Materials and Solar Cells **41/42**, 195 (1996).

[106] M. J. Keevers, F. W. Saris, G. C. Zhang, J. Zhao, M. A. Green, and R. Elliman, in *13th European Photovoltaic Solar Energy Conference: Proceedings of the International Conference, held at Nice, France, 23-27 October, 1995* (1995), p. 1215.

[107] A. Goetzberger, J. Knobloch, and B. Voss, *Crystalline Silicon Solar Cells* (Wiley, Chichester, 1998).

[108] E. Janzén, R. Stedman, G. Grossmann, and H. G. Grimmeiss, Phys. Rev. B **29**, 1907 (1984).

[109] A. L. Fahrenbruch and R. H. Bube, *Fundamentals of Solar Cells: Photovoltaic Solar Energy Conversion* (Academic Press, New York, 1983).

[110] D. M. Chapin, C. S. Fuller, and G. L. Pearson, J. Appl. Phys. **25**, 676 (1954).

[111] *http://www.nrel.gov.*

[112] J. A. Mazer, *Solar Cells: An Introduction to Crystalline Photovoltaic Technology* (Kluwer Academic Publishers, Boston, 1997).

[113] B. Rech and H. Wagner, Appl. Phys. A **69**, 155 (1999).

SIONYX1403000046.0145

SAMSUNG EX. 1002 - 1188/4148

[114] S. J. Fonash, *Solar Cell Device Physics* (Academic Press, New York, 1981).

[115] J. Knobloch, S. W. Glunz, D. Biro, W. Warta, E. Schaffer, and W. Wettling, in *Proc. 25th IEEE PV Spec. Conf.* (1996), p. 405.

[116] M.-K. Lee, C.-H. Chu, Y.-H. Wang, and S. M. Sze, Opt. Lett. **26**, 160 (2001).

[117] R. Gomer, *Field Emission and Field Ionization*, vol. 9 of *Harvard Monographs in Applied Science* (Harvard University Press, Cambridge, Massachusetts, 1961).

[118] J. D. Jackson, *Classical Electrodynamics* (John Wiley and Sons, New York, 1975).

[119] P. R. Schwoebel and I. Brodie, J. Vac. Sci. Technol. B **13**, 1391 (1995).

[120] R. H. Fowler and L. W. Nordheim, Proc. Roy. Soc. (London) A **119**, 173 (1928).

[121] S. E. Huq, P. D. Prewett, J. C. She, S. Z. Deng, and N. S. Xu, Materials Science and Engineering **B74**, 184 (2000).

[122] D. Temple, W. D. Palmer, L. N. Yadon, J. E. Mancusi, D. Vellenga, and G. E. McGuire, J. Vac. Sci. Technol. A **16**, 1980 (1998).

[123] I. Brodie and P. Schwoebel, Proc. IEEE **82**, 1006 (1994).

[124] K. L. Jensen, Physics of Plasmas **6**, 2241 (1999).

[125] D. Temple, Materials Science and Engineering **R24**, 185 (1999).

[126] A. Gorecka-Drzazga, J. Dziuban, and E. Prociow, J. Vac. Sci. Technol. B **18**, 1115 (2000).

[127] J. Liu, U. T. Son, A. N. Stepanova, K. N. Christensen, G. J. Wojak, E. I. Givargizov, K. J. Bachmann, and J. J. Hren, J. Vac. Sci. Technol. B **12**, 717 (1994).

SIONYX1403000046.0146

SAMSUNG EX. 1002 - 1189/4148

[128] M. J. Bozack, W. J. Choyke, L. Muehlhoff, and J. T. Yates, Jr., Surface Science **176**, 547 (1986).

[129] M. J. Bozack, P. A. Taylor, W. J. Choyke, and J. T. Yates, Jr., Surface Science **177**, L933 (1986).

SIONYX1403000046.0147

SAMSUNG EX. 1002 - 1190/4148

C26

JOURNAL OF APPLIED PHYSICS VOLUME 93, NUMBER 5 1 MARCH 2003

Infrared absorption by conical silicon microstructures made in a variety of background gases using femtosecond-laser pulses

R. Younkin, J. E. Carey, and E. Mazur[a)]
Harvard University, Department of Physics and Division of Engineering and Applied Science, 9 Oxford Street, Cambridge, Massachusetts, 02138

J. A. Levinson and C. M. Friend
Harvard University, Department of Chemistry, 12 Oxford Street, Cambridge, Massachusetts 02138

(Received 7 March 2002; accepted 16 December 2002)

We show that the near-unity infrared absorptance of conical microstructures fabricated by irradiating a Si(111) surface with 100 fs laser pulses depends on the ambient gas in which the structures are formed. SF_6 produces an absorptance of 0.9 for radiation in the 1.2–2.5 μm wavelength range, higher than any of the other gases. Use of Cl_2, N_2, or air produces surfaces with absorptances intermediate between that for microstructures formed in SF_6 and that for flat crystalline silicon, for which the absorptance is roughly 0.05–0.2 for a 260 μm thick sample. Secondary ion mass spectrometry shows that elements from the ambient gas are incorporated into the silicon surface in high concentration. © *2003 American Institute of Physics.* [DOI: 10.1063/1.1545159]

I. INTRODUCTION

We recently reported the formation of regular, sharply peaked, conical microstructures on the surface of silicon when it is irradiated with 100 fs laser pulses in the presence of halogen-containing gases.[1–3] Similar structures are also created using longer-duration pulses and a variety of background gases.[4–7] We observed the formation of microstructures upon irradiation with 100 fs laser pulses using nonhalogen-containing gases, such as N_2 or air, but these structures tend to be more blunt and irregular in shape. Such differences in the nature of the microstructures can be expected to alter the physical, chemical, and electronic properties of the surface.

These conical microstructures are interesting for a variety of reasons: They demonstrate a process for self-organized surface modification, and they suggest an interaction between ultrashort laser pulses and a semiconductor surface. They also absorb infrared light far more effectively than unpatterned silicon.[3] Crystalline silicon has a band gap corresponding to light with a wavelength of approximately 1.1 μm, making it unsuitable for detectors or other optoelectronic devices requiring the absorption of infrared light with a wavelength longer than 1.1 μm and the generation of infrared photocurrent. The enhancement of infrared absorption in silicon represents a critical first step toward the design of infrared detectors, solar cells, or other infrared devices fabricated with silicon.

II. EXPERIMENT

In this article, we describe the optical properties of conical microstructures formed on the surface of *n*-type Si(111) (260 μm thick, resistivity $\rho = 8 - 12\,\Omega$ m) in SF_6, Cl_2, N_2, and air upon irradiation with trains of 100 fs laser pulses with a wavelength of 800 nm. The microstructures are 1–10 μm wide at the top, with a height in the range of 1–20 μm, depending on the pressure of the ambient gas and the laser fluence. In each experiment described here, the background pressure of the ambient gas is 500 Torr. The peak laser fluence is 11 mJ/mm^2 for a laser beam with a diameter of approximately 150 μm. In order to pattern areas larger than the beam size, the beam is rastered across the surface of the sample. The translation speed of the laser is 200–300 μm/s, and is adjusted to give structures of roughly the same height (10–15 μm) regardless of the ambient gas species used.

We measured the transmittance and reflectance of a patterned 10×10 mm^2 area using a spectrophotometer equipped with a spherical detector that integrates all transmitted or scattered light, depending on the placement of the sample. The reflectance (R) and transmittance (T) were then used to obtain the absorptance of the material: $A = 1 - R - T$.

In addition to the optical properties, we used secondary ion mass spectrometry to characterize the chemical species present at the surface of the structures formed in each of the four gases. Briefly, an energetic beam of ions is used to sputter secondary ions from a surface; the chemical composition of the sputtered material is then analyzed with mass spectrometry. To determine the chemical composition of each microstructured surface, the ratio of the mass spectrometry signal from a given chemical species to that of silicon is normalized using literature values for the relative sensitivity factor of each chemical species in a silicon matrix. The relative sensitivity factors are calculated with data taken from flat silicon surfaces, so the compositions reported are approximate due to the rough surface topology of the microstructured silicon.

III. RESULTS AND DISCUSSION

The morphology of the silicon microstructures depends on the gas in which they were formed (Fig. 1). Use of SF_6 or

a)Electronic mail: mazur@physics.harvard.edu

 © 2003 American Institute of Physics

SIONYX1403000046.0148

SAMSUNG EX. 1002 - 1191/4148

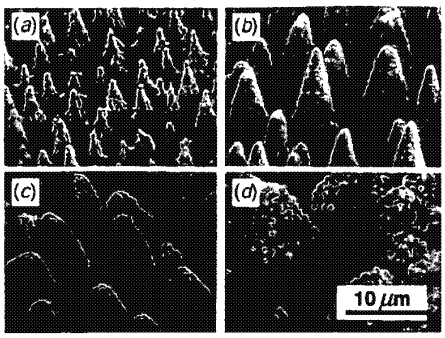


FIG. 1. Scanning electron micrograph of conical silicon microstructures formed in a background gas of (a) SF_6, (b) Cl_2, (c) N_2, and (d) air, upon irradiation with femtosecond laser pulses.

Cl_2 leads to conical structures with sharp tips with a radius of curvature of approximately 500 nm. In comparison to the Cl_2-prepared structures, the structures made in SF_6 have a greater degree of surface roughness, with a characteristic length scale of 100–200 nm for the dendritic formations on the cone surface. Structures made in air or N_2 are much more rounded than those made in the halogen-containing gases; their radius of curvature is approximately 2–3 μm. Additionally, the structures made in air show substantial surface roughness compared to the N_2-prepared structures; this roughness appears less dendritic than the formations on the SF_6-prepared cones. The number density of conical structures on the surface also depends on the ambient gas, with higher densities achieved using halogen-containing gases. Surfaces prepared with SF_6 yield the greatest number density, followed by Cl_2. The number densities obtained with N_2 and air are approximately half the density of the SF_6-prepared surfaces.

We observe a marked increase in the absorption of infrared light by patterned silicon surfaces compared to that of flat silicon. This is due to both a change in the reflectance of the surface and to a decrease in the transmittance through the patterned silicon sample. Figure 2 shows how the optical properties of the patterned silicon depend on the gas present during etching. The reflectance and transmittance change most dramatically for the structures formed in halogen-containing gases. For both SF_6- and Cl_2-prepared samples, the reflectance and transmittance are less than those for unpatterned silicon across the entire 1.2–2.5 μm wavelength range, with the reflectance and transmittance lowest for the surfaces prepared in SF_6. Samples made in air and N_2 show decreased transmittance relative to flat silicon as well as decreased reflectance in the short-wavelength region ($\lambda < 1.5\,\mu$m for air and $\lambda < 1.77\,\mu$m for N_2). Figure 3 shows the absorptance of the silicon samples, obtained from the reflection and transmission data, for structures made in the four gases. For all gases used, the drop in reflectance accounts for the increase in absorptance in the visible wavelength region. Although all samples show an increase in infrared absorption over ordinary crystalline silicon, the effect is strongest for structures formed in the presence of SF_6: The absorptance is approximately 0.9 in the wavelength region

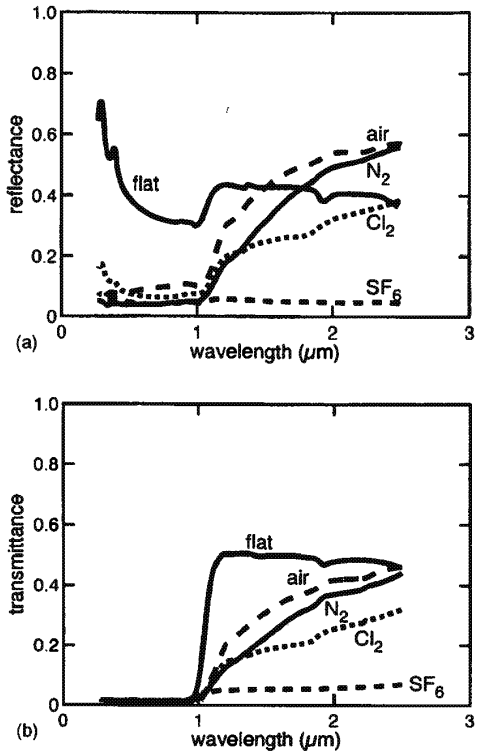


FIG. 2. Reflectance (a) and transmittance (b) of silicon samples patterned in various ambient gases (SF_6, Cl_2, N_2, and air) as a function of wavelength. Traces for flat Si(111) are included for reference. Surfaces structured in SF_6 differ most from the flat silicon.

1.2–2.5 μm. Structures made in Cl_2 show an absorptance of 0.3–0.9 in this wavelength region, while for unmodified silicon, the absorptance at these infrared wavelengths is less than 0.2. Surfaces structured in air or N_2 are less effective absorbers than those made in halogen-containing gases in the wavelength range $\lambda > 0.5\,\mu$m for air and $\lambda > 1.3\,\mu$m for N_2.

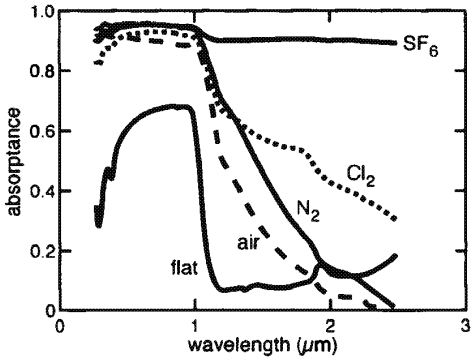


FIG. 3. Wavelength dependence of the optical absorptance of silicon surfaces for four different ambient gases present during the microstructure formation. The absorptance spectrum of an unmodified Si(111) surface is included for reference. Microstructured surfaces exhibit a marked increase in absorptance above the band edge of silicon ($\sim 1.1\,\mu$m).

SIONYX1403000046.0149

SAMSUNG EX. 1002 - 1192/4148

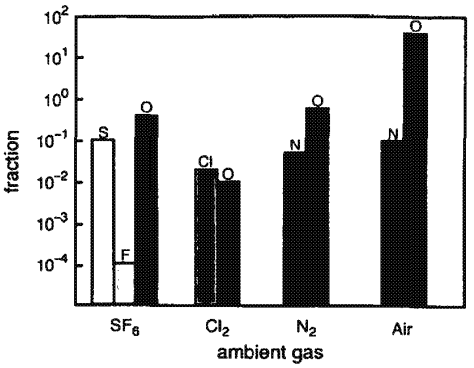


FIG. 4. Fractional concentrations of chemical species present in the surface of the microstructured silicon for each ambient gas (SF_6, Cl_2, N_2, and air). Oxygen is present in each sample due to a native oxide layer that grows after the structuring process. Each column is labeled at the top by the species it represents.

Furthermore, they show lower infrared absorptance than unmodified silicon for long wavelengths ($\lambda > 1.9\,\mu$m for air and $\lambda > 2.2\,\mu$m for N_2).

The differences in morphology of the structures made in various gases most likely stem from the relative reactivity of chemically reactive species created in those gases: It is well known that halogens create volatile compounds with silicon, whereas N_2 does not.[8] Therefore, the microstructures formed in SF_6 and Cl_2 share the same conical shape and those made in air or N_2 are more blunt and rounded.

Because the microstructures made in SF_6 and Cl_2 are very similar in shape and size, we attribute the different infrared absorptance of these surfaces to the introduction of impurities during irradiation. Secondary ion mass spectrometry shows that the elements of the ambient gas are incorporated into the surface of the silicon; different elements are incorporated to varying degrees. Figure 4 shows the fractional concentration of chemical species in the microstructured silicon surfaces. All of the samples contain oxygen from the native oxide layer that grows on the surface after texturing, but the air sample contains two orders of magnitude more oxygen than the other samples. The high oxygen content and further analysis using Rutherford backscattering and transmission electron microscopy suggests that we have formed a silicon rich layer of silica, SiO_x ($x<2$).[9] The amount of oxygen in the SF_6, Cl_2, and N_2 samples is correlated with surface roughness.

The secondary ion mass spectrometry measurements show that irradiation under these intense laser conditions incorporates high concentrations of elements from the ambient gas and surface oxide layer. Many groups use longer- pulse and continuous wave lasers to incorporate elements into silicon but the concentrations previously reported are orders of magnitude smaller than the concentrations we obtain with this method.[10–12]

After the sample is annealed in a vacuum, the sulfur signal in the secondary ion mass spectrometry measurement decreases by approximately a factor of 2 and fewer grains on the walls of the cones are present. At the same time, the absorptance in the 1.2–2.5 μm range decreases by approximately a factor of 2.[3] This result suggests that the sulfur impurities, whether in the cones themselves or in the rough features on the walls of the cones, play a role in the particularly high absorptance of the microstructures formed in SF_6.

The shape of the structures may also affect their absorptance. The conical microstructures made in the halogen-containing gases are sufficiently different from the round shapes of the structures formed in air or N_2 that their geometry can contribute to a higher absorptance. The surface topography may influence the absorptance through both the surface area of the patterned silicon, and the number of multiple reflections of light from the surfaces of the structures.

We recently demonstrated that the high absorptance of structures formed in SF_6 contributes to an increase of at least a factor of 3 in the production of photocurrent in the presence of infrared light ($\lambda = 1.064\,\mu$m and $\lambda = 1.310\,\mu$m) as compared to the photocurrent produced by flat silicon.[3] We are investigating the degree to which patterning in the presence of other gases leads to enhanced photocurrent of modified versus unmodified silicon surfaces.

In conclusion, we have demonstrated that the optical properties of silicon surfaces patterned with ultrashort laser pulses depend significantly on the background gas in which the surfaces are irradiated. Impurities introduced during irradiation are most likely the major contributor to the enhanced infrared absorptance. The shapes of the surface microstructures varies from cone-shaped for a halogen-containing background gas to rounded for air or N_2 and may contribute to the differences in absorptance. We are currently investigating how underlying defect structures depend on the background gas with cross-sectional transmission electron microscopy.

ACKNOWLEDGMENTS

This work was supported by the U. S. Army Research Office (DAAD19-99-1-0009) and by the NSF (DMR-98-09363). One of the authors (J.E.C.) acknowledges a fellowship from the NDSEG. The authors are grateful to Professor Michael J. Aziz for helpful discussions and Tom Mates for carrying out the secondary ion mass spectrometry measurements.

[1] T. H. Her, R. J. Finlay, C. Wu, S. Deliwala, and E. Mazur, Appl. Phys. Lett. **73**, 1673 (1998).
[2] T. H. Her, R. J. Finlay, C. Wu, and E. Mazur, Appl. Phys. A: Mater. Sci. Process. **70**, 383 (2000).
[3] C. Wu, C. H. Crouch, L. Zhao, J. E. Carey, R. Younkin, J. A. Levinson, E. Mazur, R. M. Farrell, P. Gothoskar, and A. Karger, Appl. Phys. Lett. **78**, 1850 (2001).
[4] F. Sanchez, J. L. Morenza, R. Aguiar, J. C. Delgado, and M. Varela, Appl. Phys. Lett. **69**, 620 (1996).
[5] A. J. Pedraza, J. D. Fowlkes, and D. H. Lowndes, Appl. Phys. Lett. **77**, 3018 (2000).
[6] A. J. Pedraza, J. D. Fowlkes, S. Jesse, C. Mao, and D. H. Lowndes, Appl. Surf. Sci. **168**, 251 (2000).
[7] A. J. Pedraza, J. D. Fowlkes, and D. H. Lowndes, Appl. Phys. Lett. **74**, 2322 (1999).
[8] See, for example, discussions in M. Köhler, *Etching in Microsystem Technology* (Wiley, New York, 1999).

SIONYX1403000046.0150

SAMSUNG EX. 1002 - 1193/4148

[9] C. Wu, C. H. Crouch, L. Zhao, and E. Mazur, Appl. Phys. Lett. **81**, 1999 (2002).
[10] D. Dimova-Malinovska, M. Tzolov, N. Malinowski, T. Marinova, and V. Krastev, Appl. Surf. Sci. **96**, 457 (1996).
[11] A. Pokhmurska, O. Bonchik, S. Kiyak, G. Savitski, and A. Gloskovsky, Appl. Surf. Sci. **154**, 712 (2000).
[12] Y. Hatanaka, M. Niraula, A. Nakamura, and T. Aoki, Appl. Surf. Sci. **175**, 462 (2001).

SIONYX1403000046.0151

SAMSUNG EX. 1002 - 1194/4148

Infrared absorption by conical silicon microstructures made in a variety of background gases using femtosecond-laser pulses

R. Younkin, J. E. Carey, and E. Mazur[a)]
Harvard University, Department of Physics and Division of Engineering and Applied Science, 9 Oxford Street, Cambridge, Massachusetts, 02138

J. A. Levinson and C. M. Friend
Harvard University, Department of Chemistry, 12 Oxford Street, Cambridge, Massachusetts 02138

(Received 7 March 2002; accepted 16 December 2002)

We show that the near-unity infrared absorptance of conical microstructures fabricated by irradiating a Si(111) surface with 100 fs laser pulses depends on the ambient gas in which the structures are formed. SF_6 produces an absorptance of 0.9 for radiation in the 1.2–2.5 μm wavelength range, higher than any of the other gases. Use of Cl_2, N_2, or air produces surfaces with absorptances intermediate between that for microstructures formed in SF_6 and that for flat crystalline silicon, for which the absorptance is roughly 0.05–0.2 for a 260 μm thick sample. Secondary ion mass spectrometry shows that elements from the ambient gas are incorporated into the silicon surface in high concentration. © *2003 American Institute of Physics.* [DOI: 10.1063/1.1545159]

I. INTRODUCTION

We recently reported the formation of regular, sharply peaked, conical microstructures on the surface of silicon when it is irradiated with 100 fs laser pulses in the presence of halogen-containing gases.[1–3] Similar structures are also created using longer-duration pulses and a variety of background gases.[4–7] We observed the formation of microstructures upon irradiation with 100 fs laser pulses using nonhalogen-containing gases, such as N_2 or air, but these structures tend to be more blunt and irregular in shape. Such differences in the nature of the microstructures can be expected to alter the physical, chemical, and electronic properties of the surface.

These conical microstructures are interesting for a variety of reasons: They demonstrate a process for self-organized surface modification, and they suggest an interaction between ultrashort laser pulses and a semiconductor surface. They also absorb infrared light far more effectively than unpatterned silicon.[3] Crystalline silicon has a band gap corresponding to light with a wavelength of approximately 1.1 μm, making it unsuitable for detectors or other optoelectronic devices requiring the absorption of infrared light with a wavelength longer than 1.1 μm and the generation of infrared photocurrent. The enhancement of infrared absorption in silicon represents a critical first step toward the design of infrared detectors, solar cells, or other infrared devices fabricated with silicon.

II. EXPERIMENT

In this article, we describe the optical properties of conical microstructures formed on the surface of n-type Si(111) (260 μm thick, resistivity $\rho = 8-12\,\Omega$ m) in SF_6, Cl_2, N_2, and air upon irradiation with trains of 100 fs laser pulses with a wavelength of 800 nm. The microstructures are 1–10 μm wide at the top, with a height in the range of 1–20 μm, depending on the pressure of the ambient gas and the laser fluence. In each experiment described here, the background pressure of the ambient gas is 500 Torr. The peak laser fluence is 11 mJ/mm^2 for a laser beam with a diameter of approximately 150 μm. In order to pattern areas larger than the beam size, the beam is rastered across the surface of the sample. The translation speed of the laser is 200–300 μm/s, and is adjusted to give structures of roughly the same height (10–15 μm) regardless of the ambient gas species used.

We measured the transmittance and reflectance of a patterned 10×10 mm^2 area using a spectrophotometer equipped with a spherical detector that integrates all transmitted or scattered light, depending on the placement of the sample. The reflectance (R) and transmittance (T) were then used to obtain the absorptance of the material: $A = 1-R-T$.

In addition to the optical properties, we used secondary ion mass spectrometry to characterize the chemical species present at the surface of the structures formed in each of the four gases. Briefly, an energetic beam of ions is used to sputter secondary ions from a surface; the chemical composition of the sputtered material is then analyzed with mass spectrometry. To determine the chemical composition of each microstructured surface, the ratio of the mass spectrometry signal from a given chemical species to that of silicon is normalized using literature values for the relative sensitivity factor of each chemical species in a silicon matrix. The relative sensitivity factors are calculated with data taken from flat silicon surfaces, so the compositions reported are approximate due to the rough surface topology of the microstructured silicon.

III. RESULTS AND DISCUSSION

The morphology of the silicon microstructures depends on the gas in which they were formed (Fig. 1). Use of SF_6 or

a)Electronic mail: mazur@physics.harvard.edu

 © 2003 American Institute of Physics

SIONYX1403000046.0152

SAMSUNG EX. 1002 - 1195/4148

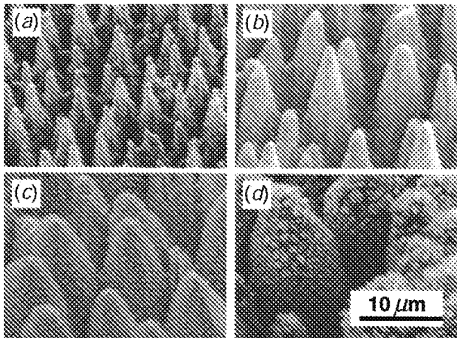


FIG. 1. Scanning electron micrograph of conical silicon microstructures formed in a background gas of (a) SF_6, (b) Cl_2, (c) N_2, and (d) air, upon irradiation with femtosecond laser pulses.

Cl_2 leads to conical structures with sharp tips with a radius of curvature of approximately 500 nm. In comparison to the Cl_2-prepared structures, the structures made in SF_6 have a greater degree of surface roughness, with a characteristic length scale of 100–200 nm for the dendritic formations on the cone surface. Structures made in air or N_2 are much more rounded than those made in the halogen-containing gases; their radius of curvature is approximately 2–3 μm. Additionally, the structures made in air show substantial surface roughness compared to the N_2-prepared structures; this roughness appears less dendritic than the formations on the SF_6-prepared cones. The number density of conical structures on the surface also depends on the ambient gas, with higher densities achieved using halogen-containing gases. Surfaces prepared with SF_6 yield the greatest number density, followed by Cl_2. The number densities obtained with N_2 and air are approximately half the density of the SF_6-prepared surfaces.

We observe a marked increase in the absorption of infrared light by patterned silicon surfaces compared to that of flat silicon. This is due to both a change in the reflectance of the surface and to a decrease in the transmittance through the patterned silicon sample. Figure 2 shows how the optical properties of the patterned silicon depend on the gas present during etching. The reflectance and transmittance change most dramatically for the structures formed in halogen-containing gases. For both SF_6- and Cl_2-prepared samples, the reflectance and transmittance are less than those for unpatterned silicon across the entire 1.2–2.5 μm wavelength range, with the reflectance and transmittance lowest for the surfaces prepared in SF_6. Samples made in air and N_2 show decreased transmittance relative to flat silicon as well as decreased reflectance in the short-wavelength region ($\lambda < 1.5\ \mu$m for air and $\lambda < 1.77\ \mu$m for N_2). Figure 3 shows the absorptance of the silicon samples, obtained from the reflection and transmission data, for structures made in the four gases. For all gases used, the drop in reflectance accounts for the increase in absorptance in the visible wavelength region. Although all samples show an increase in infrared absorption over ordinary crystalline silicon, the effect is strongest for structures formed in the presence of SF_6: The absorptance is approximately 0.9 in the wavelength region

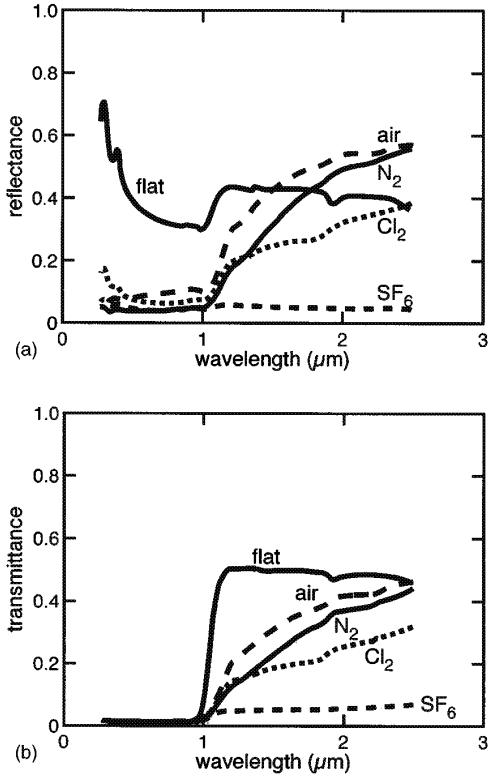


FIG. 2. Reflectance (a) and transmittance (b) of silicon samples patterned in various ambient gases (SF_6, Cl_2, N_2, and air) as a function of wavelength. Traces for flat Si(111) are included for reference. Surfaces structured in SF_6 differ most from the flat silicon.

1.2–2.5 μm. Structures made in Cl_2 show an absorptance of 0.3–0.9 in this wavelength region, while for unmodified silicon, the absorptance at these infrared wavelengths is less than 0.2. Surfaces structured in air or N_2 are less effective absorbers than those made in halogen-containing gases in the wavelength range $\lambda > 0.5\ \mu$m for air and $\lambda > 1.3\ \mu$m for N_2.

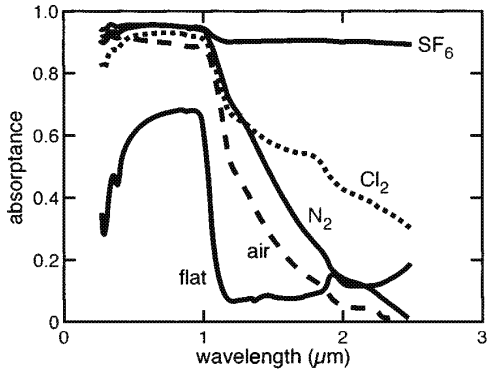


FIG. 3. Wavelength dependence of the optical absorptance of silicon surfaces for four different ambient gases present during the microstructure formation. The absorptance spectrum of an unmodified Si(111) surface is included for reference. Microstructured surfaces exhibit a marked increase in absorptance above the band edge of silicon ($\sim 1.1\ \mu$m).

SIONYX1403000046.0153

SAMSUNG EX. 1002 - 1196/4148

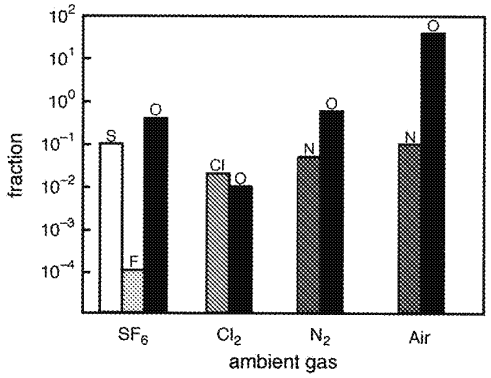


FIG. 4. Fractional concentrations of chemical species present in the surface of the microstructured silicon for each ambient gas (SF_6, Cl_2, N_2, and air). Oxygen is present in each sample due to a native oxide layer that grows after the structuring process. Each column is labeled at the top by the species it represents.

Furthermore, they show lower infrared absorptance than unmodified silicon for long wavelengths ($\lambda > 1.9\,\mu$m for air and $\lambda > 2.2\,\mu$m for N_2).

The differences in morphology of the structures made in various gases most likely stem from the relative reactivity of chemically reactive species created in those gases: It is well known that halogens create volatile compounds with silicon, whereas N_2 does not.[8] Therefore, the microstructures formed in SF_6 and Cl_2 share the same conical shape and those made in air or N_2 are more blunt and rounded.

Because the microstructures made in SF_6 and Cl_2 are very similar in shape and size, we attribute the different infrared absorptance of these surfaces to the introduction of impurities during irradiation. Secondary ion mass spectrometry shows that the elements of the ambient gas are incorporated into the surface of the silicon; different elements are incorporated to varying degrees. Figure 4 shows the fractional concentration of chemical species in the microstructured silicon surfaces. All of the samples contain oxygen from the native oxide layer that grows on the surface after texturing, but the air sample contains two orders of magnitude more oxygen than the other samples. The high oxygen content and further analysis using Rutherford backscattering and transmission electron microscopy suggests that we have formed a silicon rich layer of silica, SiO_x ($x < 2$).[9] The amount of oxygen in the SF_6, Cl_2, and N_2 samples is correlated with surface roughness.

The secondary ion mass spectrometry measurements show that irradiation under these intense laser conditions incorporates high concentrations of elements from the ambient gas and surface oxide layer. Many groups use longer- pulse and continuous wave lasers to incorporate elements into silicon but the concentrations previously reported are orders of magnitude smaller than the concentrations we obtain with this method.[10–12]

After the sample is annealed in a vacuum, the sulfur signal in the secondary ion mass spectrometry measurement decreases by approximately a factor of 2 and fewer grains on the walls of the cones are present. At the same time, the absorptance in the 1.2–2.5 μm range decreases by approximately a factor of 2.[3] This result suggests that the sulfur impurities, whether in the cones themselves or in the rough features on the walls of the cones, play a role in the particularly high absorptance of the microstructures formed in SF_6.

The shape of the structures may also affect their absorptance. The conical microstructures made in the halogen-containing gases are sufficiently different from the round shapes of the structures formed in air or N_2 that their geometry can contribute to a higher absorptance. The surface topography may influence the absorptance through both the surface area of the patterned silicon, and the number of multiple reflections of light from the surfaces of the structures.

We recently demonstrated that the high absorptance of structures formed in SF_6 contributes to an increase of at least a factor of 3 in the production of photocurrent in the presence of infrared light ($\lambda = 1.064\,\mu$m and $\lambda = 1.310\,\mu$m) as compared to the photocurrent produced by flat silicon.[3] We are investigating the degree to which patterning in the presence of other gases leads to enhanced photocurrent of modified versus unmodified silicon surfaces.

In conclusion, we have demonstrated that the optical properties of silicon surfaces patterned with ultrashort laser pulses depend significantly on the background gas in which the surfaces are irradiated. Impurities introduced during irradiation are most likely the major contributor to the enhanced infrared absorptance. The shapes of the surface microstructures varies from cone-shaped for a halogen-containing background gas to rounded for air or N_2 and may contribute to the differences in absorptance. We are currently investigating how underlying defect structures depend on the background gas with cross-sectional transmission electron microscopy.

ACKNOWLEDGMENTS

This work was supported by the U. S. Army Research Office (DAAD19-99-1-0009) and by the NSF (DMR-98-09363). One of the authors (J.E.C.) acknowledges a fellowship from the NDSEG. The authors are grateful to Professor Michael J. Aziz for helpful discussions and Tom Mates for carrying out the secondary ion mass spectrometry measurements.

[1] T. H. Her, R. J. Finlay, C. Wu, S. Deliwala, and E. Mazur, Appl. Phys. Lett. **73**, 1673 (1998).
[2] T. H. Her, R. J. Finlay, C. Wu, and E. Mazur, Appl. Phys. A: Mater. Sci. Process. **70**, 383 (2000).
[3] C. Wu, C. H. Crouch, L. Zhao, J. E. Carey, R. Younkin, J. A. Levinson, E. Mazur, R. M. Farrell, P. Gothoskar, and A. Karger, Appl. Phys. Lett. **78**, 1850 (2001).
[4] F. Sanchez, J. L. Morenza, R. Aguiar, J. C. Delgado, and M. Varela, Appl. Phys. Lett. **69**, 620 (1996).
[5] A. J. Pedraza, J. D. Fowlkes, and D. H. Lowndes, Appl. Phys. Lett. **77**, 3018 (2000).
[6] A. J. Pedraza. J. D. Fowlkes, S. Jesse, C. Mao, and D. H. Lowndes, Appl. Surf. Sci. **168**, 251 (2000).
[7] A. J. Pedraza, J. D. Fowlkes, and D. H. Lowndes, Appl. Phys. Lett. **74**, 2322 (1999).
[8] See, for example, discussions in M. Köhler, *Etching in Microsystem Technology* (Wiley, New York, 1999).

SIONYX1403000046.0154

SAMSUNG EX. 1002 - 1197/4148

[9] C. Wu, C. H. Crouch, L. Zhao, and E. Mazur, Appl. Phys. Lett. **81**, 1999 (2002).
[10] D. Dimova-Malinovska, M. Tzolov, N. Malinowski, T. Marinova, and V. Krastev, Appl. Surf. Sci. **96**, 457 (1996).
[11] A. Pokhmurska, O. Bonchik, S. Kiyak, G. Savitski, and A. Gloskovsky, Appl. Surf. Sci. **154**, 712 (2000).
[12] Y. Hatanaka, M. Niraula, A. Nakamura, and T. Aoki, Appl. Surf. Sci. **175**, 462 (2001).

SIONYX1403000046.0155

SAMSUNG EX. 1002 - 1198/4148

Efficient black silicon solar cell with a density-graded nanoporous surface: Optical properties, performance limitations, and design rules

Hao-Chih Yuan,[a)] Vernon E. Yost, Matthew R. Page, Paul Stradins, Daniel L. Meier,[b)] and Howard M. Branz
National Renewable Energy Laboratory, Golden, Colorado 80401, USA

(Received 3 August 2009; accepted 27 August 2009; published online 22 September 2009)

We study optical effects and factors limiting performance of our confirmed 16.8% efficiency "black silicon" solar cells. The cells incorporate density-graded nanoporous surface layers made by a one-step nanoparticle-catalyzed etch and reflect less than 3% of the solar spectrum, with no conventional antireflection coating. The cells are limited by recombination in the nanoporous layer which decreases short-wavelength spectral response. The optimum density-graded layer depth is then a compromise between reflectance reduction and recombination loss. Finally, we propose universal design rules for high-efficiency solar cells based on density-graded surfaces. © *2009 American Institute of Physics*. [doi:10.1063/1.3231438]

Low surface reflectance (R) of solar cells and detectors is needed to maximize the number of incident photons absorbed by the semiconductor that converts light to electrical energy. R is normally reduced in crystal Si and other solar cells with a quarter-wavelength antireflection (AR) coating applied to the top surface, although multilayer coatings have also been used to broaden the spectral width of the AR. Such AR coatings function by destructive interference of reflected waves and therefore normally have a narrow acceptance angle for AR at a given wavelength.

A density-graded surface layer can also suppress surface reflection and could replace conventional AR interference layers in Si solar cells, detectors and other photosensitive devices.[1] Such density-graded Si layers, often termed "black silicon" (bSi), can be based on a randomly nanoporous morphology[2–6] or on a "moth-eye" texture[7,8] composed of nanoscale periodic structures. A density-graded surface suppresses R exponentially as the grade depth, d, increases;[1,2] for $d \sim 500$ nm, $R < 2\%$ across the portion of solar spectrum converted by Si solar cells. Since it is not based on interference, bSi has a broad AR acceptance angle.[1,6,8] Because of the density grade, light at near-normal incidence escapes a bSi surface with little internal reflection. As in mirages and density-graded optical fibers,[9] however, light with angles larger than the critical angle ($\Theta_c \sim 10–16°$ from normal) is total internally reflected at a bSi/air interface, exactly as from a planar Si/air interface.

Demonstrations of bSi solar cells with efficiencies ranging from 8.8% to 13.9% were reported[5,6,10] but no systematic investigation of loss mechanisms was undertaken. In this letter, we analyze the optical and optoelectronic properties of 16.8% Si solar cells with nanoporous bSi layers we fabricate using our recently reported[5] one-step nanoparticle-catalyzed liquid etch. The issues that limit the efficiency of our cells represent significant challenges for developing high-efficiency solar cells with density-graded AR by any technique in any semiconductor material. After describing our methods and results on bSi devices, we present design rules for incorporating density-graded AR in solar cells.

We fabricate optical test structures and solar cells on 300 μm p-type double-side polished float-zone Si (100) substrates with resistivity of 2.7 Ω-cm. We produce bSi surfaces of various grade depths by immersing the Si substrate in 0.4 mM $HAuCl_4$ solution, adding an equal quantity of $HF:H_2O_2:H_2O$ 1:5:2 mixture, and soaking the wafer in a sonication bath for times from 1 to 8 min. Increasing the bSi etch time (t_e) increases d. Au nanoparticles are produced in the mixture and they catalyze subsequent nanoporous Si etching.[5] This method produces "double-sided bSi;" we also prepare "one-sided bSi" by protecting the back side during the bSi etching.[11] Residual Au on the surface is removed after the etch by sonicating in I_2/KI solution; however, secondary ion mass spectrometry (SIMS) analysis shows mid-10^{18} cm^{-3} of residual Au in the nanoporous layer. The Au concentration falls below the SIMS detection threshold of $\sim 10^{15}$ cm^{-3} within 0.5–1.0 μm from the surface. Hemispheric total R (R_{tot}) and transmittance (T_{tot}) for normal incidence are measured on a Varian Cary 6000i spectrophotometer with an integrating sphere. The spectrometer also provides the normal transmittance (T_{norm}).

Figures 1(a) and 1(b) show the $t_e = 3$ min spectral dependences of T_{tot} and R_{tot} for one-sided and double-sided bSi, respectively, with schematic insets showing the most important reflected and transmitted light rays. For both samples, R_{tot} is below 3% from 350 to 1000 nm wavelength, confirming the good AR properties of bSi. Figure 1(a) shows that T_{hemi} of the one-sided bSi is lower than T_{tot} at weakly absorbed infrared (IR) wavelengths, indicating IR scattering in the top bSi surface (see inset). We also plot the transmission haze, $H_T = (T_{tot} - T_{norm})/T_{tot}$, with $H_T \sim 9\%$ at 1100 nm. About 90% of IR is transmitted through the back bSi/air interface [Fig. 1(b)] meaning that the scattering from the front must be mainly in the forward direction and within a cone defined by Θ_c.

Figure 2(a) and 2(b) show optical measurements on one-sided and double-sided bSi samples, respectively, at 1200 nm wavelength (where absorption is negligible), for $t_e = 0$ (planar) to 8 min. Figure 2(c) and 2(d) display cross-sectional scanning electron microscopy (XSEM) images after 3 and 6 min of bSi etching with $d \sim 500$ and 1000 nm, respectively.

a)Author to whom correspondence should be addressed. Electronic mail: hao-chih.yuan@nrel.gov.
b)Present address: Suniva Inc., Norcross, GA 30092, USA.

 © 2009 American Institute of Physics

SIONYX1403000046.0156

SAMSUNG EX. 1002 - 1199/4148

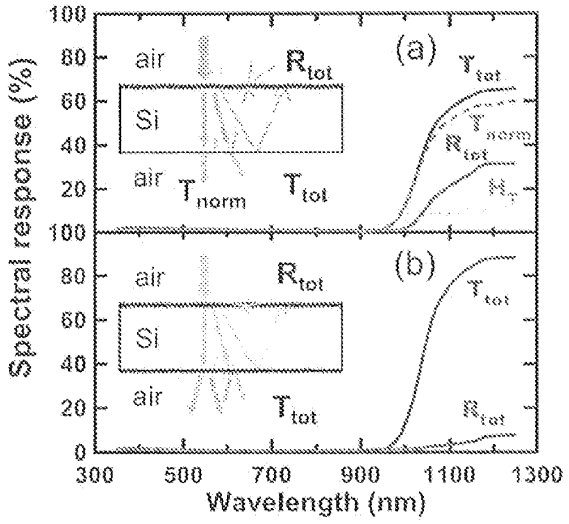


FIG. 1. (Color online) Spectral dependences of R and T for 3 min etched (a) one-sided and (b) double-sided bSi samples. Transmission haze (H_T) is also included in (a). The insets schematically show the main reflected and transmitted light paths.

Pixel-by-pixel computer analysis of a 3 min XSEM image shows a roughly linear grade in density, and therefore index of refraction. Images such as Figs. 2(c) and 2(d) show progressive development of larger lateral structures and etch-depth inhomogeneities with characteristic length scales reaching the IR wavelength in Si (~300 nm). These structures are presumably responsible for the increasing IR haze in Fig. 2(a) as t_e increases above 3 min. This IR scattering also increases R_{tot} with t_e in Figs. 2(a) and 2(b): there is progressively more back-scattering from the larger structures at the front bSi surface and also total internal reflection from the back due to the increasing fraction of light forward-scattered from the bSi front at angles greater than Θ_c. The low values of Θ_c in Si in combination with a diffuse back reflector are proven to lead to excellent light trapping in Si solar cells.[12] Therefore the bSi surface layer, with its total internal reflection, can provide efficient IR light trapping. As

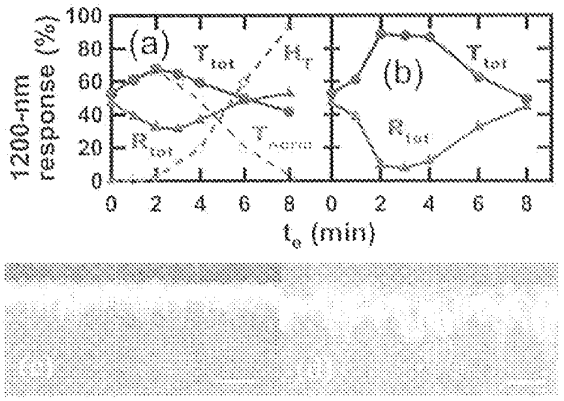


FIG. 2. (Color online) R and T at 1200 nm wavelength on (a) one-sided and (b) double-sided bSi samples, for black-etch times (t_e) from 0 (planar) to 8 min. Panels (c) and (d) present XSEM images of bSi surfaces with t_e=3 and 6 min, respectively. Scale bars are 500 nm.

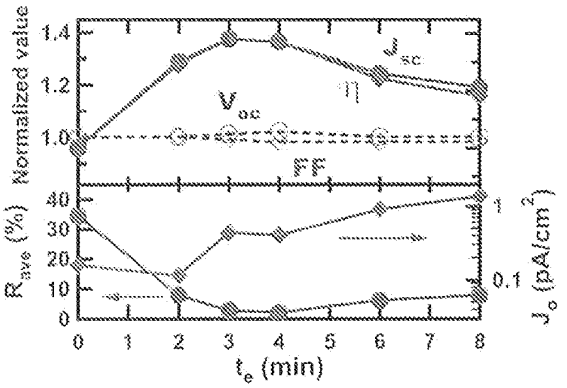


FIG. 3. (Color online) Performance comparison between planar (0 min etch) and bSi solar cells under 1-sun illumination, for black-etch times (t_e) up to 8 min.

a second-order effect, forward-scattering from inhomogeneities in the bSi layer may provide a photon path length increase that compensates for the escape through the graded-density front surface of the small amount of light reflecting from the diffuse back reflector at angles less than Θ_c.

We fabricate solar cells from one-sided bSi wafers and from double-side polished planar Si controls. We use standard processes to create a front phosphorous-diffused emitter and an Al back-surface field, as detailed in Ref. 11. A 20 nm thermal oxide is grown to passivate the black Si surface and improve blue response. We etch this oxide locally before evaporating a front metal grid. Illuminated current-voltage (IV) curves of photolithographically defined 1 cm^2 cells are measured with calibrated 1-sun simulators. Our best bSi solar cell is made with t_e=3 min and is independently confirmed at NREL to have efficiency (η) of 16.8%, with open-circuit voltage (V_{oc}) of 612 mV, short-circuit current (J_{sc}) of 34.1 mA/cm^2 and fill factor (FF) of 80.6%. This exceeds by 2.9% the highest previously reported efficiency of 13.9% for a Si solar cell[9] without any deposited AR coating.

Figure 3 shows the 1-sun IV parameters for bSi solar cells normalized to the planar control cell, the saturation current density (J_o) extracted from the illuminated IV,[13] and the average R weighted by solar photon flux (R_{ave}) from 350 to 1000 nm wavelength, versus t_e. All of our bSi solar cells have V_{oc} and FF comparable to the planar cell, suggesting little problem in making contact to the nanoporous top surface. The increase in J_o indicates increasing recombination in the thickening nanoporous layer.

Figure 4 shows the internal quantum efficiency (IQE) on planar, 3, 4, and 6 min etched bSi solar cells (lines) together with the results from our modeling with the one-dimensional device program PC1D (symbols). There is a reduction in bSi-cell IQE below ~700 nm wavelength and it worsens with increased t_e. Integration of the blue IQE loss for the 3 min bSi cell shows a J_{sc} loss of 3.6 mA/cm^2. However, the cell has R_{ave}=2.7%, corresponding to a loss of only ~1 mA/cm^2, less than conventional AR coatings. We were unable to model the IQE of the bSi cells with any combination of poor planar front-surface recombination velocity and reduced bulk lifetime. Instead, we model the IQE well by assuming that the bSi nanoporous layer acts as a low-lifetime "dead layer" which is thinner (Fig. 4 legend) than d. We

SIONYX1403000046.0157

SAMSUNG EX. 1002 - 1200/4148

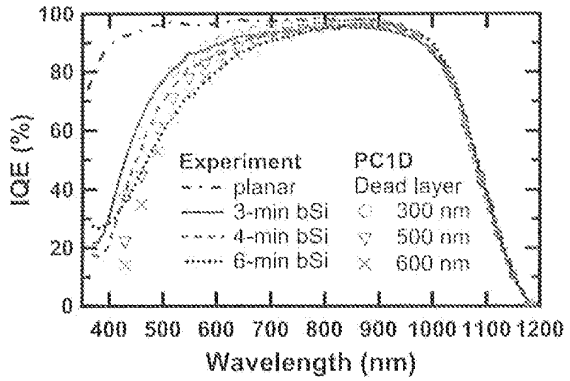


FIG. 4. (Color online) IQE of planar and bSi solar cells. Symbols show PC1D calculations of IQE assuming highly doped surface dead layers of the indicated thicknesses.

implement the nanoporous dead layers as a heavily doped Si (10^{20} cm^{-3} of P) with high Auger recombination. We attribute the dead layer to high doping concentration in the nanoporous layer and additional recombination at the enormous internal surface, perhaps exacerbated by residual Au contamination. Light scattering on the nanoporous layer may increase photon path lengths inside the dead layer and worsen IQE loss. The 4 min bSi cell has a better E_{ave} = 1.9%, but a thicker dead layer than the 3 min cell (Figs. 3 and 4). The ~500 nm nanoporous grade depth of our optimized 3 min bSi cell represents a compromise between AR and recombination. Figure 4 also shows that the IQE from 1000 to 1200 nm is not higher in the bSi than in the planar control, despite the forward-scattering of IR from our bSi surfaces. Our planar control and bSi cells all have Al-paste alloyed back surfaces that are normally effective light scatterers.[13] The effective diffuse reflection from the back side, together with excellent light trapping at the front Si/air interfaces, evidently results in little difference in IR optical path length between the two cells.

Our work leads us to suggest four design rules for solar cells based on nanostructured density-graded layers: (1) good AR requires a deep density grade depth, d. However, d must be kept as small as possible to avoid excess surface recombination in the nanoporous layer. (2) Increasing the characteristic nanoscale dimension, δ, (in this case, the pore diameter) reduces the surface area for dopant in-diffusion and for recombination because nanostructures of a given mass density have a surface area that scales as $1/\delta$. However, δ must be less than the smallest wavelength of light of interest so that the nanoporous layer acts as a laterally homogenous density-graded layer and minimizes back-scattering that increases R.[2] With $n \sim 6$ in Si in the 380–400 nm range, the nanoscale dimension should probably be less than ~60 nm. (3) The back-surface of the cell must reflect weakly absorbed light at angles greater than Θ_c to avoid the efficient escape of near-normal light from the density-graded front surface. (4) The method of fabricating the nanostructured density-graded layer must be inexpensive, such as our one-step liquid etch.

In summary, a simple, one-step, nanoparticle-catalyzed bSi etch can provide effective AR for efficient Si solar cells, without reducing V_{oc} or FF. The IQE falls significantly at short wavelength as the bSi etch time increases, due to high doping and/or surface recombination in the nanostructured density-graded layer. Although the density-graded layers provide little internal reflection of near-normal light, a diffuse back-reflector, scattering at bSi nanoporous surfaces, and total internal reflection from bSi above the critical angle leave the IR IQE little changed from a planar control. A 3 min bSi etch, producing a density grade about 500 nm deep, provides the best compromise between surface reflection and blue IQE loss; we fabricate a 16.8% Si solar cell without any deposited AR coating.

This work was supported by the U.S. Department of Energy under Grant No. DE-AC36-08GO28308. We thank Anna Duda, Lorenzo Roybal, Bobby To, Robert Reedy, and Paul Ciszek for cell fabrication and characterization assistance.

[1] R. B. Stephens and G. D. Cody, Thin Solid Films **45**, 19 (1977).
[2] H. M. Branz, V. E. Yost, S. Ward, K. M. Jones, B. To, and P. Stradins, Appl. Phys. Lett. **94**, 231121 (2009).
[3] M. Y. Stern, C. H. Crouch, J. E. Carey, and E. Mazur, Appl. Phys. Lett. **85**, 3694 (2004).
[4] X. Li and P. W. Bohn, Appl. Phys. Lett. **77**, 2572 (2000).
[5] L. Stalmans, J. Poortmans, H. Bender, M. Caymax, K. Said, E. Vazsonyi, J. Nijs, and R. Mertens, Prog. Photovoltaics **6**, 233 (1998).
[6] H. Sai, H. Fujii, K. Arafune, Y. Ohshita, Y. Kanamori, H. Yugami, and M. Yamaguchi, Jpn. J. Appl. Phys., Part 1 **46**, 3333 (2007).
[7] S. I. Wilson and M. C. Hurley, Opt. Acta **29**, 993 (1982).
[8] Z. Yu, H. Gao, W. Wu, H. Ge, and S. Y. Chou, J. Vac. Sci. Technol. B **21**, 2874 (2003).
[9] M. Young, *Optics and Lasers*, (Springer, Berlin, 1993), p. 261.
[10] S. M. Vernon, N. M. Kalkhoran, H. P. Maruska, and W. D. Halverson, Proceedings of the 24th IEEE Photovoltaic Specialist Conference, 5–9 December 1994 (unpublished), pp. 1583–1586; A. Krokas, K. Grigoras, V. Pacebutas, I. Barsony, E. Vazsonyi, M. Fried, J. Szlufcik, J. Nijs, and C. Levy-Clement, Sol. Energy Mater. Sol. Cells **45**, 267 (1997); S. Kayser, M. S. Brandt, and M. Stutzmann, Phys. Status Solidi: A **153** (2007).
[11] H.-C. Yuan, V. E. Yost, M. R. Page, J. Roybal, B. To, P. Stradins, D. L. Meier, and H. M. Branz, Proceedings of the 34th IEEE Photovoltaic Specialist Conference, 7–12 June 2009 (unpublished).
[12] A. Goetzberger, Conference Record of the 15th IEEE Photovoltaic Specialist Conference, May 1981, (unpublished), pp. 867–870.
[13] K.-I. Ishibashi, Y. Kimura, and M. Niwano, J. Appl. Phys. **103**, 094307 (2008).
[14] A. Rüstow, M. Hilali, A. Ebong, and A. Rohatgi, Proceedings of the 17th European Photovoltaic Solar energy Conference, Munich, Germany, October 2001, (unpublished), pp. 1335–1338.

SIONYX1403000046.0158

SAMSUNG EX. 1002 - 1201/4148

DIFFRACTION GRATING STRUCTURES IN SOLAR CELLS

Saleem H. Zaidi[1], James M. Gee[2], and Douglas S. Ruby[2]
[1]Gratings, Inc., Albuquerque, NM 87107
[2]Sandia National Laboratories, Albuquerque, NM 87185-0752

ABSTRACT

Sub-wavelength periodic texturing (gratings) of crystalline-silicon (c-Si) surfaces for solar cell applications can be designed for maximizing optical absorption in thin c-Si films. We have investigated c-Si grating structures using rigorous modeling, hemispherical reflectance, and internal quantum efficiency measurements. Model calculations predict almost ~ 100 % energy coupling into obliquely propagating diffraction orders. By fabrication and optical characterization of a wide range of 1D & 2D c-Si grating structures, we have achieved broadband, low (~ 5 %) reflectance without an anti-reflection film. By integrating grating structures into conventional solar cell designs, we have demonstrated short-circuit current density enhancements of 3.4 and 4.1 mA/cm^2 for rectangular and triangular 1D grating structures compared to planar controls. The effective path length enhancements due to these gratings were 2.2 and 1.7, respectively. Optimized 2D gratings are expected to have even better performance.

INTRODUCTION

In most c-Si photovoltaic modules, 50 % of the cost is associated with the c-Si wafer [1]. Therefore, a highly effective approach aimed at cost reduction in crystalline and multi-crystalline c-Si solar cells is better material utilization by using thinner (~ 1-20 μm) films. Reduced film thickness is also attractive due to lower bulk recombination and increased open-circuit voltages provided complete optical confinement can be achieved [2]. c-Si is strongly absorptive in the UV-visible spectral region. However, in near IR region (~ 0.8-1.1 μm) and particularly near the band edge, the absorption is weak; e.g. the absorption depth is ~ 100 μm at λ ~ 1 μm [3]. This weak absorption fundamentally limits the performance of thin-film c-Si solar cells. Surface texturing schemes aimed at enhancing near IR absorption by oblique optical coupling into the semiconductor have been extensively investigated [4]. Surface structuring schemes based on geometrical optics considerations may have limited applicability in thin films due to texture dimension approaching the film thickness.

A periodically textured surface such as a grating structure can be used to enhance absorption in thin films. Sheng, et al. first proposed this for thin film a-Si solar cells [5]. Using a waveguide configuration, it was shown that an appropriately designed grating structure can enhance short-circuit current by ~ 4-6 mA/cm^2 in comparison with a planar surface. Heine and Morf investigated diffraction gratings in c-Si solar cells [6]. In their scheme, grating structures were designed for optimum coupling into obliquely propagating diffraction orders inside the semiconductor material. Broadband anti-reflection characteristics of grating structures have also been extensively investigated [7].

Here, we report on an investigation of sub-micrometer c-Si grating structures by modeling, hemispherical reflectance, and internal quantum efficiency measurements. This investigation will help in optimizing grating structures aimed at maximizing optical absorption in thin-film c-Si solar cell devices.

MODELING OF GRATING STRUCTURES

Light interaction with a grating structure is a complex function of several parameters including incident wavelength, angle, polarization, period, profile, duty cycle, and depth [8]. For solar cell applications, the front-surface grating should be designed to enhance infrared absorption by efficiently coupling of light into the modes that propagate nearly parallel to the surface while minimizing coupling into the normally propagating zero-order mode. Using commercially available GSOLVER™ modeling software, we have investigated rectangular, triangular, and blazed grating structures.

Figure 1 is an example calculation. It shows the diffraction efficiency for both TE and TM-polarizations for normal incidence. The grating period was selected at 0.65 μm so that both first and second orders were propagating. Finer periods – e.g., d=0.32 μm, where only the two ±1-orders relatively weak energy coupling. For the TE-polarization, ~ 40% of the incident energy at 0.5 μm depth is coupled into the ±1-diffraction orders (propagating at ~ 30° with respect to the normal), and minimal energy is coupled into the ±2-diffraction orders (propagating at ~ 60° with respect to the normal). For TM-polarization, almost 80 % of the incident energy is coupled to the ±1 and ±2-diffraction orders. Similar calculations for triangular-profiled grating structure show that at TE-polarization, ~ 60% of incident energy is coupled into the ±1-diffraction orders and approximately 10% is coupled into the ±2-diffraction orders. At TM-polarization, ~ 80% of the energy is coupled into ±1-diffraction orders and ~ 10% into the ±2-diffraction orders. Finally, for the blazed grating profiles, nearly 100% of the incident energy is coupled into diffraction orders for the TE polarization. For TM-polarization, same behavior is seen with ~ 30% coupling into the +2-diffraction order. A comparison of the energy distribution

SIONYX1403000015.0001

SAMSUNG EX. 1002 - 1202/4148

among diffraction orders for the three profiles reveals that the blazed grating structure couples more energy into the transmitted diffraction orders, but that coupling into the second order is comparable for the three grating structures. The rectangular profile shows the least energy transfer into diffraction orders.

In general, our calculations show that high diffraction efficiencies can be achieved as long as the propagation angle is ≤ 60° with respect to the surface normal. For higher propagation angles, most of the energy is coupled back into the normally propagating zero-order modes.

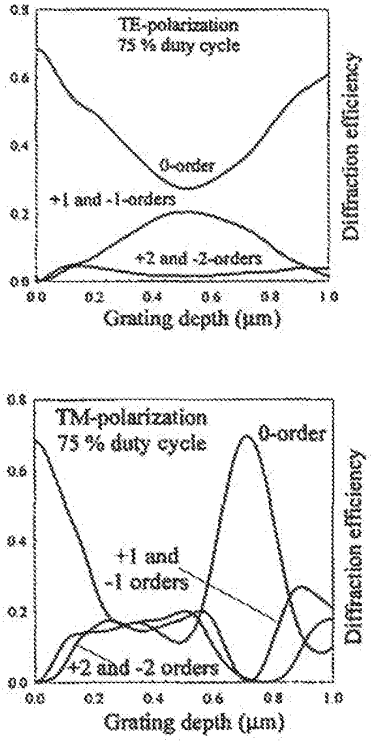


Figure 1. Diffraction efficiency calculations as a function of grating depth for symmetric rectangular profile grating structure at λ=1.0 μm.

FABRICATION OF GRATING STRUCTURES

We have developed low-cost, large-area interferometric lithography techniques to pattern a wide range of 1D and 2D periodic structures [9]. Interference between two coherent laser beams produces a simple periodic pattern at $d=\lambda/2\sin\theta$, where λ is the exposure wavelength, and 2θ is the angle between the two intersecting laser beams. For λ=355 nm, θ= 60°, periods down to ~ 200-nm can be easily fabricated. Typically, grating structures are first formed in photoresist followed by pattern transfer to c-Si using an appropriate combination of wet and dry etching techniques. Figure 2 shows scanning electron microscope pictures of 1D triangular and rectangular profile gratings, and a 2D hole pattern etched in c-Si using RIE and wet-chemical etching methods [10]. The triangular structure shown in Fig. 2 is characterized by period of ~ 420 nm with full width at half-maximum depth of ~ 100 nm etched to a depth of ~ 600 nm. The rectangular profile grating shown in Fig. 1 has a period of 500 nm, linewidth of ~ 130 nm, and depth of ~ 1000 nm. The 2D hole pattern at 800-nm period is has a linewidth ~ 270 nm and depth of ~ 800 nm.

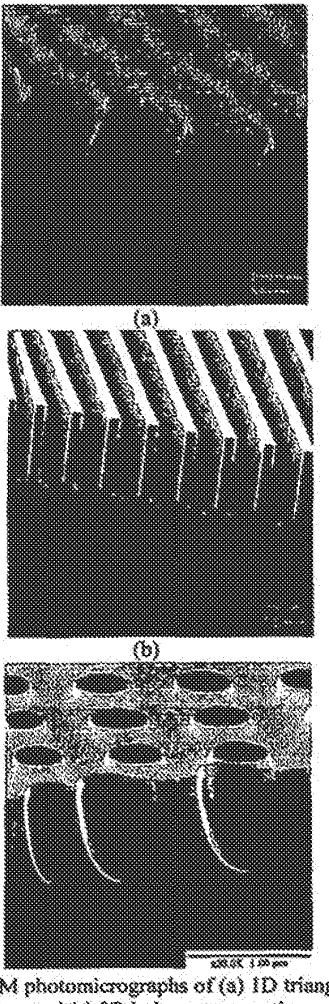


Figure 2. SEM photomicrographs of (a) 1D triangular, (b) 1D rectangular, and (c) 2D hole pattern grating.

Spectral reflectance measurements of grating structures were carried out using a Cary Model 5E (UV-VIS-NIR) spectrophotometer and a Labsphere (RSA-CA-

SAMSUNG EX. 1002 - 1203/4148

50) integrating sphere. Figure 3 shows absolute hemispherical reflectance measurements from grating structures shown in Fig. 2. It is seen that broadband reduced reflection is observed from the triangular grating profile. In contrast, the rectangular-profiled grating structure supports a number of narrow, low reflectance spectral bands. For the triangular profiles, the same broadband anti-reflection behavior is seen with both polarizations. For the rectangular profiles, these spectral bands are a critical function of the incident light polarization. For the 2D hole-pattern, a broadband anti-reflection behavior is observed. The reflection can be further reduced in all cases by application of anti-reflection films.

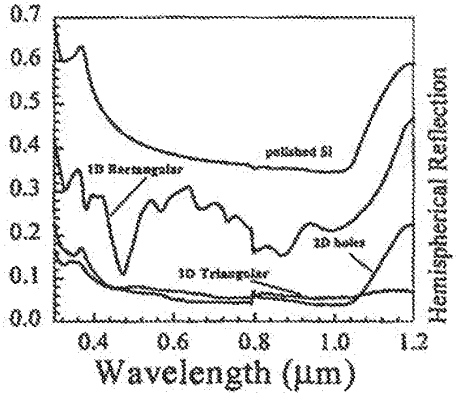


Figure 3. Hemispherical reflectance measurements from grating structures shown in Fig. 2. Reflectance from polished c-Si surface is shown for comparison.

INTERNAL QUANTUM EFFICIENCY MEASUREMENTS

Grating solar cells were fabricated on 4" diameter, p-type, 1 Ω-cm resistivity wafers at Sandia National Laboratories. Wafers were RIE textured with periodic patterns. The junction depth was ~ 0.5 μm on the planar region. A 10-nm thick passivating SiO_2 film was grown during back surface field formation at ~ 900 °C. For comparison, planar and grating regions of ~ 2x2 cm^2 were formed on each cell. Internal quantum efficiency measurements from planar and grating regions were acquired to understand the influence of grating structure on cell efficiency. The IQE measurements of triangular and rectangular profiled 1D gratings exhibited substantially reduced blue response. This was attributed to the lack of adequate passivation in the strongly absorptive grating region, and probably to some residual surface damage suffered from the RIE process. By incorporating RCA clean process prior to emitter formation, the blue response was significantly improved. Figure 4 shows the IQE response of a 1D rectangular profile grating structure. For comparison, the planar surface IQE adjacent to the grating is also plotted. It is seen that the grating structure cell still exhibits lower IQE in 0.4-0.6-μm spectral region presumably due to residual RIE-induced surface damage. The IQE response, however, is significantly enhanced in the long wavelength region. The surface reflectance has also been significantly reduced.

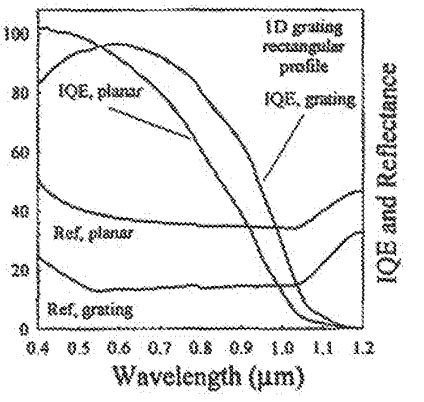


Figure 4. Internal quantum efficiency from 1D rectangular profile grating. For comparison, IQE response of planar surface is also shown.

Figure 5 shows similar IQE and reflectance measurements from a 1D triangular profiled grating structure. This grating structure exhibits slightly improved IQE response in the short wavelength region, but it is still lower than the planar surface. The enhancement in the long wavelength region is not as pronounced as for the rectangular profile.

We can eliminate the substrate variation by plotting IQE ratios from the grating and planar regions of the same wafer. Fig. 6 plots the IQE ratios for the rectangular and triangular profiled grating structures. It is seen that for the rectangular profile, the ratio is less than 1 for wavelengths < 0.55 μm, and the maximum enhancement of ~ 2.7 is observed at λ ~ 1.1 μm. For the triangular profile, the IQE ratio is less than 1 for wavelengths < 0.5 μm, while the maximum enhancement of ~ 1.6 is seen at λ ~ 1.1 μm. The IQE enhancement in the IR region can best be understood on the basis of the diffraction calculations presented earlier. The grating structure couples significant energy into the obliquely propagating diffraction orders inside c-Si. These transmitted diffraction orders generate electron-hole pairs closer to the surface, thus, enhancing the probability of collection by the junction.

ANALYSIS OF RESULTS

There is clearly an improvement in IQE due to the grating (Fig. 4-6). A convenient method to quantify

SAMSUNG EX. 1002 - 1204/4148

the effect of the grating alone on improving IQE is to analyze the inverse IQE versus absorption length [11]. The linear regime of this relationship in the near infrared region gives a measure of the internal collection length (L_{iqe} and Fig. 7). L_{iqe} is a function of the bulk material quality (e.g., bulk diffusion length) and the internal path length. Since the planar and grating regions were adjacent within the same cell and have very similar bulk properties, a ratio of L_{iqe} between the textured and planar regions gives the effective increase in path length due to the grating. We refer to "effective" path length enhancement since the generation profile with the grating is a combination of different modes traveling at different angles. The effective path length enhancement for the triangular and rectangular profiles is roughly 1.7 and 2.2, respectively. For comparison, the path length enhancement with chemically textured surfaces is around 1.3 since the light is coupled into the silicon at a well-defined angle [11].

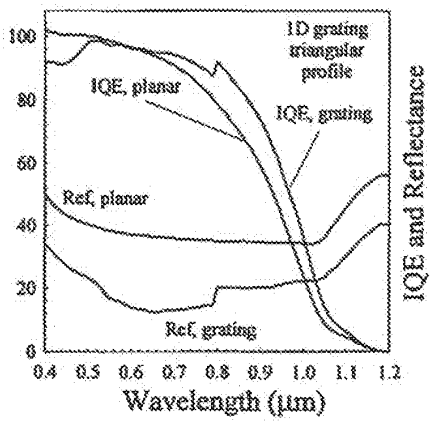


Figure 5. Internal quantum efficiency from 1D triangular profile grating. For comparison, IQE response of planar surface is also shown.

ACKNOWLEDGEMENTS

Gratings, Inc. was partially supported for this work by Sandia National Laboratories under contract BE8229. The authors would like to thank Samuel McCormack, Bev Silva, Jeannette Moore, and Barry Hansen for help with cell fabrication and measurements. Sandia National Laboratories is a multiprogram laboratory operated by Sandia Corporation, a Lockheed Martin Company, for the U. S. Department of Energy under contract DE-AC04-94AL85000.

REFERENCES

[1] A. Suzuki, M. Kaneiwa, T. Saga, and S. Matsuda, IEEE Trans. Elect. Dev., ED-46, 2126 (1999).
[2] T. Tiedje, E. Yablonovitch, G. D. Cody, and B. G. Brooks, IEEE Trans. Elect. Dev., ED-31, 711 (1984).
[3] M. A. Green and M. J. Keevers, Prog. in Photo. Research and Applications 3, 189 (1995).
[4] P. Campbell and M. A. Green, Appl. Phys. Lett. 62, 243 (1987).
[5] Ping Sheng, A. N. Bloch, and R. S. Stepleman, Appl. Phys. Lett. 43, 579 (1983).
[6] C. Heine and R. H. Morf, Appl. Opt. 34, 2476 (1995).
[7] D. H. Raguin and G. M. Morris, Appl. Opt. 32, 1154 (1993).
[8] S. Kemme, S.H. Zaidi, and J. M. Gee, 9th Workshop on c-Si Mat. and Proc., Breckenridge (1999).
[9] Saleem H. Zaidi and S. R. J. Brueck, J. Vac. Sci. Technol. B11, 458 (1993).
[10] Saleem H. Zaidi, An-Shyang Chu, and S. R. J. Brueck, J. Appl. Phys. 80, 6997 (1996).
[11] Paul A. Basore, 23rd IEEE Photo. Spec. Conf., 147 (1993).

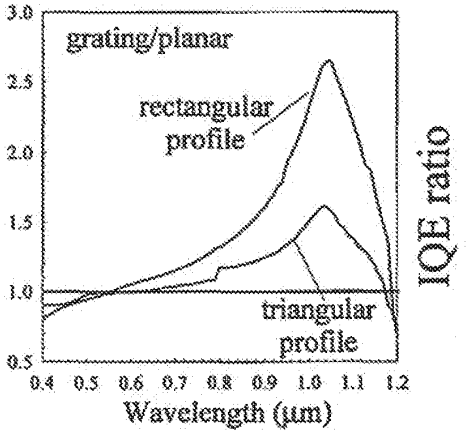


Figure 6. Ratio of IQE response from grating to the planar surfaces for rectangular and triangular profiles.

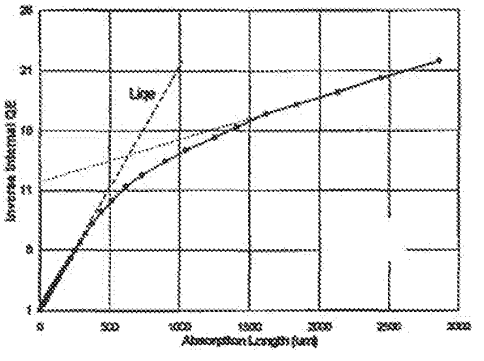


Figure 7. Plot of inverse-IQE versus photon absorption length for the planar cell of Fig. 5. L_{iqe} is the inverse slope of the initial linear regime [11].

SAMSUNG EX. 1002 - 1205/4148

Pergamon

Int. J. Heat Mass Transfer. Vol. 39, No. 18, pp. 3835–3844, 1996
Copyright © 1996 Elsevier Science Ltd
Printed in Great Britain. All rights reserved
0017–9310/96 $15.00 + 0.00

PII: S0017-9310(96)00043-9

Ultra-shallow p^+-junction formation in silicon by excimer laser doping: a heat and mass transfer perspective

X. ZHANG, J. R. HO and C. P. GRIGOROPOULOS†

Department of Mechanical Engineering, University of California, Berkeley, CA 94720, U.S.A.

(*Received* 10 *November* 1995 *and in final form* 30 *January* 1996)

Abstract—Heat and mass transfer at the nanosecond time scale and the nanometer length scale in pulsed laser fabrication of ultra-shallow p^+-junctions is studied in this work. A new technique is developed to fabricate the ultra-shallow p^+-junctions with pulsed laser doping of crystalline silicon with a solid spin-on-glass (SOG) dopant, through the nanosecond pulsed laser heating, melting, and boron mass diffusion in the 100 nm thin silicon layer close to the surface. High boron concentration of 10^{20} atoms cc^{-1} and the 'box-like' junction profile are achieved. The key mechanism determining the 'box-like' junction shape is found to be the melt–solid interface limited diffusion. The ultra-shallow p^+-junctions with the depth from 30 to 400 nm are successfully made by the excimer laser. The optimal laser fluence condition for SOG doping is found about 0.6–0.8 J cm^{-2} by studying the ultra-shallow p^+-junction boron profiles measured by the secondary ion mass spectroscopy (SIMS) vs the laser fluence and the pulse number. The one-dimensional numerical analysis agrees reasonably with the experiment, within the available physical picture. Possible mechanisms such as boron diffusivity dependence on the dopant concentration in the molten silicon are proposed. Copyright © 1996 Elsevier Science Ltd.

1. INTRODUCTION

With today's rapid development in sub-micron electronics, it is becoming increasingly urgent to fabricate a high concentration ultra-shallow p^+-junction for the source and drain of the PMOS (p-channel metal-oxide-semiconductor) transistor [1]. This need presents a challenge to current semiconductor doping technologies such as the furnace diffusion and the ion implantation. It is difficult to achieve both high concentration and ultra-shallow junctions by the conventional furnace doping due to the nature of the solid phase diffusion and the lack of controllability, even though many efforts have been made towards developing RTP (rapid thermal process) techniques [2]. On the other hand, by the ion implantation technique that has been extensively studied and implemented in the current semiconductor industry, one is still unable to form high concentration ultra-shallow p^+-junctions. The insurmountable obstacles arise because the required very low ion implantation energies reach the limit of the implantation equipment capabilities and from the greater inherent channeling effect in crystalline silicon for the light ions such as boron [3, 4]. A modified ion implantation method has been developed to amorphize the silicon wafer surface first, in order to reduce the boron channeling in the implantation process. However, several post-anneals are needed and defects are often generated within the junctions, degrading device performance [5, 6].

To meet the mandatory requirements of both high doping concentration and ultra-shallow junction depth for PMOS, it is necessary to explore new techniques. It would be interesting then to seek new techniques that can generate the transformation to the liquid silicon phase, where the boron diffusivity is extremely high, thus enabling easier and more precise control of the diffusion time. The pulsed u.v. excimer laser as an intensive heating source can provide a new avenue. With the peak power as high as 10^8 W, the excimer laser light can be strongly absorbed by the silicon surface within a depth of 10 nm, resulting in a thin molten silicon layer near the surface. Since the boron mass diffusivity in liquid silicon is by six orders of magnitude larger than that in solid silicon, excimer laser irradiation can confine the diffusion within the thin molten silicon layer at the nanosecond time scale. By controlling the laser pulse energy, the thickness of the thin molten silicon layer can be incrementally changed from a few nanometers to microns. Therefore, it is possible to precisely control the maximum diffusion depth. Also the short pulse width of the excimer laser, which is of the order of 10 ns, provides a complementary way of adjusting the diffusion zone within the molten silicon layer by varying the number of laser pulses, thereby essentially changing the mass diffusion time. Meanwhile, the high boron diffusivity in the thin liquid silicon layer results in a very high doping concentration in the region. A gas immersion layer doping process (GILD) has been developed [7],

† Author to whom correspondence should be addressed.

SIONYX1403000015.0005

SAMSUNG EX. 1002 - 1206/4148

NOMENCLATURE

C	dopant concentration	Q_{ab}	laser intensity absorbed by the crystalline silicon
C_0	surface dopant concentration	r_1	reflection coefficient at air–film interface
C_p	thermal capacity	r_2	reflection coefficient at film–substrate interface
d_1	thickness of the silicon wafer	R	reflectivity of the sample at $\lambda = 248$ nm
d_2	thickness of the thin dopant SOG film	t	time
D	mass diffusivity	T	temperature
d_j	junction depth	T_r	room temperature
Δd_j	junction transition depth	z	coordinate perpendicular to silicon surface.
h	enthalpy		
i	imaginary unit ($=\sqrt{-1}$)		
I	laser intensity		
k	thermal conductivity		
N	laser pulse number		
N_p	total number of grid points in the computational domain		
$\bar{n}_1$	complex refractive index of SOG thin film	Greek symbols	
$\bar{n}_2$	complex refractive index of silicon substrate	α	absorption coefficient
		λ	laser wavelength
		ρ	mass density.

in which dopant gas molecules such as BCl_3 and PCl_3 are dissociated upon the u.v. laser irradiation and incorporated into the think molten silicon layer. It has been demonstrated that submicron shallow junctions can be formed by this gas phase laser doping technique and good device characteristics have been achieved [8–10]. However, the gas phase immersion laser doping requires a sophisticated vacuum chamber and mass flow control systems. Solid-state dopants have been traditionally used in a furnace diffusion process for semiconductor device fabrication, because of its simplicity. In this work, a new technique is developed for fabrication of the ultra-shallow p^+-junction by the excimer laser doping of crystalline silicon with a solid dopant spin-on-glass (SOG) film. By using solid dopants in excimer laser doping, not only does the process itself become simple, but also the laser energy coupling into the silicon wafer can be enhanced up to two times due to the thin film interference effect. The boron dopant profiles in the thin layer near the silicon surface, which depend on the excimer laser fluence and the pulse number, are obtained by the secondary ion mass spectroscopy (SIMS). The rapid transient heat transfer and mass transfer in the thin molten silicon layer induced by laser heating are studied, at the time scale of nanoseconds and the length scale of nanometers. Numerical simulations are conducted to compare with the experimental dopant profiles. The p^+-junction depth and sharpness as functions of laser fluence and pulse number are revealed.

2. EXPERIMENT

The sample structure is shown in Fig. 1. Upon the excimer laser irradiation, the thin layer near the silicon surface is rapidly heated and melting starts as the surface reaches the silicon melting temperature of 1685 K. The melting turns on the boron diffusion in the liquid silicon immediately. After the melting front reaches the maximum depth, the solidification limits the boron diffusion process at the solidification front. The sample is prepared in a clean room environment at the Microfabrication Laboratory at the University of California at Berkeley. A 4-in n-type (100) CZ silicon prime wafer with the resistivity of 5–10 Ω-cm is used for the laser doping experiment. The wafer is cleaned through the standard process by a Piranha solution and rinsed in DI water tanks. The native silicon dioxide on the wafer surface is removed by a diluted 10:1 HF solution. After 1 h baking at 120°C, the wafer is coated with the boron doped spin-on-glass with dopant concentration 2×10^{21} cc^{-1} by spinning the glass solution at 3000 rpm. The sample is then baked on a hot plate at 250°C for 2 h to drive out the residue solvents inside the thin glass film. The thickness of the dopant glass film is designed as 3000 Å in this experiment to enhance the laser energy coupling into the silicon at KrF laser wavelength $\lambda = 248$ nm based on the thin film interference effect. The dopant film thickness is measured as 3050 Å by the Gaertner L116A ellipsometer and the Nanospec interferometer. A separate dopant film is spun on a quartz wafer and optical transmission is measured about 95% at 248 nm. Therefore, the film can be treated as transparent. The thickness uniformity of the thin film dopant glass is found to be better than ±5% across the wafer.

The experimental setup for the excimer laser doping is shown in Fig. 2. A Lumonics Index 200 excimer laser with the wavelength of 248 nm and pulse width of 26 ns (FWHM) is used as a heating source to induce

SIONYX1403000015.0006

SAMSUNG EX. 1002 - 1207/4148

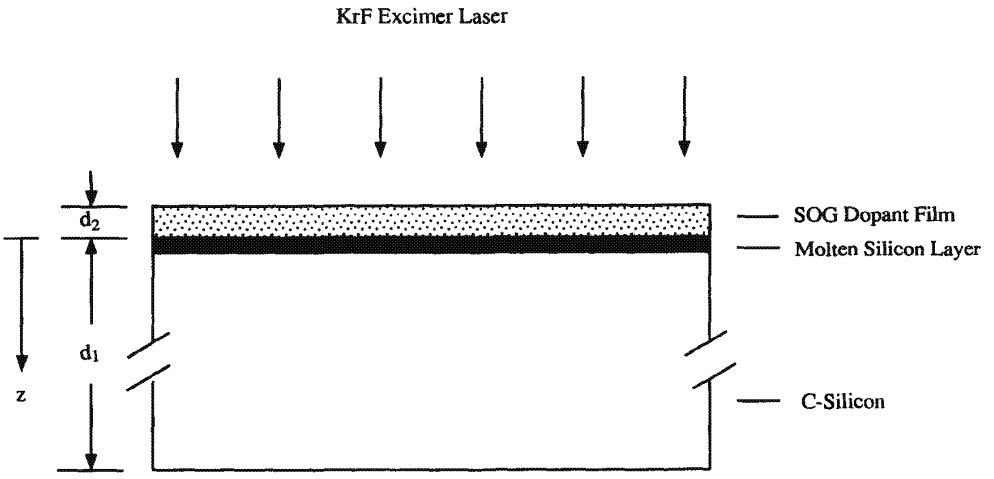


Fig. 1. Schematic sample structure for the ultra-shallow p^+-junction formation by the excimer laser doping with a solid dopant spin-on-glass.

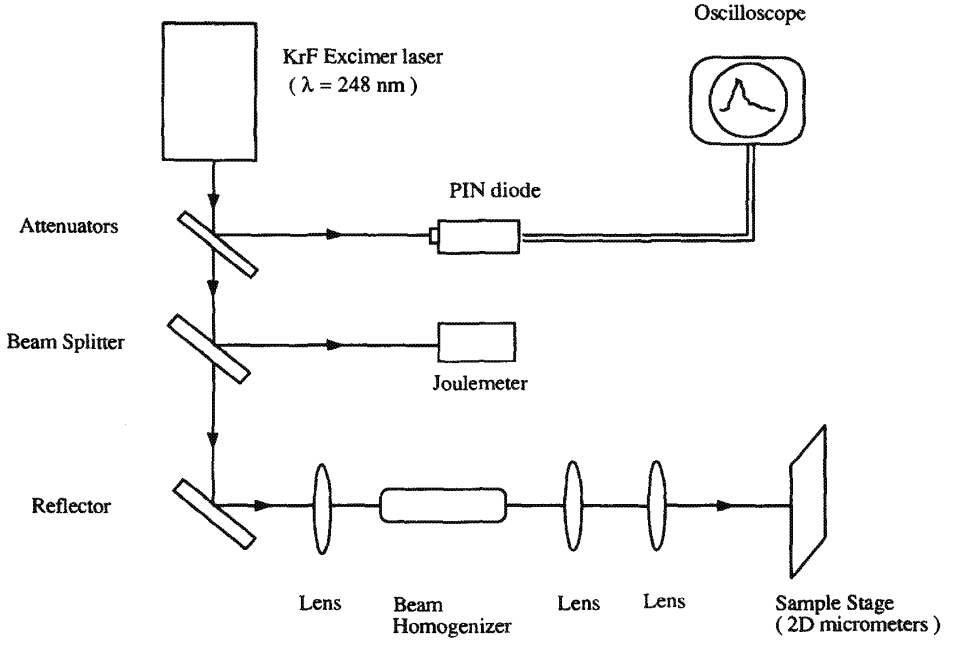


Fig. 2. Schematic experimental set-up for the excimer laser doping of the silicon dopant spin-on-glass.

the thin melting layer on the silicon surface. The pulsed laser beam is delivered through a set of optics that includes a beam homogenizer, mirrors and transfer lenses. The optical alignment is performed to ensure the system optimization and the laser spot profile uniformity on the silicon wafer. The laser fluence on the silicon wafer surface is varied by changing the excimer laser electrode voltage and by using a set of laser beam attenuators. The sample is translated through an X–Y micrometer stage. The laser pulse energy is monitored by the molectron joulemeter detecting the 10% laser beam reflected at a beam splitter, while the 90% transmitted beam is focused on the sample. The temporal laser intensity profiles are recorded by a silicon *PIN* photodiode at a HP 54510A digitizing oscilloscope with nanosecond resolution. The laser fluences studied in this work range from 0.6 J cm^{-2} which is close to the silicon melting

SIONYX1403000015.0007

SAMSUNG EX. 1002 - 1208/4148

threshold, to 0.9 J cm^{-2} where the surface temperature of molten silicon layer is still below the oxide dopant film melting point of 1980 K. Therefore, the oxide dopant film stays in the solid phase during the silicon melting process. In order to study the transient thermal and mass diffusion in the thin liquid silicon layer and optimize the process to achieve the 'box-like' dopant profile in the p^+-junction, the laser pulse number N for each fixed laser fluence is chosen as 1, 5, 10 and 20, respectively. After the laser doping, the dopant glass layer is etched away at a diluted 10:1 HF solution. Several rinses are necessary to ensure that the silicon surface is free from contaminants.

The boron dopant depth profiles are measured with the Phi 660 SEM-AUGER-SIMS system with the vacuum of 2×10^{-9} torr. The sample surface morphology is examined by the scanning electron microscope (SEM). A liquid gallium ion beam with a diameter of 2 μm is used for sputtering by scanning an area of 50×50 μm or 100×100 μm on the laser doped p^+-junction region. A quadrupole mass spectrometer analyzes the sputtered material from the p^+-junction sample and counts the boron ions instantaneously with the sputtered depth into the sample. Ion gun alignment is carried out to ensure both the gallium ion beam and the mass spectrometer are focused at the same area on the sample. A boron-implanted silicon reference sample from the Charles Evans Associates (Redwood City, CA) is used for calibration of the boron concentration in the p^+-junctions fabricated in this work. The calibration is performed at the same SIMS (secondary ion mass spectroscopy) operation conditions such as the magnification and the gallium ion current [11]. The depth calibration is done by measuring the sputtered crater depth in the reference sample at the Tencor Alpha-Step 200 surface profilometer.

3. NUMERICAL SIMULATION

In order to understand the heat and the mass transfer in the ultra-shallow p^+-junction formation under the excimer laser irradiation on the silicon wafer with a thin solid diffusion oxide film, a one-dimensional numerical analysis is developed to simulate the transient heat and mass diffusion of the boron atoms across the thin molten silicon layer. The laser energy intensity absorbed by the silicon, Q_{ab}, is represented as a volumetric source term in the energy equation, as is given by

$$Q_{ab}(z, t) = (1 - R)I(t)\alpha \exp(-\alpha z) \tag{1a}$$

$$R = \left| \frac{r_1 + r_2 \exp(-i4\pi\bar{n}_1 d_2/\lambda)}{1 + r_1 r_2 \exp(-i4\pi\bar{n}_1 d_2/\lambda)} \right|^2, \tag{1b}$$

where R is the reflectivity of the thin SOG film on the silicon substrate and α is the absorption coefficient of the silicon at laser wavelength $\lambda = 248$ nm. d_2 is the thickness of the film which is 3050 Å. r_1 and r_2 are reflection coefficients containing refractive indices of $\bar{n}_1 = (1.5, 0)$ and $\bar{n}_2 = (3.58, 1.68)$ for the dopant film and silicon substrate, respectively. Taking advantage of the thin film interference effect, the reflectivity from the sample can be reduced from 0.67 for bare silicon to 0.56 for the SOG thin film on crystalline silicon substrate. Therefore, the laser energy coupling into silicon substrate is increased by 17%. The 100% enhancement in laser energy coupling into the sample can be achieved by carefully designed thin film thickness for the devices manufacturing environment. The distance from the wafer surface into the silicon z is defined in Fig. 1. The laser absorption depth is of the order of 10 nm and the thermal penetration depth is about a few microns in solid silicon, while the cross-section of the laser beam is of the order of millimeter. Thus, the heat transfer in the silicon can be approximated as a one-dimensional conduction problem described by

$$(\rho C_p)(T)\frac{\partial T}{\partial t} = \frac{\partial}{\partial z}\left(k(T)\frac{\partial T}{\partial z}\right) + Q_{ab}. \tag{2}$$

Two boundary conditions and an initial condition are required

$$T(z = d_1, t) = T_r, \quad \frac{\partial T}{\partial z}(z = -d_2, t) = 0,$$

$$T(z, t = 0) = T_r \tag{3}$$

where d_1 and d_2 are thicknesses of the silicon wafer and the dopant SOG film, respectively, shown in Fig. 1. T_r is the room temperature. The heat conduction equation, in the enthalpy formulation for the solution of phase change problems [12, 13], can be written as

$$\frac{\partial h(T)}{\partial t} = \frac{\partial}{\partial z}\left(k(T)\frac{\partial T}{\partial z}\right) + Q_{ab}, \tag{4}$$

where the enthalpy h is a function of temperature, $h = h(T)$. The enthalpy equation and the associated BCs and IC are discretized using the Crank–Nicolson formulation incorporating temperature-dependent material properties. A nonuniform grid system is used in the computational domain. The maximum grid size for the possible melting regime was set smaller than 10^{-11} m. At each time step, the numerical solution is iterated upon, with the convergence criterion set as

$$\max\left|\frac{T_i^{new} - T_i^{old}}{T_i^{old}}\right| \leqslant 10^{-10} \quad \text{for i} = 1, N \tag{5}$$

where the subscript i denotes the grid position, the superscripts new and old represent the consequent two iterations. N_p indicates the total number of grid points in the computation domain.

As a first-order approximation, the thermal properties are independent of the concentration and the mass diffusivity in the molten silicon layer is independent of the temperature. Therefore, the mass diffusion is decoupled from the thermal equations. The mass

SIONYX1403000015.0008

SAMSUNG EX. 1002 - 1209/4148

diffusion can be solved numerically at each time step after the temperature field and melt–solid interface are found. Transient boron mass diffusion in this work is modeled by the one dimensional Fick's equation

$$\frac{\partial C}{\partial t} = \frac{\partial}{\partial z}\left(D\frac{\partial C}{\partial z}\right). \tag{6}$$

The boundary conditions and the initial condition for the mass transport are given by

$$C(z=0,t) = C_0 \quad C(Z=d_2,t) = 0 \quad C(z,t=0) = 0 \tag{7}$$

where the surface boron concentration C_0 is chosen as the experimentally measured value. Since the dopant concentration is about 2×10^{21} cc^{-1} in SOG film and the boron solubility in silicon is about order of 10^{20} cc^{-1}, the amount of boron diffused into the silicon at this work does not exceed 5% of the total dopant in the SOG film. Therefore, the surface of the silicon can be treated as saturated at a constant concentration C_0, which agrees with experimental observations described in the following section. Boron diffusivity D is set as a constant 2.3×10^{-4} cm^2 s^{-1} in liquid silicon [14] and zero in solid due to the six orders of magnitude difference between the mass diffusivities in the two phases. The thermal properties and mass diffusivities used in numerical simulation are listed in Table 1.

4. RESULTS AND DISCUSSION

The morphology of the laser doped p^+-junction region after the removal of thin SOG layer is smooth, as shown in Fig. 3 by the scanning electron microscopy (SEM). Smaller scale SEM also shows no surface topography generation. This suggests that the one-dimensional heat and mass transfer approach in both a solid and molten silicon thin layer is reasonable. The thin oxide dopant film actually helps to stabilize the molten surface during the transient melting, while the boron atoms diffuse into the melt. However, at this point, it is not clear yet whether the molten silicon solidification process is epitaxial for the laser fluences in the range of 0.6–0.9 J cm^{-2}. The microstructure generated in the recrystallized junction region plays an important role in the heat and mass transfer driven by the following pulses, because of the possible changes in the physical properties of the surface layer [15]. Ultimately, this affects the p^+-junction quality.

Boron dopant concentration profiles at a fixed energy 700 mJ cm^{-2}, are shown in Fig. 4. p^+-Junctions with depth of 70 to 140 nm are successfully fabricated. The boron concentration as high as 2×10^{20} atoms cc^{-1} is obtained, which is about the boron solubility in crystalline silicon. Such a high doping level is mainly due to the high boron mass diffusivity in the thin liquid silicon layer induced by the pulsed laser irradiation. The diffusion profiles extend further into the thin molten silicon as the laser pulse number increases, although the highest concentration is upbound by the boron solubility. It is interesting that, as the laser pulse number increases, the dopant profile shape is more 'box-like' rather than the gradual decrease observed in most diffusion cases. The abrupt or 'box-like' dopant profiles render the ideal p^+-junction properties [8]. The art in the formation of this 'box-like' shape lies on the fact that, as the pulse number increases, the boron diffusion is limited by the maximum melting depth determined by the pulsed laser energy and pulse width. After the boron diffusion reaches the maximum melting depth, more boron atoms are piled up and accumulated in the molten layer instead of crossing the melt–solid interface, because of the very low boron diffusivity in the solid silicon. At 20 laser pulses, almost the entire thin molten layer of 140 nm thickness is saturated with boron dopant. It is also demonstrated that the p^+-junction depth can be incrementally changed by varying the laser pulse number at a fixed laser fluence. Numerical simulation based on a one-dimensional transient thermal and mass diffusion model predicts similar p^+-junction profiles. Both the experimental and numerical dopant profiles at larger pulse numbers coincide to a certain depth of about 140 nm, which is found through computation to be the maximum

Table 1. Thermal properties and mass diffusivities used in numerical simulation of ultrashallow p^+-junction formation

Melting temperature [K]	$T_m = 1685$	Si
	$= 1980$	SOG (SiO_2)
Density [kg m^{-3}]	$\rho = 2.33\times10^3$	Solid Si
	$= 2.52\times10^3$	Liquid Si
	$= 2.2\times10^3$	SOG (SiO_2)
Thermal conductivity [W m^{-1} K^{-1}]	$k(T) = 2.99\times10^4/(T-99)$	Solid Si
	$= 67$	Liquid Si
	$= 1.39$	SOG (SiO_2)
Thermal capacity [J kg^{-1} K^{-1}]	$C_p = (1.4743+5.689\times10^{-4}T)\times10^6/\rho$	Solid Si
	$= 9.6045\times10^2$	Liquid Si
	$= 740$	SOG (SiO_2)
Boron diffusivity [cm^2 s^{-1}]	$D = 0$	Solid Si
	$= 2.3\times10^{-4}$	Liquid Si
Latent heat [J kg^{-1}]	$\Delta h = 1.4\times10^6$	Silicon

SIONYX1403000015.0009

SAMSUNG EX. 1002 - 1210/4148

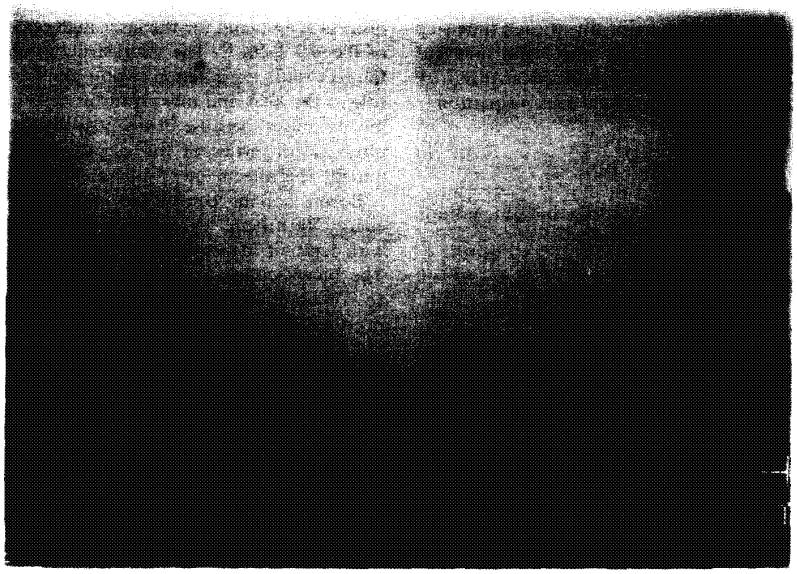


Fig. 3. Ultra-shallow p^+-junction surface morphology imaged by a scanning electron microscopy (SEM).

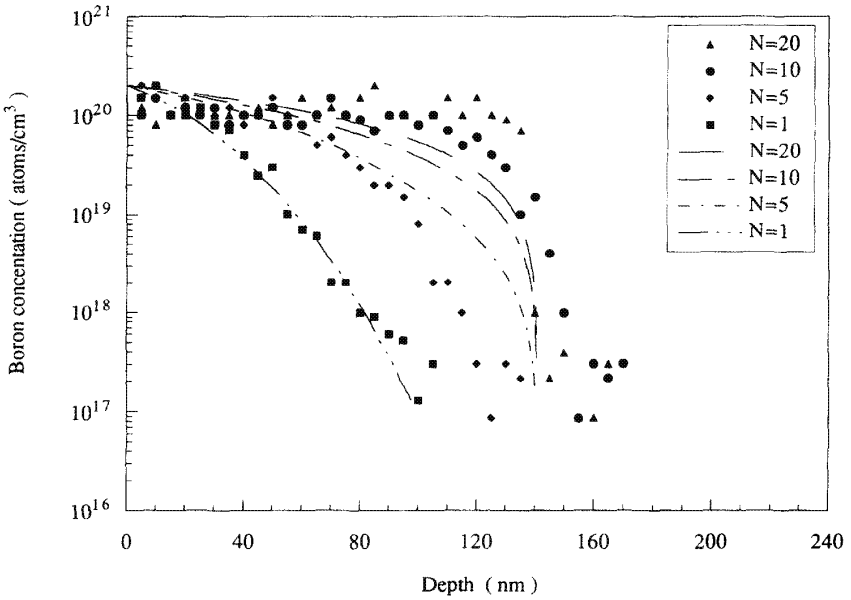


Fig. 4. Ultra-shallow p^+-junction dopant concentration depth profiles at different laser pulse number N with a fixed laser fluence 0.7 cm^{-2}. The solid dots are experimental data measured by the second ion mass spectroscopy (SIMS) and the lines are numerical results.

melting depth at the laser fluence of 700 mJ cm^{-2}. The computational results fit the experimental profile well for the first laser pulse, but deviate substantially as the pulse number N increases. Numerically predicted dopant concentrations are generally lower than the experimental ones. It is believed that the boron diffusivity may depend on the boron concentration if the region is heavily doped, compared with the silicon intrinsic carrier density of the order of 10^{19} cc^{-1} at the melting temperature [16]. For the first few pulses, the heavily doped region is so small that the effect from the concentration dependence of the boron diffusivity

SIONYX1403000015.0010

SAMSUNG EX. 1002 - 1211/4148

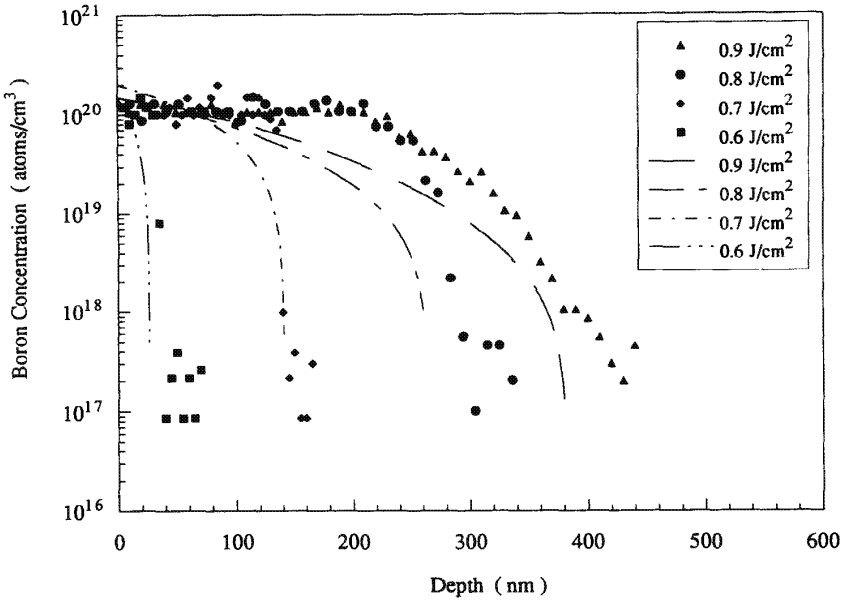


Fig. 5. Ultra-shallow p^+-junction dopant concentration depth profiles at different laser fluence with a fixed pulse number $N = 20$. The solid dots are experimental data measured by the second ion mass spectroscopy (SIMS) and the lines are numerical results.

is not significant. Boron diffusivity can be treated as a constant in the computations. As the pulse number increases, a larger fraction of the molten region becomes heavily doped, leading to a change in the boron diffusivity. A larger boron diffusivity could result in higher computed concentration for $N = 10$ and $N = 20$ in Fig. 4. There are other factors possibly causing the differences between the experimental profiles and numerical profiles at higher pulse numbers. First, the laser fluence measured by the Joulemeter is averaged over the pulses for the case of multiple laser pulses. Pulse to pulse fluence fluctuations generated by the excimer laser can be as large as 10%. The fluctuations can result in not only changes in the thermal process, but also in the mass diffusion. The final dopant profiles are affected more strongly by the higher fluence pulses than the lower ones during the multi-phase doping. Second, the microstructure in the resolidified thin layer is also of importance during the multi-pulse laser irradiation. Assuming epitaxial recrystallization in the thin liquid silicon layer, the numerical simulation in this work may not be accurate enough to predict the thermal transport due to possible changes in physical properties such as the thermal diffusivity in the recrystallized silicon. Third, the absorption coefficient of c-silicon may change due to the heavily doped silicon surface during multiple laser irradiation. Lastly, the thermal conductivity of solid silicon layer can be decreased by a factor of 2–5 in the temperature range from room temperature to 600 K because of the heavy doping with boron [17, 18]. At higher temperatures, the thermal conductivity becomes less affected by the high dopant concentration. The decrease in thermal conductivity can lead to deeper and longer melting in silicon. The 10% increase in the liquid silicon thermal conductivity from 1685 to 1980 K during the pulsed laser doping may also influence the transient thermal and mass transport [19].

Figure 5 shows boron dopant depth profiles for different laser fluences at a fixed pulse number $N = 20$. It is demonstrated that the p^+-junctions are 'box-like' for 0.6, 0.7 and 0.8 J cm^{-2}, but not for 0.9 J cm^{-2}. The difference can be explained by the maximum melting depth. For the fixed pulse number $N = 20$, the boron diffusion depths already exceed the maximum melting depth at the laser fluences 0.6, 0.7 and 0.8 J cm^{-2}. The accumulation of the dopant atoms blocked by the liquid–solid interface results in the 'box-like' dopant distributions. However, for the higher laser fluence like 0.9 J cm^{-2}, the diffusion penetration length at $N = 20$ is smaller than the maximum melting length and therefore, no dopant accumulation occurs. The p^+-junction depth increases with the laser fluence because of the increase in both the melting depth and the melting duration. By defining the p^+-junction depth d_j as the distance from the surface to the position where the concentration drops below 10^{18} cc^{-1}, the junction depths vs the laser fluences at two different pulse numbers $N = 1$ and $N = 20$ are shown in Fig. 6. The computed junction depths are plotted for comparison. The gradual saturation of the junction depths

SIONYX1403000015.0011

SAMSUNG EX. 1002 - 1212/4148

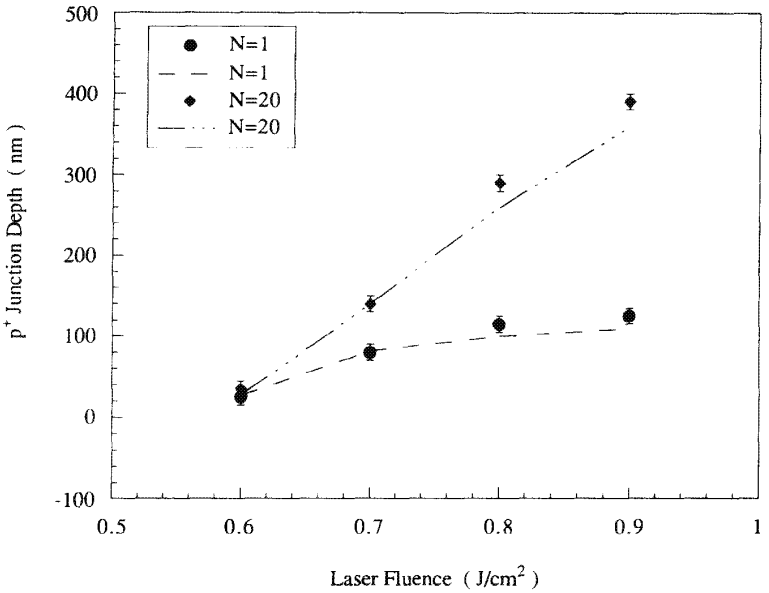


Fig. 6. Ultra-shallow p^+-junction depth dependence on the laser fluence for $N = 1$ and $N = 20$. The solid dots are experimental data measured by the second ion mass spectroscopy (SIMS) and the lines are numerical results.

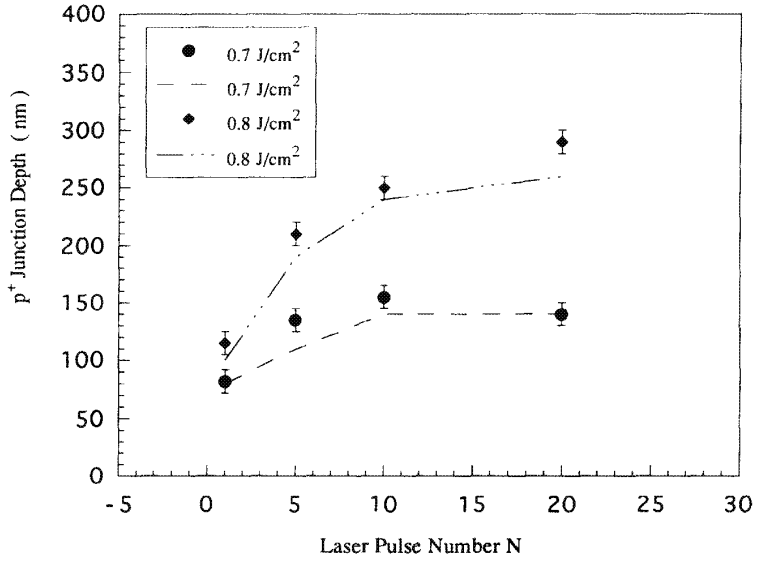


Fig. 7. Ultra-shallow p^+-junction depth dependence on the laser pulse number for laser fluences 0.7 and 0.8 J cm^{-2}. The solid dots are experimental data measured by the second ion mass spectroscopy (SIMS) and the lines are numerical results.

with the pulse number N at fixed laser fluences is observed in Fig. 7, which shows the melt–solid interface limited diffusion. The ultra-shallow p^+-junctions of 30 nm depth at the laser fluence of 0.6 J cm^{-2} are successfully fabricated with this spin-on-glass (SOG) pulsed laser doping technique. It is demonstrated that the incremental depth achieved by varying the pulse number N can be as small as 20–30 nm. However, by varying the laser fluence at an experimentally controllable level (about 0.1 J cm^{-2}), the incremental

SIONYX1403000015.0012

SAMSUNG EX. 1002 - 1213/4148

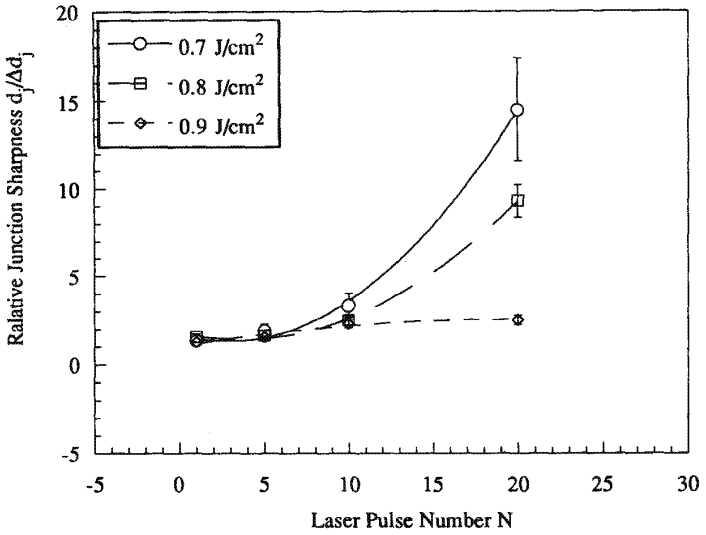


Fig. 8. Relative p^+-junction sharpness dependence on the laser pulse number at laser fluences as 0.6, 0.7, 0.8, 0.9 J cm^{-2}.

depth is relatively larger than that obtained by varying the pulse number because the melt depth is mainly dominated by the larger melting depth and longer melting duration. The p^+-junction sharpness is an important factor in the device performance. By defining the relative junction sharpness as $d_j/\Delta d_j$, where Δd_j is the junction transition depth, it is found that the p^+-junction sharpness increases rapidly as the pulse number N increases for the lower laser fluences of 0.6, 0.7 and 0.8 J cm^{-2}, as shown in Fig. 8. For the laser fluence of 0.9 J cm^{-2}, the p^+-junction sharpness grows much slower than the lower fluence cases due to the fact that the melting depth is longer than the diffusion depth up to 20 pulses, as mentioned earlier. Again, the melt–solid interface limited diffusion is confirmed in Fig. 8. The optimal fluence range in pulsed laser SOG doping is therefore positioned at about 0.6–0.8 J cm^{-2}.

The transient pulsed laser induced melting and diffusion in silicon is a complex phenomenon. Several factors, especially the physical properties of the thin silicon layer can be altered during the multiple laser pulses. It should be pointed out that the boron diffusivity dependence on the concentration and the temperature in the thin liquid silicon layer is not known yet.

5. CONCLUSIONS

Ultra-shallow p^+-junctions ranging from 30 to 400 nm are successfully fabricated by the pulsed excimer laser doping of crystalline silicon with a solid dopant film SOG. The idea is to melt a thin layer of silicon by the pulsed laser irradiation so that the diffusion can be confined within the thin liquid silicon layer, because of the much higher boron diffusivity in liquid silicon compared with that in solid silicon. The p^+-junction depth is essentially controlled by the pulsed laser fluence and the number of the laser pulses. The high boron concentration of 10^{20} atoms cc^{-1} which is close to the solubility in silicon is achieved in the p^+-junctions as a result of the high boron diffusivity in the liquid silicon. The boron depth profiles as a function of the laser fluence and the pulse number are studied by SIMS. It is demonstrated that the junction depth can be changed incrementally by varying either the laser fluence or the pulse number N. The latter is a finer adjustment than the former. Experiments also confirm that the 'box-like' p^+-junctions are formed by multiple laser irradiation as long as the induced maximum melting depth is smaller than the boron diffusion length. The optimal pulsed laser SOG doping fluence range is found about 0.6–0.8 J cm^{-2}. Above this range, the dopant profiles are less sharp because the induced melting depth is larger than the boron diffusion length. This melt–solid interface limited diffusion is found as a key factor in the optimization of the ultra-shallow p^+-junction fabrication. Numerical simulations are carried out to compare with the experimental profiles. It is found that, within the available physical picture, the one-dimensional transient thermal and mass transport model agrees reasonably with the experimental results at the first pulse, but deviates gradually as the laser pulse number increases. Possible mechanisms causing this deviation are discussed, including the boron diffusivity and the solid silicon thermal conductivity dependence on the dopant concentration in the heavily doped region during the multiple laser pulses. Further investigation is needed to elucidate these important issues in the complex tran-

SIONYX1403000015.0013

SAMSUNG EX. 1002 - 1214/4148

sient thermal and mass transport in the thin liquid silicon layer induced by the pulsed laser irradiation.

Acknowledgements– Support from the National Science Foundation under grant no. CTS-9210333 is gratefully acknowledged. X. Zhang thanks Dr F. Ogletree of Lawrence Berkeley Laboratory for SIMS training and helpful discussions on SIMS calibration.

REFERENCES

1. K. K. Ng and W. T. Lynch, The impact of intrinsic series resistance on MOSFET scaling, *IEEE Trans. Electron Devices* **ED-34,** 503–511 (1987).
2. A. Usami, M. Ando, M. Tsunekane and T. Wada, Shallow-junction formation on silicon by rapid thermal diffusion of impurities from a spin-on-source, *IEEE Trans. Electron Devices* **39,** 105–110 (1992).
3. T. M. Liu and W. G. Oldham, Channeling effect of low energy boron implant in (100) silicon, *IEEE Electron Devices Lett.* **EDL-4,** 59–62 (1983).
4. D. Fan, J. Huang and R. J. Jaccodine, Enhanced tail diffusion of ion implanted boron in silicon, *Appl. Phys. Lett.* **50,** 1745–1747 (1987).
5. T. Sands, J. Washburn, R. Gronsky, W. Maszara, D. K. Sadana and G. A. Rozgonyi, Near-surface defects formed during rapid thermal annealing of pre-amorphized and BF_2^+-implanted silicon, *Appl. Phys. Lett* **45,** 982–984 (1984).
6. R. B. Fair, Damage removal/dopant diffusion tradeoffs in ultra-shallow implanted p^+-n junctions, *IEEE Trans. Electron Devices* **ED-37,** 2237–2242 (1990).
7. T. F. Duesch, D. J. Ehrlich, D. D. Rathman, D. J. Silversmith and R. M. Osgood, Electrical properties of laser chemically doped silicon, *Appl. Phys. Lett.* **39,** 825–827 (1981).
8. K. H. Weiner, P. G. Carey, A. M. McCarthy and T. W. Sigmon, An excimer-laser-based nanosecond thermal diffusion technique for ultra-shallow *pn* junction fabrication, *Microelectron. Engng* **20,** 107–130 (1993).
9. K. Sugioka, and K. Toyoda, Generation of carrier concentrations as high as $5 \times 10^{19}\,cm^{-3}$ in GaAs by Si doping using a KrF excimer laser, *Appl. Phys. Lett.* **61,** 2817–2819 (1992).
10. A. Slaoui, F. Foulon and P. Siffert, Excimer laser induced doping of phosphorus into silicon, *J. Appl. Phys.* **67,** 6197–6201 (1990).
11. R. G. Wilson, F. A. Stevie and C. W. Magee, *Secondary Ion Mass Spectrometry: a Practical Handbook for Depth Profiling and Bulk Impurity Analysis*, pp. 3.1.1–3.2.4. Wiley, New York (1989).
12. D. R. Atthey, A finite difference scheme for melting problems, *J. Inst. Math. Applics* **13,** 353–366 (1974).
13. N. Shamsundar and E. M. Sparrow, Analysis of multidimensional conduction phase change via the enthalpy model, *J. Heat Transfer* **97,** 333–340 (1975).
14. H. Kodera, Diffusion coefficients of impurities in silicon melt, *Jpn. J. Appl. Phys.* **2,** 212–219 (1963).
15. B. S. W. Kuo, J. C. M. Li and A. W. Schmid, Thermal conductivity and interface thermal resistance of Si film on Si substrate determined by photothermal displacement interferometry, *Appl. Phys. A.* **55,** 289–296 (1992).
16. S. Wolf and R. N. Tauber, *Silicon Processing for the VLSI Era*, Vol. 1, p. 251. Lattice Press, CA (1984).
17. Y. C. Tai, C. H. Mastrangelo and R. S. Muller, Thermal conductivity on heavily doped low-pressure chemical vapor deposited polycrystalline silicon films, *J. Appl. Phys.* **63,** 1442–1447 (1988).
18. G. Slack, Thermal conductivity of pure and impure silicon, silicon carbide and diamond, *J. Appl. Phys.* **35,** 3460–3466 (1964).
19. R. F. Wood and G. E. Jr Jellison, Melting model of the pulsed laser process. In *Semiconductors and Semimetals* (Edited by R. F. Wood and C. W. White), Vol. 23, pp. 165–250. Academic Press, Orlando, FL (1984).

SIONYX1403000015.0014

SAMSUNG EX. 1002 - 1215/4148

Available online at www.sciencedirect.com
SCIENCE DIRECT
ELSEVIER
Applied Surface Science 245 (2005) 102–108
applied surface science
www.elsevier.com/locate/apsusc

Evolution of silicon surface microstructures by picosecond and femtosecond laser irradiations

Jingtao Zhu[a], Gang Yin[a], Ming Zhao[a], Deying Chen[b], Li Zhao[a,*]

[a]*Surface Physics Laboratory (National Key Laboratory), Fudan University, Handan Rd. 220, Shanghai 200433, PR China*
[b]*Institute of Opto-electronics, Harbin Institute of Technology, Harbin 15001, PR China*

Received 30 May 2004; received in revised form 29 September 2004; accepted 30 September 2004
Available online 11 November 2004

Abstract

We report the evolution of sharp conical spike array formed on the silicon surface under the cumulative picosecond (ps) and femtosecond (fs) laser pulse irradiations in SF_6 ambient. The experimental results suggest that the physical mechanisms of conical spike evolutions under ps and fs laser irradiations are different. Under the ps laser irradiation, silicon surface is melted before the spike arrays formed, while under the fs laser irradiation, the formation of spike arrays does not pass through the liquid phase. The evolution of microstructure is strongly dependent on the laser duration.
© 2004 Elsevier B.V. All rights reserved.

PACS: 68.35.Bs; 61.82.Fk; 61.80.Ba

Keywords: Laser material processing; Surface modification of solid; Laser ablation; Microstructuring; Femtosecond pulse; Picosecond pulse

1. Introduction

The surface modification of solids by laser pulses has been studied for a wide range of materials including metals, semiconductors and dielectrics [1–6]. For silicon, cumulative irradiation with laser pulses can produce regularly micrometer-scale surface structures [2–10], which possess some novel optical properties promising for new device applications, such as solar cells, infrared photo-detectors, sensors and field emission devices [7–9,15]. Arrays of sharp conical spikes located below the original silicon surface have been formed by femtosecond (fs) and picosecond (ps) pulsed laser irradiations of silicon in the presence of an ambient gas SF_6 or Cl_2 [3,4]. The formation of silicon microcolumns that protrude above the initial surface by cumulative nanosecond (ns) pulsed-excimer laser irradiation has also been reported [5,6,10]. These experimental results suggest that the laser duration operates the balance between the redeposition and the ablation, resulting the formed spikes above or below the original surface. In this

* Corresponding author. Tel.: +86 2165642167; fax: +86 2165641344.
E-mail address: lzhao@fudan.ac.cn (L. Zhao).

0169-4332/$ – see front matter © 2004 Elsevier B.V. All rights reserved.
doi:10.1016/j.apsusc.2004.09.113

BNSDOCID: <XP_____25284516A _1_>

SIONYX1403000015.0015

SAMSUNG EX. 1002 - 1216/4148

work, we report a comparative study of the microstructure evolutions on Si surface under the irradiations of femtosecond and picosecond laser pulses, which correspond to the characteristic time for the electrons cooling to the lattice temperature in solid [11–13]. The different morphologies appeared at these two pulse-duration regimes suggest that the laser duration plays an important role in the evolution of the spikes on silicon surface, which hints that the electron–phonon interaction may response to the evolution process of microstructure formation. Under the ps laser irradiation, silicon surface is melted before the spike arrays formed for the laser duration is much longer than the relaxation time of electron–phonon interaction, while under the fs laser irradiation, the formation of spike arrays does not pass through the liquid phase. The molten layer formed on the ps-formed structure hints that the sulfur may be incorporated into the surface by a different process, which affects the optical property of laser-structured silicon [15].

2. Experimental

The silicon wafers used were p-type polished monocrystalline (1 0 0) with the resistivity of 10 Ω cm. The surfaces of samples were fabricated into microstructures under the irradiations of ps and fs laser pulses. The ps and fs pulses were generated by a Nd:YAG laser at the wavelength of 1064/532 nm, pulse width of 35 ps and repetition frequency of 10 Hz and a Ti:sapphire laser at the wavelength of 800 nm, pulse width of 120 fs and repetition frequency of 10 Hz, respectively. The laser beam was incident normal to the sample surface and focused with a 281 mm focal length lens. The laser spot sizes are around 200 μm (fs) and 400 μm (ps) in diameter with Gaussian spatial profile. All specimens were irradiated at same laser energy density of 1.0 J/cm^2 and in 70 kPa SF_6 ambient. The same energy density and repetition frequency for the ps and fs lasers make all the experiments performed under the same irradiation power and thus only the pulse width plays the role in the comparison. The number of pulse shots can be adjusted from 1 to 9000 by a mechanical shutter. After irradiation, the morphologies of the specimens were examined with a scanning electron microscope (SEM).

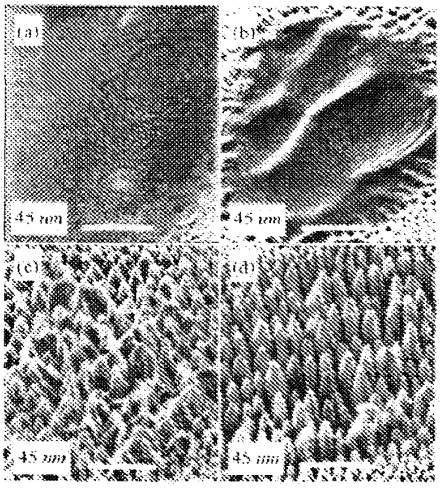


Fig. 1. SEM (viewed at 45°) showing the evolution of the surface morphology of Si produced with 35-ps laser pulses in the SF_6 ambient upon irradiation with the given number of pulses: (a) 50, (b) 200, (c) 800 and (d) 2400.

3. Results and discussion

Fig. 1 shows the evolution of microstructures on silicon surface produced by cumulative 1064-nm ps laser pulse irradiation. After irradiated by 50 pulses, the surface shows the ripple-like pattern (Fig. 1a). And then, it has been molten with widely spaced ridges at the center after 200 pulses (Fig. 1b). After 800 pulses irradiation, some segregated protrusions form on the surface (Fig. 1c). The protrusions develop into sharp conical spikes irradiated by sequent pulses. After irradiated by 2400 pulses, the spikes become narrower and higher (Fig. 1d). A crater is produced by 7500 pluses (Fig. 3a). On the bottom of the crater, the spikes are same as shown in Fig. 1d. The same phenomenon was observed under the irradiation of a 532-nm pulse laser with the same pulse width of 35 ps and same repetition frequency of 10 Hz.

Fig. 2 shows the evolution of microstructures on silicon surface produced by cumulative fs laser pulse irradiation. The ripple-like pattern appears quite early even after two laser pulses (Fig. 2a). After about 10 pulses, the one-dimensional pattern changes into a two-dimensional pattern with small hillocks and pits

BNSDOCID: <XP 2528451 6A 1 >

SIONYX1403000015.0016

SAMSUNG EX. 1002 - 1217/4148

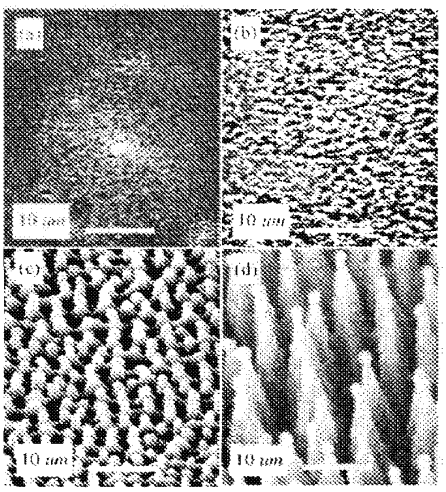


Fig. 2. SEM (viewed at 45°) showing the evolution of the surface morphology of Si produced with 120-fs laser pulses in the SF_6 ambient upon irradiation with the given number of pulses: (a) 2, (b) 10, (c) 50 and (d) 800.

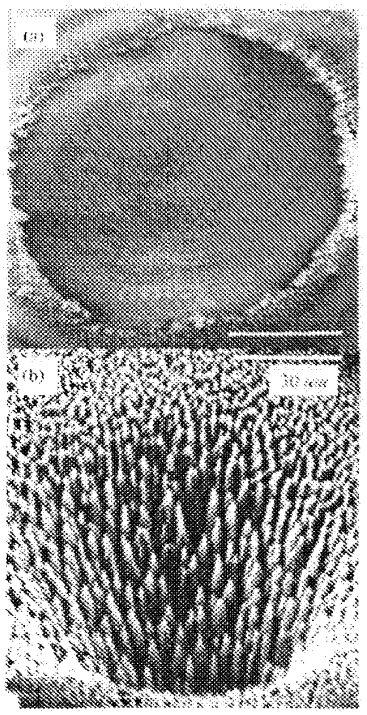


Fig. 3. SEM images created by 7500 laser pulses of 35-ps duration (a) and 3000 laser pulses of 120-fs duration (the parameters are same as in Figs. 1 and 2, respectively).

(Fig. 2b). There is no trace of molten layer; only some "droplets" on the surface are visible. This phenomenon is different from the case shown in Fig. 1b, where a molten layer appears in the ps situation. This indicates the different ablation mechanism from the ps irradiation. After 50 pulses, the surface morphology changes into columns with rounded tips (Fig. 2c). Then they develop into conical spikes, with spherical caps (Fig. 2d). As the number of pulse increases, the conical spikes get slender and higher. The droplets seem to the seeds of the spikes: subsequent laser pulses differentially remove the silicon substrate around of them and the remaining under of them form the spikes. After the irradiation of more than 1000 pulses, the spikes begin to be destroyed in the center and a deep hole formed. This indicates very high ablation efficiency. But the conical spikes still remain at the side of hole and the edge of irradiation spot (Fig. 3b). No molten layer is visible during the evolution of fs-formed spikes.

Based on the observations just described above, we postulate that the evolution of the spikes in three stages: (i) firstly, the ripples developing on the surface (Figs. 1a and 2a) and then (ii) evolving into some protrusions (Figs. 1b–c and 2b–c) through self-organization whose physical mechanism is still unknown and (iii) subsequent laser pulses differentially removing the silicon substrate around the protrusions and depositing on their tips, eventually forming the spikes shown in Figs. 1d and 2d.

Ripple structures are found on the silicon surface at the early stage of the spikes evolution (Figs. 1a and 2a), which has been observed as a result of repetitive pulsed-laser by other authors (referred to as laser induced periodic surface structures, spontaneous periodic surface structures, or laser driven corrugation). And considerable effort has been used in trying to explain their origin [1,2,16–18,24]. However, the physical mechanism of the origin of the ripple structure is still unknown. Most of models are attributed to interference

BNSDOCID: <XP..... 25284516A...1 >

SIONYX1403000015.0017

SAMSUNG EX. 1002 - 1218/4148

of the incident and a scattered or stimulated wave at the surface [2]. Other possible origins for the ripple are capillary wave, surface acoustic wave [19,20,24], surface tension gradient [21], or freezing of surface wave [22]. Recently, Emel'yanov and Babak [23], developed the model of periodic defect deformational surface defect structure formation under fs multi-pulse laser irradiation of semiconductors and demonstrated its feasibility for explain the origin of fs-formed spikes reported in [3]. In our experiments, we find that the periodicity of surface ripples produced by ps laser pulse, shown in Fig. 1a, is much longer than one produced by fs laser, shown in Fig. 2a. These experimental results suggest that the periodicity of surface ripples depends on the laser pulse duration, which appears to support the conclusion reported in [24].

We compare the morphology of silicon microstructures formed in the presence of SF_6 by fs laser irradiation and by ps laser irradiation. The fs-formed spikes, shown in Fig. 2d, are roughly 15 μm tall and separated by 6–8 μm in the center of the irradiation spot. Each spike is caped by a ball 2 μm in diameter and the side of the spike is covered with nanometer-scale dendritic roughness that appears to have been deposited on the spikes (Fig. 4b). The ps-formed spikes, shown in Fig. 1d, are blunter than the fs-formed spikes. They are about 40–50 μm tall and separated by 10–20 μm. While the surface of the ps-formed spike is much smoother and typically lack the spherical cap on the tip (Figs. 1d and 3a). In the Figs. 1d and 2d, the spike densities (the number of the spikes per area in the center of the irradiation spot, where the spikes were fully developed and note that the density decreases with the number of irradiation

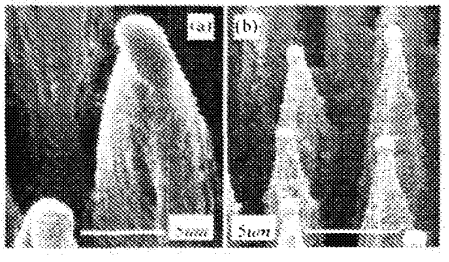


Fig. 4. The spike surface of laser-structured silicon formed by (a) ps laser pulses and (b) fs laser pulses.

laser pulses) are about 6×10^5 spike/cm^2 and about 3×10^6 spike/cm^2, respectively. We believe that the difference of spike density between ps and fs pulse is related to the periodicities of ripples shown in Figs. 1a and 2a.

However, the most striking difference between the above two evolution cases is the existence or absence of a melting process under the laser irradiation. The ps-formed spikes show molten layer features not only on the tips of the spikes, but also on their sides (Fig. 3a), which is similar to the microcolumns formed by ns laser pulses [5,6,10]. In contrast, the frozen-droplets appear only on the tips of the fs-formed spikes, just like caps covering on their tips (Figs. 2d and 3b).

During the formation of the spikes, both laser-assisted chemical etching and laser ablation are involved. Our experimental results suggest that the actual mechanisms of ablation are considerably different for ps and fs laser pulses under the same experimental conditions.

This difference between ps and fs ablation can be explained qualitatively by considering the laser-solid interaction, which has been extensively studied in recent years [11–13]. Upon impact of a laser beam on a solid, electromagnetic energy is converted first into electronic excitation and then into thermal, or mechanical energy. That is to say, the primary laser-solid interaction process is the excitation of electrons from their equilibrium states to some excited states by absorption of photons. A quasi-equilibrium situation is established by electron–electron scattering on the time scale of about 10^{-13} s. At this stage, electron temperature is much higher than the lattice temperature. Then, the high temperature electrons cool down by means of emitting phonons and transferring considerable energy to the lattice on the time scale of about 10^{-12} s. The equilibrium between electron and lattice could be realized. After photon relaxation, the diffusion of heat from the surface to the bulk follows on the time scale of about 10^{-11} s, which can efficiently transfer the energy into the bulk. Subsequent processes are of thermal nature. When sufficient amount of energy is transferred into the bulk, the melting temperature is eventually reached and a transition from the solid to the liquid state takes place. Therefore, $\tau_{e\text{-}p}$, τ_D and τ_L are important

RNSDOCID: <XP 2528451 6A 1 >

SIONYX1403000015.0018

SAMSUNG EX. 1002 - 1219/4148

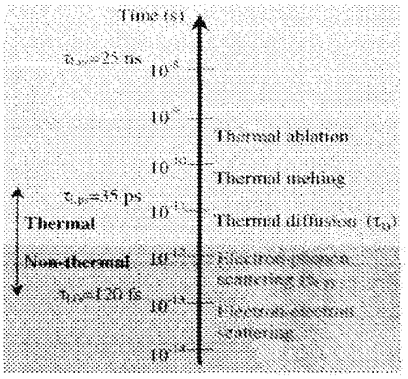


Fig. 5. Timescales of the energy relaxation processes in laser-solid interaction.

characteristic time scales to understand the process of laser-solid interaction. Here, τ_{e-p} is the time of lattice heating by electron–phonon scattering, which is in the order of 10^{-12} s in Si [11–13]. The τ_D is the time of thermal diffusion, which is on a time scale of 10^{-11} s [11–13]. The τ_L is the duration of laser pulse. The time of laser heating solid depends on the laser pulse duration in the laser-solid interaction. So, the laser pulse duration τ_L plays an important role in the initial laser energy deposition on the solid surface. The characteristic time scale τ_{e-p} and τ_L separate the laser-solid interaction into two different regimes, which we call thermal ($\tau_L > \tau_{e-p}$) and non-thermal ($\tau_L < \tau_{e-p}$) ablation regimes. Fig. 5 crudely shows the time scales of energy relaxation processes in the laser-solid interaction [12]. Mechanisms leading to structural modifications using ps and longer laser pulses are thermal ablation in nature, i.e., they take place on timescales longer than 10^{-12} s. In contrast, fs laser pulses open up non-thermal processes that take place on a timescale shorter than 10^{-12} s, hence before thermal processes kick in. In particular, with high intensity fs laser pulses, ultra-fast phase transition and ablation can occur, which is considerably different from thermal process. Now, we discuss our experimental results shown in Figs. 1 and 2 using the characteristic timescales shown in Fig. 5.

In our experiments, the duration of the fs pulse (τ_{Lfs} = 120 fs) is much smaller than the lattice heating time τ_{e-p}. The equilibrium between electron and lattice cannot be established during the laser irradiation period and even the heat diffusion happened is not sufficient to transfer the energy away from the surface. The deposited laser energy results directly in a solid–vapor (or plasma phase) transition, which is followed by a rapid expansion on the surface in a very short time interval. Much material is ablated from the surface, which carried considerable energy away. During all these processes, thermal diffusion into the bulk can be neglected due to the ultra-short duration. That is to say, the laser ablation is a direct solid–vapor transition and the non-thermal ablation occurs. Since most of the energy is used to create the solid–vapor transition, the ablation action is dramatic violence and a great deal of material is removed from the surface. After the columns (Fig. 2c) are formed, most of laser irradiation is absorbed in the grooves because of the multi-reflection and the ablation in the grooves is accelerated. As the laser pulse increases, the columns gradually develop into conical spikes and get higher and higher. After thousands of pulse irradiation, a deep crater leaves because too much material is ablated away from the surface in the center of the irradiation spot (Fig. 3b).

However, in the case of ps laser pulses irradiation, the duration of pulse (τ_{Lfs} = 35 ps) is longer than τ_{e-p}. There is enough time to establish equilibrium between electron and lattice. In this case, thermal diffusion takes place on a time scale of the order 10^{-11} s and most of the deposited laser energy is transferred from surface into bulk via thermal diffusion. The absorbed laser energy will heat the silicon surface. As the cumulative pulse laser irradiation, the temperature of silicon surface reaches to its melting point gradually. Surface gradually melts and molten layer develops on the surface just as shown in Fig. 1b. On the other hand, the thermal diffusion is not sufficient for $\tau_{Lps} \sim \tau_D$. Subsequent irradiation makes the surface temperature reach to evaporization temperature and silicon is vaporized eventually. The ablation material is removed away little by little from the surface via evaporization process to produce segregated protrusions (Fig. 1c). This is to say, laser ablation in this case is accompanied by the thermal diffusion and evaporization occur from molten layer. Therefore, the ablation efficiency is lower than the fs laser pulse ablation and less ablated material is removed from surface. That is the reason that thousands of pulses just

BNSDOCID: <XP 25284516A 1 >

SIONYX1403000015.0019

SAMSUNG EX. 1002 - 1220/4148

create a crater, not a deep hole, in the central of the irradiation spot (Fig. 3a).

Here, we briefly discuss ns-formed structures shown in [5,6,10,14]. Silicon microcolumns protrude above the original surface formed by ns pulse laser irradiation in ambient gases. In this case, the duration of laser pulse ($\tau_{L,ns} = 25$ ns) is much longer than τ_D. There is enough time for thermal wave to propagate into bulk and the laser energy deposited on the surface is sufficiently transferred into the bulk. Therefore, a relatively larger layer melts than ps formed. The absorbed laser energy firstly heats the surface to melting point and then to the evaporization temperature. The evaporization only occurs from the liquid phase and less material is removed from surface via such evaporization process due to the sufficient thermal diffusion. The ablation efficiency is very low. The silicon microcolumns are formed above the original surface by transport from the base of cones to their tips via the evaporization process from the molten layer. The growth mechanisms developed by [5,6,10,14] suggest ns-formed microcolumns grow via evaporization process to transport silicon from the base to their tips.

We note that the microcolumns are above the original surface for long pulse laser (ns pulse), but below the original surface for short pulse laser (ps and fs pulse). This indicates that laser-generated microstructures strongly depend on laser pulse duration. For short laser pulse, the removal of the material is preferential. Mechanisms leading to structural modification using long laser pulse are thermal process in nature. It appears that the laser duration operates the balance between the redeposition and the ablation.

4. Conclusions

This article has emphasized the morphology evolution of arrays of conical spikes formed by cumulative ps and fs laser irradiation on silicon surface in SF_6 ambient. The microstructure evolutions are fundamentally different. The experimental results suggest that laser duration is of key importance in the evolution of laser-generated spikes on silicon surface, which determines thermal diffusion and operates ablation. In the case of fs laser irradiation, the ablation can be considered as a direct solid–vapor transition. Molten layer is absent during the evolution the fs-formed spikes. But in the case of ps laser irradiation, molten layer is visible before the spikes formation due to the thermal diffusion. As regards the first stage of the evolution and formation mechanisms of the spikes, they are only briefly mentioned and not discussed in this article, for example, the origin of the ripples on initial surface and then how to evolve into two-dimensional pattern, the role of the ambient gas. They require further analysis and will be discussed elsewhere.

Acknowledgements

This work was supported by the National Natural Science Foundation of China under the Grant No. 60076025 and 10321003, the Shanghai Natural Science Foundation under the Grant No 01JC14010 and the National Key Basic Research Special Foundation of China. We are grateful to the State Key Laboratory for Advanced Photonic Materials and Devices, Fudan University, for the assistance in performing the ps experiments.

References

[1] J.F. Yong, J.S. Preston, H.M. van Driel, J.E. Sipe, Phys. Rev. B 27 (1983) 1155.
[2] P.M. Fauchet, A.E. Siegman, Appl. Phys. Lett. 40 (1982) 824.
[3] T.H. Her, R.J. Finlay, C. Wu, S. Deliwala, E. Mazur, Appl. Phys. Lett. 73 (1998) 1673.
[4] M. Zhao, G. Yin, J.T. Zhu, L. Zhao, Chin. Phys. Lett. 20 (2003) 1789.
[5] A.J. Pedraza, J.D. Fowlkes, D.H. Lowndes, Appl. Phys. Lett. 74 (1999) 2322.
[6] Douglas H. Lowndes, Jason D. Fowlkes, Antonio J. Pedraza, Appl. Surf. Sci. 154/155 (2000) 647.
[7] C. Wu, C.H. Crouch, L. Zhao, J.E. Carey, R. Younkin, J.A. Levinson, E. Mazur, R.M. Farrell, P. Gothoskar, A. Karger, Appl. Phys. Lett. 78 (2001) 1850.
[8] R. Younkin, J.E. Carey, E. Mazur, J.A. Levinson, C.M. Friend, J. Appl. Phys. 93 (2003) 2626.
[9] C. Wu, C.H. Crouch, L. Zhao, E. Mazur, Appl. Phys. Lett. 81 (2002) 1999.
[10] J.D. Fowlkes, A.J. Pedraza, D.H. Lowndes, Appl. Phys. Lett. 77 (2000) 1629.
[11] J.R. Goldman, J.A. Prybyla, Phys. Rev. Lett. 72 (1994) 1364.
[12] D. von der Linde, K. Sokolowski-Tinten, J. Bialkowski, Appl. Surf. Sci. 109/110 (1997) 1.

SIONYX1403000015.0020

SAMSUNG EX. 1002 - 1221/4148

[13] D. von der Linde, K. Sokolowski-Tinten, Appl. Surf. Sci. 154/155 (2000) 1.
[14] F. Sánchez, J.L. Morenza, V. Trtik, Appl. Phys. Lett. 75 (1999) 3303.
[15] C.H. Crouch, J.E. Carey, J.M. Warrender, M.J. Aziz, E. Mazur, F.Y. Genin, Appl. Phys. Lett. 84 (2004) 1850.
[16] Z. Guosheng, P.M. Fauchet, A.E. Siegman, Phys. Rev. B 26 (1982) 5366.
[17] J.E. Sipe, J.F. Young, J.S. Preston, H.M. van Driel, Phys. Rev. B 27 (1983) 1141.
[18] J.F. Young, J.E. Sipe, H.M. van Driel, Phys. Rev. B 30 (1984) 2001.
[19] G. Grorodetsky, J. Kanicki, T. Kazyaka, R.L. Melcher, Appl. Phys. Lett. 46 (1985) 547.
[20] S.I. Kudryashov, S.D. Allen, J. Appl. Phys. 92 (2002) 5627.
[21] T.R. Anthony, H.E. Cline, J. Appl. Phys. 48 (1977) 3888.
[22] Y.F. Lu, J.J. Yu, W.K. Choi, Appl. Phys. Lett. 71 (1997) 3439.
[23] V.I. Emel'yanov, D.V. Babak, Appl. Phys. A 74 (2002) 797.
[24] D. Jost, W. Lüthy, H.P. Weber, R.P. Salathé, Appl. Phys. Lett. 49 (1986) 625.

BNSDOCID: <XP_____25284516A_I_>

SIONYX1403000015.0021

SAMSUNG EX. 1002 - 1222/4148

Electronic Acknowledgement Receipt

EFS ID:	26312351
Application Number:	14747875
International Application Number:	
Confirmation Number:	1722
Title of Invention:	Pixel Isolation Elements, Devices and Associated Methods
First Named Inventor/Applicant Name:	Martin U. Pralle
Customer Number:	136549
Filer:	Andrew W. Schultz
Filer Authorized By:	
Attorney Docket Number:	143705.05211
Receipt Date:	11-JUL-2016
Filing Date:	23-JUN-2015
Time Stamp:	16:26:45
Application Type:	Utility under 35 USC 111(a)

Payment information:

Submitted with Payment	no

File Listing:

Document Number	Document Description	File Name	File Size(Bytes)/ Message Digest	Multi Part /.zip	Pages (if appl.)
1	Non Patent Literature	Murkin_2009.pdf	1051527 ed82a967493463dba55c09341c3a3b76f681d49f	no	15

Warnings:

SIONYX1403000015.0022

Information:					
2	Non Patent Literature	Myers_HarvardPhysDept.pdf	297169 5c076fb04a7350ee859cf34e7d607df9878fb82d	no	13
Warnings:					
Information:					
3	Non Patent Literature	Nauka_1985.pdf	2802659 0d4bbcb9933b8c247b07685332ac2f4b91a753c4	no	3
Warnings:					
Information:					
4	Non Patent Literature	Nauka_1986_NewIntrinsicGettering.pdf	1498268 dee37a707ed04ec875637bf52efaa524162859e3	no	7
Warnings:					
Information:					
5	Non Patent Literature	Nayak_2003_SPIEDigitalLib.pdf	4699960 f53ed004110770164cfdf4ecdee509e0aff0d385	no	4
Warnings:					
Information:					
6	Non Patent Literature	Nayak_2005_SemiconductorLaserCrystal.pdf	7440996 77545d59e74cc599ec58758401f57416653 35c34	no	4
Warnings:					
Information:					
7	Non Patent Literature	Nayak_2007_ApplSurfaceSci.pdf	6070517 91fdf8278550591372f9984269a788161858bfb9	no	4
Warnings:					
Information:					
8	Non Patent Literature	Nayak_2009_MaterialsResearchSociety.pdf	690647 e0566ef6bcfa56a042844138608ae9131ae6d9b4	no	6
Warnings:					
Information:					

9	Non Patent Literature	Nayak_2011_ResearchAndApplications.pdf	723536 5962f8532b08326c570027c3b30dcda6a4c5ca92	no	9
Warnings:					
Information:					
10	Non Patent Literature	Oden_2010.pdf	12994610 7619d42f7745b2a5e06988bbe9e4de2d3f1bf671	no	10
Warnings:					
Information:					
11	Non Patent Literature	Pain_2005_ABackIlluminated.pdf	313751 bbfedca0fabc7aacc8097f138e2be35873f5a94d	no	4
Warnings:					
Information:					
12	Non Patent Literature	Pain_2009.pdf	797555 99c2b23f735387b1206552f23ea2a51e0b82fbea	no	23
Warnings:					
Information:					
13	Non Patent Literature	Palm_2004.pdf	614777 d95cd48628fd404b77dfab12f4f84a141668cce4	no	8
Warnings:					
Information:					
14	Non Patent Literature	Payne_2010.pdf	1457070 6a2c938f8676532cb21c25fea10cd0ea1223d44d	no	5
Warnings:					
Information:					
15	Non Patent Literature	Pedraza_1999_AppliedPhysicsLtrs.pdf	725054 b8cee7b67b96749802bfbd3afe33793138fa9b5f	no	8
Warnings:					
Information:					

16	Non Patent Literature	Pedraza_2003_AppliedPhysics A.pdf	725054 b8cee7b67b96749802bfbd3afe33793138fa 9b5f	no	8
Warnings:					
Information:					
17	Non Patent Literature	Rashkeev_2001.pdf	4725777 741a9b26114e89792107925fcc74aca6470 de0f3	no	3
Warnings:					
Information:					
18	Non Patent Literature	Russell_1989.pdf	485495 24ab2d32fc8e7a506a601c31ec6829490aaa 0269	no	6
Warnings:					
Information:					
19	Non Patent Literature	Russell_2003_SSCPacific.pdf	974057 7338b26469e9a0345bc218fb1b717f0fba72 4259	no	6
Warnings:					
Information:					
20	Non Patent Literature	Sai_2008.pdf	6207622 4c70bde62df23f4549aa8315679a2fda361a 184d	no	3
Warnings:					
Information:					
21	Non Patent Literature	Sanchez_1996_Whiskerlike.pdf	5134904 2d2c9ece091fb35e9609e605f7e56d8ddcd 35406	no	3
Warnings:					
Information:					
22	Non Patent Literature	Sanchez_1998_DynamicsOfThe .pdf	4810445 896cc8a084a80dff6bfa6931b30e3a7dcf81f 182	no	4
Warnings:					
Information:					

23	Non Patent Literature	Sarnet_2008.pdf	2704794 8657bc415f08f3b20ac5dc9c4c60630485b471c9	no	15
Warnings:					
Information:					
24	Non Patent Literature	Senoussaoui_2003.pdf	1261403 b3960f68513cda8cf304626a23894b38ca854b63	no	5
Warnings:					
Information:					
25	Non Patent Literature	Serpenguzel2004.pdf	275277 68003afce7ba9e340e3533e45ed944882a39ed99	no	9
Warnings:					
Information:					
26	Non Patent Literature	Shen_2007.pdf	347566 f2406eacdb44ce08e3940ef97ddfb93724789a50	no	3
Warnings:					
Information:					
27	Non Patent Literature	SolarEnergyResearchInstitute_1984.pdf	12512054 78cfed4b5537043952fdf10b9f981d6592c30d29	no	10
Warnings:					
Information:					
28	Non Patent Literature	Solhusvik_2009.pdf	5934788 9e030d00bc3754335b1b09d8a366bc18a55d13ec	no	3
Warnings:					
Information:					
29	Non Patent Literature	Stone_2001.pdf	10391786 fd946586593fa5ad2ce1300a6f24de893a5dcb10	no	6
Warnings:					
Information:					

30	Non Patent Literature	Szlufcik1991.pdf	799386 c5d0c30e5063740935704a9deeff9ab29008c41a	no	3
Warnings:					
Information:					
31	Non Patent Literature	Tabbal_2007.pdf	527746 a0b82bd850fbee796872187b5fda4e60f8f986c1	no	6
Warnings:					
Information:					
32	Non Patent Literature	Takayanagi_2007.pdf	1294056 ed844f4cb85c12e1b0fdca0022967f85234f0ca2	no	4
Warnings:					
Information:					
33	Non Patent Literature	Tower_2003.pdf	2310811 eba3d772edb3a8407054a5100b887df095969f51	no	7
Warnings:					
Information:					
34	Non Patent Literature	Tull_2007.pdf	8153883 037c360c382fc2b9bf47362776b2da2b1d7a52aa	no	174
Warnings:					
Information:					
35	Non Patent Literature	Uehara_2004.pdf	480240 e4bc10071ad2c99e3f1f89dd6465a3101df930c9	no	6
Warnings:					
Information:					
36	Non Patent Literature	Wilson_1984.pdf	2049764 94f5694e894ac0ad75200a7faa4ddb5a0885132b	no	5
Warnings:					
Information:					

37	Non Patent Literature	Winderbaum_1997.pdf	8729122 9319f5b306628ebc2e8589da04e30f5336174832	no	10
Warnings:					
Information:					
38	Non Patent Literature	Wu_1999_APSCentennialMeeting.pdf	5020631 58fc0cf21a7da2ea09d0d8f84f73889a92d4710b	no	36
Warnings:					
Information:					
39	Non Patent Literature	Wu_2000_Thesis.pdf	5410273 6fd36a6c384a92d1ae9e5cfe85571a725a43d659	no	138
Warnings:					
Information:					
40	Non Patent Literature	Wu_2001_AppliedPhysicsLettersVol78.pdf	361848 e8f4a9215584d7f12d792e893bb335c965930908	no	3
Warnings:					
Information:					
41	Non Patent Literature	Wu_2002_AppliedPhysicsLettersVol81.pdf	291419 b60e60b201a7b431540d1bce3bdd3a8b749d8946	no	3
Warnings:					
Information:					
42	Non Patent Literature	Wu_BlackSilicon_1999.pdf	4227673 2bb6a45c93823c3b50a73852894adf51c931267a	no	40
Warnings:					
Information:					
43	Non Patent Literature	Xu_1993.pdf	12016946 54790907dc94a867bbae847d9f2822435f6c4bc0	no	9
Warnings:					
Information:					

44	Non Patent Literature	Yablonovitch_1982.pdf	1273767 a8def6fed8fe5508e6ec06b9cc9362c738a746ce	no	6
Warnings:					
Information:					
45	Non Patent Literature	Yamamoto_2010.pdf	421949 effa345fb9f171099ecb37b26501e0d038296e7d	no	4
Warnings:					
Information:					
46	Non Patent Literature	Yasutomi_2009.pdf	238518 7dd16cbccbd8fdba5a76a7d409d7f6ffa0b71bd6	no	4
Warnings:					
Information:					
47	Non Patent Literature	Yan_2010.pdf	1739419 b48980f55f8edb3e772ffb0f1bacbb6d5440bcaf	no	7
Warnings:					
Information:					
48	Non Patent Literature	Younkin_2001_Thesis.pdf	5144732 1f0e3703a2b18be1ab76bd3dd7c21651f222721c	no	136
Warnings:					
Information:					
49	Non Patent Literature	Younkin_2003_JournalOfAppliedPhysicsVol93.pdf	325011 838dec3f7c57b9f19cd4066c297850246bb9a856	no	4
Warnings:					
Information:					
50	Non Patent Literature	Yuan_2009_AppliedPhysicsLetters.pdf	414073 38ba48c35faa2e90282720908d4cca24d895ea69	no	3
Warnings:					
Information:					

SAMSUNG EX. 1002 - 1230/4148

51	Non Patent Literature	Zaidi_2000.pdf	1086636 0ac5f6c1490b85075cc6d3e4a1e0a361d04fa132	no	4
Warnings:					
Information:					
52	Non Patent Literature	Zhang_1996.pdf	814553 27f139c127e7023b37d9b18e8605ef9769f1d680	no	10
Warnings:					
Information:					
53	Non Patent Literature	Zhu_2004.pdf	669226 c1232928e940617b23d88819971bf6e7f56d4fe8	no	7
Warnings:					
Information:					
		Total Files Size (in bytes):	162470800		

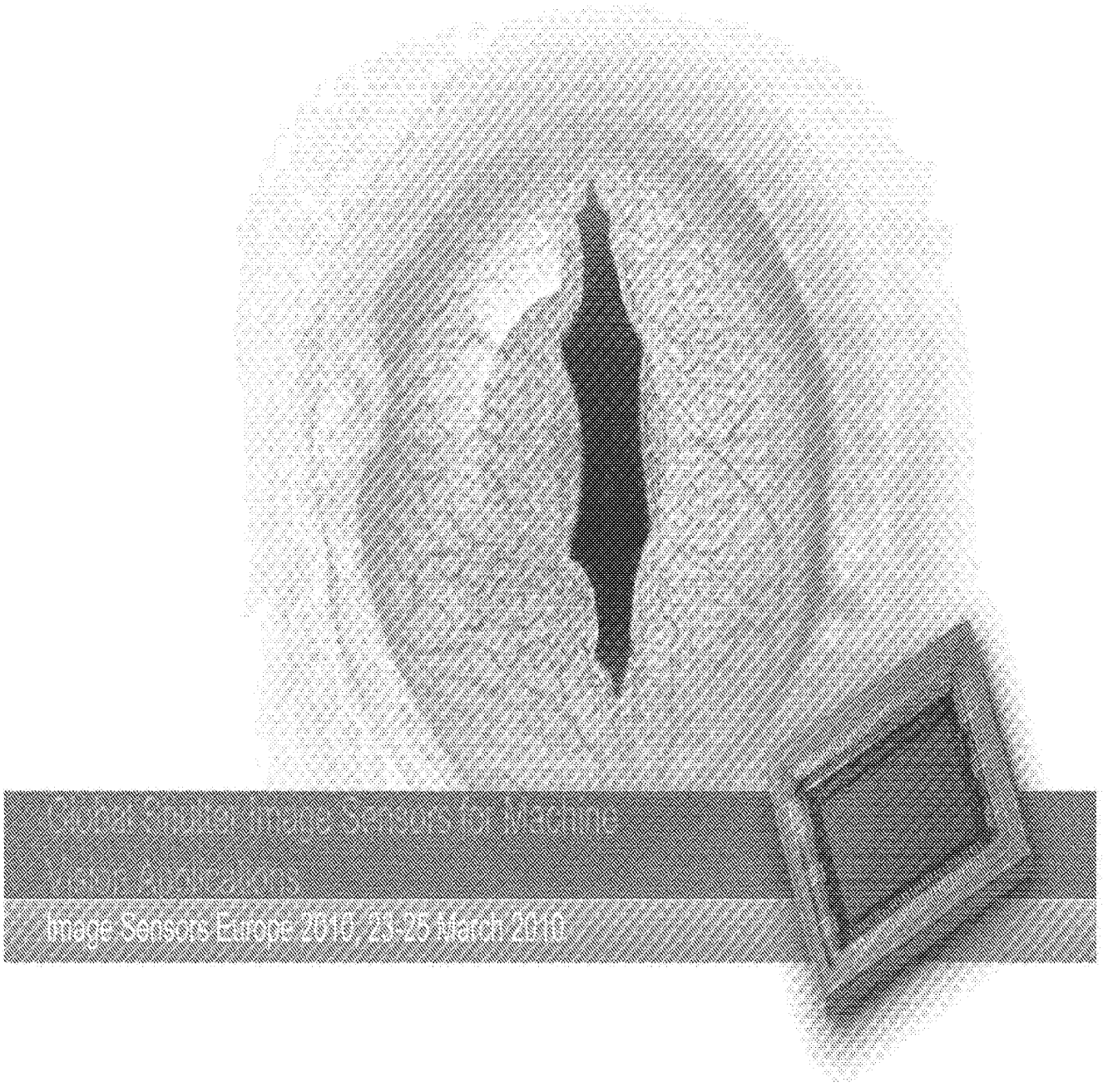
This Acknowledgement Receipt evidences receipt on the noted date by the USPTO of the indicated documents, characterized by the applicant, and including page counts, where applicable. It serves as evidence of receipt similar to a Post Card, as described in MPEP 503.

New Applications Under 35 U.S.C. 111
If a new application is being filed and the application includes the necessary components for a filing date (see 37 CFR 1.53(b)-(d) and MPEP 506), a Filing Receipt (37 CFR 1.54) will be issued in due course and the date shown on this Acknowledgement Receipt will establish the filing date of the application.

National Stage of an International Application under 35 U.S.C. 371
If a timely submission to enter the national stage of an international application is compliant with the conditions of 35 U.S.C. 371 and other applicable requirements a Form PCT/DO/EO/903 indicating acceptance of the application as a national stage submission under 35 U.S.C. 371 will be issued in addition to the Filing Receipt, in due course.

New International Application Filed with the USPTO as a Receiving Office
If a new international application is being filed and the international application includes the necessary components for an international filing date (see PCT Article 11 and MPEP 1810), a Notification of the International Application Number and of the International Filing Date (Form PCT/RO/105) will be issued in due course, subject to prescriptions concerning national security, and the date shown on this Acknowledgement Receipt will establish the international filing date of the application.

SAMSUNG EX. 1002 - 1231/4148



SIONYX1403000015.0031

SAMSUNG EX. 1002 - 1232/4148

Contents

- Introduction
  - Machine vision sensor demands
  - Products definition
  - Current standard products
- Technology developments
  - Image sensor architecture
  - Low noise global shutter pixel
  - High speed column ramp ADCs
- Sensor characterization
  - Features and electro-optical specifications
  - Sample images & movie

Machine vision sensor demands

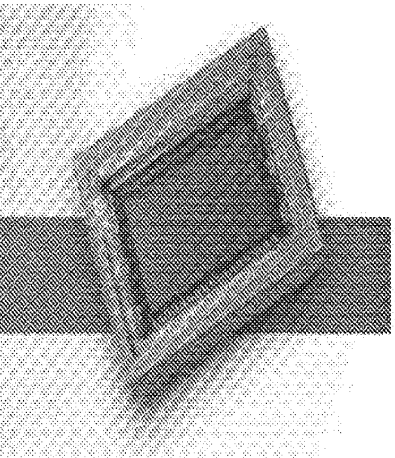
- Global shutter
  - Freeze fast moving object
  - No smear
- High sensitivity with low noise
  - Need enough image data with short exposure times
  - Low light sensitivity (apply gain if necessary)
  - Low parasitic light sensitivity (high shutter efficiency)
- Minimal 1.3 Mpixels, preferably higher
  - High detail in large field of view
  - Use digital zoom

SAMSUNG EX. 1002 - 1234/4148

Machine vision sensor demands

- High frame rate
  - Take a fast sequence of images to track movement
  - Exposure of an image while the previous is read out (pipelining)
- Ease of use
  - Implement on-board features
  - Programming of exposure and read-out modes using a SPI
- No image correction needed off-chip
  - No image post-processing needed
  - No dark frame subtraction (FPN correction)

Definition of the products



- Talked to many potential customers
- Defined what was needed
- Proposed a specification list
- Feedback on product definition from beta customers
- Development of final product according to feedback

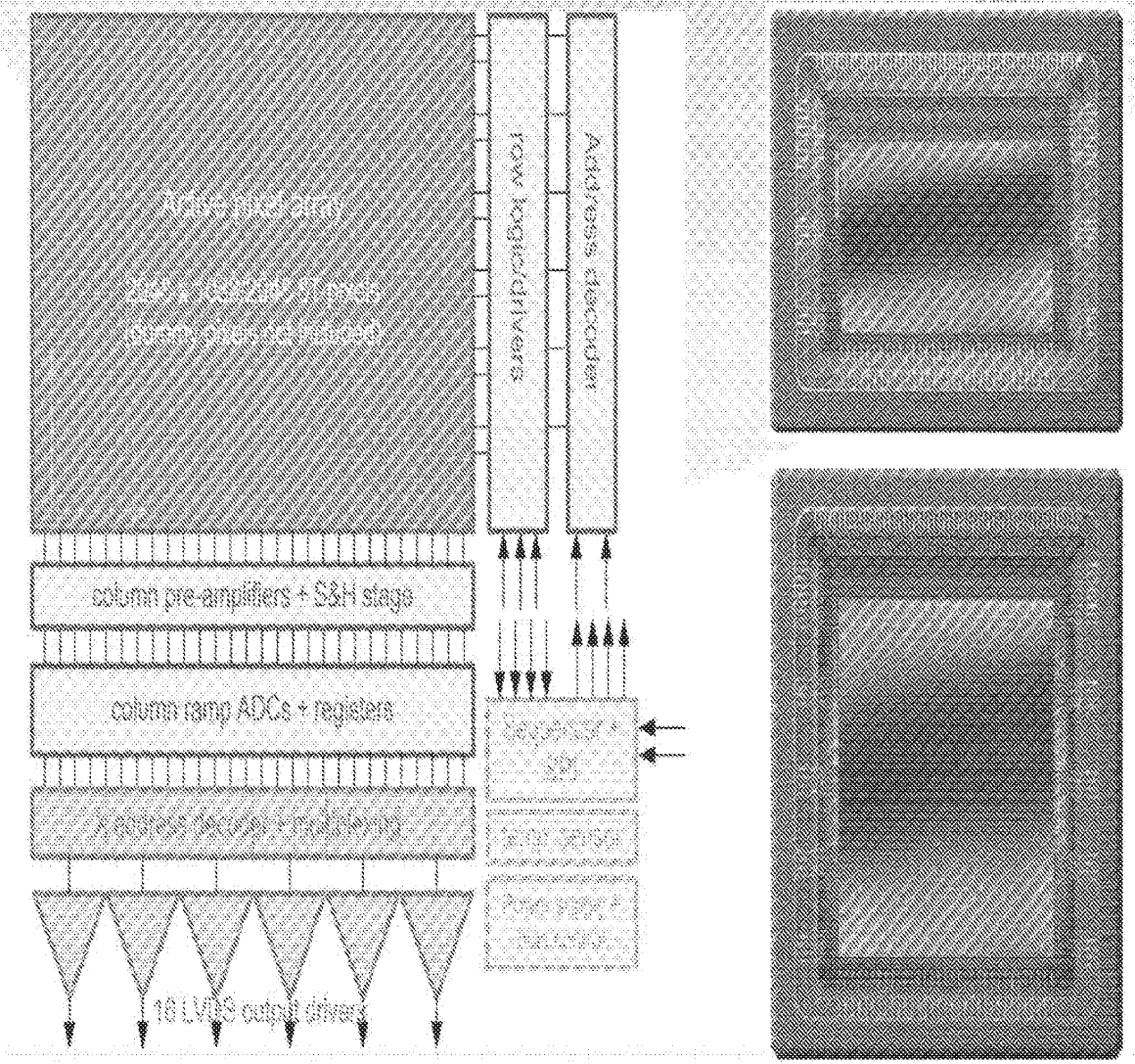
➔ Industry driven spec list!

Current products: 2 resolutions

- CMV2000 – 2048 x 1088 pixels
  - Small form factor (2/3")
  - Support full HD
- CMV4000 – 2048 x 2048 pixels
  - Square format for optimal lens area coverage

➔ Pin compatible with identical on-board features and electro-optical specifications

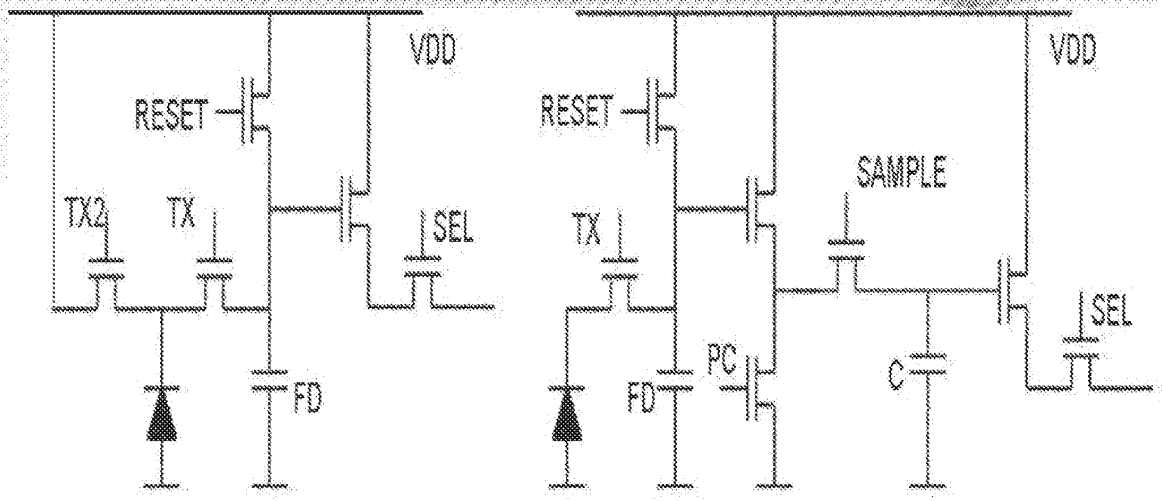
Sensor architecture



Architecture: highlights

- High speed
  - High speed column ADCs
  - Pipelined global shutter with CDS
  - 16 parallel high speed LVDS outputs (multiplexing possible)
- High sensitivity with low noise
  - Achieved by using a unique global shutter pixel with correlated double sampling (CDS)
  - High fill factor for high sensitivity
- Ease of use:
  - LVDS outputs
  - On-board sequencer
- Small form factor
  - 95 pin package (18.6mm x 13.5mm or 18.6mm x 18.6mm)

Pixel architecture: previous art



a: 5T pixel

b: 7T pixel

- Poor parasitic light sensitivity
- Reset noise is not cancelled

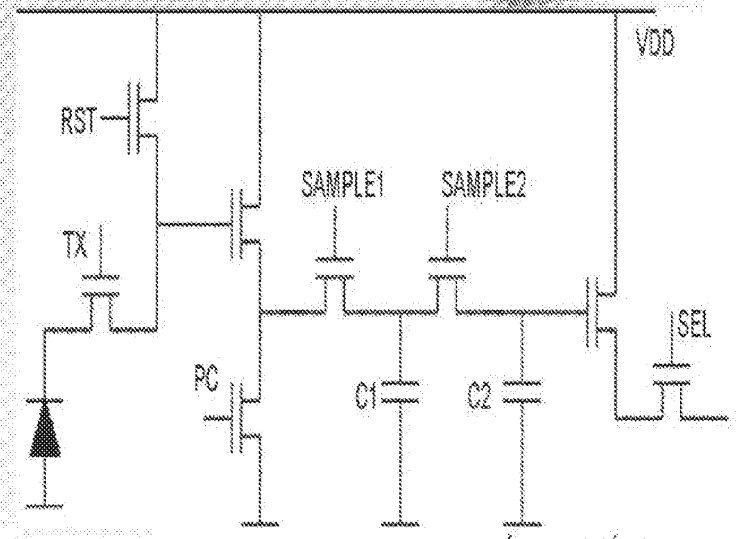
- Improved parasitic light sensitivity
- Reset noise is not cancelled

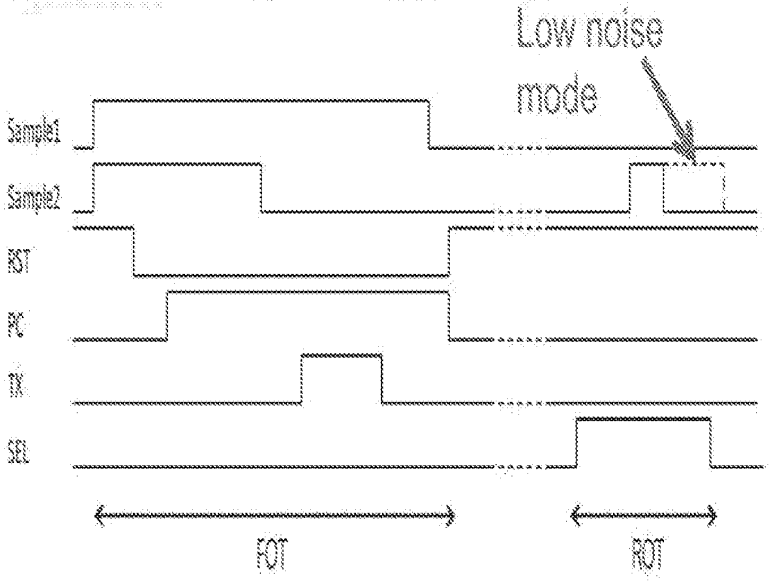
conversion gain (CvG) vs. dynamic range

SIONYX1403000015.0039

Pixel architecture: CMOSIS 8T

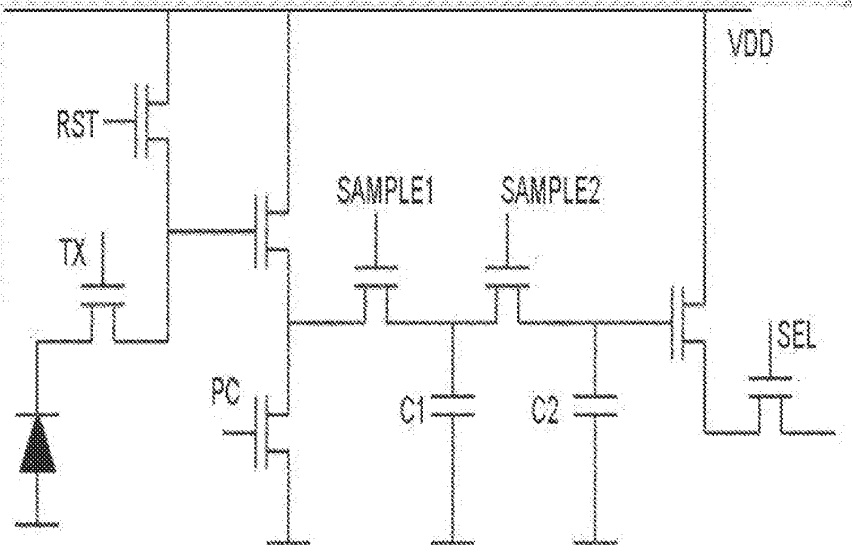
- Frame overhead time:
  - I. release RST
  - II. sample reset level on C2
  - III. charge transfer
  - IV. sample signal level on C1





- Row overhead time:
  - I. read reset level
  - II. short C1 & C2
  - III. read signal level

Pixel architecture: noise analysis



Pixel output after CDS:

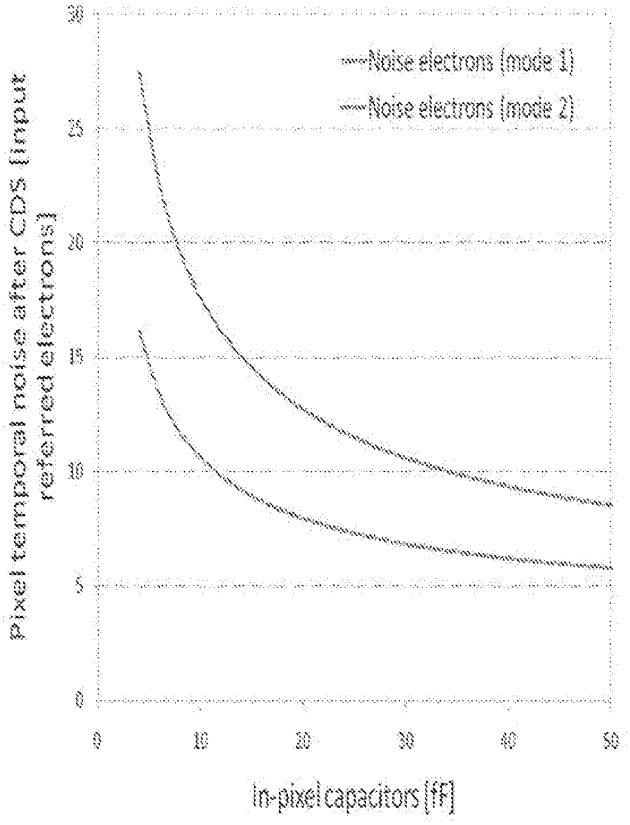
$$\frac{Vsig}{2} + \sqrt{\frac{N^2(KTCs2)}{4} + \frac{N^2(KTCs1)}{4} + N^2(KTCs2)} \quad \Longrightarrow \quad \frac{Vsig}{2} + \sqrt{1.5 * KT/C}$$

Assuming C1 = C2 = C

Low noise mode: $\frac{Vsig}{2} + \sqrt{\frac{N^2(KTCs2)}{4} + \frac{N^2(KTCs1)}{4}} \quad \Longrightarrow \quad \frac{Vsig}{2} + \sqrt{0.5 * KT/C}$

Pixel architecture: CMOSIS 8T

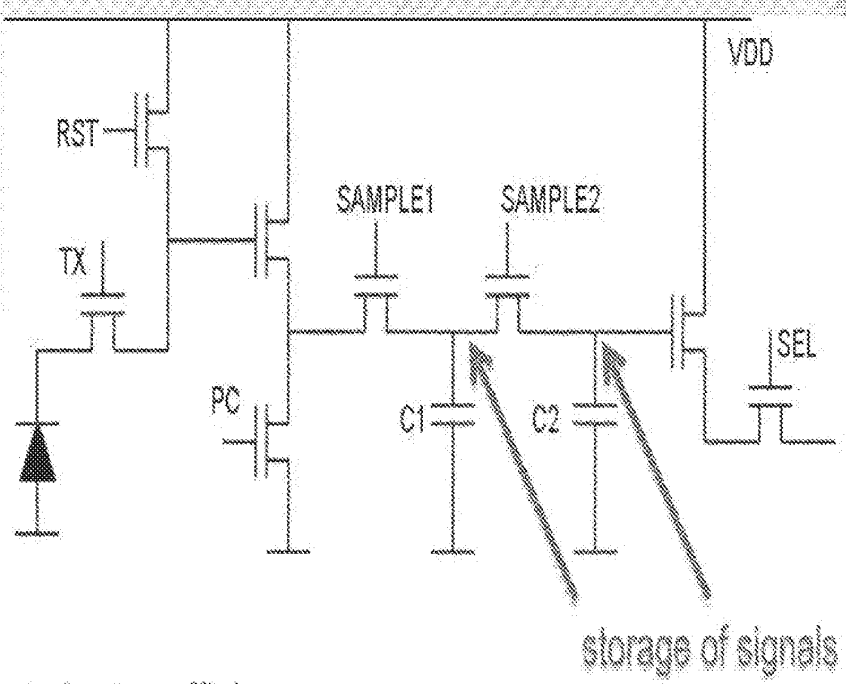
- Pixel noise (in voltage) only determined by C
- High CvG desired
  - low noise (in input referred e-)
  - better sensitivity
- Dynamic range (DR) independent of CvG, only determined by swing and C
- Only small FWC is required for desired swing (i.e. dynamic range)



CDS in 8T pixel offers combination of low noise and high DR

CMOSIS

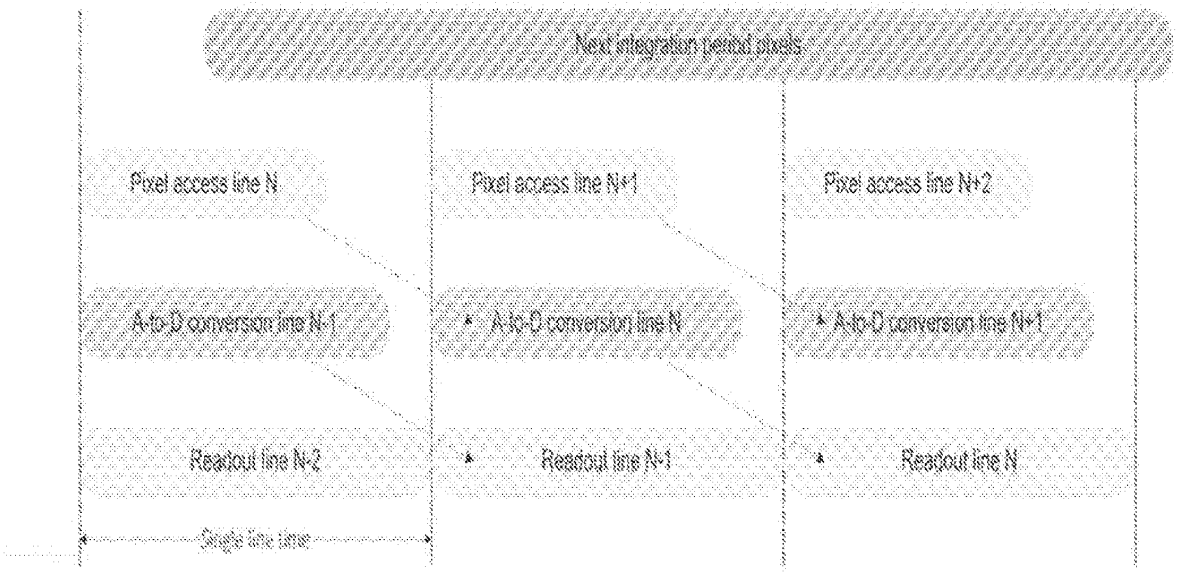
Pixel architecture: PLS



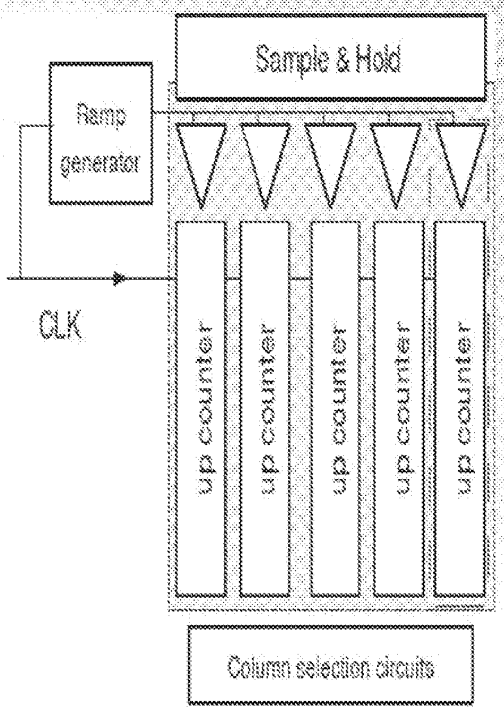
- Excellent shutter efficiency:
  - I. Storage C (C1 & C2) >> C_{FD}
  - II. Storage capacitors have low parasitic light sensitivity
  - III. Parasitic leakage is cancelled by CDS operation
- Measured shutter efficiency: > 99,998 % (PLS < 1/60000)

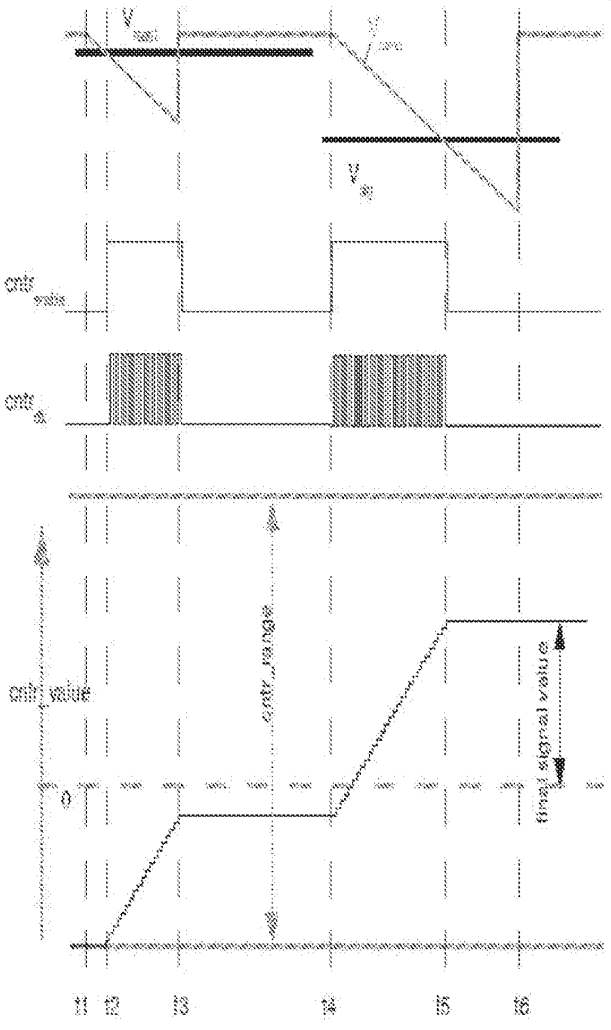
Pipelined architecture

- Fully pipelined architecture
  - Integration: next integration period starts while previous frame is being read out (pipelined global shutter)
  - Readout processes are pipelined:
    - Pixel access and sampling
    - A-to-D conversion in column
    - Data readout to LVDS outputs

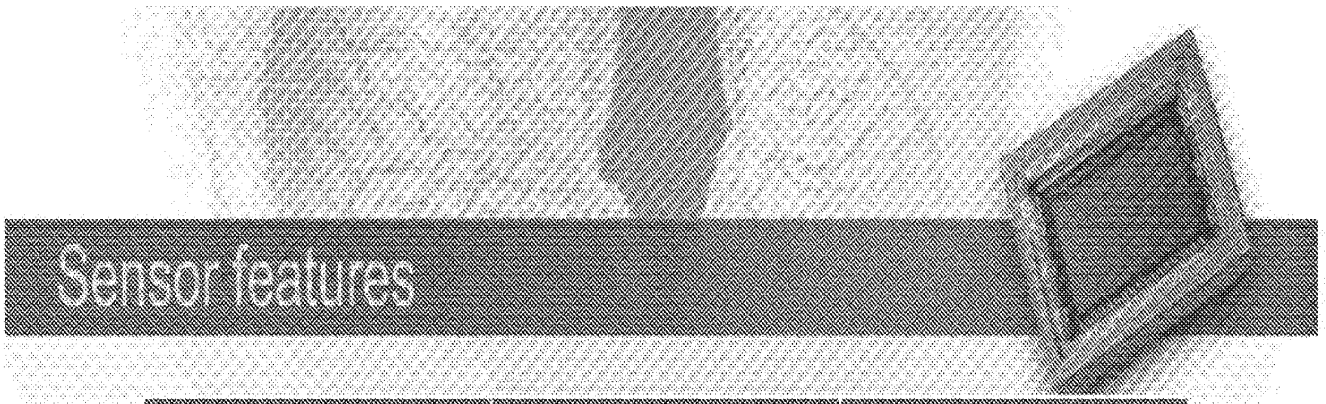


Column ramp ADCs





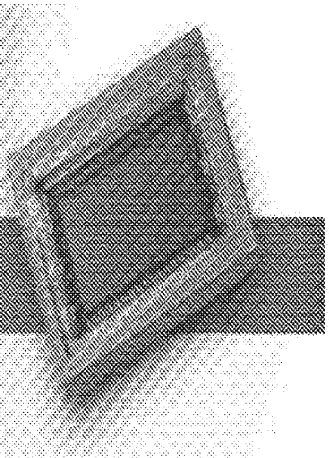
- Single distributed clock:
  - I. Clocked at 480 MHz
  - II. 10 bit: 2.7 µs/row
  - III. 12 bit: 10.8 µs/row



Sensor features

Feature	CMV2000	CMV4000
Resolution	2048 x 1088	2048 x 2048
Pixel size	5.5 um x 5.5 um	
Max. frame rate	340 fps	180 fps
Windowing	Row windowing (up to 8 separate ROIs)	
Image flipping	X and Y mirroring	
Output	16 LVDS outputs @ 480 MHz	
Multiplexing	To 8, 4 and 2 outputs	
ADC	10 bit, 12 bit at reduced frame rate	
High dynamic range	Multiple modes supported	
Programming	Over SPI interface	
Temperature control	On chip temperature sensor	
Sequencer	On chip timing generation	
Package	Ceramic µPGA package (95 pins)	

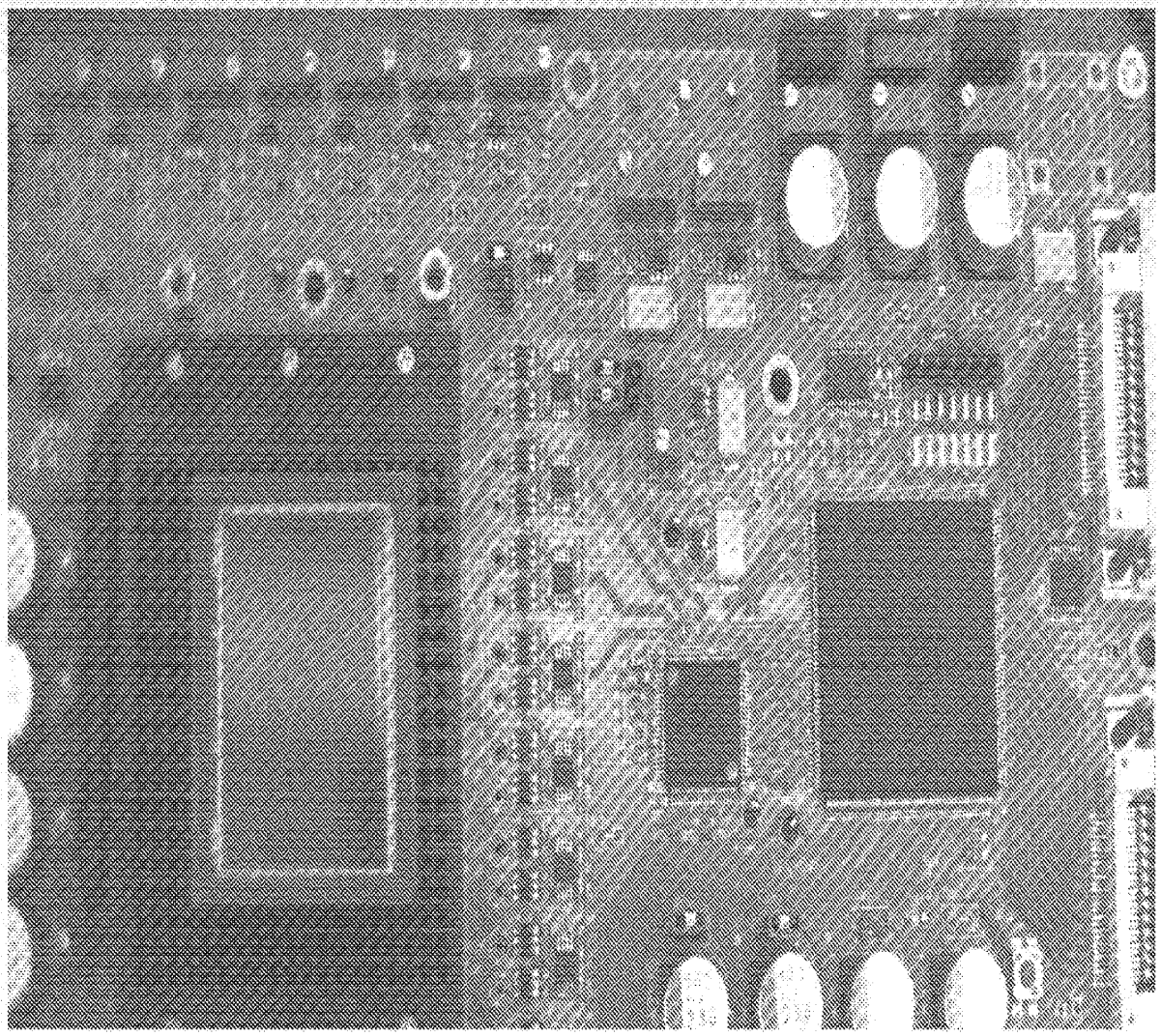
Sensor specifications



Specification	Value
Full Well charge	> 12.5 Ke⁻
Sensitivity	4.64 V/lux.s
Dark noise	< 13 e⁻
Conversion factor (10 bit mode)	~ 0.070 LSB/e⁻
Dynamic range	> 60 dB
Parasitic light sensitivity	< 1/60000
Dark current (10 bit mode)	22 LSB/s (@ room temp)
Fixed pattern noise (10 bit mode)	< 1 LSB
Power consumption	600 mW

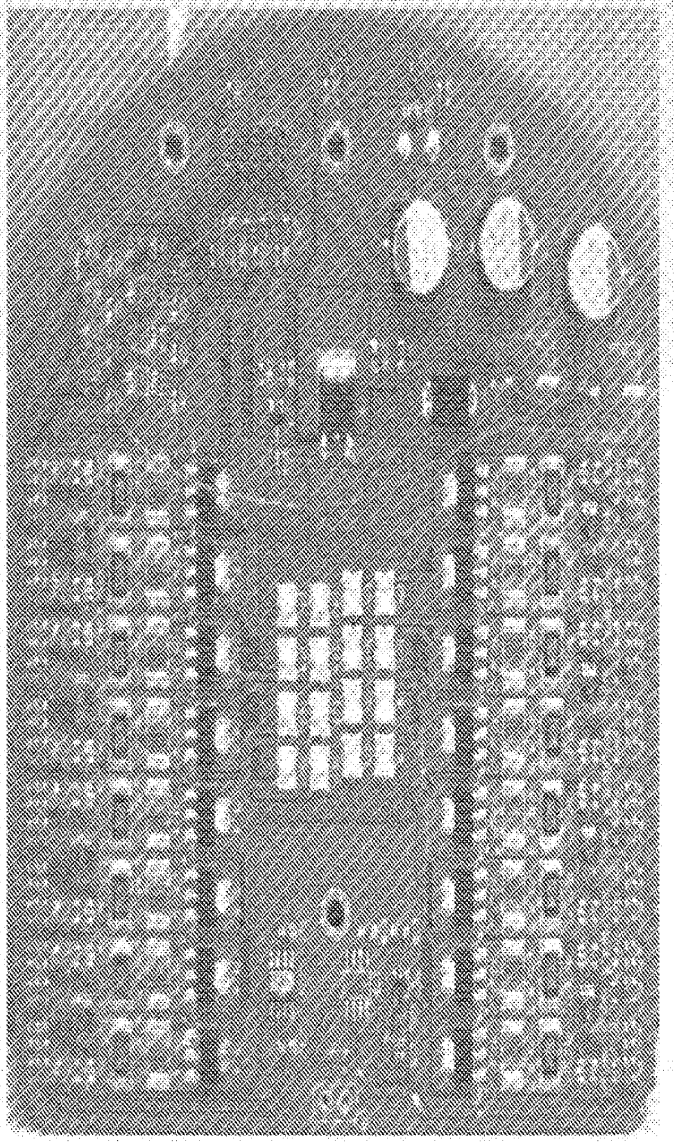
Example CMV2000

F/3, exposure 32ms, 300lux



Example CMV4000

F/3, exposure 32ms, 300 lux



Movie example CMV2000

Full resolution, 280 fps (340 fps max)



Summary

- Industry driven feature and specification list
- CMOSIS has developed new technologies:
  - 8T pixel architecture allowing pipelined global shutter with CDS
  - CDS in 8T pixel brings combination of low noise (high sensitivity) and excellent dynamic range
  - Pixel with very high shutter efficiency
  - High speed pipelined readout architecture with column ramp ADCs
  - High frame rate combined with excellent image quality due to on-chip analog and digital CDS
- Future CMOSIS standard and custom designed sensors:
  - Pixel technology allows trade-off in terms of noise and SNR_{max} with high DR
  - Various pixel pitch and pixel resolution
  - Increase of I/O speed

Optical intensity of light in layers of silicon with rear diffuse reflectors

Jeffrey E. Cotter[a)]
AstroPower, Inc., Newark, Delaware 19716-2000

(Received 17 October 1997; accepted for publication 21 March 1998)

Light trapping is essential to the performance of thin-layer polycrystalline silicon solar cells. One relatively new method of light trapping is the use of textured or pigmented dielectric layers on the rear surface which diffuse and reflect light reaching the rear surface. This article presents a one-dimensional optical model of thin silicon solar cells with such rear diffuse dielectric reflectors. Experimental front reflectance measurements and ray tracing simulations of thin, planar silicon layers with rear diffuse dielectric rear reflectors are presented and compared to the model with good agreement. Finally, an expression for the upper limit of the optical enhancement factor is developed for this type of light trapping. © *1998 American Institute of Physics*. [S0021-8979(98)08512-0]

I. INTRODUCTION

One of the key challenges for thin-layer polycrystalline silicon photovoltaic technologies is overcoming the relatively weak absorption of light in the solar spectrum near and below the band gap energy of silicon (1.1 eV). At typical thicknesses (10–35 μm), the absorber of a thin-layer polycrystalline silicon solar cell is transparent to a large fraction of the solar spectrum, and consequently its light-generated current is severely reduced. For this reason, thin silicon solar cell structures often incorporate some from of light trapping: altering the refractive and reflective properties of the two surfaces to trap light inside the solar cell.

Schemes based on randomizing reflecting textures are potentially very effective at trapping light and have the added benefit of conceptual simplicity. Goetzberger,[1] Yablonovitch and Cody,[2] for example, predict that a randomly textured silicon surface that behaves like a Lambertian emitter is especially well suited for light trapping. However, this type of surface is rarely incorporated in silicon solar cells (excluding)[3,4] perhaps because the most easily conceivable method of forming the surface, i.e., sand blasting or other abrasion techniques, would result in unacceptable surface damage. Recently, several researchers have been exploring the use of reflective dielectric coatings, which take advantage of either a random texture formed during their deposition (e.g., tin oxide,[5] zinc oxide,[6,7] titanium dioxide,[8] or thin-film diamond)[8] or incorporate pigments to reflect and scatter the light in the dielectric layer,[9] to improve the optical characteristics of polycrystalline thin-layer and amorphous thin-film silicon solar cells. Figure 1 illustrates this concept.

The diffuse reflector has three benefits to absorption of near-band gap light. First, light not absorbed by the thin silicon layer on the first pass is reflected back into the silicon layer. Second, the diffusely reflected light travels at an oblique angle to the surface normal increasing the average distance traveled through the thin silicon layer. Third, a fraction of the diffuse light reaching the front surface can be reflected again by total internal reflection back into the thin silicon layer.

This article first presents a model which predicts the intensity of light and the electron-hole pair generation profile in a thin silicon layer with a rear diffuse dielectric reflector. In the second part of this article, the model will be used to predict the wavelength-dependent, total front surface reflectance. Experimental measurements made on thin silicon layers with rear diffuse dielectric reflectors and ray tracing simulations are also presented to corroborate the model. Finally, the model will be used to derive an upper limit for the optical enhancement factor and predict the maximum light-generated current as a way to evaluate the potential of rear diffuse dielectric reflecting layers to achieve a high degree of light trapping in thin silicon solar cells.

II. OPTICAL MODEL OF LIGHT IN THE SILICON LAYER

The light traveling in a silicon layer with parallel planar surfaces and a rear diffuse dielectric reflector can be characterized by forward and reverse traveling fluxes. In each direction, the fluxes can be divided into direct (I_i) and diffuse (L_i) components. A valid first order approximation is that the diffuse fluxes behave according to Beer's law in one dimension, characterized by weighted-average absorption and transmission coefficients which account for the three-dimensional nature of diffuse light. In this model, the effects such as carrier-density-dependent free-carrier absorption and doping-density-dependent band gap narrowing are neglected. Furthermore, if the thin layer is relatively thick compared to the coherence length of sunlight in silicon ($\sim$0.3 μm), interference effects can also be neglected.

With these assumptions, it is only necessary to know the intensity of each of the fluxes at one point within the silicon layer. Then, the total intensity at any other point can be easily determined using the one-dimensional form of Beer's law and summing the four fluxes at that point. In this article, each of the fluxes are specified as they depart from each of the two silicon surfaces, as illustrated in Fig. 2.

Expressions for each I_i and L_i can easily be written by in terms the other I_i and L_i by inspection of Fig. 2,

a)Electronic mail: j.cotter@unsw.edu.au

 © 1998 American Institute of Physics

Copyright © 1998. All rights reserved.

SIONYX1403000015.0052

SAMSUNG EX. 1002 - 1253/4148

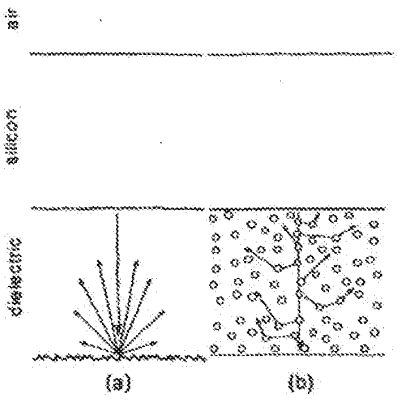


FIG. 1. Diagram of: (a) randomly textured rear dielectric reflector, (b) pigment added to rear dielectric layer to reflect and scatter light.

$$
\begin{aligned}
I_1 &= t_1 I_0 + (1-t_4)\exp(-kw) I_3, \\
I_2 &= t_2 \exp(-kw) I_1 + (1-t_3)\rho_{int}(1-\beta_{int}) I_2, \\
I_3 &= t_3 \rho_{int}(1-\beta_{int}) I_2 + (1-t_2)\exp(-kw) I_1, \\
I_4 &= t_4 \exp(-kw) I_3 + (1-t_1) I_0, \\
L_1 &= T_1 L_0 + (1-T_4)\exp(-Kw) L_3, \\
L_2 &= T_2 \exp(-Kw) L_1 + (1-T_3)\rho_{int}(L_2 + \beta_{int} I_2), \\
L_3 &= T_3 \rho_{int}(L_2 + \beta_{int} I_2) + (1-T_2)\exp(-Kw) L_1, \\
L_4 &= T_4 \exp(-Kw) L_3 + (1-T_1) L_0.
\end{aligned}
\tag{1}
$$

The incident fluxes are denoted by I_0 and L_0 and can represent the direct and diffuse components of sunlight, for example. The I_i or L_i are coupled by the transmission coefficients t_i or T_i, which represent the transmission of direct or diffuse light through the silicon surfaces, respectively. The exponential terms containing the product of w, the silicon layer thickness, and either k or K, the absorption coefficient

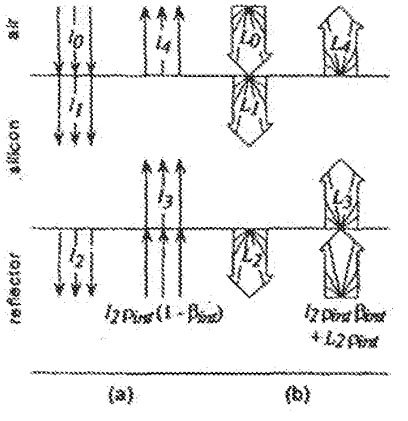


FIG. 2. Diagram of the four-fluxes model showing forward and reverse (a) direct fluxes (I_i), and (b) diffuse fluxes (L_i) leaving the silicon layer surfaces. The quantities ρ_{int} and β_{int}, which are the internal reflectance of the rear reflector and the fraction of internal light coupled from the direct to diffuse flux by the rear reflector, respectively, are also defined.

of direct and diffuse light, respectively, accounts for absorption of light in the silicon layer. Light inside the rear reflector is reflected by a factor ρ_{int}, and the fraction of the direct flux converted to the diffuse flux by each reflection in the rear reflector is described by the factor β_{int}. The reflected flux intensities are also indicated in Fig. 2. Although not explicitly written, each of the coefficients in Eq. (1) depend on the wavelength of light. Furthermore, absorption in the dielectric material is neglected here, but could be incorporated by including appropriate exponential terms.

These eight equations are more compactly expressed and more easily solved when in matrix form, i.e.,

$$\mathbf{I} = \mathbf{c}\cdot\mathbf{I} + \mathbf{d} \quad \text{and} \quad \mathbf{L} = \mathbf{C}\cdot\mathbf{L} + \mathbf{D},$$

where $\mathbf{I}$ and $\mathbf{L}$ are column vectors containing I_i and L_i, $\mathbf{c}$ and $\mathbf{C}$ contain the transmission and exponential absorption factors, and $\mathbf{d}$ and $\mathbf{D}$ contain the incident fluxes and the coupling of light from the direct flux to the diffuse flux by the rear diffuse reflector. The matrix algebra solutions of the above expressions are

$$\mathbf{I} = -[\mathbf{c}-\mathbf{I}]^{-1}\cdot\mathbf{d} \quad \text{and} \quad \mathbf{L} = -[\mathbf{C}-\mathbf{I}]^{-1}\cdot\mathbf{D}, \tag{2}$$

where $\mathbf{I}$ is the identity matrix. Since no light is coupled from the diffuse fluxes to the direct fluxes, $\mathbf{d}$ contains no $\mathbf{L}$ terms, and Eq. (2) can be relatively easily solved algebraically or numerically, especially using PC mathematics software.

In general, w, ρ_{int}, and β_{int} can be determined by separate experimental measurements (see Sec. III). k is known from published experimental data,[10] and expressions for t_i are well known for bare surfaces and single- or multilayer optical coatings.[11] For T_i and K, however, it is necessary to know or assume the angular distribution of diffuse light. For this work, it is assumed that the angular distribution of light is uniform inside the rear diffuse dielectric reflector. This assumption is valid for both cases where the textured bottom surface of the dielectric behaves like a Lambertian emitter and where light is scattered in random directions by pigments dispersed in the dielectric material. Then, the differential flux at any point on the silicon surface incident from inside the dielectric layer is described by the Lambertian distribution

$$d\Phi_L(\theta,\xi) = \phi\cos(\theta)\sin(\theta)\,d\theta\,d\xi, \tag{3}$$

where θ and ξ are the altitude (defined with respect to the surface normal) and azimuth angles and ϕ is the radiant intensity contained within a differential solid angle of $\sin(\theta)d\theta d\xi$.

The weighted-average transmission from the rear diffuse reflector into the silicon, i.e., T_3, can be found by integrating the product of Eq. (3) and an appropriate angle-dependent transmission function $t_3(\theta)$ and dividing by the total incident flux (after Goetzberger).[3] The limits of integration are the solid angle containing the flux distribution, in this case, the hemisphere defined by the bottom silicon surface.

$$T_3 = \frac{1}{\Phi_{total}}\int_0^{2\pi}\int_0^{\pi/2} t_3(\theta)\cdot d\Phi_L(\theta,\xi), \tag{4}$$

where $\Phi_{total} = \pi\phi$.

Copyright © 1998. All rights reserved.

SIONYX1403000015.0053

SAMSUNG EX. 1002 - 1254/4148

The Lambertian distribution cannot be assumed for the diffuse fluxes inside the silicon layer. Refraction at the reflector-silicon interface focuses the angular distribution according to Snell's law

$$n_{re\theta}\sin(\theta_{re\theta}) = n_{Si}\sin(\theta_{Si}),$$

where $n_{re\theta}$ and n_{Si} are the refractive indices in the dielectric reflector and the silicon layer, respectively, and $\theta_{re\theta}$ and θ_{Si} are similarly defined. The focused Lambertian distribution inside the silicon layer can be described by solving Snell's law for $\theta_{re\theta}$ and substituting for θ in Eq. (3):

$$\begin{aligned} d\Phi_R(\theta,\xi) &= \phi\cos\left[\arcsin\left(\frac{n_{Si}}{n_{re\theta}}\sin(\theta)\right)\right] \\ &\quad\times\sin\left[\arcsin\left(\frac{n_{Si}}{n_{re\theta}}\sin(\theta)\right)\right] \\ &\quad\times\left|\frac{d}{d\theta}\arcsin\left(\frac{n_{Si}}{n_{re\theta}}\sin(\theta)\right)\right| d\theta\,d\xi \\ &= \phi\left(\frac{n_{Si}}{n_{re\theta}}\right)^2\cos(\theta)\sin(\theta)\,d\theta\,d\xi. \end{aligned} \tag{5}$$

Note that most dielectric materials have refractive indices less than silicon ($n_{Si}\approx 3.53$ near 1.1 eV) and, for this case, all of the diffuse flux is contained within a solid angle defined by $\theta_R \le \arcsin(n_{re\theta}/n_{Si})$. The weighted-average transmission for diffuse light escaping through the front surface, T_4, and for diffuse light escaping back into the rear diffuse reflector, T_2, can be found by integrating the product of Eq. (5) and an appropriate angle-dependent transmission function. In this case, the limits of integration are the solid angle bounded by θ_R. Then,

$$T_{2,4} = \frac{1}{\Phi_{total}}\int_0^{2\pi}\int_0^{\theta_R} t_{2,4}(\theta)\cdot d\Phi_R(\theta,\xi), \tag{6}$$

where, again, $\Phi_{total} = \pi\phi$.

In general, the complexity of $t_i(\theta)$ makes closed-form solutions to Eqs. (4) and (6) difficult and numerical techniques are required. However, for a hypothetical ideal antireflection coating [i.e., $t_i(\theta) = 1$ for all angles except those satisfying criteria for total-internal reflection, where $t_i(\theta) = 0$], Eqs. (4) and (6) reduce to $T_2 = T_3 = 1$ and $T_4 = 1/n_{re\theta}^2$.

The diffuse fluxes travel, on average, a greater distance through the silicon layer, resulting in a greater effective absorption coefficient, K. An expression for K can be determined using a similar weighted-average approach. The fraction of diffuse light absorbed on a single pass through the silicon layer, as a function of altitude angle is

$$f_A(\theta) = 1 - \exp\left(-\frac{kw}{\cos(\theta)}\right). \tag{7}$$

Therefore, the weighted average fraction of diffuse light absorbed is given by the integral over the distribution:

$$f_A = \frac{1}{\Phi_{total}}\int_0^{2\pi}\int_0^{\theta_R} f_A(\theta)\cdot d\Phi_R(\theta,\xi), \tag{8}$$

which can be solved numerically. An effective absorption coefficient K can be defined by

$$f_A = 1 - \exp(-Kw), \tag{9}$$

which leads to an expression for K in terms of f_A

$$K = \frac{-\ln(1-f_A)}{w}. \tag{10}$$

In general, the ratio of K/k is less than the average path length, implying that the per-pass absorption enhancement factor is also less than the path-length enhancement factor. In the limit of vanishing absorption coefficient, the per-pass absorption enhancement factor approaches the path-length enhancement factor, which, for the focused Lambertian distribution, is

$$\frac{K}{k} \approx \frac{W}{w} = \frac{2n_{Si}}{n_{Si}+\sqrt{n_{Si}^2 - n_{re\theta}^2}}, \tag{11}$$

where W is the per-pass average path length for diffuse light. The value of W/w varies from 1.02 to 2.0 as $n_{re\theta}$ varies from 1.0 to n_{Si}.

One implicit assumption contained in Eqs. (6) and (11) is that the distribution of the diffuse flux is not distorted as it travels through the silicon layer or as it is reflected by the silicon surfaces. Absorption will tend to attenuate the distribution at high angles of θ due to the longer distance traveled. Also, transmission at the surfaces tend to attenuate the distribution of the reflected portion of the diffuse flux for θ below the critical angle for total internal reflection. These effects are small, however, as will be seen in the experimental and ray tracing results of Sec. III.

Finally, from the entrant flux intensities at the silicon surfaces, I_1, L_1, I_3, and L_3, the total flux profile, $F(z)$, and carrier generation profile, $g(z)$, can be written for a given wavelength of light

$$\begin{aligned} F(z) &= I_1\exp(-kz) + L_1\exp(-Kz) \\ &\quad + I_3\exp(-k(w-z)) + L_3\exp(-K(w-z)), \end{aligned} \tag{12}$$

and

$$\begin{aligned} g(z) &= I_1 k\exp(-kz) + L_1 K\exp(-Kz) + I_3 k \\ &\quad\times\exp(-k(w-z)) + L_3 K\exp(-K(w-z)). \end{aligned} \tag{13}$$

Note that the units of $F(z)$ and $g(z)$ are determined by those expressed in the incident fluxes, I_0 and L_0. Therefore, for example, I_0 and L_0 must be expressed in photons-s^{-1}-cm^{-2} for $g(z)$ to have units of electron-hole pairs-s^{-1}-cm^{-3}.

III. FRONT REFLECTION IN THIN PLANAR SILICON LAYERS WITH REAR DIFFUSE DIELECTRIC REFLECTORS

Measurement of front-surface reflection of thin silicon layers with rear dielectric reflectors over the wavelength range of 750–1250 nm is a straightforward way to corroborate the model outlined above. For shorter wavelengths, light is relatively strongly absorbed in the silicon layer, and the front reflection is dominated by the front surface. For longer wavelengths, light is relatively weakly absorbed, and light is

Copyright © 1998. All rights reserved.

SIONYX1403000015.0054

SAMSUNG EX. 1002 - 1255/4148

reflected and scattered by the rear reflector many times before escaping back through the front surface. Therefore, the model can be tested at two extremes and, importantly, through the transition between them.

A. Fabrication of diffuse dielectric reflectors

Two types of rear diffuse reflector were used in this work. The first was a commercially available, highly reflective, diffuse reflector similar to white standards commonly used for calibration of integrating spheres. The second was constructed by mixing 1 or 5 vol. % of titanium dioxide powder with a thermoplastic of known refractive index. The titania-loaded plastic reflector was formed by a crude casting technique.

B. Measurement and extraction of β_{int} and ρ_{int}

The external total and external diffuse-component reflectivities ($R_{ext,tot}$ and $R_{ext,dif}$) of the dielectric reflectors were measured over the wavelengths between 750 and 1250 nm using a Perkin Elmer Lambda-9 spectrophotometer. A gloss trap in the integrating sphere allowed $R_{ext,tot}$ and $R_{ext,dif}$ to be measured separately. From these two measurements, the external direct-component reflectance ($R_{ext,dir}$) can be calculated using

$$R_{ext,dir} = R_{ext,tot} - R_{ext,dif}. \tag{14}$$

The measurements were made in air, therefore to calculate β_{int} and ρ_{int} it is necessary to account for reflection at the reflector-air interface. The fraction β_{int} can be determined by analyzing the direct-component reflectance data

$$\beta_{int} = 1 - \frac{R_{ext,dir} - r}{(R_{ext,dir} - r)\cdot r + t^2}, \tag{15}$$

where t and r ($r = 1 - t$) are the transmission and reflection coefficients for direct light due to the refractive index change at the surface, which are given by Eq. (17) in this case. Because $R_{ext,dir} = r$ was measured for each reflector at all wavelengths, $\beta_{int} = 1$.

For the case where $\beta_{int} = 1$, the internal reflectance, ρ_{int}, can be calculated from the measured external total reflectance, $R_{ext,tot}$, by accounting for the effect of the change in refractive index at the surface

$$\rho_{int} = \frac{R_{ext,tot} - r}{R_{ext,tot}R + Tt - Rr}, \tag{16}$$

where t and r are the transmission and reflection coefficients for direct light, respectively, and T and R ($R = 1 - T$) are the transmission and reflection coefficients for diffuse light escaping into air, respectively. The values of t and T are calculated using Eqs. (17) and (4), respectively, and the method outlined in Sec. II.[12] Equation (16) is commonly known as the Saunderson correction, and is often used to correct surface transmission effects for optical measurements of pigment-loaded materials.[13]

Figure 3 shows the measured $R_{ext,tot}$ and calculated ρ_{int} of the dielectric reflectors used here. The small bumps in the data at $\lambda = 860$ nm are due to the fact that the spectrophotometer changes detectors at that wavelength. The obvious notch in the measured reflectance of the two pigment-loaded reflectors at $\lambda = 1140$ nm is due to an absorption peak in the thermoplastic medium, which reduces the reflectance at that wavelength. The transmission of a clear slab of the thermoplastic is also shown in Fig. 3, indicating this absorption peak at $\lambda = 1140$ nm.

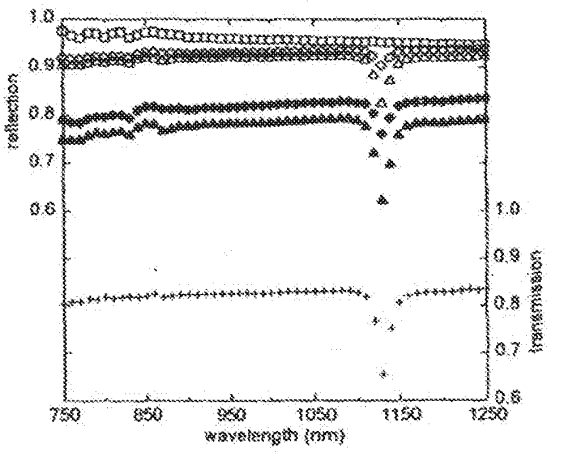


FIG. 3. Measured external total reflectance (♣-1% titania, ♦-5% titania) and calculated internal reflectance (Δ-1% titania, ◇-5% titania, □-diffuse white reflector) of various dielectric reflectors, and the transmission characteristics of a slab of pure thermoplastic (+) showing an absorption peak at 1140 nm.

C. Measurement and prediction of front reflection for thin silicon layers

Thin silicon layers were prepared by chemically thinning double-sided polished, 3–5 Ω cm, (100) silicon wafers in a 22 wt. % NaOH solution at 105–110 °C. The thicknesses were measured with a microscope. For a polished silicon surface with no optical coating, and assuming randomly polarized light, an appropriate expression for $t_i(\theta)$ is

$$t_i(\theta) = 1 - \frac{1}{2}\left[\frac{n_i^2\cos(\theta) - \sqrt{n_i^2 - n_{i-1}^2\sin(\theta)^2}\,n_{i-1}}{n_i^2\cos(\theta) + \sqrt{n_i^2 - n_{i-1}^2\sin(\theta)^2}\,n_{i-1}}\right]^2 - \frac{1}{2}\left[\frac{n_{i-1}\cos(\theta) - \sqrt{n_i^2 - n_{i-1}^2\sin(\theta)^2}}{n_{i-1}\cos(\theta) + \sqrt{n_i^2 - n_{i-1}^2\sin(\theta)^2}}\right]^2, \tag{17}$$

where n_i and n_{i-1} are the refractive indices on either side of the interface, and θ is defined on the incident side of the surface. When $n_i < n_{i-1}$ and $\theta \geq \theta_c = \arcsin(n_i/n_{i-1})$, which are the conditions for total internal reflection, $t_i(\theta \geq \theta_c) = 0$.

The refractive index of silicon follows a well-behaved dispersion relation between 750 and 1250 nm, and is given by[10]

$$n_{Si}(\lambda) = \sqrt{1 + \frac{(\lambda\cdot 10^{-3})^2}{0.0938(\lambda\cdot 10^{-3})^2 - 0.00\,866}},$$

for λ expressed in nm.

Copyright © 1998. All rights reserved.

SIONYX1403000015.0055

SAMSUNG EX. 1002 - 1256/4148

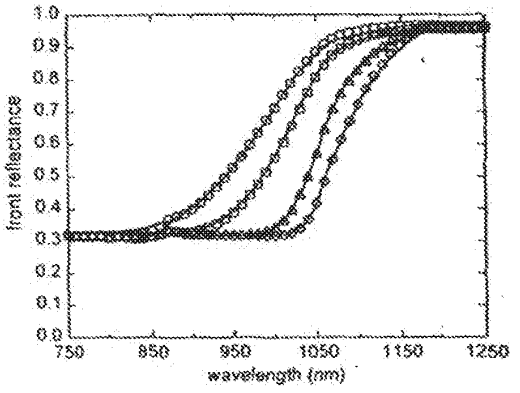


FIG. 4. Front reflectance of silicon layers of varying thicknesses (○-27.5 μm, □-57.5 μm, △-220 μm, ◇-480 μm) using the detached diffuse white reflector ($n_{refl}=1$) and model predictions (solid line).

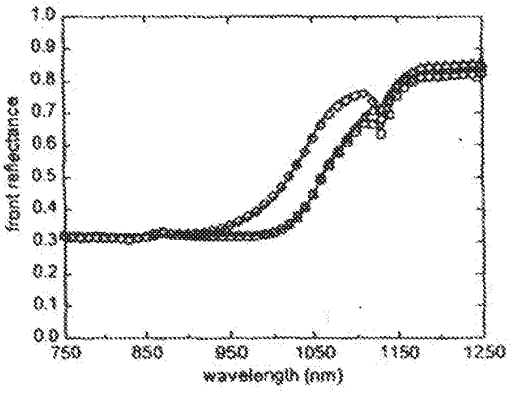


FIG. 5. Front reflectance of silicon layers of varying thicknesses with the titanium dioxide-loaded thermoplastic (○-57.5 μm, 1% titania, □-220 μm, 1% titania, △-220 μm, 5% titania) attached diffuse rear reflector ($n_{refl}=1.66$) and model predictions (solid line).

The two dielectric reflectors were attached to the thinned silicon layers. For the white standard reflector, the reflector was held against the silicon layer and a small air gap was present between the silicon layer and the reflector. Therefore, the effective refractive index for this reflector is $n_{refl}=1$. The titania-loaded thermoplastic reflector was cast directly onto the thin silicon layers, and since the volumetric fraction of pigment is small (≤5%), the effective refractive index of the mixture was assumed equal to that of the thermoplastic, given by[14]

$$n_{refl}(\lambda)=1.663\,869+\frac{1\,284\,123}{(10\cdot\lambda)^2}+\frac{3.804\,718\times10^{12}}{(10\cdot\lambda)^4},$$

for λ expressed in nm.

From the fluxes defined in Fig. 1, the front reflectance of thin silicon layers with rear dielectric reflectors can be written

$$R_{front}=\frac{I_4+L_4}{I_0+L_0},$$

where I_4 and L_4 are given by the solution of Eq. (2). Since a direct beam of monochromatic light was used to illuminated the samples in this case, L_0 is zero. Figures 4 and 5 show the results of front reflectance measurement for the two reflector materials with different thicknesses of silicon, along with the model predictions of Sec. II.

The data support the model very well and lend credit to the various assumptions made in Sec. II. Again, the small discontinuity in the measured front reflectance at $\lambda=860$ nm is due to the spectrophotometer, which changes detectors at this wavelength.

D. Comparison to three dimensional ray tracing simulations

To support the model of Sec. II for rear diffuse dielectric reflectors of higher refractive index, detailed ray tracing analysis in three dimensions was carried out. The ray tracing simulator uses a recursive algorithm to keep track of the rays as they are reflected, transmitted, or scattered. Below a certain intensity, the simulator switches to a Monte–Carlo algorithm, whereby rays are transmitted, reflected, or scattered with a probability proportional to the value of the transmission, reflection, or scattering coefficient. The hybrid recursive/Monte–Carlo algorithm leads to fast convergence and reduces the number of trials required to obtain a statistically significant result.

Both types of rear diffuse dielectric layer described in Fig. 1 were simulated. Rays incident on a textured surface at the rear of the dielectric reflector are reflected with an angular distribution statistically equivalent to a Lambertian distribution. Rays incident on pigments in the rear dielectric reflector are scattered with an angular distribution statistically equivalent to a uniform angular distribution.

The front reflection was simulated for a 100-μm-thick silicon layer with planar front and rear surfaces (no optical coatings), and $\beta_{int}=1.0$, and $\rho_{int}=1.0$. Six different refractive indices were simulated ($n_{refl}=1.0$, 1.5, 2.0, 2.5, 3.0, and $n_{refl}=n_{Si}$) for both textured and pigmented reflectors. The results of the ray tracing simulation are shown in Fig. 6, along with the model predictions. Note that the worse-case deviation between the ray trace simulation results and the

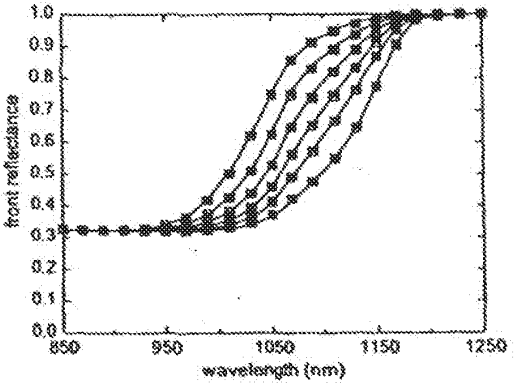


FIG. 6. Ray trace simulation (□-textured, ×-pigmented) compared to model predictions (solid lines) of front reflectance for reflectors of different refractive indices (left to right: $n_{refl}=1.0$, 1.5, 2.0, 2.5, 3.0, and $n_{refl}=n_{Si}$).

Copyright © 1998. All rights reserved.

SIONYX1403000015.0056

SAMSUNG EX. 1002 - 1257/4148

model predictions due to the assumptions described in Sec. II regarding the distortion of the optical distribution occurs for $n_{refl}=n_{Si}$ between 950 and 1110 nm, however this deviation is small and not apparant in Fig. 6.

IV. THE UPPER LIMIT ON OPTICAL ENHANCEMENT FACTOR AND SHORT CIRCUIT CURRENT FOR REAR DIFFUSE REFLECTORS

Yablonovitch and Cody[2] first performed this type of analysis for the case where the rear surface of the silicon was randomly textured. They showed that the upper limit for optical enhancement factor, which is the ratio of effective optical thickness to physical thickness, is given by $Z=4n_{Si}^2$, which, for near-band gap light in silicon, is approximately 49. Here, the analysis is extended to include diffuse reflecting dielectric layers on the rear surface.

Consider a thin silicon layer in air with an ideal antireflection coating on the front surface and an ideal diffuse reflecting dielectric layer on the rear surface. The ideal diffuse reflecting dielectric layer has unity reflectance and a uniform angular distribution of light in its interior. Also, assume that light is weakly absorbed in the silicon layer, and finally assume that, on its first incidence, light is immediately coupled into the diffuse flux described by the focused Lambertian distribution [Eq. (5)]. Although this final assumption is not strictly true in real situations, it is useful for finding the upper limit on the optical enhancement factor.

The optical enhancement factor, Z, can be defined as the equivalent thickness of silicon, Zw, that a nonlight-trapping layer of silicon requires to absorb the same amount of light as a given light trapping structure of thickness w. Then,

$$A_{LT}=1-\exp(-kZw), \tag{18}$$

where A_{LT} is defined as the fraction of incident light absorbed by a light trapping structure and the right-hand side is the fraction of light absorbed by a nonlight-trapping structure of thickness Zw. An expression for A_{LT} can be derived using the above mentioned assumptions and the optical model described in Sec. II. First, an expression for L_1 and L_3 are written in matrix notation,

$$\begin{bmatrix} L_1 \\ L_3 \end{bmatrix} = -\left[\begin{bmatrix} 0 & (1-T_4)\exp(-Kw) \\ \exp(-Kw) & 0 \end{bmatrix} - I\right]^{-1} \times \begin{bmatrix} I_0 \\ 0 \end{bmatrix},$$

for which the solutions are

$$L_1=\frac{I_0}{1-(1-T_4)\exp(-2Kw)},$$

and

$$L_3=\frac{I_0\exp(-Kw)}{1-(1-T_4)\exp(-2Kw)}.$$

The fraction of light absorbed by the light trapping structure is then

$$A_{LT}=\frac{1}{I_0}(L_1+L_3)(1-\exp(-Kw)) = \frac{1-\exp(-2Kw)}{1-(1-T_4)\exp(-2Kw)}. \tag{19}$$

This expansion can be simplified by noting that, with the assumption that light is weakly absorbed (i.e., $2Kw\ll 1$), $\exp(-2Kw)\approx 1$, and $1-\exp(-2Kw)\approx 2Kw$. Also, for the ideal antireflection coating defined previously, $T_4=1/n_{refl}^2$. Therefore, Eq. (19) simplifies to

$$A_{LT}=2Kwn_{refl}^2.$$

Substituting this expression into Eq. (18) and solving for Z, realizing that, for weakly absorbed light, $\ln(1-2Kwn_{refl}^2)\approx -2Kwn_{refl}^2$,

$$Z=2\frac{K}{k}n_{refl}^2. \tag{20}$$

For small absorption coefficient, K/k is approximately given by Eq. (11). In this case, Eq. (20) is analogous to Yablonovitch and Cody's result, reducing to $Z=4n_S^2$ for $n_{refl}=n_S$.

It is immediately obvious from Eq. (20) that a high refractive index for the dielectric is desirable for maximum enhancement factor. Candidate materials include common transparent dielectric materials, transparent conducting oxides, direct-band gap semiconductors with band gap energy greater than that of silicon and white reflecting materials. Table I lists some possible materials that could be used, assuming that a deposition technique which yields a suitably textured surface is available or that it is possible to incorporate pigments into the material. Table I also lists the calculated upper limit of optical enhancement factor for these materials.

Finally, with the ideal antireflection coating and ideal rear diffuse reflector assumptions described above, assuming perfect collection efficiency for generated charge carriers, and using terrestrial solar spectrum data,[15] an upper limit on the light generated current can be calculated. Figure 7 shows the calculated result as a function of refractive index and solar cell thickness. Again, it is apparant that high refractive index is desired for maximum current generation.

TABLE I. Refractive index and optical enhancement factor for various dielectric materials, conducting oxides, and direct-band gap semiconductors with band gap higher than that of silicon.

Dielectric material	Refractive index	Z
Air (i.e., detached)	1.0	2.04
SiO_2, glasses, *EVA*[a]	1.45–1.65	4.4–5.8
Thermoplastic used in Sec. III	≈1.66	5.9
SnO_2, ZnO	1.9, 1.9	7.8, 7.8
ZnS, TiO_2	2.3, 2.4	12.0, 13.3
C, SiC, ZnSe	2.4, 2.57, 2.7	13.3, 15.7, 17.7
GaP, InP, GaAs	3.08, 3.33, 3.42	25.5, 33.3, 37.5

[a]A common module encapsulant material.

Copyright © 1998. All rights reserved.

SIONYX1403000015.0057

SAMSUNG EX. 1002 - 1258/4148

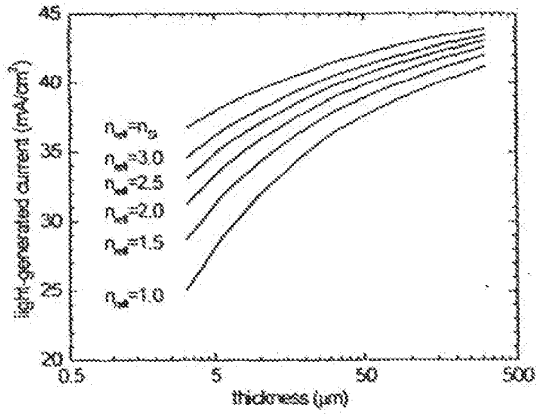


FIG. 7. Predicted maximum light-generated current as a function of solar cell thickness and reflector refractive index.

V. CONCLUSIONS

The four fluxes approach presented here is a compact representation of the optics of untextured thin silicon solar cells with diffuse rear dielectric reflectors. It accounts for the forward and reverse traveling direct and diffuse components and the coupling of light between them. Using weighted-average transmission coefficients, the three-dimensional nature of diffuse fluxes can be reduced to one dimension, simplifying analysis. If the Lambertian distribution is known or assumed in the dielectric layer, the focused Lambertian predicted from Snell's law is an appropriate description of the diffuse fluxes inside the silicon layer. Experimental measurements and ray tracing simulations support this model for the case where the refractive index of the rear diffuse reflector is lower than or equal to that of silicon.

The work of Yablonovitch and Cody[2] was extended to develop an upper limit to the optical enhancement factor for silicon solar cells incorporating diffuse rear dielectric layers. This result, along with predicted maximum light-generated current, indicates that a high refractive index as well as high reflectance is needed for a high degree of light trapping with rear diffuse dielectric reflectors.

ACKNOWLEDGMENTS

The author would like to thank Robert B. Hall and Michael G. Mauk of AstroPower, Inc. for their valuable discussions, Steven Hegedus of the Institute of Energy Conversion at the University of Delaware for his assistance with the reflectance measurements, and David Thorp of the Photovoltaic Special Research Center at the University of New South Wales for his help developing the ray tracing simulator and his comments on this manuscript.

[1] A. Goetzberger, in *Proceedings of the 15th IEEE Photovoltaic Specialists Conference* (IEEE, New York, 1981), p. 867.
[2] E. Yablonovitch and G. D. Cody, IEEE Trans. Electron Devices ED-29, 300 (1982).
[3] H. W. Deckman and J. H. Dunsmuir, Appl. Phys. Lett. 42, 377 (1983).
[4] M. Cudzinovic and B. Sopori, in *Proceedings of the 25th IEEE Photovoltaic Specialists Conference*, (IEEE, New York, 1996), p. 501.
[5] J. M. Gee, R. Gordon, and H. Liang, in *Proceedings of the 25th IEEE Photovoltaic Specialists Conference*, (IEEE, New York, 1996), p. 736.
[6] K. Winz, C. M. Fortmann, Th. Eickhoff, C. Beneking, B. Rech, O. Kluth, and H. Wagner, in *Proceedings of the 25th IEEE Photovoltaic Specialists Conference*, (IEEE, New York, 1996), p. 1147.
[7] H. Takato, M. Yamanaka, Y. Hayashi, R. Shimokawa, I. Bide, S. Gohda, F. Nagamine, and H. Tsuboi, Jpn. J. Appl. Phys. 31, 1665 (1992).
[8] J. M. Gee, H. L. Tardy, T. D. Hund, R. Gordon, and H. Liang, in *Proceedings of the 1st World Conference on Photovoltaic Energy Conversion*, (IEEE, New York, 1994), 1274.
[9] J. E. Cotter, Ph.D. dissertation, University of Delaware, 1996.
[10] M. A. Green and M. J. Keevers, Prog. Photovoltaics 3, 189 (1995).
[11] E. Hecht, *Optics* (Addison–Wesley, Reading, MA, 1978).
[12] For $n_{ref}\sim 1$, $t=T\sim 1$ while for $n_{ref}\sim 1.66$, $t\sim 0.938$, and $T\sim 0.321$, assuming a uniform angular distribution of diffuse light within the dielectric reflector.
[13] H. G. Völz, *Industrial Color Testing: Fundamentals and Techniques* (VCH, Weinheim, Germany, 1995).
[14] Cargill Laboratories, Inc., physical constants data sheet.
[15] R. Hulstrom, R. Bird, and C. Riordan, Sol. Cells 15, 365 (1985).

Copyright © 1998. All rights reserved.

SIONYX1403000015.0058

SAMSUNG EX. 1002 - 1259/4148

Comparison of structure and properties of femtosecond and nanosecond laser-structured silicon

C. H. Crouch,[a] J. E. Carey, J. M. Warrender, M. J. Aziz, and E. Mazur[b]
Division of Engineering and Applied Sciences, Harvard University, Cambridge, Massachusetts 02138

F. Y. Génin
Lawrence Livermore National Laboratory, Livermore, California 94550

(Received 8 August 2003; accepted 7 January 2004)

We compare the optical properties, chemical composition, and crystallinity of silicon microstructures formed in the presence of SF_6 by femtosecond laser irradiation and by nanosecond laser irradiation. In spite of very different morphology and crystallinity, the optical properties and chemical composition of the two types of microstructures are very similar. The structures formed with femtosecond (fs) pulses are covered with a disordered nanocrystalline surface layer less than 1 μm thick, while those formed with nanosecond (ns) pulses have very little disorder. Both ns-laser-formed and fs-laser-formed structures absorb near-infrared (1.1–2.5 μm) radiation strongly and have roughly 0.5% sulfur impurities. © *2004 American Institute of Physics.*
[DOI: 10.1063/1.1667004]

Many types of micrometer-scale surface structures develop spontaneously on silicon surfaces after repeated pulsed laser irradiation.[1] In particular, sharp conical microstructures form on silicon surfaces in the presence of SF_6 with either femtosecond (fs)[2] or nanosecond (ns)[3] laser irradiation. Mazur and co-workers previously found that fs-laser-formed structures exhibit below-band gap light absorption and photocurrent generation;[4,5] these remarkable optoelectronic properties are attributed to sulfur impurities in a microcrystalline surface layer.[4,6] Although the fs-laser-formed and ns-laser-formed structures resemble one another superficially, the differences in formation conditions and morphology suggest that the formation mechanisms of the two types of structures differ significantly. We set out to determine whether the optoelectronic properties, chemical composition, and crystallinity of the ns-formed and fs-formed structures also differ.

We made samples by irradiating a silicon wafer with a train of laser pulses in a vacuum chamber backfilled with SF_6.[4] (Mazur and co-workers found previously that the doping, resistivity, and crystal plane of the substrate do not affect the optical properties.[6]) The pressure of SF_6 was chosen to match the conditions used in initial reports of these structures (0.67 bar of SF_6 with fs pulses[2] and 1 bar of SF_6 with ns pulses[3]). A regeneratively amplified Ti:sapphire laser delivered a train of 800 nm, 100 fs pulses with a Gaussian spatial profile; the average fluence of the laser spot was 8 kJ/m^2. A KrF^+ excimer laser delivered a train of 248 nm, 30 ns laser pulses with a flat-top spatial profile and a fluence of 30 kJ/m^2. Irradiation creates an array of structures on the sample surface only in the region illuminated by the laser.

We structure areas up to 10 mm$\times$10 mm by scanning the laser beam across the sample. The average number of laser pulses on any part of the surface is determined by the scan speed, the size of the laser spot on the sample surface, and the laser repetition rate. To produce fully developed spikes, an average of 500 laser pulses was delivered to each area with fs pulses,[4] and an average of 1500 laser pulses with ns pulses.[3]

Images of the structures are shown in Fig. 1. The structures formed with the fs laser are one-fifth the size of those formed with the ns laser. The fs-formed structures are roughly 8 μm tall and separated by 4 μm; the ns-formed structures are roughly 40 μm tall and separated by 20 μm. The tips of the fs-formed structures are at the level of the original surface of the wafer [Fig. 1(e)], while the ns-formed structures protrude above the original surface [Fig. 1(f)]. Fi-

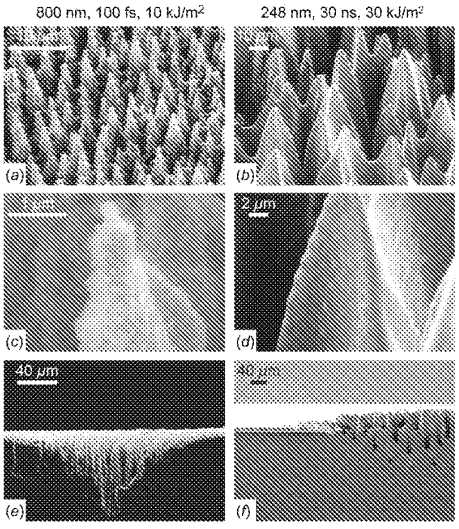


FIG. 1. Scanning electron micrographs of laser-microstructured Si surface formed in SF_6 [(a), (c), (e)] with fs laser pulses, and [(b), (d), (f)] with ns laser pulses. In (a)–(d) the sample is viewed at 45° to the normal; in (e) and (f) the sample is snapped in half and viewed edge-on.

[a]Electronic mail: mazur@physics.harvard.edu
[b]Present address: Dept. of Physics & Astronomy, Swarthmore College, Swarthmore, PA 19081.

 © 2004 American Institute of Physics

SIONYX1403000015.0059

SAMSUNG EX. 1002 - 1260/4148

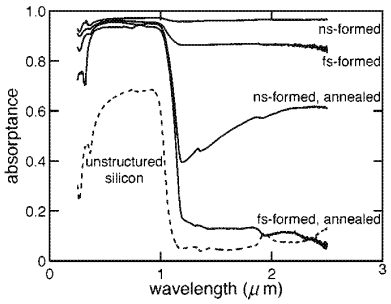


FIG. 2. Dependence of absorptance (A) on wavelength of fs-laser-formed and ns-laser-formed microstructures, before and after thermal annealing at 875 K for 45 min in flowing Ar. The absorptance of the unstructured Si substrate is also shown.

nally, the fs-formed structures are covered with nanoparticles 10–50 nm in diameter that appear to have been deposited on the structures [Fig. 1(c)], while the surface of the ns-formed structures is much smoother, with 500 nm size protrusions that appear to grow out of the surface [Fig. 1(d)].

We measured total hemispherical (specular and diffuse) reflectance (R) and transmittance (T) to determine the absorptance ($A=1-R-T$) of the structured surfaces. Measurements were performed with a Hitachi U-4001 UV-VIS spectrophotometer equipped with an integrating sphere detector. Figure 2 shows the wavelength dependence of the absorptance of both structured surfaces and of the unstructured substrate silicon. The absorptance of the ns- and fs-formed structures is very similar: near-unity, featureless absorptance from 0.4 to 1 μm, a small decrease in absorptance around 1.1 μm (the band edge of ordinary silicon), and strong featureless absorptance from 1.1 to 2.5 μm. The absorptance at wavelengths longer than 1.1 μm is particularly remarkable, as unstructured silicon is nearly transparent at these below-band gap wavelengths. The absorptance of the ns-structured material (98% in the visible, 95% in the infrared) is somewhat stronger than that of the fs-structured material (95% in the visible, 85% in the infrared).

Annealing the structured surfaces at 875 K for 45 min in flowing Ar leaves the visible absorptance essentially unchanged, but dramatically decreases the below-band gap absorptance (Fig. 2). The below-band gap absorptance of the ns-structured material changes less with annealing than that of the fs-structured material, and further annealing of the ns-structured material for up to 12 h causes little additional change. The morphology of the structures observed with scanning electron microscopy is unchanged by annealing at 875 K.[6] These observations suggest that the visible absorptance is due to amplification of the intrinsic visible absorptance of silicon by multiple reflections from the rough surface, but the below-band gap absorptance must come from electronic structure changes that are affected by annealing. (In the 40-μm-deep ns-formed structures, the below-band gap absorptance should also be significantly amplified by multiple reflections; geometric effects may be less important to the below-band gap absorption in the fs-formed structures because these infrared wavelengths are not much less than the 8 μm structure depth.)

Both the fs-structured and the ns-structured material exhibit photocurrent generation at wavelengths from 0.4 to 1.65 μm; annealed samples have the greatest photoresponsivity. Both the fs-structured and the ns-structured materials, when annealed, have a photoresponsivity on the order of 10 mA/W in the near infrared, with the responsivity at 1.31 μm roughly twice that at 1.55 μm.[5] The infrared photoresponsivity is orders of magnitude lower in unannealed samples, although the below-band gap absorptance is several times greater; we surmise that annealing dramatically increases the mobility of the photocarriers, and the increased mobility more than compensates for the loss in absorptance.

Mazur and co-workers found previously that fs structuring must take place in the presence of sulfur to produce featureless, near-unity below-band gap absorption; structures formed in air or in vacuum do not absorb strongly at wavelengths longer than 1.1 μm.[7,8] Likewise, ns-formed structures formed in air do not absorb at below-band gap wavelengths. Sulfur impurities in the structures therefore appear to be critical to the below-band gap absorption.

To determine the concentration of sulfur impurities, we performed Rutherford backscattering spectrometry (RBS) and ion channeling on the structured samples, and compared the measured RBS spectra to simulated spectra from planar material. We measured the backscattering spectrum from 2.0 MeV He^+ with an annular solid state detector. As the RBS signal from deeper sulfur is masked by the silicon signal, the spectrum measures only the average sulfur concentration in the uppermost 100 nm of the surface. To simplify the RBS spectra, the surface oxide layer, which also includes fluorine impurities, is removed from the samples by etching for 4 min in 5% HF; etching has no effect on the optical properties or surface morphology.

The RBS spectra of the fs-structured samples indicate that the sulfur concentration in the uppermost 100 nm is 0.7 ± 0.1 at. % before annealing and 0.5 ± 0.1 at. % after annealing. The sulfur signal obtained with ion channeling is slightly lower than that obtained with randomly aligned RBS, suggesting that some of the sulfur impurities are substitutional. The fs-structured samples channel poorly ($\chi_{\min}^{(Si)}$ $\sim$50%), however, and the reduction in sulfur signal with channeling is comparable in magnitude to the possible sources of error. Hence we can only determine that between 20% and 70% of the sulfur in the unannealed fs-structured sample is substitutional, and we cannot determine how much sulfur is substitutional in the annealed fs-structured sample. In the ns-structured samples, the sulfur concentration in the observable near-surface region is 0.5 ± 0.1 at. % before annealing, and 0.4 ± 0.1 at. % after annealing. The ns-structured samples show much stronger silicon channeling ($\chi_{\min}^{(Si)}$ $=5.6\%$ before and 6.6% after annealing), and nearly half of the sulfur is substitutional ($43\%\pm7\%$ before and 48% $\pm8\%$ after annealing). The sulfur concentration is therefore very similar in the two types of structures, but much more of the affected material in the ns-structured samples is single crystal than in the fs-structured samples, and a great deal of the sulfur is definitely substitutional in the ns-structured samples. The sulfur may or may not be incorporated differently into the silicon in the two types of structures.

Given that annealing changes the optical properties dramatically, but only reduces the amount of observable sulfur by about 20%, it is likely that the local environment of the

SIONYX1403000015.0060

SAMSUNG EX. 1002 - 1261/4148

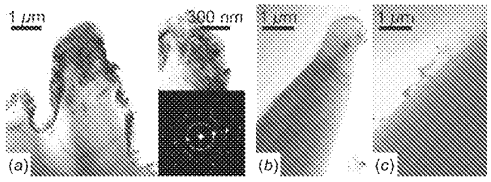


FIG. 3. Bright-field transmission electron micrographs of (a) cross section of fs-laser-formed microstructure [insets: (upper panel) higher magnification view of disordered material, (lower panel) selected area electron diffraction pattern obtained from the tip of the sample]; (b) cross section of tip of ns-laser-formed microstructure; and (c) cross section of side of ns-laser-formed microstructure.

sulfur impurities is important to the optical properties. To learn more about the material structure, we examined cross sections of the structures with bright-field transmission electron microscopy (TEM). Figure 3 shows micrographs of a fs-structured sample [Fig. 3(a)] and a ns-structured sample [Figs. 3(b) and 3(c)]. The fs-formed structures consist of a core of undisturbed silicon covered with a highly disordered layer of silicon less than 1 μm thick including nanocrystallites, nanopores, and sulfur impurities. Selected area diffraction [inset to Fig. 3(a)] indicates that the core is crystalline and the surface layer is polycrystalline or microcrystalline; energy dispersive x-ray spectroscopy detects roughly 1% sulfur impurities in the disordered layer but none in the core.[6] The TEM images and diffraction patterns obtained from annealed samples are similar.[6] The ns-formed structures likewise have a crystalline core, but the disordered layer is even thinner (200 nm or less) and covers only parts of the structures; the tips of the structures are free of visible disorder. Although the bases of the ns-formed structures [visible in Fig. 1(f)] cannot be observed in TEM, they are visible to ion channeling, which averages over the projected surface. Hence the observed good channeling indicates that even at the bases, the surface of the ns-formed structures cannot be as disordered as that of the fs-formed structures.

How do such different structures have such similar optoelectronic properties? In both the ns- and fs-formed structures, sulfur is required for strong below-band gap absorptance, and thermal annealing reduces the absorptance strongly while reducing the observable sulfur content by only 20% and having no obvious effect on the crystallinity. The disordered layer covering the fs-formed structures is not essential for below-band gap absorption, as both TEM and RBS indicate that the ns-formed structures are nearly single crystal. Most likely, laser structuring incorporates sulfur into silicon in an optically active configuration; then, during thermal annealing, some of the sulfur is deactivated by complexing with other defects or by forming precipitates. Sulfur is known to stabilize ion implantation-induced damage against thermal annealing,[9] so it is plausible that sulfur can form relatively stable defect complexes. Annealing at 875 K for 45 min would indeed permit both defect annihilation in the silicon lattice[10] and diffusion of sulfur over hundreds of nanometers;[11] the observed reduction in sulfur concentration most likely comes from sulfur diffusing to depths greater than can be observed with RBS.

Such an optically active configuration of sulfur may be able to exist in either the single crystal ns-formed structures or the highly disordered fs-formed structures; the deactivation process must not require a significant increase in the crystallinity of the fs-formed structures. Alternatively, different optically active configurations of sulfur could be present in the fs-formed and ns-formed structures, although none of our results directly suggest this interpretation.

In the ns-formed structures, the sulfur incorporation process is probably similar to gas immersion laser doping,[12] in which a semiconductor is doped by melting the surface with ns laser pulses in the presence of a gas containing the desired dopants. The dopants are incorporated into the melt and rapid solidification that follows laser melting can produce highly supersaturated solid solutions.[13] Sulfur may be incorporated into the fs-formed structures by a similar process; the fs laser fluences used are not far above the ablation threshold, and so a molten layer forms at the surface after the laser-induced plasma recombines and the electrons and lattice equilibrate.[14]

In summary, laser microstructuring of silicon surfaces in the presence of SF_6 with either ns or fs laser pulses produces strong below-band gap absorption and photocarrier generation. Both types of structures exhibit these remarkable optoelectronic properties in spite of significant differences in crystallinity and morphology. Our results suggest that laser structuring and sulfur doping of silicon is a robust way to extend the photoresponsivity of silicon into the near-infrared.

We thank J. Chervinsky, J. Harper, E. Hoke, J. Sage, and M. Sheehy for experimental assistance, and Professor C. M. Friend, Professor E. Kaxiras, Professor J. Leonard, Professor W. Paul, and Professor F. Spaepen for helpful discussions. Work at Harvard was supported by the Harvard MRSEC (NSF/DMR-98-09363), the Dept. of Energy (DOE DE FC36 01GO11053), and the Army Research Office (DAAD19-99-1-0009). Work at LLNL was performed under the auspices of the U.S. Dept. of Energy by the Univ. of CA, Lawrence Livermore National Laboratory under Contract No. W-7405-Eng-48.

[1] S. R. Foltyn, in *Pulsed Laser Deposition of Thin Films*, edited by D. B. Chrisey and G. K. Hubler (Wiley-Interscience, New York, 1994), Chap. 4, and references therein.
[2] T. H. Her, R. J. Finlay, C. Wu, S. Deliwala, and E. Mazur, Appl. Phys. Lett. **73**, 1673 (1998).
[3] A. J. Pedraza, J. D. Fowlkes, and D. H. Lowndes, Appl. Phys. Lett. **74**, 2322 (1999).
[4] C. Wu, C. H. Crouch, L. Zhao, J. E. Carey, R. Younkin, J. A. Levinson, E. Mazur, R. M. Farrell, P. Gothoskar, and A. Karger, Appl. Phys. Lett. **78**, 1850 (2001).
[5] J. E. Carey, C. H. Crouch, M. Shen, M. A. Sheehy, C. M. Friend, and E. Mazur (unpublished).
[6] C. H. Crouch, J. E. Carey, M. Y. Shen, E. Mazur, and F. Génin, Appl. Phys. A (to be published).
[7] R. Younkin, J. E. Carey, E. Mazur, J. A. Levinson, and C. M. Friend, J. Appl. Phys. **93**, 2626 (2003).
[8] M. Sheehy, L. Winston, J. E. Carey, E. Mazur, and C. M. Friend (unpublished).
[9] R. Wilson, J. Appl. Phys. **55**, 3490 (1984).
[10] A. Agarwal, H. J. Gossmann, D. J. Eaglesham, L. Pelaz, D. C. Jacobson, J. M. Poate, and T. E. Haynes, Mater. Sci. Eng., A **253**, 269 (1998).
[11] The diffusion coefficient of S in *c*-Si at 875 K was estimated to be 1.6×10^{-13} cm^2/s by extrapolation from data in S. M. Sze, *Physics of Semiconductor Devices*, 2nd ed. (Wiley, New York, 1981), p. 68.
[12] P. G. Carey and T. W. Sigmon, Appl. Surf. Sci. **43**, 325 (1989).
[13] R. Reitano, P. M. Smith, and M. J. Aziz, J. Appl. Phys. **76**, 1518 (1994).
[14] V. I. Emel'yanov and D. V. Babak, Appl. Phys. A **74**, 797 (2002).

SIONYX1403000015.0061

SAMSUNG EX. 1002 - 1262/4148

Appl. Phys. A 79, 1635–1641 (2004)
DOI: 10.1007/s00339-004-2676-0

Applied Physics A
Materials Science & Processing

C.H. CROUCH[1,2,*]
J.E. CAREY[2]
M. SHEN[2]
E. MAZUR[1,2,✉]
F.Y. GÉNIN[3]

Infrared absorption by sulfur-doped silicon formed by femtosecond laser irradiation

[1] Department of Physics, Harvard University, 9 Oxford St., Cambridge, MA 02138, UK
[2] Division of Engineering and Applied Sciences, Harvard University, 9 Oxford St., Cambridge, MA 02138, UK
[3] Lawrence Livermore National Laboratory, Livermore, CA USA

Received: 13 August 2003/Accepted: 4 February 2004
Published online: 23 June 2004 • © Springer-Verlag 2004

ABSTRACT We microstructured silicon surfaces with femtosecond laser irradiation in the presence of SF_6. These surfaces display strong absorption of infrared radiation at energies below the band gap of crystalline silicon. We report the dependence of this below-band gap absorption on microstructuring conditions (laser fluence, number of laser pulses, and background pressure of SF_6) along with structural and chemical characterization of the material. Significant amounts of sulfur are incorporated into the silicon over a wide range of microstructuring conditions; the sulfur is embedded in a disordered nanocrystalline layer less than 1 μm thick that covers the microstructures. The most likely mechanism for the below-band gap absorption is the formation of a band of sulfur impurity states overlapping the silicon band edge, reducing the band gap from 1.1 eV to approximately 0.4 eV.

PACS 78.68.+m; 81.15.Fg; 81.40.Tv; 81.65.Cf; 85.60.Gz

1 Introduction

Silicon is widely used for solar cells and photodetectors, but the band gap of crystalline silicon renders it transparent to wavelengths longer than 1.16 μm; amorphous silicon and microcrystalline silicon have band gaps similar to crystalline silicon. Silicon is, therefore, not used to absorb or detect light at wavelengths longer than 1.1 μm. Near-infrared detectors for wavelengths longer than 1.1 μm are widely used for both telecommunications and scientific instrumentation. Consequently, a silicon-based near-infrared detector that can be integrated with other electronics through standard silicon processing has many applications.

We previously reported that silicon surfaces microstructured in the presence of SF_6 with high-intensity femtosecond laser pulses have near-unity absorption from the near-ultraviolet (250 nm) to the near-infrared (2.5 μm) [1, 2]. We recently found that microstructuring in H_2S [3] or in the presence of elemental sulfur has the same effect, as does microstructuring with excimer laser pulses in the presence of SF_6 [4, 5]; microstructuring in gases that do not contain sulfur does not produce comparable below-band gap absorption [3, 6]. Silicon surfaces microstructured in SF_6 also produce significant photocurrent from 1.31 or 1.55 μm illumination [7].

Here we report the effects of processing conditions and thermal annealing on the below-band gap absorption, chemical composition, and lattice structure of these microstructured silicon surfaces. We observe below-band gap absorption in samples produced under a wide range of conditions; the maximum wavelength of strong below-band gap absorption is 3.5 μm. We attribute the absorption to sulfur impurities in a nanocrystalline layer covering the microstructures.

2 Experimental methods

The samples are microstructured by irradiating a silicon (111) wafer (n-Si(111), 260 μm thick, with resistivity $\varrho = 8$–$12\ \Omega$ m) with a train of 800-nm, 100-fs laser pulses in the presence of SF_6 [2]. The samples discussed in this paper were all made on the same substrate silicon; we previously found that the doping, resistivity, and crystal plane of the initial substrate do not affect the optical properties. Irradiation creates a quasi-ordered array of microstructures on the surface of the sample. The microstructures form only in the region illuminated by the laser. We microstructured areas up to 10 mm × 10 mm by scanning the laser beam across the sample; the laser fluence [8] and average number of pulses delivered to each region of the sample determined the shape and depth of the microstructures. The number of pulses was set by the scan speed, the size of the laser spot on the sample surface, and the repetition rate of the laser [9].

We determined the absorptance (A) of the microstructured surfaces by measuring the total hemispherical (specular and diffuse) reflectance (R) and transmittance (T) with a UV-VIS spectrophotometer equipped with an integrating sphere detector; we then calculated the absorptance $A = 1-R-T$. We measured transmittance at longer wavelengths with a Fourier transform infrared spectrophotometer.

3 Experimental results

Figure 1 shows the microstructures formed by laser irradiation under our standard conditions of 500 laser pulses, 8 kJ/m^2, and 0.67 bar SF_6. These conditions produce sharp

✉ Fax: +1-240/255-4622, E-mail: mazur@physics.harvard.edu
*Present address: Dept. of Physics & Astronomy, Swarthmore College, Swarthmore, PA 19081

SIONYX1403000015.0062

SAMSUNG EX. 1002 - 1263/4148

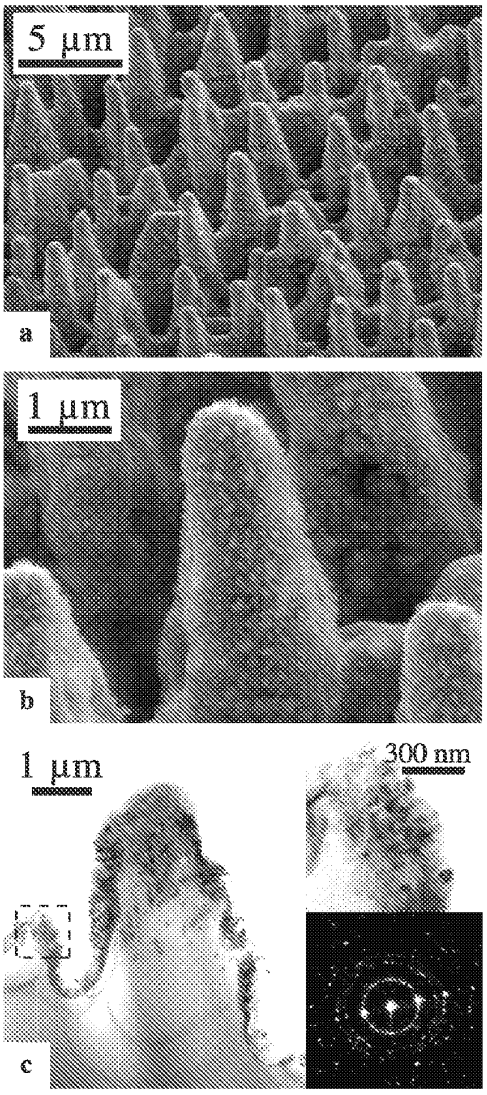


FIGURE 1 **a**,**b** Scanning electron micrographs of laser-microstructured silicon surface formed in SF_6 under "standard" conditions for this paper (laser pulse duration: 100 fs; 500 laser pulses; laser fluence: 8 kJ/m^2; SF_6 pressure: 0.67 bar). The sample is viewed at 45° to the normal. **c** Bright-field transmission electron micrograph of cross-section through a row of microstructures. *Insets*: (*upper*) high-magnification view of the disordered region at the tip of the spike (indicated on main image with *dashed square*) and (*lower*) selected area electron diffraction pattern obtained from the disordered region

conical microstructures about 8 μm tall and 1 μm across at the tip, separated by 3–4 μm (Fig. 1a), and covered with nanoscale particles (Fig. 1b). As can be seen in the bright-field transmission electron micrograph of a cross-section through one of the microstructures (Fig. 1c), the microstructures consist of a crystalline silicon core covered with a layer of disordered material less than 1 μm thick. The surface layer contains silicon nanocrystals (~ 10–50 nm in diameter), pores, and impurities. Selected-area electron diffraction (inset) indicates that the surface layer has a crystalline order. Energy dispersive X-ray emission spectroscopy indicates a sulfur concentration of roughly 1% in this layer; there is no detectable sulfur in the crystalline core.

Figure 2 shows scanning electron micrographs of the microstructures formed with an increasing number of laser pulses (a–c), laser fluence (d–f), and the background pressure of SF_6 (g–i). All of these samples were made by varying just one processing condition relative to the standard conditions of Fig. 1. At fewer than 10 laser pulses or less than 4 kJ/m^2 fluence, we observe ridges parallel to the laser polarization rather than conical microstructures. Increasing the number of laser pulses or laser fluence produces conical microstructures that are shorter and blunter than those obtained under the standard conditions. For SF_6 pressures between 27 mbar and 400 mbar, ridges form; at lower pressures, larger, blunt structures form.

Figure 3 shows that the absorptance at 1550 nm increases strongly with the number of pulses delivered to the sample, up to 20 pulses; additional pulses have little effect. The inset shows that the absorptance increases over the entire wavelength range as the number of laser pulses increases. For unstructured (crystalline) silicon, the absorptance drops sharply around 1.16 μm, corresponding to the band gap of silicon, and is very low for longer wavelengths. For the microstructured samples, the absorptance is essentially constant between 1.2 and 2.5 μm, with its value increasing with the number of pulses.

Figure 4 shows that the absorptance at 1550 nm increases strongly with fluence for fluences up to about 5 kJ/m^2 and increases more slowly for higher fluences. Surfaces made with 4 kJ/m^2 or more display constant absorptance vs. wavelength at below-band gap wavelengths; at lower fluences, the absorptance decreases gradually with increasing wavelength. With 500 laser pulses, fluences below 2.5 kJ/m^2 do not produce uniform microstructuring of the surface (fluence less than 2.0 kJ/m^2 neither alters the surface nor affects the optical properties).

Figure 5 shows that the absorptance also increases with increasing SF_6 pressure, and the greatest rate of increase is observed at low pressures. Above 27 mbar, the below-band gap absorptance does not vary with wavelength, while at lower pressure, it decreases with increasing wavelength. For samples made in vacuum, the gradual decrease of absorptance for wavelengths longer than 1.2 μm is consistent with the presence of band tails of Urbach states due to a high density of defects [10].

Figure 6 shows the effects of annealing for 30 minutes in flowing Ar on the absorptance of samples made under standard conditions. Annealing at temperatures below 575 K has little effect on the absorptance. Annealing between 575 K and 875 K does not affect absorptance above the band gap, but lowers the below-band gap absorptance; the higher the temperature, the greater the decrease in absorptance. Raising the annealing temperature above 875 K does not produce any additional change. As shown in Fig. 7, annealing has no visible effect on the shape of either the microstructures or the surface nanoparticles.

To determine the extent of the below-band gap absorptance, we measured specular infrared transmittance at wavelengths longer than 2.5 μm. For a standard sample (8 kJ/m^2, 500 pulses, 0.67 bar SF_6), the transmittance is only a few percent at 2.5 μm but begins to rise at approximately 3.5 μm,

SIONYX1403000015.0063

SAMSUNG EX. 1002 - 1264/4148

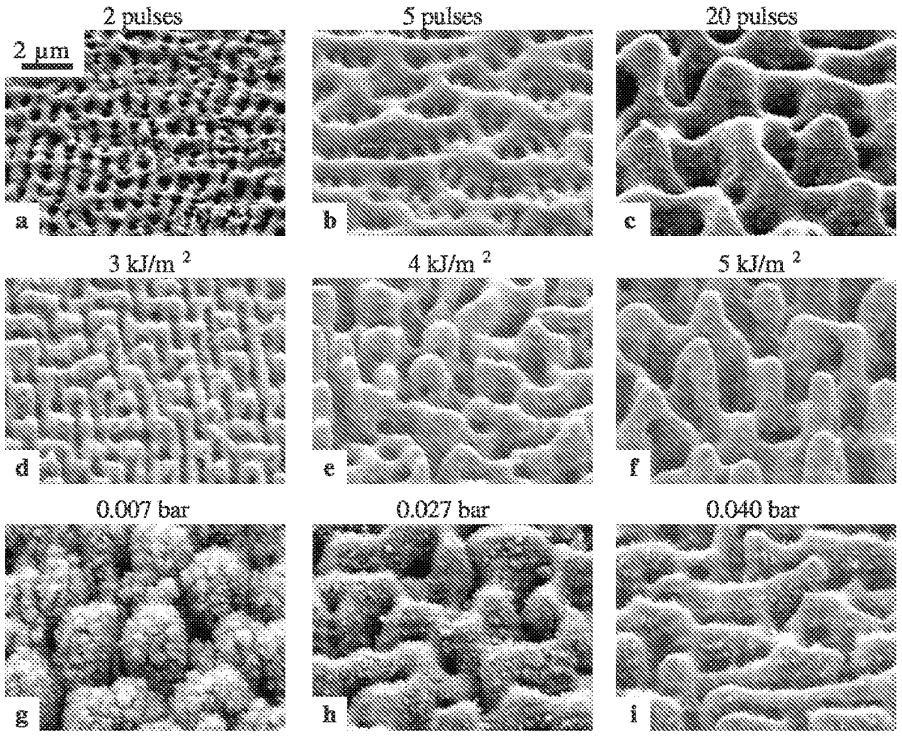


FIGURE 2 Scanning electron micrographs of laser-microstructured silicon surfaces formed in SF_6 with **a** 2, **b** 5, and **c** 20 laser pulses (fluence: 8 kJ/m^2; SF_6 pressure: 0.67 bar); with laser fluence **d** 3, **e** 4, and **f** 5 kJ/m^2 (500 pulses, 0.67 bar SF_6); with SF_6 pressure **g** 7 mbar, **h** 27 mbar, and **i** 400 mbar (500 pulses, 8 kJ/m^2). Samples are viewed at 45° to the normal

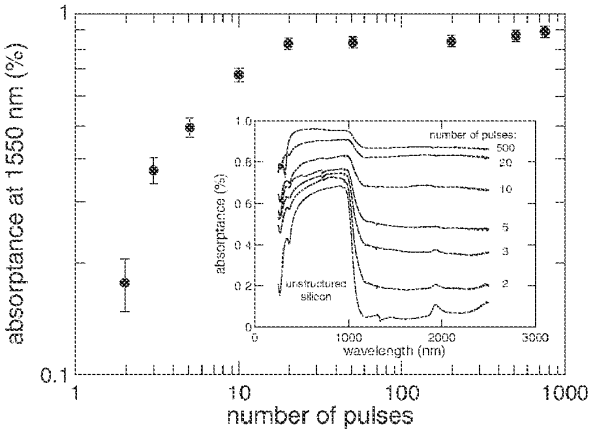


FIGURE 3 Dependence of the absorptance at 1550 nm of microstructured silicon surfaces on the number of laser pulses used in microstructuring. All samples were made with 8 kJ/m^2 laser fluence and 0.67 bar SF_6 pressure. Inset: Wavelength dependence of absorptance for a subset of the samples shown in Fig. 3 and for the unstructured silicon substrate

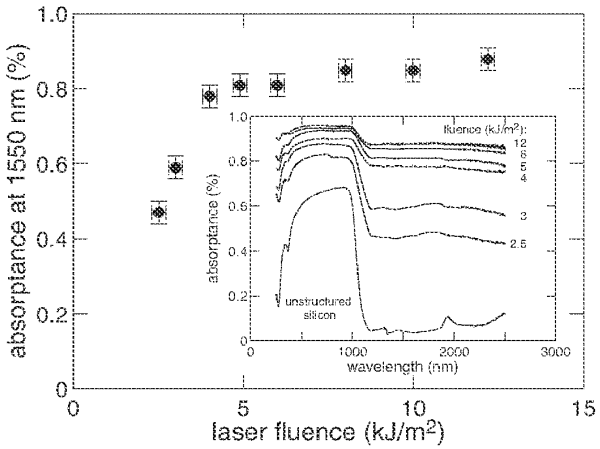


FIGURE 4 Dependence of the absorptance at 1550 nm of microstructured silicon surfaces on the laser fluence used in microstructuring. All samples were made with 500 laser pulses and 0.67 bar SF_6 pressure. *Inset*: Wavelength dependence of the absorptance for a subset of the samples shown in Fig. 4 and for the unstructured silicon substrate

and reaches 50% at roughly 6 μm. Because this measurement was not made with an integrating sphere, scattering reduces the transmittance; 3.5 μm is therefore an upper bound on the wavelength at which the below-band gap absorptance begins to decrease.

To determine the effect of the microstructuring parameters on lattice structure and chemical composition of the microstructures, we performed Rutherford backscattering spectroscopy (RBS) on selected samples. We measured the backscattering spectrum from 2.0 MeV alpha particles with an annular solid state detector. To determine the chemical composition of the microstructured material, we compared the measured RBS spectra to simulated spectra [11] from planar material. The observable sulfur signal measures only the average sulfur concentration in the uppermost 100 nm of the surface; the RBS signal from deeper sulfur is masked by the silicon signal. Transmission electron microscopy indicates that the uppermost few hundred nanometers of the structures is modified, with crystalline silicon beneath (Fig. 1c), and energy dispersive X-ray emission spectroscopy indicates that

SIONYX1403000015.0064

SAMSUNG EX. 1002 - 1265/4148

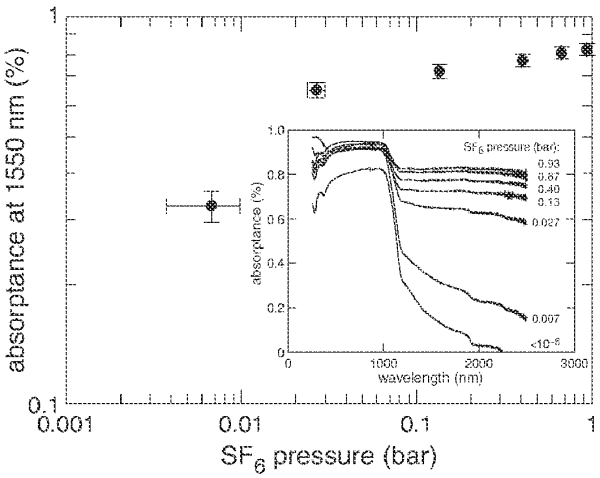


FIGURE 5 Dependence of the absorptance at 1550 nm of microstructured silicon surfaces on the pressure of SF_6 used in microstructuring. All samples were made with 500 laser pulses and 8 kJ/m^2 laser fluence. *Inset*: Wavelength dependence of absorptance for a subset of the samples shown in Fig. 5 and one made in vacuum (base pressure less than 10^{-6} bar)

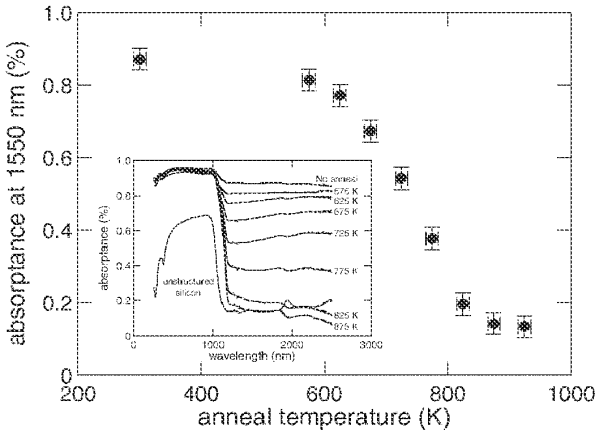


FIGURE 6 Effect of annealing temperature on absorptance at 1550 nm of microstructured silicon surfaces. The data point at room temperature (300 K) corresponds to a sample that was not annealed. All samples were made with 500 laser pulses and 8 kJ/m^2 laser fluence in 0.67 bar SF_6, and were annealed for 30 minutes. *Inset*: Wavelength dependence of absorptance for the samples shown in Fig. 6 and for the unstructured silicon substrate

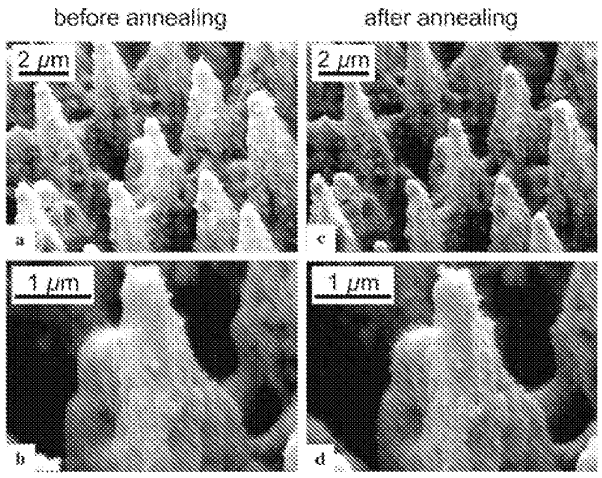


FIGURE 7 Microstructured silicon **a**,**b** before annealing and **c**,**d** after annealing at 800 K for 3 h. The same region of the sample is shown in all four panels

Average laser fluence (kJ/m^2)	Number of pulses	Annealing temperature (30 min)	Sulfur concentration ±0.1 at. %	Absorptance at 1550 nm
2.5	500	–	0.3	0.47
3.0	500	–	0.3	0.59
4.0	500	–	0.4	0.78
4.9	500	–	0.6	0.81
8.0	500	–	0.7	0.85
10.0	500	–	0.7	0.85
8.0	2	–	0.2	0.18
8.0	3	–	0.4	0.37
8.0	5	–	0.4	0.48
8.0	10	–	0.5	0.68
8.0	20	–	0.6	0.83
8.0	50	–	0.6	0.84
8.0	500	–	0.7	0.87
8.0	500	875 K	0.5	0.14
8.0	500	725 K	0.5	0.54

TABLE 1 Sulfur concentration in samples determined by Rutherford backscattering spectroscopy

the sulfur is in the modified layer. Consequently, to determine sulfur concentrations, we simulate just the modified layer.

The RBS spectra indicate that the modified surface layer consists of oxidized silicon with fluorine and sulfur impurities. Neither the oxide nor the fluorine contributes to the optical properties; etching the samples in 5% HF for 4 min removes the fluorine and the oxide without changing either the sulfur concentration or the optical properties. To simplify simulation of the spectra, we therefore measured RBS spectra on samples etched in HF.

Table 1 shows that the concentration of sulfur follows a trend similar to the below-band gap absorptance with processing conditions. The amount of sulfur increases from roughly 0.2% for the sample made with two pulses to roughly 0.7% for the sample made with 50 pulses. Additional pulses have no effect; the sample made with 500 pulses also has 0.7% sulfur. Likewise, the sulfur content increases from 0.4% for the sample made with 2.5 kJ/m^2 to 0.7% for the sample made with 8 kJ/m^2; the sample made with 10 kJ/m^2 also has 0.7% sulfur.

Sulfur concentrations in the annealed samples, however, do not mirror the below-band gap absorptance. Upon annealing a standard sample at either 725 K or 875 K for 30 min, the sulfur content in both cases decreases by only 40%, while the infrared absorptance decreases by almost an order of magnitude. The concentration of sulfur in the annealed samples is comparable to that of the sample made with 4 kJ/m^2 and 500 pulses, or the sample made with ten pulses and 8 kJ/m^2; for these samples, the infrared absorptance is only 20% less than that of a standard sample [12].

Finally, we performed bright-field transmission electron microscopy (TEM) on cross-sections prepared from a sample made with 10 laser pulses, a sample made with a laser

SIONYX1403000015.0065

SAMSUNG EX. 1002 - 1266/4148

fluence of 4 kJ/m^2, and an annealed standard sample. These micrographs are shown in Fig. 8. We find that the samples made with 10 pulses (Fig. 8a) and 4 kJ/m^2 (Fig. 8b) show a disordered surface layer that is similar to that of the sample made under standard conditions (Fig. 1c), although the microstructures themselves are smaller than the microstructures made under standard conditions. The annealed sample (Fig. 8c) also has a disordered surface layer similar to the non-annealed standard sample of Fig. 1c. Selected area diffraction indicates that for all three samples, the surface layer (insets to Fig. 8) has significant crystalline order, and the core is crystalline. The diffraction rings are sharper for the annealed sample (Fig. 8c) than for the others, which most likely indicates that annealing increases the crystallinity of the sample somewhat, as would be expected. Other factors such as the different crystal plane of the specimen could also sharpen the diffraction pattern.

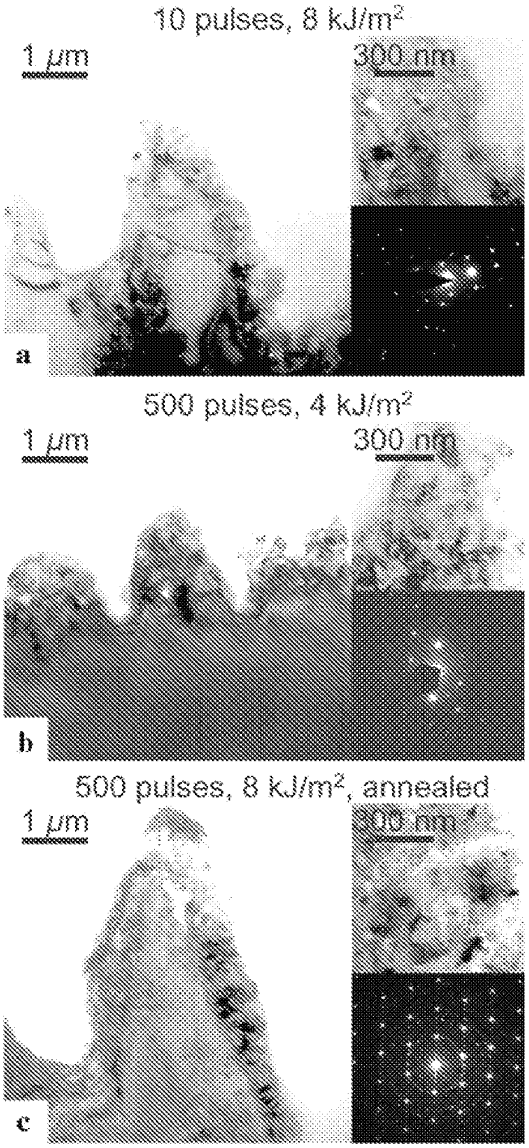


FIGURE 8 Bright-field transmission electron micrographs of cross-sections of microstructures formed with **a** 10 laser pulses, laser fluence 8 kJ/m^2; **b** 500 laser pulses, laser fluence 4 kJ/m^2; and **c** 500 laser pulses, laser fluence 8 kJ/m^2, and annealed at 875 K for 30 minutes. All three samples were made in 0.67 bar SF_6. *Insets*: (*upper*) high-magnification view of the disordered region at the tip of the spike and (*lower*) selected area electron diffraction pattern obtained from the disordered region

4 Discussion

Surfaces laser-microstructured in SF_6 using a wide range of processing conditions exhibit strong, featureless below-band gap absorptance from 1.2 to at least 2.5 μm. The samples also display very high visible absorptance, as reported previously; as the visible absorptance is not affected by annealing, we attribute it to amplification of the intrinsic visible absorptance of ordinary silicon by multiple reflections [2]. The transmittance at longer infrared wavelengths rises at roughly 3.5 μm, indicating that the absorptance decreases in this wavelength range. These optical properties suggest an altered band structure in which the band gap is reduced to roughly 0.4 eV. Further evidence for this altered band structure comes from our recent finding that the microstructured material has a diodic I–V characteristic and high photoresponse to wavelengths longer than 1.1 μm, indicating that the band gap of the surface layer is different from that of the substrate [7].

We attribute this altered band structure to the formation of an impurity band due to the presence of high concentrations of sulfur in the nanocrystalline layer at the surface of the sample. We established previously that sulfur is essential to the below-band gap absorptance; surfaces microstructured in the presence of sulfur or sulfur-containing gases show strong below-band gap absorptance, while surfaces microstructured in environments that do not contain sulfur show absorptance that resembles that of surfaces structured in vacuum [3, 6]. At low concentrations, sulfur impurities introduce states into the band gap of crystalline silicon [13, 14]. Bands of impurity states can form at concentrations as low as 10^{16} /cm^3 [15], so at the sulfur concentrations we observe, it is plausible that a sulfur impurity band forms.

As described in the previous section, we find significant concentrations of sulfur even in samples processed with very few laser pulses or with laser fluences near the threshold for plasma formation, and such samples display significant below-band gap absorptance. In samples that have not been annealed, the sulfur concentration observed by RBS follows a trend similar to the below-band gap absorptance.

Annealing causes the below-band gap absorptance to decrease in a manner that does not mirror the sulfur concentration. For example, samples annealed at 725 K and at 875 K have the same sulfur concentration, but the absorptance at 1550 nm of the sample annealed at 725 K is five times that of the sample annealed at 875 K. The observed sulfur concentration in the sample annealed at 875 K is the same as that from the 10-pulse or 4-kJ/m^2 samples, but the 10-pulse and 4-kJ/m^2 samples display 80% of the below-band gap absorptance of a standard sample, while the below-band gap absorptance of the sample annealed at 875 K is reduced to essentially the same value as the original substrate silicon. The

SIONYX1403000015.0066

SAMSUNG EX. 1002 - 1267/4148

decrease in the observed sulfur concentration upon annealing most likely reflects sulfur diffusing deeper into the sample than can be observed by RBS [16].

The annealing results indicate that absorption is not determined by sulfur concentration alone. The most likely explanation of the below-band gap absorption is that laser microstructuring incorporates the sulfur impurities into the silicon matrix in optically active states, and annealing causes bond rearrangement within the silicon matrix that renders the sulfur impurities optically inactive. (Complete recrystallization of the material is not necessary to eliminate the below-band gap absorption; the annealed material is still significantly disordered [17].) It is also possible that optically inactive precipitates or sulfur-silicon complexes form upon annealing.

While we cannot identify specific optically active sulfur states, we do have some information about them. The TEM images of Figs. 1 and 8 indicate that samples made over a wide range of conditions are covered with a layer of nanocrystalline material containing the sulfur impurities. It is known that after ion implantation of sulfur into silicon, the sulfur impurities form complexes with the implantation-induced damage [18]. After laser microstructuring, it is therefore likely that the sulfur is present in close proximity to defects rather than in the nanocrystalline grains. It is also possible that amorphous-like material is present between the nanocrystalline grains. Keblinski et al. [19] found that the structure of the intergranular phase in nanocrystalline silicon is remarkably similar to that of bulk amorphous silicon. The presence of either defects or amorphous material is likely to provide a wide variety of electronic environments for the sulfur impurities, producing a band of impurity states.

Further work is required to determine the mechanism by which sulfur is incorporated into the surface layer. However, the results presented here provide some clues. The sulfur concentrations in our structures exceed the solid solubility of sulfur in silicon [20] by many orders of magnitude, indicating that sulfur is incorporated through a highly nonequilibrium process. The fact that the sulfur content reaches its maximum value with just 20 pulses, and that the surface layer formed with just 10 pulses is similar in both thickness and structure to that formed with 500 pulses, suggests that the surface layer may re-form with each laser pulse once the pattern of microstructures is established. The increase of sulfur with increasing laser fluence indicates that more sulfur is incorporated when more energy is deposited in the surface. This result would be consistent with sulfur being incorporated into a melted layer formed on the surface of the microstructures after equilibration of the electrons with the lattice; such a layer is expected to form [21] because the laser fluences used for these samples are near or not far above the ablation threshold of approximately 3 kJ/m^2 [22].

Silicon can be doped by melting the surface with excimer laser pulses in the presence of a gas containing the desired dopants [23]. The dopants are incorporated into the melt and the rapid solidification that follows laser melting can produce highly supersaturated solid solutions [24]. We recently found that microstructuring with excimer laser pulses [5] also produces strong below-band gap absorptance. Our femtosecond laser microstructuring process may incorporate sulfur in a similar fashion.

5 Conclusions

We report here the dependence of the below-band gap absorptance of laser-structured silicon on the laser conditions used to structure the surface and on the sulfur content of the microstructured surfaces. Our observations suggest an altered band structure in a layer of sulfur-doped nanocrystalline silicon covering the microstructures; the band gap is reduced to roughly 0.4 eV by the formation of a sulfur impurity band. The sulfur may be present in regions of amorphous or highly disordered silicon that fill spaces between submicrometer-size crystalline grains. The dependence of the optical properties on annealing temperature is consistent with sulfur-doped amorphous silicon.

The altered surface layer forms over a wide range of processing conditions; consequently, different conditions can be designed for different applications. For example, for field emitters, high aspect ratio, sharp conical structures can be formed with large numbers of pulses and high fluence; for detectors or other devices fabricated on a heterostructured substrate, lower fluence or fewer pulses can be used to form shallower microstructures, in order not to disrupt the underlying heterostructure.

ACKNOWLEDGEMENTS We thank Dr. J. Chervinsky, J. Harper, E. Hoke, J. Sage, M. Sheehy, and D. Wolfe for experimental assistance, and Prof. M.J. Aziz, Prof. C. Friend, Prof. E. Kaxiras, Prof. J. Leonard, Prof. W. Paul, and Prof. F. Spaepen for helpful discussions. Work at Harvard was supported by the Harvard University MRSEC (NSF/DMR-98-09363), the Department of Energy (DOE DE FC36 01GO11053), and the Army Research Office (DAAD19-99-1-0009). Work at LLNL was performed under the auspices of the U. S. Department of Energy by the University of California, Lawrence Livermore National Laboratory under Contract No. W-7405-Eng-48.

REFERENCES

1 T.-H. Her, R.J. Finlay, C. Wu, S. Deliwala, E. Mazur: Appl. Phys. Lett. **73**, 1673 (1998)
2 C. Wu, C.H. Crouch, L. Zhao, J.E. Carey, R. Younkin, J.A. Levinson, E. Mazur, R.M. Farrell, P. Gothoskar, A. Karger: Appl. Phys. Lett. **78**, 1850 (2001)
3 M. Sheehy, L. Winston, J.E. Carey, E. Mazur, C.M. Friend: unpublished results
4 A.J. Pedraza, J.D. Fowlkes, D.H. Lowndes: Appl. Phys. Lett. **74**, 2322 (1999)
5 C.H. Crouch, J.E. Carey, J.M. Warrender, M.J. Aziz, E. Mazur: Appl. Phys. Lett. **84**, 1850 (2004)
6 R. Younkin, J.E. Carey, E. Mazur, J.A. Levinson, C.M. Friend: J. Appl. Phys. **93**, 2626 (2003)
7 J.E. Carey, C.H. Crouch, M. Shen, M.A. Sheehy, E. Mazur: unpublished results
8 The laser beam has a Gaussian spatial profile; the fluence reported here is the average fluence determined over the entire laser spot, and the peak fluence (in the center of the spot) is twice the average fluence
9 The average number of laser pulses used to structure a sample is defined as $\langle N \rangle = df/s$, where d = the FWHM of the Gaussian beam profile, f = the frequency of the laser pulse train, and s = the scan speed. The natural frequency of the laser pulse train is 1 kHz, but we can reduce the frequency to 150 Hz or less using a fast mechanical shutter
10 Z.R. Zanatta, I. Chambouleyron: Phys. Rev. B **53**, 3833 (1996)
11 www.genplot.com
12 The RBS spectra may be affected slightly by the changing morphology of the surface, as the surface area of the samples changes as processing conditions change. However, the microstructures made with 2, 3, and 5 laser pulses are similar in size and shape, as are the microstructures made with 3, 4, and 5 kJ/m^2, so the sulfur concentrations for those samples can be confidently compared. As the shape of the microstructures is unchanged by annealing, the concentrations before and after annealing can also be compared with confidence

SIONYX1403000015.0067

SAMSUNG EX. 1002 - 1268/4148

13 E. Janzen, R. Stedman, G. Grossmann, H.G. Grimmeiss: Phys. Rev. B **29**, 1907 (1984)
14 W. Fahrner, A. Goetzberger: Appl. Phys. Lett. **21**, 329 (1972)
15 J.I. Pankove: *Optical Processes In Semiconductors* (New York: Dover Publications, Inc. 1971) p. 9
16 The diffusion length of S in c-Si in 30 minutes at 775 K was estimated to be 25 nm by extrapolation from data in: S.M. Sze: *Physics of Semiconductor Devices*, 2nd ed. (New York: Wiley & Sons 1981) p. 68. In microcrystalline or amorphous silicon, the diffusion length may be somewhat different but is unlikely to increase more than threefold
17 Annealing temperatures that completely eliminate the below-band gap absorptance are much lower than the temperatures at which significant grain growth would be expected in microcrystalline or polycrystalline silicon. See S. Roorda, S. Saito, W.C. Sinke: Mat. Res. Soc. Symp. Proc. **100**, 417 (1988)
18 R. Wilson: J. Appl. Phys. **53**, 3490 (1984)
19 P. Keblinski, S.R. Phillpot, D. Wolf, H. Gleiter: Phys. Lett. A **226**, 205 (1997)
20 F.A. Trumbore: Bell System Tech. J. **39**, 205 (1960)
21 V.I. Emel'yanov, D.V. Babak: Appl. Phys. A **74**, 797 (2002)
22 D. von der Linde, K. Sokolowski-Tinten, J. Bialkowski: Appl. Surf. Sci. **109/110**, 1 (1997)
23 P.G. Carey, T.W. Sigmon: Appl. Surf. Sci. **43**, 325 (1989)
24 R. Reitano, P.M. Smith, M.J. Aziz: J. Appl. Phys. **76**, 1518 (1994)

SIONYX1403000015.0068

SAMSUNG EX. 1002 - 1269/4148

Thin Film Silicon Solar Cell on Highly Textured Substrates for High Conversion Efficiency

M. Despeisse, C. Ballif, G. Bugnon, M. Boccard, P. Cuony, C. Eminian, F-J. Haug, F. Meillaud, S. Nicolay, T. Soderstrom, N. Wyrsch.

Ecole Polytechnique Fédérale de Lausanne (EPFL), Institute of Microengineering (IMT), Photovoltaics and thin film electronics laboratory, Rue Breguet 2, CH-2000 Neuchatel, Switzerland.

The development of high-efficiency thin-film silicon solar cells requires a cell design allowing for a high light trapping while maintaining optimum cell electrical properties. Light scattering at highly textured interfaces is first a decisive feature to improve the light management in the cells [1–3]. In the superstrate configuration, efficient light trapping can be realized with the use of zinc-oxide (ZnO) front electrode textured as grown via low-pressure chemical vapor deposition (LP-CVD). The control of the ZnO growth modes allows for the design of front electrodes with varying surface morphologies [4] (Fig. 1), so that layers can be developed with different haze in transmission, angle of light diffusion and free carrier absorption. Studies presented led to the development of low free-carrier absorption TCO allowing for a high total short circuit current of 28 mA/cm^2 in micromorph (hydrogenated amorphous silicon / microcrystalline silicon tandem) solar cells.

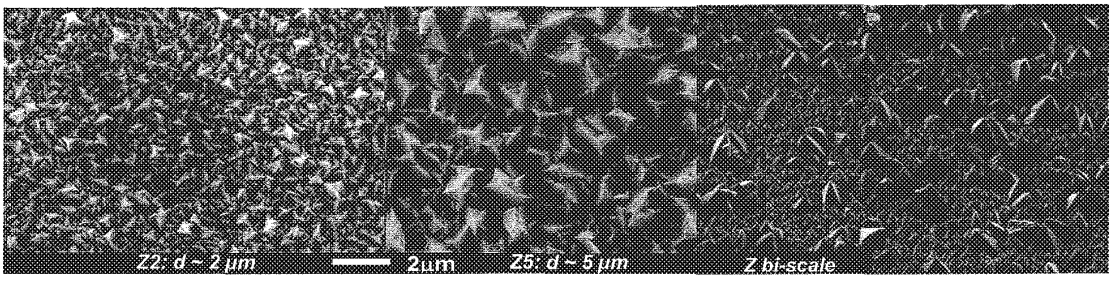


Figure 1.SEM top view of different ZnO front electrodes grown by LPCVD, from standard pyramidal layers to controlled growth layers demonstrating multi-scale texturing.

In combination to an efficient light scattering at the interfaces, light trapping can be improved in the top cell of a micromorph solar cell by the use of an intermediate reflector layer (IRL), realized here as a silicon oxide matrix incorporating silicon nano-crystals [5], developed in semi-industrial reactor with an index of refraction down to 1.7 at 600 nm wavelength. The combination of such IRL with a multi-scale textured ZnO front electrode (Fig. 1) with quasi-lambertian light diffusion potential permitted to reach a short circuit current density approaching 15 mA/cm^2 in a 250 nm a-Si:H top cell. This demonstrates the importance of the angular diffusion of the scattered light to reach a high current in the top cell and therefore to improve stabilized efficiencies of micromorph solar cells. The light management approach developed for micromorph solar cells in the substrate configuration will also be presented. The use of a periodic sinusoidal structured substrate and of a textured asymmetric IRL permitted the development in this configuration of micromorph cells with up to 12.5 mA/cm^2 matched current [6].

A possible limitation to the development of thin film silicon solar cells onto substrates with higher light trapping potential can originate from local variations of the silicon layers when grown on rough surfaces, with potential local variations of the material and diode quality. A rough substrate can lead to the creation of undesired local current drains, degrading performance and reliability of the cells [7-8].

SIONYX1403000015.0069

SAMSUNG EX. 1002 - 1270/4148

The optimization of the cell processing and of the cell design can first lead to an improvement of the electrical properties of cells grown on highly textured substrates. An improved microcrystalline silicon deposition process is shown to lead to a single junction cell with an initial efficiency of 9.5 % fully developed in a KAI large-area reactor, and to allow for the development of a micromorph cell with 13 % initial efficiency while incorporating reasonable junction thicknesses (250 nm a-Si:H cell and 1.8 µm µC-Si:H cell). Moreover, the incorporation of a thin resistive interlayer is shown to allow for a quenching of the cells leakage current, improving the electrical properties of a-Si:H single junction solar cells developed onto highly textured substrates [9].

Advanced concepts are still required to continue improving the thin film silicon solar cell efficiency. In the substrate configuration, silver nanoparticles embedded in a dielectric material have strong scattering properties, due to localized surface plasmons, and were studied as back reflector. In order to achieve high light trapping, the concept of a-Si:H solar cells deposited on nanorods was also studied and preliminary results are presented demonstrating the high potential of such solution, also applicable for the superstrate configuration. An alternative approach to improve micromorph solar cell performance is also reported, with the possible surface morphology adaptation at the IRL in the superstrate configuration, allowing for the growth of a microcrystalline bottom cell with improved electrical properties, and possibly leading to an asymmetric intermediate reflector design (Figure 2).

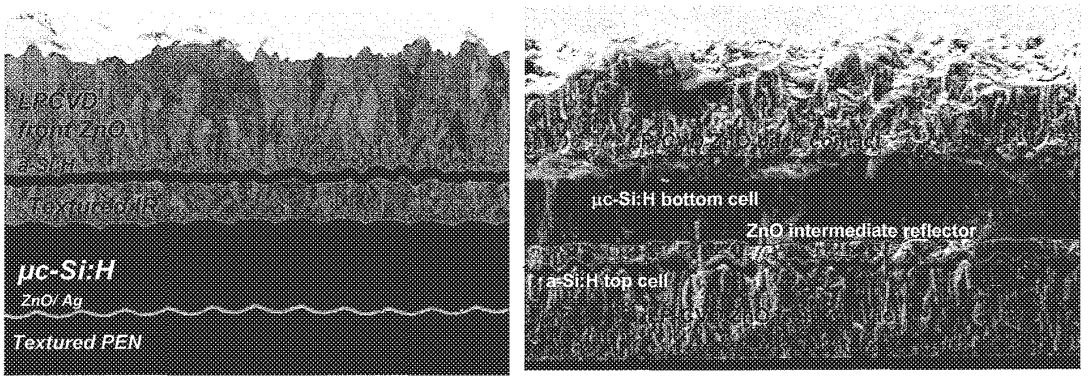


Figure 2.SEM cross-section of a micromorph solar cell in the substrate configuration (n-i-p, left), and in a superstrate configuration (p-i-n, right) with a surface morphology adaptation at the intermediate reflector layer, here realized with ZnO.

Advanced concepts were studied to improve the light trapping of thin film silicon solar cells and are presented. The impact of the proposed cell design onto the cell electrical properties could be mitigated by optimization of the cell structure. The presented advancements should allow for an increase of thin-film silicon solar cells stabilized efficiency in a near future.

[1] J. Muller, B. Rech, J. Springer, M. Vanecek. Sol. Energy, 77, 917, (2004).
[2] D. Dominé, P. Buehlmann, J. Bailat, A. Billet, A. Feltrin, and C. Ballif. Phys. stat. sol. (RRL), **2**, 163, (2008).
[3] M. Berginski, J. Hupkes, M. Schulte, G. Schope, H. Stiebig, B. Rech, M. Wuttig. Journal of Applied Physics, **101**, 074903, (2007).
[4] S. Nicolay, S. Faÿ and C. Ballif. Cryst. Growth Des., **9**, 4957, (2009).
[5] P. Buehlmann, J. Bailat, D. Dominé, A. Billet, F. Meillaud, A. Feltrin, and C. Ballif. Applied Physics Letters, **91**, 143505, (2007).
[6] T. Söderström, F.-J. Haug, X. Niquille, and C. Ballif. Prog. Photovoltaics, **17**, 165, (2009).
[7] U. Malm and M. Edoff. Prog. Photovolt: Res. Appl., **17**, 306, (2009).
[8] M. Python, E. Vallat-Sauvain, J. Bailat, D. Dominé, L. Fesquet, A. Shah, C. Ballif. Journal of Non-Crystalline Solids, **354**, 2258, (2008).
[9] M. Despeisse, G. Bugnon, A. Feltrin, M. Stueckelberger, P. Cuony, F. Meillaud, A. Billet, and C. Ballif. Appl. Phys. Lett. **96**, 073507 (2010)

Detection of X-ray and Gamma-ray

Photons Using Silicon Diodes

Detection Technology, Inc.

Micropolis, Finland

December, 2000

Direct Detection in Silicon -- DC Current Mode

Direct detection of X-ray and Gamma-ray photons in Silicon utilizes PIN diodes with a relatively thick active (wholly or partially depleted) region, as exemplified by the XRA, XRB, and PDC-series of devices from Detection Technology, Inc.

When x-ray or gamma ray photons penetrate the active region of a PIN diode, some (or in certain cases all) of the photons' kinetic energy may be absorbed through interactions with bound electrons resulting in ionization -- liberation of unbound charge in the form of hole-electron pairs.

3.6 eV of gamma or x-ray photon energy absorbed in silicon are required to liberate one electron-hole pair. The ***holes*** (+ charges) drift toward the anode, and the electrons (- charges) drift toward the cathode under the influence of an internal electric field which is directed across the diode junction from cathode to anode.

This electric field arises -- even in the absence of any external applied voltage -- from a concentration gradient of donor and acceptor atoms at the interface between ***P-type*** and ***N-type*** material, and results in the well-known ***built-in junction voltage*** [1](~0.6V) which is typical of silicon diodes. In some applications, an additional, external back-bias may be utilized to augment this built-in voltage.

The (+) and (-) charges drift in opposite directions, summing together to form a current which, in turn, can be measured with the aid of an external amplifying circuit.

Example 1: Calculate the current produced in a Si PIN diode for 1000 MeV per second of absorbed energy from x-ray or gamma ray photons.

Solution: 3.6 eV of gamma or x-ray photon energy absorbed in silicon are required to liberate 1 electron-hole pair.

$(10^9$ eV / sec) ÷ (3.6 eV per electron-hole pair) x

$(1.6 \times 10^{-19}$ coulombs per electron-hole pair) = 4.444×10^{-11} amperes.

But 1000 MeV / sec = 1.6×10^{-10} watts

Thus, the ***responsivity***, expressed in amperes per watt for x-ray or gamma ray photons absorbed in Si is:

$(4.444 \times 10^{-11}$ amperes) ÷ $(1.6 \times 10^{-10}$ watts) = 0.2777 amperes per watt.

Spectral Responsivity

SAMSUNG EX. 1002 - 1272/4148

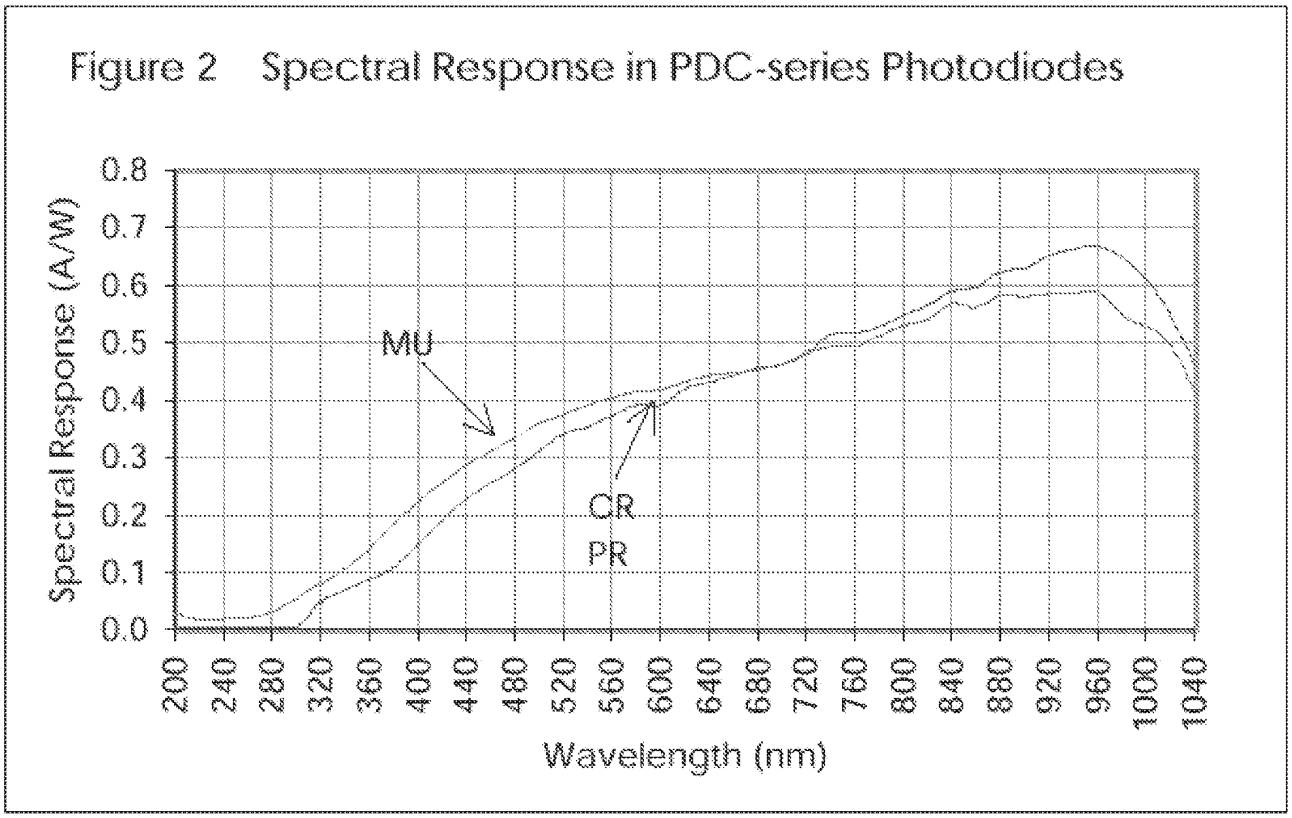


Fig. 2: Spectral Responsivity for PDC-series Photodiodes

Figure 2 (above) shows the response in amperes per watt for light of different wavelengths incident on PDC-series PIN photodiodes. The two curves are for different entrance window materials. A wavelength of 1100 nm (just beyond the extreme right side of the graph) corresponds to a photon energy of 1.12 eV, below which photons cannot excite electrons into the conduction band. Thus, silicon "goes blind" at wave-lengths of 1100 nm and longer.

Compare the value (0.277 amperes per watt) for the responsivity for penetrating x-rays or gamma-rays, found earlier, with the ***spectral responsivity*** for photons in the visible and infra-red portion of the spectrum, shown in Fig. 2 for PDC-series photodiodes.

Dose and Dose Rate

In many applications it is ***dose*** or ***dose rate***, rather than absorbed energy that is the quantity of interest. ***Dose*** is defined as *Energy absorbed per unit mass*. ***Dose rate*** is defined as *energy absorbed per unit mass per unit time*. The standard ***SI unit*** for dose is the joule per kilogram, which has been named the ***gray***.

Example 2: Calculate the current produced in a DTI type PDC-24S-CB diode (2.4 mm x 2.4 mm x .380 mm thick) for a dose-rate in Si of 1 gray per hour.

Solution:

$$\text{Volume} = .24 \times .24 \times 0.038 = .00219 \text{ cm}^3$$

$$\text{Density (of Silicon)} = 2.336 \text{ g / cm}^3$$

SAMSUNG EX. 1002 - 1273/4148

Mass of active region = .00219 x 2.336 = .00511 g = .00000511 Kg

Dose-rate = 1 joule / (Kg 3600 sec) = .00028 joule / (Kg sec)

Rate of energy absorption, or "Power" absorbed in diode =

[.00028 joule / (Kg sec)] x [0.00000511 Kg] =

1.43×10^{-9} joules / second , or 1.43×10^{-9} watts

Current (per gray per hr in a 2.4 mm x 2.4 mm x .38 mm thick diode) =

[0.2777 amperes per watt] x [1.43×10^{-9} watt] = 3.97×10^{-10} amperes

An older unit of dose, the ***rad,*** (100 ergs per gram) is still in wide use. One gray equals 100 rads, so that:

Current = 3.97×10^{-12} amperes per rad hr^{-1} in a 2.4 mm x 2.4 mm diode.

In round numbers, this is ~0.7 pA per (rad / hour) per square mm.

Or 70 pA per (gray / hour) per square mm.

Response to external radiation

In many applications a measurement of the intensity of an external radiation field, rather than an explicit measure of absorbed dose or dose-rate in the diode, is required. In radiation protection applications, the intensity of the external radiation field is termed ***exposure dose-rate*** and is commonly expressed in units of ***roentgens per hour***. The roentgen is defined as an amount of x-ray or gamma radiation which produces 3.33×10^{-10} coulombs of electronic charge in 1 cm^3 of air at standard temperature and pressure.

Calculating the current-response to an external radiation field is somewhat more complicated than the previous examples, since both the probability of photon interaction in the silicon diode (detection efficiency) and the amount of energy deposited per photon interaction are complex functions of photon energy.

For the moment, we shall define detection efficiency rather loosely as the ratio (x 100%) of the number of photons which deposit some (as yet undetermined) energy in our diode, divided by the total number of photons which are incident on the face of the Si diode. For direct detection in a Si PIN diode (i.e., without the use of a scintillating screen or crystal) the detection efficiency is a function of the thickness of the silicon wafer, as shown in Fig. 3 below. For a wafer thickness of 380 microns (the thickness which is now used in DTI's standard line of diode products) the detection efficiency is close to 100% at 10 KeV, falling to approximately 1.60% at 100 KeV.

The curves shown in Fig. 3 below are for the Si wafer only, and do not take into account any effects due to the window, substrate, or package in which the diode is mounted. At low energies (below ~30 KeV), photon interactions in Si are primarily photo-electric. For energies above approximately 60 KeV, photons interact in Si almost entirely through Compton scattering.

SAMSUNG EX. 1002 - 1274/4148

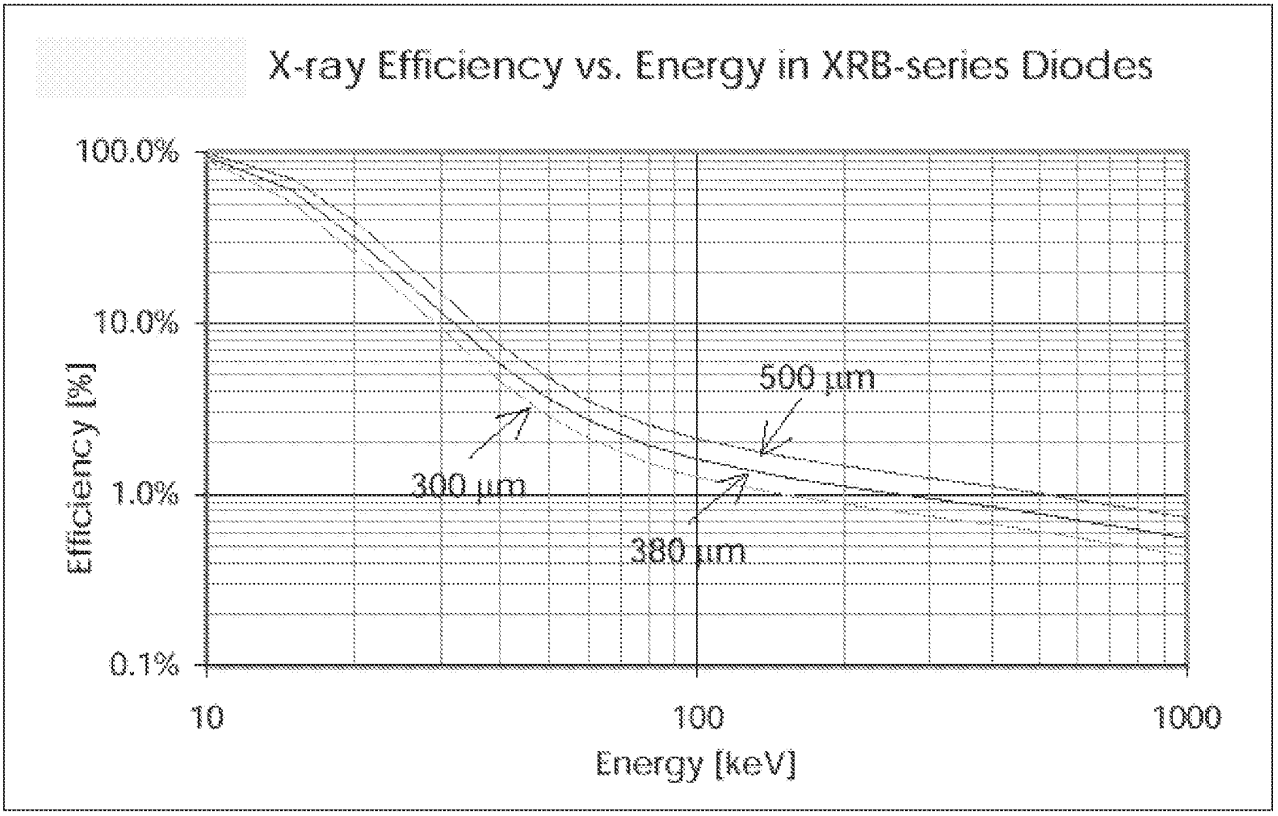


Figure 3

Example 3: Calculate the DC-current response for a 20 mCi point-source of β^+ - emitting activity (gamma-ray energy = 511 KeV annihilation radiation) at a distance of 10 cm from a type XRB-24S-CB PIN diode detector.

Solution:

Let A = area of the diode in cm^2 = .057 cm^2

N = flux of incident gamma rays (gamma's / second-cm^2 on face of diode)

r = detection efficiency at 511 KeV = .0077 from Fig. ___.

$\hat{E}$ = average energy of recoil electrons in Si detector, expressed in eV

s = ionization constant in silicon = 3.6 eV / electron-hole pair

e = electronic charge = 1.6×10^{-19} coulombs

Then the average current produced in the diode is given by:

$I = N A r \hat{E} e / s$

In this example, two 511 KeV gamma rays are emitted back-to-back from the source for each β^+ event. The photon flux at the detector is: $N = (2 \times 20 \times 3.7 \times 10^7) / (4 \times 10^2) = 1{,}177{,}740$ gamma photons / cm^2-second. This is equivalent to an exposure dose-rate at the face of the diode of ~1.08 roentgens / hour. An exact expression for the average energy of a Compton recoil electron may be found in [2]. An approximate formula -- accurate enough to be useful over a wide range of gamma ray energies [3] -- is given by $\hat{E}$

SAMSUNG EX. 1002 - 1275/4148

= 1/2 E_{max}, where E_{max} is derived from Compton's formula for the energy of the 180° (back-scattered) photon: [4]

$E_{max} = h \{2 hv / (m_0c^2 + 2 hv)\}$ = energy of the back-scattered photon

hv = the energy of the incident photon (expressed in eV)

$m_0c^2 = 511{,}000$ eV

In this example hv = 511,000 eV, so that E_{max} = 340,000 eV, and $\hat{E}$ = 170,000 eV. Therefore, the radiation - induced current in the diode = 1,177,740 x .057 x .0077 x 170,000 x 1.6 x 10^{-19} / 3.6 = 3.90 x 10^{-12} amperes.

Notice that, in this example, an ***exposure dose-rate*** of ~ 1 roentgen per hour produces approximately the same current in the diode as an ***absorbed dose-rate*** (i.e., energy absorbed in Si) of 1 rad per hour. This generally holds for gamma ray energies above ~100 KeV, where Compton interactions predominate within materials of relatively low atomic number (as in the constituents of human tissue).

The scale factor relating total charge to exposure dose for this example is:

(3.90 x 10^{-12} amperes) x (3600 seconds per hour) / (1.08 roentgens per hour), or

1.30 x 10^{-8} coulomb / roentgen.

One roentgen produces, by definition, 3.33 x 10^{-10} coulombs in 1 cm^3 of air at standard temperature and pressure. Thus, our XRB-24S-CB diode (.057 cm^2 x 380 microns thick) produces approximately the same radiation-induced current as a (1.30 x 10^{-8}) / (3.33 x 10^{-10}) = 39 cm^3 standard air-ionization chamber.

The effect of the window and device packaging

Some sort of "window" is always required on the face of the diode to maintain chemical passivation of the surface of the silicon. Even a "window-less" diode must have such protection in the form of a very thin aluminum or silicon nitride layer. At very low photon energies, the thickness and type of material used for the window can introduce substantial attenuation, as shown in figures 4 and 5 below.

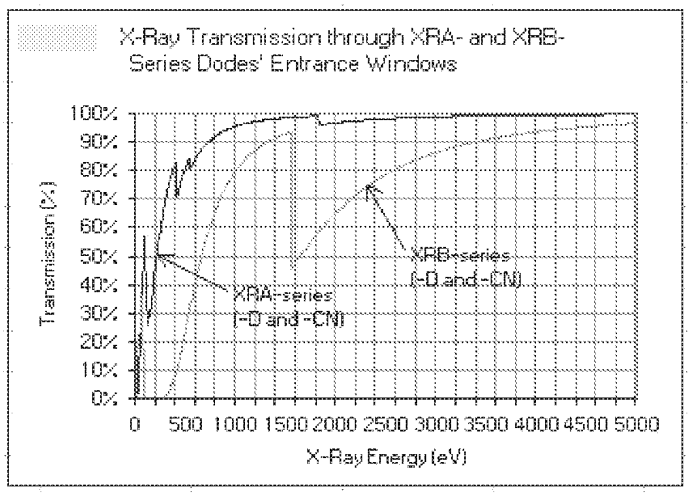


Fig. 4

SAMSUNG EX. 1002 - 1276/4148

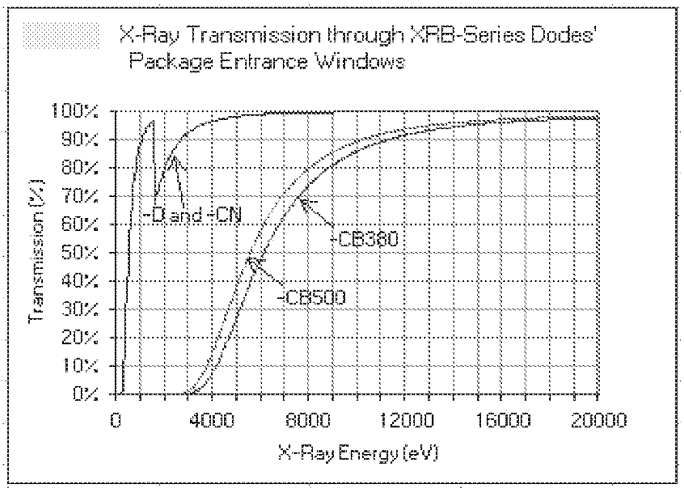


Fig. 5

If the diode is mounted in some sort of package (which is almost always the case) the active region of the diode is in electronic equilibrium with the surrounding medium comprising the diode package, substrate, window and outer coating, etc., so that at higher gamma energies Compton recoil electrons which are produced near -- and close enough to penetrate -- the active volume of the diode, are also detected. For this reason the overall effective volume (or equivalently, the overall, effective efficiency) at 100 KeV and above may actually be somewhat greater than shown in fig. 3.

Amplifying small currents

For dose-rates encountered in laboratory monitoring or general survey applications, the radiation-induced photo-current produced in Si diodes normally ranges between ~10^{-12} and ~10^{-8} amperes. Such small currents demand particular care in the design and implementation of amplifying circuitry.

Utilizing the diode's terminal voltage is generally not advisable, since the diode voltage is a logarithmic rather than linear function of dose-rate. In order to preserve linearity of response, the diode must be connected across a very low-resistance circuit. For this reason, diode current is almost always measured with the aid of a ***transimpedance amplifier*** (current-to-voltage converter).

A transimpedance amplifier is generally implemented as a high-gain, inverting amplifier (usually in the form of an integrated-circuit operational amplifier) with a feedback resistor connected from output to input, as shown in Fig. 6 below. This particular example shows the photodiode with its cathode grounded (+ current flowing into the amplifier) producing a negative voltage at the output of the amplifier. High forward gain forces the voltage at the amplifier's inverting input to be essentially zero, thus satisfying the requirement for low resistance across the diode.

SAMSUNG EX. 1002 - 1277/4148

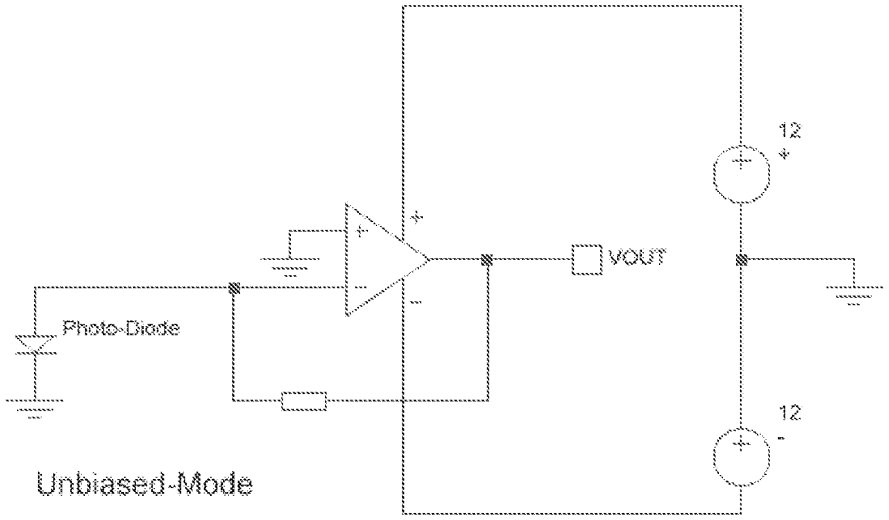


Fig. 6

Assuming the amplifier's open loop gain is sufficiently high ($A_V > 10^6$), the ***transimpedance gain*** of this circuit is just the value of the feedback resistor, in ohms. Thus, for example, a 100 megohm feedback resistor provides a gain of 10^8 ohms (1 volt output for 10^{-8} amperes input).

Speed of response

Some applications, such as pulsed X-ray measurements, require precise measurement of rapidly-varying signals. A system rise-time response in the micro-second range, or faster, requires that the diode be operated in ***biased mode*** in order to maintain a low ***junction capacitance***, and also to insure rapid and complete collection of all the available charge - particularly the holes -- which drift more slowly than electrons. Biased - mode operation is illustrated in Fig. 7 below.

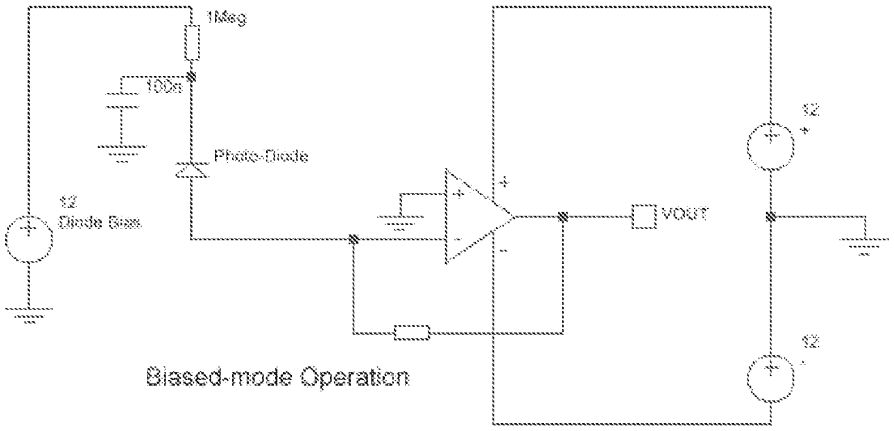


Fig. 7:

Both ***junction capacitance*** and ***leakage current*** or ***dark current*** are functions of ***reverse bias***, as illustrated

SAMSUNG EX. 1002 - 1278/4148

in Figs. 8 and 9 below.

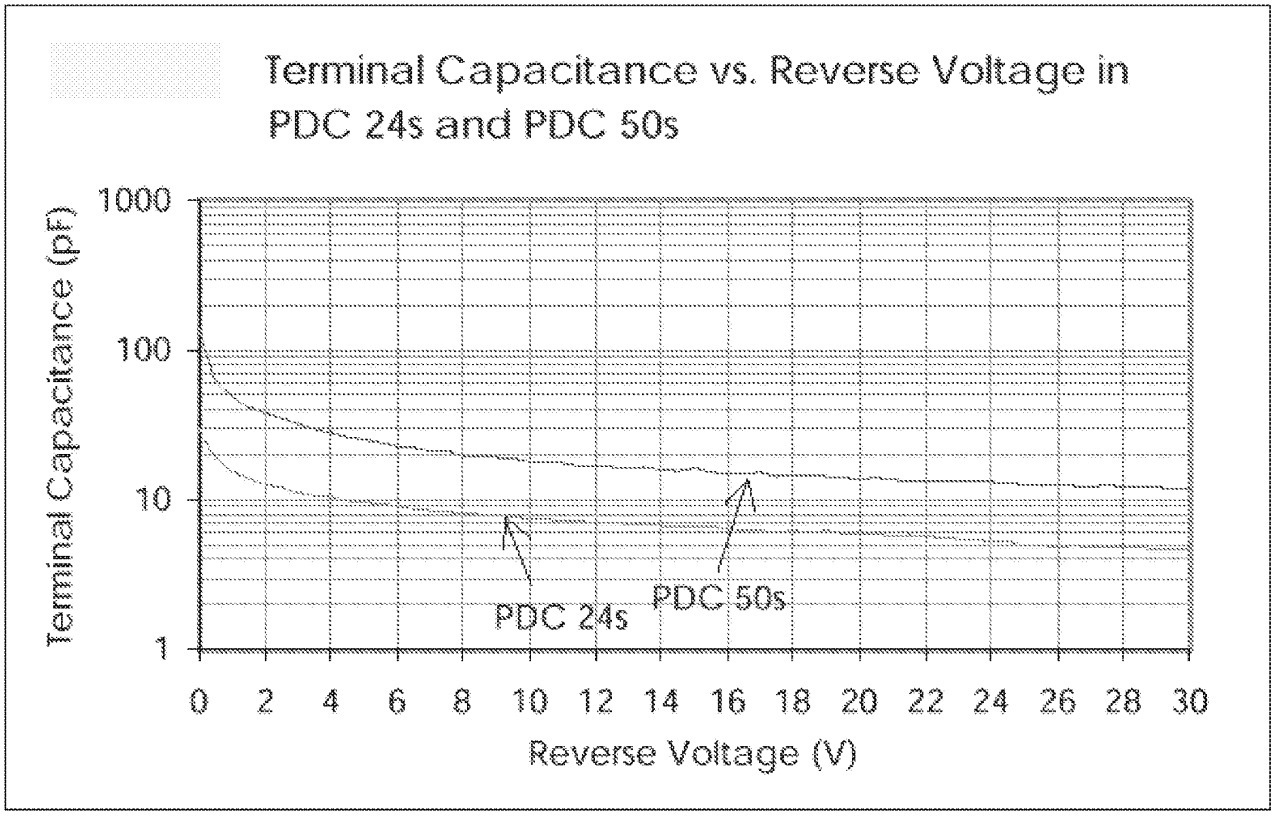


Fig. 8

Dark Current

Dark current is also a very strong function of temperature, increasing by a factor of ~2 for every 5-6 deg. C increase in temperature. Since dark current cannot readily be distinguished from radiation-induced photo-current, it may become a significant source of error when undertaking low-level radiation measurements. This is particularly true if the temperature is not held constant (a back-biased Si diode makes a highly sensitive -- albeit non-linear -- thermometer!)

Guard Ring

Leakage current in a planar diode generally comprises three components: 1) a current component flowing fully vertically in the depletion region of the diode, 2) a component due to the edge-field of the depletion region, which is generated just outside the true active area and, 3) a component due to surface effects in the oxide layer. This last component is one which is most heavily affected by radiation damage in the silicon / silicon dioxide interface outside the active area, and is also strongly affected by temperature changes.

The magnitude of the dark current can be reduced by exploiting DTI's unique, proprietary guard ring. This feature is particularly useful when operating in biased mode; the guard ring collects most of the latter two components of dark current (noted above), and thereby decreases the dark current by approximately a factor of 0.5.

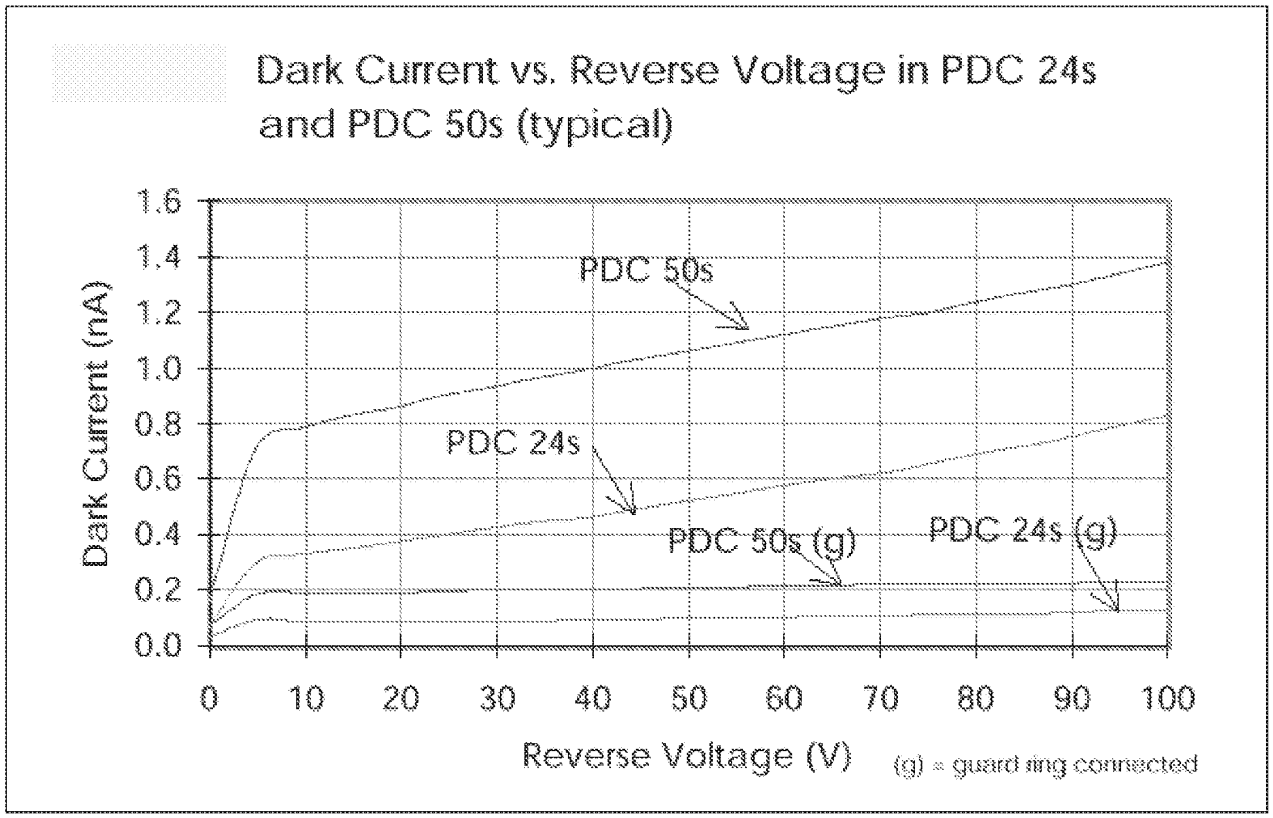


Fig. 9

Another advantage of the guard ring is that it reduces potential gradients at the edge of the diode's active area, thereby increasing the breakdown voltage rating. A third advantage becomes important in spectroscopic applications (to be covered in more detail in a subsequent tutorial) wherein the guard ring collects most of the signal charge which is generated close to -- or outside of -- the actual active area, reducing the number of interactions in which imperfect or incomplete charge collection would otherwise occur.

Compare the respective values of dark current (for the same device and the same reverse bias) with the data in Fig 9 in which the guard ring was not used. Equally dramatic is the comparison between different devices; A 5 x 5 mm diode (PDC-50S) with the guard ring connected shows less than half the leakage current compared to a 2.4 x 2.4 mm diode (PDC-24S) whose guard ring is not connected!

The circuit connection for the guard ring is shown in the schematic in Fig. 10. Please observe that the cathode of the diode is common to both the main diode and the guard ring. Therefore, the guard ring is useful only when the cathode is connected to a positive voltage supply, and the input of the preamplifier is connected to the **anode** of the diode. We strongly recommend this configuration. (Some users prefer connecting to the cathode since that provides a positive signal output from an inverting amplifier. However, in most applications, this will result in poorer performance.)

SAMSUNG EX. 1002 - 1280/4148

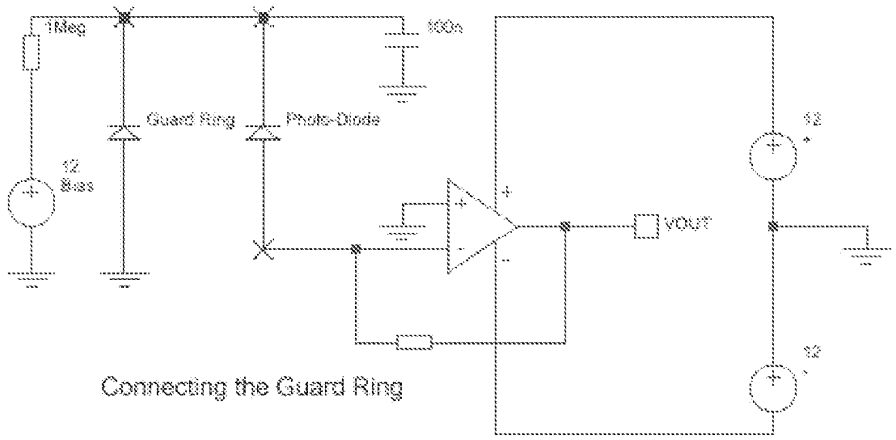


Fig. 10

Amplifier Offset

If high-speed response is not required, then errors due to dark current are substantially reduced by operating the diode radiation detector in unbiased mode. However, there is yet an additional confounding factor which must be taken into account: the amplifier's ***input offset-voltage error***.

Unless precisely and specifically "trimmed out", some degree of input offset error is present in virtually all amplifiers. Offset voltage error is represented schematically as a voltage source in series with the (+) input terminal of the amplifier. In our transimpedance amplifier (fig. 6 & fig. 10), this offset voltage is returned via the feedback resistor so as to appear at the (-) input terminal of the amplifier.

Thus, the "unbiased" diode is not actually operating at zero bias, but rather at a small positive or negative bias (depending on the polarity of the offset voltage) which is on the same order as the amplifier's offset voltage and which, in turn, introduces a finite dark-current component.

Shunt Resistance

Potentially much more serious is the effect of the diode's ***shunt resistance***. The quotient of (voltage ÷ current) at a diode bias V = 10 mV is defined as the device's shunt resistance. If the value of the diode shunt resistance is substantially less than the value of the transresistance amplifier's feedback resistor, then the voltage gain of the amplifier, referred to the (+) input terminal is approximately: $(R_{shunt} + R_{feedback}) / (R_{shunt})$

Example 4: Estimate a transresistance amplifier's output voltage assuming the following:

1) doserate = 0

2) diode shunt resistance = 100 megohms

3) operational amplifier offset voltage = 1 mV, and

4) amplifier feedback resistor = 10^9 ohms

Solution: The output voltage error (for zero doserate) is dominated by the amplifier's offset error voltage multiplied by the gain of the

SAMSUNG EX. 1002 - 1281/4148

amplifier referred to the (+) input terminal....

$$V_{out} = V_{offset} \times (R_{shunt} + R_{feedback}) / (R_{shunt}) =$$

$$(.001) \times (10^9 + 10^8) / (10^8) = 0.011 \text{ volts}$$

This is equivalent to an input offset current (at zero doserate) of 11 pA in the diode detector.

Worse yet, dark current is a very strong function of temperature as we saw earlier. If the diode's dark current increases by a factor of two for every 5 - 6 deg. C increase in temperature, then so too must the diode's shunt resistance *decrease* by a factor of two for the same temperature rise, leading to a near doubling of the output voltage error (or, equivalently, the input current error) for every 5- 6 deg. C temperature increase.

Further Reading

While the topic of transimpedance amplifier circuit design principles and techniques is far too broad to cover in any detail in this article, the good news is that a variety of excellent -- yet relatively inexpensive -- integrated-circuit operational amplifiers are available from a number of vendors. Some of these[5] feature extremely low input bias currents (in the range of ~10^{-14} amperes at normal room temperature) and very respectable offset voltages on the order of 100 µV (typical) . Many manufacturers also provide extensive and detailed application data[6], with tips and techniques for minimizing sources of error in precision, low-current measurements.

REFERENCES

1. Words and phrases which are highlighted in ***bold Italic*** are "terms of art". A list of key technical terms and their definitions may be found at a new website currently being developed by Detection Technology, Inc:http://www.detectorportal.net .

2. Fitzgerald, J.J., Brownell, G.L., Mahoney, F.J., Ch 2 in **Mathematical Theory of Radiation Dosimetry**Gordon and Breach Science Publishers, New York, 1967

3. The estimate, Ê is ~ 2% high at 80 KeV, dropping to ~3% low at 511 KeV, dropping further to ~10% low at 1000 KeV.

4. **op. cit.**, Chapter 4

5. Exemplified by the LMC60XX series from National Semiconductor Corporation.

6. Example: **Operational Amplifiers DataBook, 1995 Edition**. Published by National Semiconductor Corporation, 2900 Semiconductor Drive, P.O. Box 58090, Santa Clara, California 95052-8090

SAMSUNG EX. 1002 - 1282/4148

Light trapping in thin-film silicon solar cells with submicron surface texture

Rahul Dewan,[1] Marko Marinkovic,[1] Rodrigo Noriega[2], Sujay Phadke[2], Alberto Salleo[2] and Dietmar Knipp[1,*]

[1]*School of Engineering and Science, Electronic Devices and Nanophotonics Laboratory, Jacobs University Bremen, 28759 Bremen, Germany*

[2]*Department of Materials Science and Engineering, Geballe Laboratory for Advanced Materials, Stanford University, Stanford, CA 94305, USA*

**d.knipp@jacobs-university.de*

Abstract: The influence of nano textured front contacts on the optical wave propagation within microcrystalline thin-film silicon solar cell was investigated. Periodic triangular gratings were integrated in solar cells and the influence of the profile dimensions on the quantum efficiency and the short circuit current was studied. A Finite Difference Time Domain approach was used to rigorously solve the Maxwell's equations in two dimensions. By studying the influence of the period and height of the triangular profile, the design of the structures were optimized to achieve higher short circuit currents and quantum efficiencies. Enhancement of the short circuit current in the blue part of the spectrum is achieved for small triangular periods (P<200 nm), whereas the short circuit current in the red and infrared part of the spectrum is increased for triangular periods (P = 900nm) comparable to the optical wavelength. The influence of the surface texture on the solar cell performance will be discussed.

©2009 Optical Society of America

OCIS codes: (350.6050) Solar energy; (050.1950) Diffraction gratings; (050.6624) Subwavelength structures; (310.6845) Thin film devices and applications.

References and links

1. B. Rech, and H. Wagner, "Potential of amorphous silicon for solar cells," Appl. Phys., A Mater. Sci. Process. 69(2), 155–167 (1999).
2. J. Meier, J. Spitznagel, U. Kroll, C. Bucher, S. Faÿ, T. Moriarty, and A. Shah, "Potential of amorphous and microcrystalline silicon solar cells," Thin Solid Films **451–452**, 518–524 (2004).
3. M. A. Green, K. Emery, Y. Hishikawa, and W. Warta, "Solar cell efficiency tables (version 33)," Prog. Photovolt. Res. Appl. 17(1), 85–94 (2009).
4. K. Yamamoto, M. Yoshimi, Y. Tawada, Y. Okamoto, A. Nakajima, and S. Igari, "Thin-film poly-Si solar cells on glass substrate fabricated at low temperature," Appl. Phys., A Mater. Sci. Process. 69(2), 179–185 (1999).
5. J. Müller, B. Rech, J. Springer, and M. Vanecek, "TCO and light trapping in silicon thin film solar cells," Sol. Energy 77(6), 917–930 (2004).
6. C. Haase, D. Knipp, and H. Stiebig, "Optics of thin-film silicon solar cells with efficient periodic light trapping textures," Proc. SPIE, **6645**, (2007).
7. C. Haase, and H. Stiebig, "Thin-film silicon solar cells with efficient periodic light trapping texture," Appl. Phys. Lett. **91**(6), 061116 (2007).
8. A. Lin, and J. Phillips, "Optimization of random diffraction gratings in thin-film solar cells using genetic algorithms," Sol. Energy Mater. Sol. Cells 92(12), 1689–1696 (2008).
9. A. Čampa, J. Krč, and M. Topič, "Analysis and optimisation of microcrystalline silicon solar cells with periodic sinusoidal textured interfaces by two-dimensional optical simulations," J. Appl. Phys. **105**(8), 083107 (2009).
10. S. S. Lo, C. C. Chen, F. Garwe, and T. Pertch, "Broad-band anti-reflection coupler for a:Si thin-film solar cell," J. Phys. D Appl. Phys. 40(3), 754–758 (2007).
11. A. Cuevas, R. A. Sinton, N. E. Midkiff, and R. M. Swanson, "26-percent efficient point-junction concentrator solar cells with a front metal grid," IEEE Electron Device Lett. 11(1), 6–8 (1990).
12. T. Yagi, Y. Uraoka, and T. Fuyuki, "Ray-trace simulation of light trapping in silicon solar cell with texture structures," Sol. Energy Mater. Sol. Cells **90**(16), 2647–2656 (2006).
13. J. Zhao, A. Wang, P. Altermatt, and M. A. Green, "Twenty-four percent efficient silicon solar cells with double layer antireflection coatings and reduced resistance loss," Appl. Phys. Lett. 66(26), 3636 (1995).
14. S. Fahr, C. Ulbrich, T. Kirchartz, U. Rau, C. Rockstuhl, and F. Lederer, "Rugate filter for light-trapping in solar cells," Opt. Express **16**(13), 9332–9343 (2008).

#116966 - $15.00 USD Received 9 Sep 2009; revised 2 Oct 2009; accepted 3 Oct 2009; published 2 Dec 2009
(C) 2009 OSA

SIONYX1403000015.0082

SAMSUNG EX. 1002 - 1283/4148

15. A. Banerjee, and S. Guha, "Study of back reflectors for amorphous silicon alloy solar cell application," J. Appl. Phys. 69(2), 1030 (1991).
16. J. Meier, S. Dubail, S. Golay, U. Kroll, S. Faÿ, E. Vallat-Sauvain, L. Feitknecht, J. Dubail, and A. Shah, "Microcrystalline silicon and the impact on micromorph tandem solar cells," Sol. Energy Mater. Sol. Cells 74(1-4), 457–467 (2002).
17. N. Senoussaoui, M. Krause, J. Müller, E. Bunte, T. Brammer, and H. Stiebig, "Thin-film solar cells with periodic grating coupler," Thin Solid Films 451–452, 397–401 (2004).
18. T. Söderström, F.-J. Haug, X. Niquille, and C. Ballif, "TCOs for nip thin film silicon solar cells," Prog. Photovolt. Res. Appl. 17(3), 165–176 (2009).
19. Y. Mai, S. Klein, R. Carius, H. Stiebig, X. Geng, and F. Finger, "Open circuit voltage improvement of high-deposition-rate microcrystalline silicon solar cells by hot wire interface layers," Appl. Phys. Lett. 87(7), 073503 (2005).
20. H. Stiebig, and C. Haase, IEF-5, Research Center Jülich, 52428 Jülich, Germany (personal communication).
21. R. Dewan, D. Madzharov, A. Raykov, and D. Knipp, "Optics in thin-film silicon solar cells with integrated lamellar gratings," Mater. Res. Soc. Symp. Proc. Vol. 1153 (2009)

1. Introduction

Thin-film solar cells based on microcrystalline silicon (μc-Si:H) or amorphous silicon (a-Si:H) have gained considerable attention as promising candidates for future generation of photovoltaics [1,2]. With an absorber layer in the range of 1 μm, complete utilization of light incoupling and light trapping is imperative for realizing efficient thin-film solar cells based on these materials. Efficiencies higher than 10% have been achieved for microcrystalline silicon solar cells by introducing textured interfaces in the solar cell [3–5]. Introducing nano textured interfaces leads to reduced reflection losses and enhanced scattering and diffraction of light in the device. Whilst these optical phenomenons can be measured in the far-field, in order to understand the optical propagation within such thin-film devices, it is imperative to use numerical methods and solve the Maxwell's equations rigorously. By considering the near field optics, the nano texturing process for efficient solar cells can be understood and optimized. In this work, a Finite Difference Time Domain (FDTD) simulation tool (OptiFDTD®) was used to investigate the wave propagation for nano textured microcrystalline silicon solar cells. So far the optics in such structures has been investigated by solving the Maxwell's equations using the Finite Integration Technique (FIT) and Finite Element Method (FEM) algorithm [6–9]. FDTD approach has also been used, but to analyze the wave propagation in amorphous silicon solar cells [10]. In this study the nano texturing of the front interface of the microcrystalline solar cell property was investigated by introducing a triangular grating which represents the textured front interface of a real thin-film silicon solar cell. Triangular and pyramidal structures have been extensively investigated for solar cell applications in the past decade [11–13]. But they were mostly addressed for crystalline silicon solar cells, where the period of the structures were larger than the wavelength of the incident light in many folds. Hence, geometric optics was sufficient to understand the behavior of optics for such solar cells. A recent paper has studied pyramidal textures in thin-film silicon solar cells [7]. However, the manuscript does not provide a detailed description of the wave propagation for small surface textures. Such small textures have distinct influence on the incoupling of blue light in the solar cell.

The influence of the period and height of the triangular profile on the short circuit was investigated for a microcrystalline silicon solar cell to determine the optimal geometries. Results on smooth substrates were used as a reference to investigate the influence of the grating parameters on the solar cell parameters. Optimized designs of the triangular structure were derived to maximize the short circuit current and the efficiency of the microcrystalline silicon solar cells. The optical model used to calculate the optical power losses in the individual regions of the solar cell is introduced in Section 2. Simulation results including power loss profiles, quantum efficiencies and short circuits currents are described in Section 3. The manuscript is summarized in Section 4.

2. Optical simulation model

To increase the effective thickness of thin-film silicon solar cells, many different concepts exist. More light can be coupled into or trapped within the solar cell by applying anti-

#116966 - $15.00 USD Received 9 Sep 2009; revised 2 Oct 2009; accepted 3 Oct 2009; published 2 Dec 2009
(C) 2009 OSA

SIONYX1403000015.0083

SAMSUNG EX. 1002 - 1284/4148

reflection coatings [10,13], optical filters [14], or using highly reflective back contacts [15]. In the case of microcrystalline silicon thin-film solar cells randomly textured contact layers have resulted into the highest efficiencies [4,5]. These textured layers have been realized by direct growth of zinc oxide films by low pressure chemical vapor deposition or etching of sputtered zinc oxide [5,16]. A surface profile of such an etched aluminum doped zinc oxide (ZnO:Al) is shown in Fig. 1. The sputtered zinc oxide film was etched for 10 seconds in a 0.5% diluted hydrochloric acid (HCl) solution. Figure 1(a) shows a three dimensional surface profile of the substrate. Surface texturing of the film leads to surface morphology that very closely resembles a pyramid-like structure, albeit not perfectly symmetrical ones.

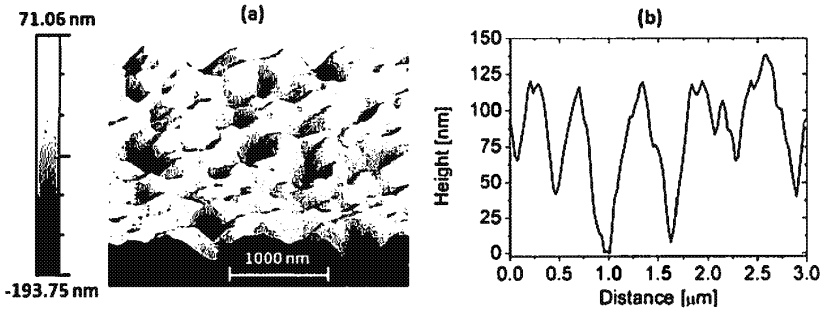


Fig. 1. (a) Atomic Force Microscope (AFM) image of a randomly textured aluminum doped zinc oxide (ZnO:Al) film. (b) Surface profile of the same textured substrate, showing the triangular grooves that are formed due to etching by a hydrochloric acid solution.

A line profile of the nanotextured surface is shown in Fig. 1(b). In this figure, the triangular profiles exhibit an almost periodic arrangement with a period of around 500 nm. Based on these observations, the model investigated in this study consisted of periodic arrangements of triangular gratings. A schematic cross section of the investigated unit cells is shown in Fig. 2. The microcrystalline silicon solar cell structure consists of a 500 nm thick aluminum doped zinc oxide (ZnO:Al) front contact, followed by a (p-i-n) hydrogenated microcrystalline silicon diode (μc-Si:H) with a total thickness of 1000 nm and a back reflector consisting of an 80 nm thick ZnO:Al layer and a metal reflector. The device structure is consistent with the standard microcrystalline silicon solar cell process used by several research groups like the Research Center Jülich and University of Neuchâtel [17,18].

Maximal conversion efficiencies of 10.3% have been achieved for microcrystalline silicon solar cells with an absorber thickness of just 1000 nm [19]. The cross section of a solar cell deposited on a smooth substrate and a triangular texture is shown in Fig. 2(a) and 2(b). In this study the period of the unit cell and height of the triangular profile was varied. The period of the unit cell was varied from 50 nm up to 6000 nm and the height was varied from 0 nm up to 500 nm. Alternatively, the triangular structure can be described by the opening angle of the triangle, which was varied from 6° to 176°. The unit cell was illuminated under normal incidence for the entire spectrum of wavelength 300 – 1100 nm. The complex optical constants used in the model system were determined by optical measurements of the individual layers [20]. Since a two dimensional FDTD algorithm was utilized, it splits the Maxwell's equations into two independent sets of equations for transverse electric (TE) and transverse magnetic (TM) polarized waves. The polarization of the input wave was assumed to be TE, thus only one component of the electric field, E_y had to be solved.

#116966 - $15.00 USD Received 9 Sep 2009; revised 2 Oct 2009; accepted 3 Oct 2009; published 2 Dec 2009
(C) 2009 OSA

SIONYX1403000015.0084

SAMSUNG EX. 1002 - 1285/4148

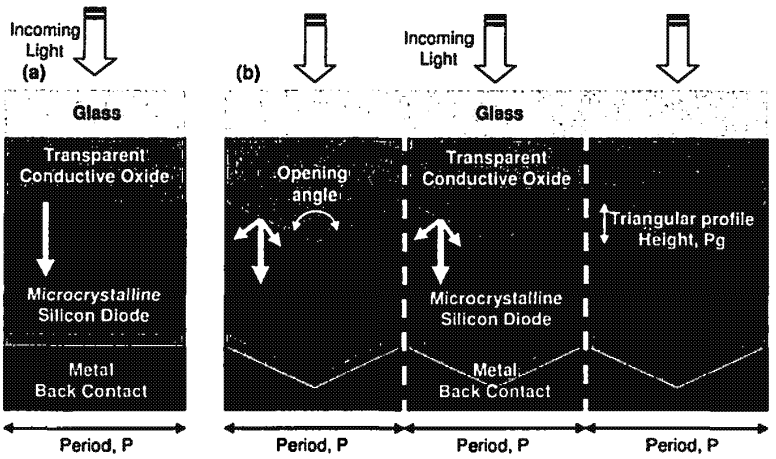


Fig. 2. Schematic sketch of a thin film microcrystalline silicon solar cell (a) on a smooth substrate and (b) with triangular textured substrate. The different unit cells in Fig. (b) are separated by dashed lines.

3. Results and Discussion

In order to compare different textured designs the power loss profiles within the solar cell, the quantum efficiency, the short circuit current were utilized. The power loss was calculated using the equation

$$Q(x,y)=\frac{1}{2}c\varepsilon_0 n\alpha\cdot\left|E(x,z)\right|^2 \qquad (1)$$

where c is the speed of light in free space, ε_0 the permittivity of free space, α is the energy absorption coefficient ($\alpha=4\pi k/\lambda$), with n and k being the real and imaginary part of the complex refractive index, λ is the wavelength and E is the electric field. The power loss profile for thin film solar cells with integrated triangular structures under blue and red illumination are shown in Fig. 3.

The period of the triangular profile for all the cases was 900 nm with heights of 100 nm (Fig. 3(a) and 3(c)) and 400 nm (Fig. 3(b) and 3(d)), respectively. The incident light has a wavelength of 400 nm and 700 nm with amplitude of 1 V/m. In the case of short wavelength illumination (λ = 400nm) photons get absorbed within the first 200 nm of the silicon absorber layer. The high absorption coefficient of silicon for wavelength 400 nm inhibits the propagating wave to hit the back reflector. By having a small period height, like in Fig. 3(a), the opening angle is close to 180°. Hence the high power loss pattern concentrated around the front interface almost resembles that of a solar cell on a smooth substrate; it is almost continuous along the boundary. Whereas, by having an opening angle close to 90°, a "flame-like" power loss pattern is seen in Fig. 3(b). The "flame-like" power loss pattern is caused by the formation of evanescent fields at the boundary between the zinc oxide texture and the p-i-n solar cell. Such "flame-like" patterns are observed because the refractive index difference between zinc oxide and silicon is relatively large for short wavelengths. As a consequence a relative large fraction of the incident light is reflected by the interface. Due to the triangular shape of the interface, a standing wave pattern is formed in the region close to the tip of the triangle. Since the electric field at the boundary between zinc oxide and the silicon diode cannot be discontinuous, an evanescent field extends in the silicon diode. The "flame-like" power loss pattern disappears for longer wavelength and smaller periods of the texture.

#116966 - $15.00 USD Received 9 Sep 2009; revised 2 Oct 2009; accepted 3 Oct 2009; published 2 Dec 2009
(C) 2009 OSA

SIONYX1403000015.0085

SAMSUNG EX. 1002 - 1286/4148

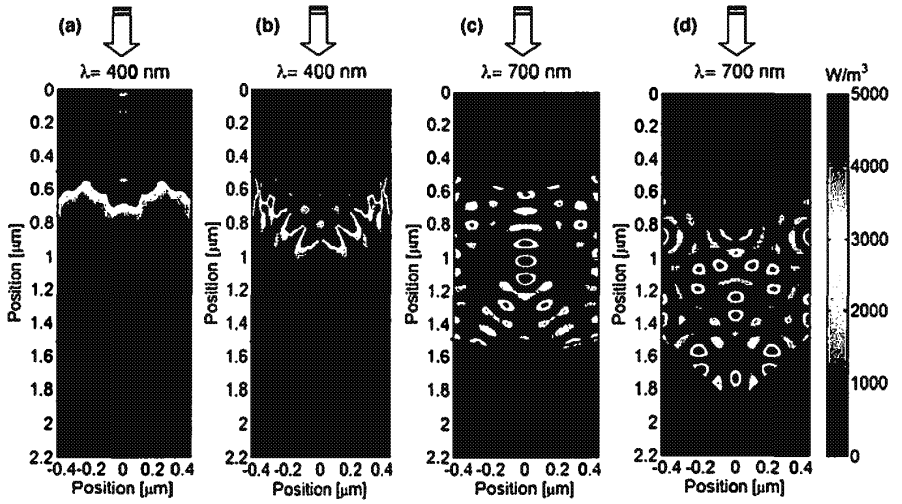


Fig. 3. Simulated power loss profile for textured unit cell with period 900 nm and profile heights of (a, c) 100 nm and (b, d) 400 nm under monochromatic illumination of (a, b) wavelength 400 nm and (c, d) wavelength 700 nm.

Due to a low absorption coefficient of silicon for longer wavelengths, the incident light has to be confined in the solar cell. Only if the light completes multiple passes inside the silicon layer the light can be completely absorbed. The power loss profile for a structure under monochromatic illumination of wavelength 700 nm is shown in Fig. 3(c) and 3(d). Diffraction from the front and back grating constructively interfere towards higher absorption. Within the multiple passes, the diffracted light interferes with the backward propagating waves and also with other diffracted waves from neighboring unit cells. By following the path of the different diffracted orders from the front and back grating, the highest intensities are observed where the second diffraction (front grating) orders from the neighboring cells meet at the center of the unit cell. A similar behavior is observed for lamellar gratings integrated in microcrystalline silicon solar cells [21]. The diffraction from the back reflection does not play a significant role in creating high intensities at the center of the unit cell. But the back grating contributes to the formation of high power losses close to the back reflector. The power loss close to the back reflector depends on the confinement angle of the back reflector. If the opening angle is close to 90°, the power loss close to the back reflector, as seen in Fig. 3(d), is maximized.

In the next step the quantum efficiency was determined The quantum efficiency is defined as the ratio of the power absorbed in the silicon layer with respect to the total power incident on the unit cell. The quantum efficiency was calculated using the equation

$$QE = \frac{1}{P_{opt}} \int Q(x,z)\,dx\,dz \qquad (2)$$

where $Q(x,z)$ is the time averaged power loss and P_{opt} is the optical input power. The collection efficiency taking the electronic properties of the material into account is assumed to be 100%. In other words, the internal quantum efficiency is assumed to be 100%. Therefore, the determined quantum efficiency defines an upper limit of the achievable external quantum efficiency. The calculated quantum efficiency is shown in Fig. 4 for a solar cell on a flat substrate, and two solar cells with integrated triangular gratings. The triangular profiles have periods of 100 nm and 900 nm, both with a profile height of 400 nm. For shorter wavelengths (300 – 500 nm), the quantum efficiency for the solar cell with a texture period of 100 nm is higher than that of the flat case. But with increasing wavelength, both devices exhibit the

#116966 - $15.00 USD Received 9 Sep 2009; revised 2 Oct 2009; accepted 3 Oct 2009; published 2 Dec 2009
(C) 2009 OSA

SIONYX1403000015.0086

SAMSUNG EX. 1002 - 1287/4148

same quantum efficiency. The thickness of the p-layer of the microcrystalline silicon p-i-n solar cell was assumed to be 30 nm for all the cells. For small and very small texture periods ($P \leq 200$ nm) the grating acts as effective index matching layer, so that the incoupling of light with short wavelength is improved. Due to the enhanced incoupling, the quantum efficiency for the shorter wavelengths is increased, whereas it remains almost unchanged for longer wavelengths (600 – 1100 nm). For longer wavelengths, the solar cells with grating period of 900 nm exhibits distinctly enhanced quantum efficiency compared to a solar cell on smooth substrates. Compared to that of a solar cell on smooth substrates, the optical path length is increased. For the blue and green part of the optical spectrum the quantum efficiency remains almost constant, since the absorption length for blue and green light is significantly smaller than the thickness of the solar cell. Subsequently the blue and green light will be absorbed within the first few hundred nanometers of the cell.

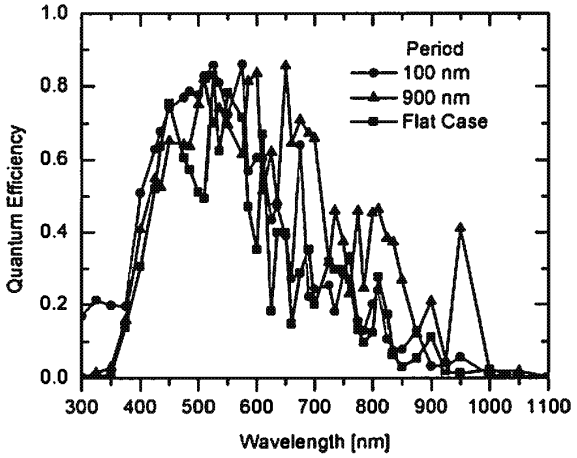


Fig. 4. Comparison of quantum efficiency for solar cell on smooth substrate with triangular structures of height 400 nm and periods of 100 nm and 900 nm.

Based on the quantum efficiency, the short circuit current was calculated for the sun spectra. The short circuit current was determined by

$$I_{SC} = \frac{q}{hc} \int_{\lambda_{min}}^{\lambda_{max}} \lambda \cdot QE(\lambda) \cdot S(\lambda) d\lambda \qquad (3)$$

where q is elementary charge, λ is wavelength, h is Planck constant, c is the speed of light and $S(\lambda)$ is the weighted sun spectrum (AM 1.5 spectral irradiance). The influence of the grating dimensions on the short circuit current in blue and the red/infrared part of the optical spectrum is shown in Fig. 5(a) and 5(b) as a function of the grating period. In Fig. 5(a) the short circuit current was calculated for a spectral range from λ_{min} = 300 nm to λ_{max} = 500 nm. The dashed line represents the short circuit current of a solar cell on a flat substrate. For larger texture periods the short circuit current is comparable to the solar cell on flat substrates. Due to the small penetration depth in this range of the spectrum, light trapping is negligible. For smaller and very small periods an enhancement of the short circuit current is observed. The enhancement of the short circuit current is caused by an improved incoupling of the light. Compared to that of a solar cell on a smooth substrate, enhanced short circuit current in this spectral range is increased from 2.9 mA/cm^2 to 3.6 mA/cm^2. This increase in the short circuit current is observed for periods smaller than 200 nm. For such small periods the wavelengths of the incident light is much larger than the period of the triangular grating, so that the

#116966 - $15.00 USD Received 9 Sep 2009; revised 2 Oct 2009; accepted 3 Oct 2009; published 2 Dec 2009
(C) 2009 OSA

SIONYX1403000015.0087

SAMSUNG EX. 1002 - 1288/4148

triangular grating acts as an effective refractive index gradient. The refractive index linearly increases from a refractive index of zinc oxide to the index of microcrystalline silicon. As a consequence the reflection at this particular interface is reduced and more light is coupled in the solar cell. If the grating period is smaller than $\lambda/(2n)$, where λ is the wavelength of the incident light and n the refractive index of the grating, the behavior of the grating can be described by an effective refractive index gradient. The triangular grating can be approximated by an effective refractive index gradient for periods equal to or less than 100 nm. For texture periods larger than 200 nm the short circuit current starts converging towards the value calculated for the solar cell on a smooth substrate.

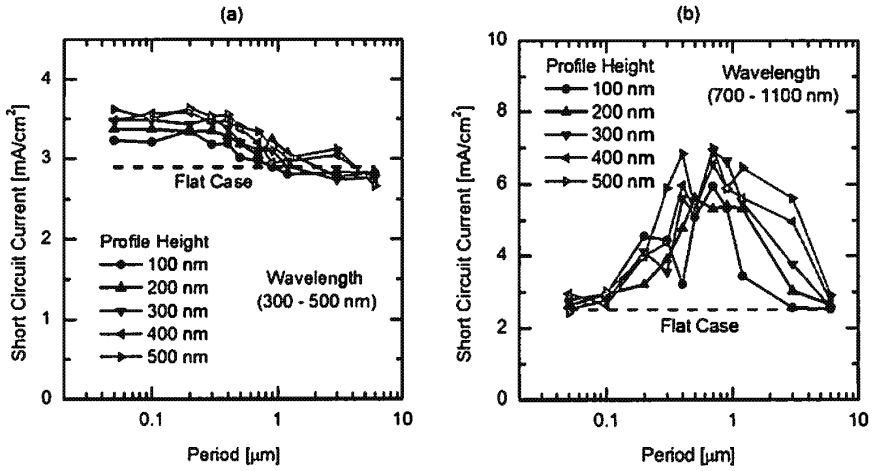


Fig. 5. Short circuit current for different triangular profile heights as a function of the period of the unit cell under (a) blue illumination (wavelength 300 – 500 nm) and (b) red and infrared illumination (wavelength 700 – 1100 nm).

The short circuit current under red and infrared illumination (from λ_{min} = 700nm to λ_{max} = 1100 nm) as a function of the period is shown in Fig. 5(b). The highest short circuit current is achieved for periods of 700 nm and 900 nm and a triangular profile height of 400 nm to 500 nm. Compared to the short circuit current of a solar cell on a smooth substrate, the short circuit current is increased by almost 200% from 2.5 mA/cm^2 to 7 mA/cm^2. The gain in the short circuit current for this part of the optical spectrum is due to light trapping of the incident light inside the silicon absorber layer. Figure 5(b) can be divided into three regions. For texture periods much smaller than the incident wavelength, the triangular grating can be described by an effective refractive index gradient. One might expect an effect similar to the previously described situation under blue illumination. However, the refractive index difference between zinc oxide and microcrystalline silicon is small for longer wavelengths, whereas the refractive index difference for short wavelength is relatively large. For a wavelength of 400nm 21% of the incoming light is reflected by the interface between zinc oxide and microcrystalline silicon, whereas the reflection is reduced to 12% for a wavelength of 800 nm. Therefore, the effective refractive index gradient has a distinct influence under blue illumination, whereas the influence is significantly reduced for red and infrared illumination.

For texture periods which are much larger than the incident wavelengths (Period > 3 μm); the short circuit current drops as well. Light is only diffracted at small diffraction angles, which can be seen by the grating equation

$$P \cdot n \cdot \sin(\theta_m) = m \cdot \lambda \qquad (4)$$

#116966 - $15.00 USD Received 9 Sep 2009; revised 2 Oct 2009; accepted 3 Oct 2009; published 2 Dec 2009
(C) 2009 OSA

SIONYX1403000015.0088

SAMSUNG EX. 1002 - 1289/4148

where P is the period of the grating, n denotes the refractive index of the propagating media after diffraction, m specifies the diffraction order and θ_m being the diffraction angle. With an increasing period, the diffraction angle for the integrated triangular grating is reduced. Henceforth the diffracted orders do not interfere with diffracted orders from neighboring unit cells. The constructive interference of the diffracted orders is essential for effectively trapping light inside the absorber layer. Thus the short circuit current for such large texture periods converges towards that of a solar cell on a flat substrate.

If the period of the triangular grating is comparable to the incident wavelengths the diffraction angles are large enough to propagate into their neighboring unit cell. Diffracted waves can thus interfere constructively within the thin absorber layer contributing to the higher short circuit current that is observed for periods of 700 nm and 900 nm. The higher current values are obtained for structures with triangular profile heights of 300 nm and above.

For the entire spectrum (300 nm – 1100 nm) the short circuit current was calculated to be 12.3 mA/cm^2, 15.33 mA/cm^2 and 18.9 mA/cm^2 for the solar cell on smooth substrate, with triangular structures of period 100 nm and 900 nm, respectively. The latter, where the period is in the range of the incoming wavelengths, has the highest short circuit current because it best utilizes the diffraction and scattering of light. The enhancement comes from light trapping of the longer wavelengths. On the other hand, with a texture period of 100 nm, the small gain in short circuit current is due to its better incoupling of the shorter wavelengths into the cell.

4. Summary

Light trapping and incoupling of light in thin-film microcrystalline silicon solar cells with periodic triangular profiles was investigated. Compared to that of a solar cell on a smooth substrate with 1 µm thick absorber layer, the short circuit current and quantum efficiency are enhanced with the introduction of triangular texturing. The degree of enhancement highly depends on the period of the triangular profile unit cell. When periods of the texture are smaller than the incident wavelength, enhancement in the shorter wavelengths (300 – 500 nm) of the spectrum comes as a result of better incoupling of the light into the absorber layer. For longer wavelengths (700 – 1100 nm) the short circuit current is distinctly enhanced if the period of the triangular profile unit cell is in the range of the incident wavelength. Along with the period, combination of the period and height of the triangular unit cell is also important. Optimal dimensions were found to be for combinations of the triangular profile where the opening angle of the triangle is equal or close to 90°. The total short circuit current for the entire spectrum is increased from 12.3 mA/cm^2 by 60% up to 20 mA/cm^2 for the best case triangular profile (period of 700 nm and height of 500 nm).

Acknowledgements

The authors would like to acknowledge the Institute of Energy Research (IEF-5) Photovoltaics, Research Center Jülich. Specifically, the authors thank C. Haase for providing optical data of the thin films. Furthermore, the authors like to acknowledge H. Stiebig from Malibu Solar for helpful discussions. A. S., R. N. and S. P. acknowledge financial support from the Global Climate Energy Project at Stanford and the Department of Energy Solar America Initiative (grant #DE-FG36-08GO18005).

#116966 - $15.00 USD Received 9 Sep 2009; revised 2 Oct 2009; accepted 3 Oct 2009; published 2 Dec 2009
(C) 2009 OSA

SIONYX1403000015.0089

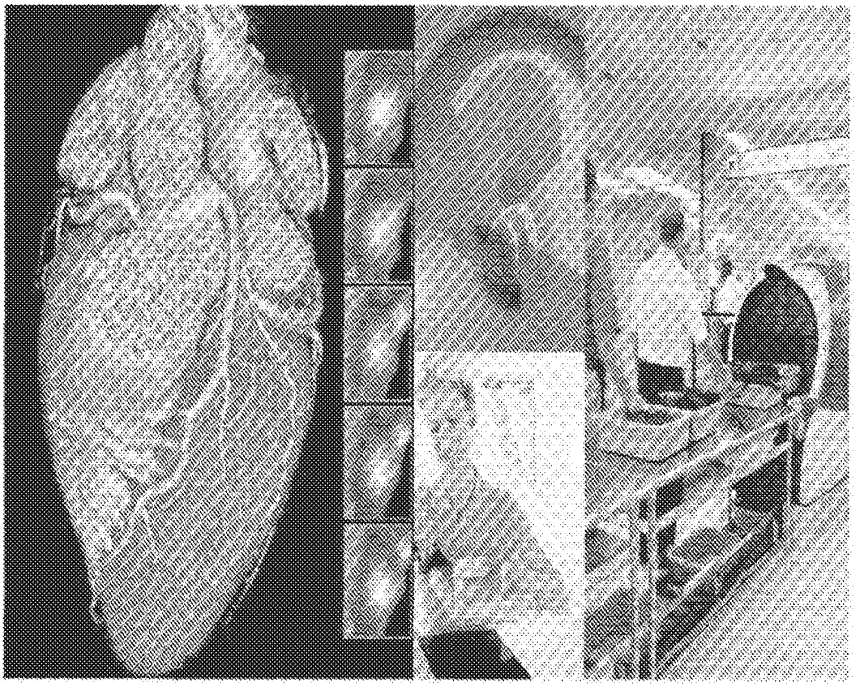
SAMSUNG EX. 1002 - 1290/4148

ANALOGIC

The World Resource for Health & Security Technology

Advances in Computed Tomography and Digital Mammography

Ruvin Deych and Sorin Marcovici
Analogic Corporation
Peabody, MA 01960, USA



ISMART, November 18, 2008, Kharkov

SIONYX1403000015.0090

SAMSUNG EX. 1002 - 1291/4148

Outline

ANALOGIC
The World Resource for Health & Security Technology

- **Advances in Medical X-Ray CT**
  - World market of X-Ray CT
  - Principles of third generation CT
  - Main performance parameters of modern CT
  - Data Measurement System in modern X-Ray CT
  - Future trends in X-Ray CT
- **Advances in Digital mammography**
  - Selenium/TFT technology
  - Performance of Selenium based mammography detectors
  - Manufacturing
  - Tomosynthesis

SIONYX1403000015.0091
SAMSUNG EX. 1002 - 1292/4148